Radiation Induced Processes in Biomolecules and Clusters in Controlled Beams

Thesis

Radiation Induced Processes In Biomolecules And Clusters In Controlled Beams

by

Michal Ryszka

A thesis submitted in partial fulfillment for the degree of Doctor of Philosophy

in the

Faculty of Science
Department of Physical Sciences

Supervisors:

Dr Samuel Eden

Prof. Nigel J. Mason

Milton Keynes

01 February 2016

THE OPEN UNIVERSITY

DEPARTMENT OF PHYSICAL SCIENCES

ABSTRACT

Doctor of Philosophy

by Michal Ryszka

The fundamental nanoscale processes that initiate radiation damage in biological material have not yet been fully elucidated. This represents a significant barrier to developing multi-dimensional simulations of radiation effects that can lead to advances in radiotherapy and radioprotection. This thesis explores UV- and electron-induced processes in DNA and RNA bases. Pure and hydrated clusters are studied in order to better understand the effects of the chemical environment on the radiation response of these important biomolecules.

Although extensive research has been carried out on the relaxation pathways of UV-excited nucleobases, no previous experiments have investigated bond breaking in neutral electronic excited states. This thesis reveals a new fragment ion from uracil ($C_3H_4N_2O^+$) that can be accessed by multi-photon ionization (MPI) but not by electron impact ionization (EII). This provides the first experimental demonstration that neutral excited state dynamics in a nucleobase can lead to bond breaking in the aromatic ring, as predicted in recent theoretical studies. The specific excited state dynamics have not yet been identified definitively and are the subject of on-going ultrafast pump-probe experiments in collaboration with Townsend and co-workers (Heriot-Watt University). The time-resolved measurements provide new evidence supporting a theoretically predicted relaxation pathway into long-lived triplet states.

Dissociative ionization of hydrated nucleobases and uracil–adenine clusters has been studied experimentally for the first time. Evidence for deamination reactions is observed in hydrated adenine complexes. The production of $C_3H_4N_2O^+$ fragments from uracil is strongly suppressed by clustering with water whereas the channel remains open in uracil–adenine complexes. To unravel the specific cluster-mediated dynamics and reactions responsible for these effects, further experiments are required with greater control over the cluster targets. Indeed the range of monomers and cluster configurations in neutral beams currently limits interpretations and direct comparisons with calculations. In response to this challenge, a new experiment has been built that enables radiation effects to be studied on molecules and clusters in Stark-deflected beams (MPI, EII, and future electron attachment measurements). Early results on nitromethane beams include a demonstration that studying EII as a function of the Stark deflector voltage can be used to deduce whether certain product ions came from monomers or from clusters.

Contents

List of Figures

List of Tables

List of Acronyms

DEA	Dissociative Electron Attachment
DFT	Density Functional Theory
DNA	Deoxyribonucleic Acid
EA	Electron Attachment
EII	Electron Impact Ionisation
IC	Internal Conversion
ISC	Intersystem crossing
MPI	Multi-photon Ionisation
REMPI	Resonance-Enhanced Multi-photon Ionisation
RNA	Ribonucleic Acid
TOF	Time-of-flight

ACKNOWLEDGEMENTS

During my PhD, I have had the privilege to work with many generous and inspiring people. I would like to choose this moment to acknowledge their impact on me and my project, as it would not be possible to complete it without them.

First and foremost, I would like to thank my supervisor, Sam Eden who has guided me throughout my PhD, and introduced me to the world of science. Many thanks go to Sam for giving me the opportunity to attend many conferences, workshops and scientific community meetings, and for introducing me to the members of scientific communities we participated in. Also, I would like to thank my second supervisor, Nigel Mason for all of his support and guidance.

A great deal of appreciation goes to Rahul Pandey, who has worked with me on the experiments, and who continued the projects when I had to retire from laboratory work to write this thesis up. I would also like to thank Marcin Dampc for his help with the ion trajectory simulations and low-energy electron physics.

Special thanks go to Jean-Christophe Poully, whose visits to The Open University were always very fruitful times. I also wish to thank Dave Townsend and all his team members for welcoming me to his laboratory in Heriot-Watt University, Edinburgh. I was very kindly received and learnt a great deal. I am very grateful to Jochen Küpper for his role in the Stark deflection experiment. Also I would like to mention here Jimena Gorfinkiel and her group for the interesting discussions we had on our meetings.

I am very grateful for the technical support at the Open University. My thanks go to Fraser Robertson for electronics, Chris Hall and his team (Kevin Dewar and Michael Abbott), and also Martin Percy for patiently making, and then remaking many parts for the experiments. I am also very grateful for the support from laboratory managers, Sandra Mills and later Jill Clarke, and for the help with orders from Beverley Bishop. All of you have made my life much easier.

I would like to offer my deepest thanks to Ewelina Szymańska-Skolimowska, who had supported me from the day I started my PhD project. Special thanks go to Gosia Śmiałek-Telega for all of her support.

I would like to also thank all my friends and colleagues, in particular to Anthony Davenport, Kasia Krzyżanowska, Binu Kumar Nair, Alex Nominé, Ziad el-Otell, Chris Rizk, Agnieszka Sieradzka, Bogumił Zalewski and, last but not least, Lily Ellis-Gibbings for making my life in Milton Keynes very enjoyable.

Finally, I would like to acknowledge the EPSRC (grant EP/J002577/1) and The Open University for funding my PhD.

Chapter 1

Introduction

This thesis investigates radiation-induced processes in biomolecules and their clusters. Electronic excitation, ionisation, and fragmentation pathways of DNA and RNA bases are studied following exposure to UV light and high-energy electrons. Concurrently, the thesis reports on the development of a unique experiment to probe the interactions of low-energy electrons with biomolecules and clusters in controlled beams. The common aim is to enhance our understanding of the fundamental processes by which radiation can initiate structural and chemical changes in biological macromolecules [49]. In particular, DNA lesions are understood to be key precursors of lasting biological damage (cell death, mutations, and cancers) and a major international research effort is currently devoted to applying nanoscale insights to improve cancer therapies [50, 51]. The present experiments also contribute to our understanding of the mechanisms responsible for the remarkable radio-stability of DNA and RNA, with implications for evolution and the molecular origins of life [52]. Despite the extensive applied interest, there is only limited understanding of the effects of the chemical environment (approximated here by clustering) on the radiation response of key biomolecules. This chapter introduces the general motivations and context for the present research.

1.1 Radiation induced processes in fundamental biomolecules and their clusters: this thesis and the wider field

While studies of isolated molecules generally provide the clearest data interpretations [53], equivalent experiments on clusters enable closer analogies to be drawn with biological environments where different isomeric forms, intermolecular energy transfer processes, and reactivity can be significant. Indeed molecular clusters are of fundamental interest as an intermediary between isolated molecules and bulk material. Clusters provide an important test case to extend the scope of experimental and theoretical techniques, for example surface analytical methods [54] and quantum chemical calculations [55], in order to characterise progressively more complex systems. Research of this kind provides insights to relate the specific information gained from studies of isolated molecules to a microscopic understanding of radiation-induced processes in condensed media. The study of clustering effects on molecular geometries [56], electronic configurations [57], and diverse types of reactivity [58, 59] has thus developed into a major interdisciplinary field. Indeed cluster research has demonstrated important new fundamental molecular interactions, notably *Intermolecular Coulombic Decay* [60]. A selection of significant research topics on molecular clusters are listed below.

- Creation and geometric form of clusters [61, 62, 63, 64]
- Changes of ionisation potentials, as well as the energies and (vibrational) coupling of excited and ionic states upon clustering [65, 66, 67]
- Transfer of charge and transfer of vibrational energy to inter-molecular modes [68, 69, 70]
- Dissociation of clusters [71, 72, 73]
- Characteristic properties of cluster-assembled materials [74, 75, 76]
- Microscopic aspects of nucleation phenomena [77]

The results in Chapters 4–7 were mainly recorded using an experimental system at the Open University (OU) to probe the electronic excited state dynamics and the ionic

states of biomolecules in isolation and in dipole-bonded clusters (hydrogen bonds and π-stacking). In particular, the experiments applied multi-photon ionisation (MPI) to investigate UV induced processes in DNA and RNA bases. The photophysics of nucleobases has attracted considerable interest as the electronic excitation and relaxation pathways can play important roles in the formation of DNA lesions [78, 79]. Understanding and, where possible, quantifying the dynamics and reactivity of excited nucleobases is therefore important for building molecular-scale models of DNA damage [80].

The present MPI and electron impact ionisation (EII) experiments have focused on adenine, uracil, and their hydrated clusters. We have also carried out experiments on thymine, deuterated uracil and hypoxanthine. In all of these molecules, ultrafast (sub-picosecond) relaxation to the electronic ground state is the dominant relaxation pathway following electronic excitation in the near UV [49] and this plays a central role in their radio-stability. However competing relaxation routes into relatively long-lived electronic excited states have also been identified and theoretical calculations have predicted that some of these pathways lead to significant structural changes in the excited molecules such as ring-opening [3]. These relatively long-lived excited states and structural changes can be an important source of radiation damage in DNA and RNA. However, to our knowledge, no previous experiments have been carried out on electronically excited nucleobabses to look for evidence of major structural changes (e.g. bond breaking on the aromatic ring as opposed to hydrogen abstraction and / or the modification of bond lengths / angles). Similarly, no previous experiments have been carried out on clustered nucleobases to look for signs of (unimolecular or intermolecular) reactivity initiated by electronic excitation. The experiments in Chapters 4–7 contribute to addressing these important gaps in the literature.

In addition to neutral electronic excitation, ionisation is a key process in radiation damage to biological tissue. Clearly, the break up of an excited nucleobase ion within a macromolecule represents a damage site and the fragments (neutral and ionic) can then react with nearby molecules to exacerbate the effect. Therefore the dissociative ionisation pathways of DNA and RNA bases have been studied for many years, stretching back to the 1960s [47, 81]. Nonetheless, a number of details remain unresolved including

the identification of certain fragment ions. The MPI mass spectra in this thesis answer some of these questions, taking advantage of good mass resolution, high signal to noise ratios, and comparisons with deuterated molecules. However, a much more striking issue in the literature is the scarcity of research (experimental or theoretical) into how clustering affects the dissociative ionisation pathways of nucleobases. The first PhD thesis by a member of the OU Molecular Clusters Group [2] presented MPI mass spectra of hydrated nucleobases but analysis of fragment ion production was restricted by high background signals. Aside from Barć's thesis, the closest precedent for the present experiments is Schlathölter et al.'s [82] study of ion impact induced dissociative ionisation in pure clusters of nucleobases. The present MPI and electron impact ionisation (EII) measurements in Chapters 4 and 7 provide the most detailed information to date on how clustering with water affects the fragmentation of nucleobase ions. Furthermore, the fragmentation of mixed nucleobase clusters (uracil–adenine: a base pair in RNA) is studied here for the first time.

It is challenging to derive detailed interpretations from the presently observed clustering effects. Indeed, comparisons between measurements and theory in this area of research are severely compromised by the experimental difficulty of selecting distinct neutral cluster targets as opposed to a broad distribution of monomer and cluster configurations. Therefore, a significant effort has been directed into the developing a new experiment that allows for better control over the molecular and cluster targets. The experiment utilises a *Stark deflection* method developed and optimised by Küpper (DESY, Hamburg), Meijer (Fritz Haber Inst., Berlin), and co-workers [16, 83, 84, 85]. These researchers have made considerable advances in the manipulation of neutral molecular beams using inhomogeneous electric fields, in particular separating specific cluster configurations from mixed supersonic jet [85], as well as different structural conformers [84] of gas-phase biomolecules. This method is based on accelerating molecules or clusters in strong electric field gradients, with resulting deflections as a function of the *effective dipole moment* / mass ratio. Indeed, large variations [86] in the dipole moments and polarisabilities of DNA base monomers, pure complexes, base pairs, and hydrates

provide considerable scope to improve target definition using Stark deflection. In addition to MPI and EII, the new experiment will probe electron attachment (EA) to Stark deflected targets for the first time.

The EA project is being carried out in parallel with Gorfinkiel, Fabrikant, and co-workers' development of theoretical methods to simulate low-energy electron interactions with clusters [87]. It is envisaged that the measurements will thus provide a test for the theory and hence lead to advances in our fundamental understanding of electron attachment in multi-molecular environments. The importance of studying EA to biomolecules arises from the observation that DNA strand breaks can be induced efficiently by sub-ionisation energy electrons [88] - the most abundant secondary product of ionizing radiation (5×10^4 electrons per MeV deposited). Free electrons are analogues of the secondary electrons released by ionisation events. The importance of elucidating electron attachment processes in biomolecular clusters has led to a significant number of internationally renowned groups currently focusing on the subject. Current high-impact experimental work includes Scheier, Märk (Innsbruck), Ellis (Leicester), and co-workers' studies of EA to clustered nucleobases, sugars, and amino acids embedded in helium droplets . Brøndsted-Nielsen (Aarhus), Cederquist (Stockholm), Huber (Caen), and co-workers [89] have revealed that a critical number of associated water molecules can completely suppress the collision-induced fragmentation of nucleotide anions. Denifl and co-workers' recent DEA experiments on pyrimidine clusters and pyrimidine-water clusters showed that hydration causes a strong modification of DEA *resonances* [90]. Understanding EA processes in biomolecular clusters can lead to improvements in biophysical models of radiation-induced damage and also has potential to stimulate radiotherapy innovations based on the use of radio-sensitising dopants to modify EA-induced damage processes.

1.2 Radiation damage to biological material

The effect of radiation on biological material is complex and involves a wide range of processes. Therefore the research effort into elucidating these phenomena is multi-dimensional and requires both bottom-up and top-down approaches. The timescales of radiation damage events are listed in Table 1.1 and cover 24 orders of magnitude [42] ranging from 10^{-15} s to 10^{9} s.

Table 1.1: Timescales of radiation damage in biological material. [42]

Stage	Time	Events
Physical stage	10^{-15} s	Electronic excitation and ionisation
	10^{-14} s	Vibrational excitation, dissociation and electron thermalisation
Chemical stage	10^{-12} s	Diffusion of free radicals
	10^{-10} s	Free radical reactions with the solute
	10^{-8} s	Formation of molecular products
	10^{-5} s	Completion of chemical reaction
Biochemical	1 s–1 hr	Enzymatic reactions, repair processes
Biological	1 hr–100 yrs	Genomic instability, aberration, mutation, cell killing, appearance of tumours and secondary tumours

This thesis provides information to help understand processes in the physical stage of radiation damage, most of all excitation (electronic and / or vibrational), ionisation, and dissociation. The increasing temporal scales in Table 1.1 are broadly linked to increasing spatial scales, extending to whole-body-scale effects such as the initiation of secondary tumours (*metastases*). In the bottom-up approach, understanding and modelling large-scale damage (cell, tissue, organ or organism) requires detailed knowledge of all nanoscale processes [78, 91]. Cellular damage begins with radiation interactions with important molecular constituents, notably proteins [92] or DNA. The molecules investigated in this thesis play essential biological roles: nucleobases are subunits of DNA and RNA, while their hydrated clusters are model systems for the aqueous conditions

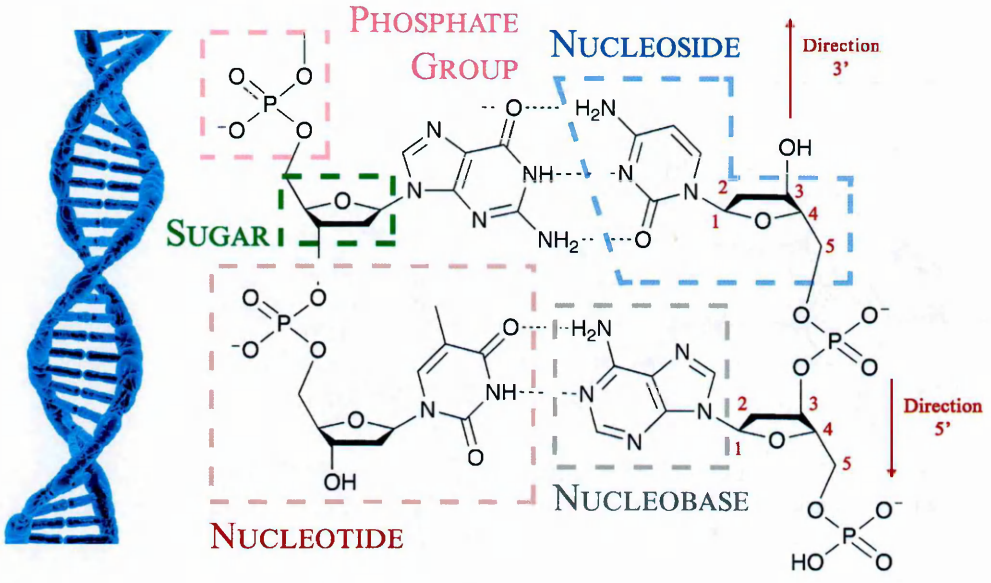

Figure 1.1: The structure of DNA: (left) an artist's impression on the double helix structure, and (right) the key molecular sub-units.

within a cell. The experiments mainly mimic direct (or *primary*) radiation interactions with nucleobases (notably UV absorption and fast electron impact). The planned electron attachment experiments will mimic indirect (or *secondary*) processes whereby a low-energy electron released by an ionisation event can interact with a nearby molecule of interest and potentially initiate nanoscale damage. Indeed the formation and dissociation of transient negative ions (*TNI*) is now recognised to play a major role in secondary radiation damage to DNA [88], adding to the important contribution of reactivity involving radical cations and neutrals (notably $OH^{\bullet}$) [93, 94].

Watson and Crick [95] were the first to identify the DNA structure – the right-handed double helix. The helix is made of a sequence of nucleotides, each consisting of a nucleoside and a phosphate group [96]. A diagram of DNA is shown in Figure 1.1. Nucleosides in turn are made of a five-carbon sugar, deoxyribose, and a nucleobase: adenine, thymine, guanine and cytosine. The coding of genetic information is performed by the specific sequence of nucleobases. Gregory et al. [97] have determined than the first human chromosome contains approximately 224 million nucleotides.

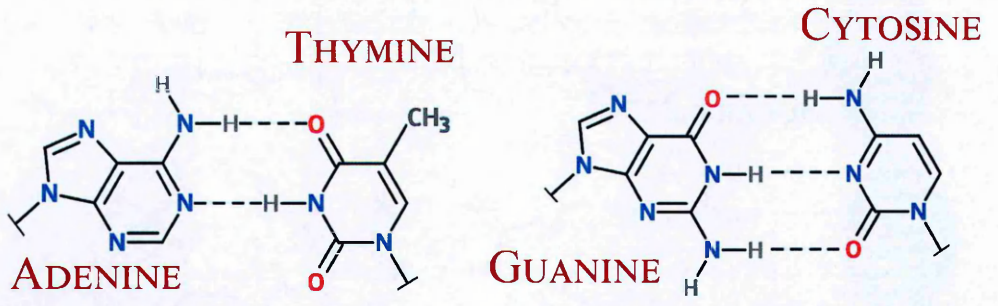

Figure 1.2: Complementary base pairs in the Watson-Crick bonding configurations. Adenine is bonded to Thymine (A–T pair) via two hydrogen bonds, whereas Guanine share's three hydrogen bonds with Cytosine (G–C pair).

The two strands of DNA are held together by hydrogen bonds between individual bases, with adenine always binding to thymine, and guanine to cytosine. Figure 1.2 shows the two base pairs in the *Watson-Crick* bonding configurations of stable DNA (although other hydrogen bonding configurations are possible between nucleobases in different situations). The π-stacking of nucleobases along the length of a DNA strand also plays an important role in the dynamics of DNA, for example by providing a pathway for Proton-Coupled Electron Transfer (*PCET*) [98]. This provides an incentive to study π-stacked nucleobase clusters as well as hydrogen-bonded complexes. It is also worth noting that nucleosides of the two strands are bonded to the phosphate groups in two different places – either via carbon C3 or C5 (see Figure 1.1). Therefore, the two strands have opposite directionality [99]. This opposite yet complementary nature of strands plays a critical role in DNA replication. Most cells in the human body replicate many times during a lifetime. In the context of this thesis, the key point here is that the chemical environment of a nucleobase changes significantly during the DNA replication process. Therefore we should not only consider the most stable structure of DNA when considering its nanoscale radio-sensitivity. Indeed, cellular radio-sensitivity is well known to vary between different stages of the cell cycle [100].

The chemical environment plays an important role in determining the structure of DNA, with the level of hydration being particularly significant [101]. Indeed, adequate hydration ($\sim$ 30 % by mass) is necessary to support the double-helical structure of the DNA [102]. Furthermore, solvation of the bases creates a unique pattern of water

molecules, depending on the sequence of the nucleotides. This helps the proteins to sense the base sequence from the outside of DNA [101, 103, 104]. The solvation shell around the double helix also allows specialised proteins to slide along the strands more easily [101]. Moreover, water molecules have been shown to mediate proton transfer reactions [105], stabilise neutral excited states [106], and lower ionisation energy [67]. However, while extensive studies have been carried out on condensed hydrated DNA and on its subunits in solution, the previous experimental research on hydrated clusters of DNA / RNA bases (notably offering more direct detection of radiation products) is scarce.

Although DNA stores the genetic information, another nuclei acid, RNA, is used in cells for carrying instructions for protein synthesis. The structure of RNA is similar to DNA, but with several key differences. Typically RNA has a single strand, with the deoxyribose replaced with ribose. Furthermore, thymine is replaced in RNA by uracil. Indeed, most of the results presented in Chapters 4–7 are on uracil or its clusters (including hydrated uracil and adenine–uracil complexes). Three types of RNA are used in the protein synthesis process: *messenger* (mRNA, shown in Figure 1.3) to carry genetic information from the DNA into to the ribosome (where the protein synthesis takes place), *transfer* (tRNA) to transfer amino acids to the ribosome, and *ribosomal* (rDNA) which is a building block of the ribosome itself. It is also interesting that RNA preceded DNA as the vessel to store genetic information in early life forms . Greater chemical- and radio-stability is believed to have driven the evolutionary transition from RNA to DNA [107], although the specific nanoscale mechanisms responsible for the increased radio-stability of DNA are not yet fully elucidated. Apart from its important role as an RNA base, another incentive to study uracil arises from the role of its derivatives (notably halogenated uracils) in chemo-radiotherapy as radiosensitisers [108, 109].

Figure 1.4 shows schematically the most common types of DNA damage found in irradiated media. The formation of nucleobase radical cations and pyrimidine dimers (i.e. the formation of a covalent bond between the neighbouring pyrimidine bases) make up 80 % of the UV induced damage [110]. The ionisation measurements on isolated and clustered nucleobases in this thesis are particularly relevant to these damage

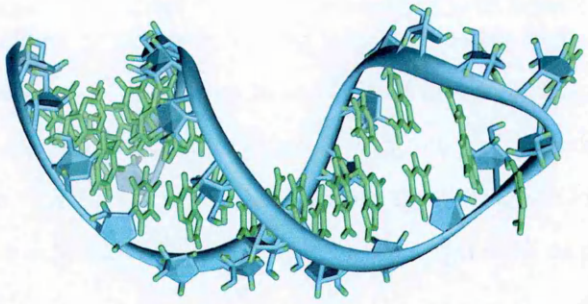

Figure 1.3: A hairpin loop of mRNA. The single strand loops onto itself. [1]

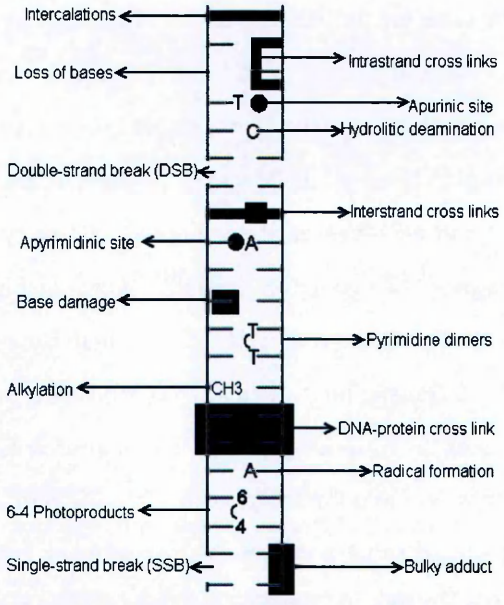

Figure 1.4: Common types of DNA damage. Reproduced from [2].

routes. Other important types of damage include intrastrand, interstrand, and DNA-protein cross links, where the sequence of links between the two strands is corrupted. Intercalations (i.e. insertion of molecules between the stacked bases) can also play a significant role. Moreover, DNA can suffer either loss or addition of bases, or base damage by dissociative ionisation. Although the quantities of these damages are measurable macroscopically, the underlying physical pathways leading to their creation are only partially elucidated. The study of gas phase biomolecules and clusters can provide insight to better understand these processes.

Single-strand breaks (*SSB*) and double-strand breaks (*DSB*) are recognised as particularly important classes of DNA damage. DSBs form when single strand breaks on opposite complementary strands occur in close proximity. The main cellular repair mechanisms for strand breaks are homologous recombination [111] (not always possible) and nonhomologous end joining [112]. However, the latter method can be viewed as imprecise because the break can be rebuilt with a different sequence of nucleotides. SSBs and DSBs can be measured macroscopically using the agarose gel electrophoresis method [113]. However, the electrophoresis method does not provide information on the location of the strand break or on the specific interaction that initiated it. Hence, it is important to complement these studies with more fundamental experiments and calculations. For example, in their seminal paper in 2000, Boudaïffa et al. [88] were able to demonstrate that DEA plays a central role in radiation damage to DNA by matching electrophoresis results with DEA measurements on gas-phase nucleobases.

Biologically relevant conclusions cannot be drawn from knowledge of the physical stage of radiation damage alone. In particular, physical damage to DNA or another key macromolecule must be considered in the context of biochemical repair. For example, the majority of cells possess defence mechanisms against oxidative damage, including base excision repair (*BER*) and nucleotide excision repair (*NER*) enzymes. Different types of DNA damage can be more or less dangerous according to the corresponding repair efficiency. Hence the propagation of harmful radiation effects is highly dependent on the specific nanoscale damage process. This point highlights the fundamental limitation of using macroscopic measures of radiation interactions with material (notably *dose*: energy deposited per unit mass) to predict biological effects. Indeed, current radiobiology and radiotherapy depends on empirical correction factors to adjust dose-based predictions according to radiation type (for example incident X-ray photons compared ions) and tissue type. Nanoscale mechanistic characterisation of radiation damage is required to advance beyond these approximations. Indeed, the evidence base is widely recognised as being inadequate to support dose-based predictions of the effects low-intensity radiation exposure.

1.3 Summary

The first stages of radiation damage in biological material (the excitation, ionisation and dissociation of important molecules due to primary and secondary radiation interactions) have not been fully elucidated. This represents a significant barrier to building multi-dimensional simulations of radiation effects that can overcome the limitations of models based on macroscopic data alone. Furthermore, understanding the radiation response of fundamental biological blocks in isolation and in diverse chemical environments can provide clues into the molecular origins of life. This thesis explores UV- and electron-induced process in DNA and RNA bases. Studies of pure and hydrated clusters contribute to bridging the complexity gap between understanding radiation effects in isolated molecules and in condensed biological media.

1.4 Layout of the thesis

Chapter 2 introduces the fundamental concepts that govern radiation interactions with single molecules and clusters, as well as the principles of *Stark deflection*. Chapter 3 gives a detailed description of the experimental setups that I have exploited and developed during this PhD. Multi-photon ionisation (MPI) and electron impact ionisation (EII) experiments on adenine and its hydrated clusters are presented in Chapter 4, with a particular focus on intra-cluster reactivity. The MPI and EII results in Chapter 5 provide insights into bond breaking and dissociation of electronically-excited and ionised gas-phase uracil. These measurements inspired the ultrafast, time-resolved MPI experiments in Chapter 6. The effects of clustering on the radiation response of uracil are studied in Chapter 7. Chapter 8 summarises the main results in the thesis and discusses future work.

Chapter 2

Theory

The first aim of this chapter is to give an introduction to the interactions of photons and electrons with molecules and molecular clusters. The chapter then addresses the principles of molecular manipulation using electric field gradients (Stark deflection). After a brief introduction to the Born-Oppenheimer approximation, molecular orbitals, electronic excitation, electron attachment, ionisation, and fragmentation processes are discussed. Intermolecular forces responsible for the creation of molecular clusters are introduced, with an emphasis on hydrogen bonding, as this is the strongest bonding mechanism of the clusters studied in this work. Understanding the non-radiative relaxation processes that govern the energy dissipation pathways is crucial to interpret the results presented in Chapters 4–7, while knowledge of electric field effects on molecules is required to understand the experimental development work in Chapter 3.

2.1 Molecules and clusters

2.1.1 The Born-Oppenheimer approximation

The Born-Oppenheimer approximation allows for the separation of molecular dynamics into separate, non-coupled electronic, vibrational, and rotational modes. Under this approximation, the total internal energy of a molecule can be expressed as the sum of the energies associated with the respective modes (equation 2.1).

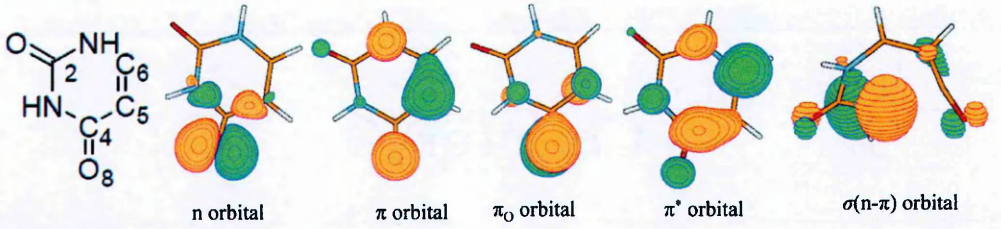

Figure 2.1: Electron density for five orbitals in the valence shell of uracil. Reproduced from reference [3].

$$E_{\text{total}} = E_{\text{electronic}} + E_{\text{vibrational}} + E_{\text{rotational}} \tag{2.1}$$

$$E_{\text{total}} = E_{\text{electronic}} + E_{\text{vibrational}} + E_{\text{rotational}}$$

This provides an invaluable framework to help us understand excited molecules, but it is important to keep in mind that it is only an approximation of nature. Coupling between electronic and vibration motions is discussed in Section 2.1.4.3. Rotational motion influences vibrational excitation in a manner similar to a centrifugal force, i.e. by elongating bonds [8]. However, these couplings are weak, and can be treated effectively as perturbations in most situations.

2.1.2 Molecular orbitals

The molecular orbital model describes electronic motion in molecules according to quantum-mechanical principles, i.e. using Schrödinger equation. Electrons are not assigned to individual atoms, but rather their quantum state is determined by taking into account all nuclei as well as other electrons. Molecular orbitals represent these quantum states in the same language as atomic orbitals describe electrons' states in isolated atoms, i.e. as a region of space with high probability of finding the electron. The measure of this probability is called electron density. In stable molecules, regions of high density are usually found around atoms and along bonds. Figure 2.1 shows the density of the valence shell electrons for five molecular orbitals in uracil. The right-most orbital if of particular importance for this thesis, as it corresponds to a ring-opening transition discussed in Section 5.4.2.

Solving the Schrödinger equation for molecular orbitals is not possible analytically except for the simplest molecules such as homo-nucleic diatomics. A number of numerical methods have therefore been developed to tackle this problem, with the *LCAO* (Linear Combination of Atomic Orbitals) [8] methods being the most readily used. Equation 2.2 shows how single electron molecular orbitals, φ_i, are built.

$$\varphi_i = \sum_s c_{si}\chi_s \tag{2.2}$$

Where c_{si} are weighing coefficient, and χ_s are the atomic orbitals. Specific selection of χ_s is called a basis set.

Molecular orbitals in the valence shell are often delocalised over two or more nuclei – allowing for the electrons to be shared, and lowering the total energy of the system. Delocalisation of orbitals plays a critical role in chemistry, producing orbitals of significantly more complex shapes than atomic orbitals. The highest occupied molecular orbital is often referred to as the *HOMO*, while the lowest unoccupied molecular orbital is known as the *LUMO*. Experiments presented in Chapters 4–7 only probe the valence shell. Valence orbitals obtained through *LCAO* are given letter designation according to their shapes and function:

- σ – for perfectly symmetrical orbitals about the internuclear axis
- π– a π-type orbital is created by sideways overlap of two adjacent p-orbitals
- n– for orbitals not contributing to the binding energy of the molecule.

If the orbitals have antibonding character, a star is added after the letter to indicate this, e.g. π^*. These definitions are descriptive and not mutually exclusive for molecular orbitals. Hence, some orbitals are described with two letter designation. For example, nucleobases studied in Chapters 4, 5 and 7 all have states of $n\pi$ or $\sigma\pi$ character, some of them also exhibiting antibonding character. Other types of orbitals (e.g. Rydberg) can also mix with valence orbitals. A detailed description of molecular orbitals and molecular bonding is available in reference [114].

2.1.3 Intermolecular forces

Intermolecular interactions are central to this thesis, as they determine the forces responsible for the aggregation of molecules into clusters. Throughout this thesis, the term "molecular cluster" is used to represent a complex consisting of two or more molecules. The molecules can be the same (homo-molecular), e.g. nitromethane dimers (and higher nitromethane clusters, see Section 3.5.1.1), or different (hetero-molecular clusters), e.g. uracil–water complexes described is Chapter 7. Other types of clusters (such as "valence clusters" with covalent bonds such as fullerenes [55], or atomic clusters, e.g. helium nano-droplets [115, 116, 117]), are not studied here. In this work, hydrogen bonding plays a particularly important role as it the mechanism responsible for both hydration of DNA / RNA bases and producing their dimers and base pairs. Intermolecular forces can split into the following categories [118]:

2.1.3.1 The London Dispersion forces & the Lennard-Jones potential

The London dispersion force arises due to fluctuations in electron density in atoms and molecules. A multipolar expansion is often used to describe the attractive part of dispersion forces, with the first non-vanishing term being the instantaneous dipole-dipole interaction. The interaction potential, V_{disp}, for the London dispersion forces is given in equation 2.3.

$$V_{\text{disp}} = -\frac{C}{r^6} \tag{2.3}$$

Where r is the intermolecular distance, and C is a constant dependent on polarisability and ionisation energy. Higher multipoles are often omitted. At short distances, repulsion due to electrostatic charge and (mainly) the Pauli Exclusion Principle starts to dominate, typically as $1/r^{12}$. Combining this with 2.3 gives the Lennard-Jones potential, V^{LJ}, shown in equation 2.4.

$$V^{\text{LJ}}(r) = \epsilon \left(\frac{r_0}{r}\right)^{12} - 2\left(\frac{r_0}{r}\right)^{6} \tag{2.4}$$

With ϵ and r_0 being the binding energy and equilibrium distance, respectively. Due to the weak nature of these forces [118], binding energies are relatively low, ranging from $<$ meV to several tens of meV (e.g. 24 meV for the Xe dimer)

2.1.3.2 Dipole-dipole and higher multipole interaction

For molecules possessing permanent dipole moments, their interactions tend to orient the molecules to achieve the minimum total potential energy of the system. For co-planar molecules with dipoles at an angle θ, the dipole-dipole interaction potential V^{DD} can be written in the form of equation 2.5:

$$V^{\mathrm{DD}}(r) = -\frac{2\mu_1\mu_2}{4\pi\epsilon_0 r^3}\left(1 - 3\cos^2\theta\right) \tag{2.5}$$

With μ_1, μ_2 being the permanent dipole moments, For two interacting dipoles of 1 Debye each, the bonding energy will be [118] approximately 15 meV at room temperature. Higher multipoles, despite generally not contributing much to the binding energy of the cluster, may play a role in determining the structure of the cluster. For example, the structure of $(HF)_2$ determined exclusively by considering dipole-dipole interaction would be linear. However, Dyke et al. have experimentally determined [119] that the angle between the molecular dipoles is approximately 60°. Examples of molecular clusters where quadrupole interactions dominate include dimers of C_6H_6 and perfluorobenzene (C_6F_6). Highly symmetrical molecules with low dipole moments, but strong quadrupole moments can result in T-shaped geometries for clusters [118], or π-stacking (shown in Figure 2.2). π-stacking is a broad term referring to a number of non-covalent interactions between π electrons. A detailed review of several types of interaction often refered to as π-stacking is available in reference [4].

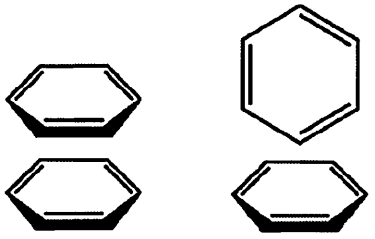

Figure 2.2: π-stacked (a) and T-shaped (b) benzene dimer. Reproduced from [4].

2.1.3.3 Induction forces

Asymmetry of the charge distribution of a molecule can result in an induced dipole moment in a nearby molecule. In this case, the two induced dipoles now interact with each other with an attractive potential V^{DID} given by equation 2.6.

$$V^{\mathrm{DID}}(r) = -\frac{\mu_1^2 \alpha_2}{(4\pi\epsilon_0)^2 r^6} \tag{2.6}$$

Where α_2 is the polarizability of the second molecule. Despite having a very similar mechanism to dipole-dipole forces, induction forces are far less susceptible to thermal effects – the induced dipole moment follows the permanent dipole moment if it gets thermally reorganised. For a 1 Debye molecule with a neighbouring molecule with polarizability volume of 10^{23} cm^3, binding energy will be approximately 8 meV.

2.1.3.4 Hydrogen bonding

A hydrogen bond can be schematically written as $A - H \cdots B$. The hydrogen is covalently bound to A, which is electronegative (e.g. Nitrogen, Oxygen, Fluorine etc.), and also interacts [118] with a second electronegative atom, B. Since A is electronegative, the charge concentrates around it, and moves away from the hydrogen. Hence, B, which is also electronegative, is electrostatically attracted to the hydrogen. At the same time, A and B repel each other, which tends to keep the hydrogen bond approximately linear. The binding energy is in 80% electrostatic, with the other 20% arising from induction and dispersion interactions, as well as charge transfer interactions. Figure 2.3 shows

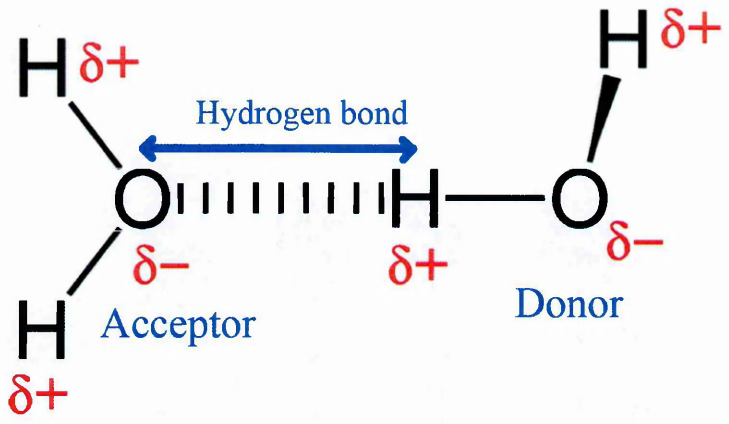

Figure 2.3: Hydrogen bonding in water dimer. Bond length and angles for temperatures from 0 to 80° C. can be found in [5] Local charge density denoted by δ

a schematic diagram of the hydrogen bonded water dimer. The hydrogen bond donor is the molecule that is covalently bonded to the hydrogen. The second molecule participating in the bond, with a partial negative charge, is the bond's acceptor. Typical hydrogen bonding energies lie in the range $100-250\,\mathrm{meV}$, but much stronger bonds have also been observed. For example, the strongest hydrogen bonded is difluoride negative ion [120, 121], with a bonding energy of $7\,\mathrm{eV}$. Properties of hydrogen bonding include:

- Bond angle is close to 180°.
- H$\cdots$B distance is significantly longer than the AH covalent bond.
- The associated covalent bond is stretched and its vibration is red-shifted

Hydrogen bonding is particularity important in the context of this thesis. Hydrogen bonds are the strongest bonds that form between the neutral molecules discussed in Chapters 4 and 7. In particular, purine derivative nucleobases bases (adenine, guanine) form hydrogen bonds with pyrimidine derivatives (thymine, cytosine and uracil) in DNA and RNA. Hydrogen bonds provide a potential "bridge" for proton transfer, and also participate in determining secondary and tertiary structures of proteins.

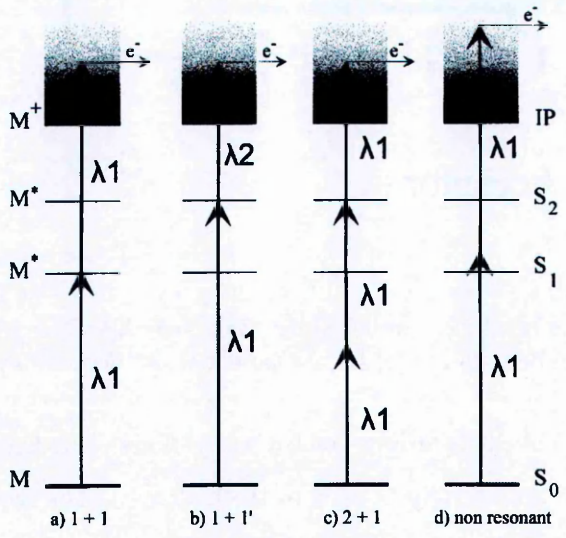

Figure 2.4: Four types of MPI processes: (a) one photon resonant one-colour two photon ionisation (1+1); (b) one photon resonant two-colour two photon ionisation (1+1'); (c) two photon resonant one-colour three photon ionisation; and (d) non-resonant two photon ionisation. Reproduced from [6]

2.1.4 Multiphoton ionisation

Photon absorption processes that lead to the ionisation of the molecule can be characterised by the number of photons absorbed: single or multiphoton. Multiphoton processes are typically labelled in a $(n + m)$ fashion, where n is the number of photons that bring (or "pump") a ground state molecule into a neutral excited state, and m is the number of photons that are further required to remove (or "probe") the electron from the bound state into the continuum. For example, a process that requires only one photon to promote the molecule from the ground state into an excited neutral state, and one further photon to ionise it, will be labelled as (1+1). If wavelengths of n and m are the same, the technique is called one colour, and if different, two colour. Two colour MPI is denoted by putting a prime next to the m number, e.g. (1+2'). Figure 2.4 shows four types of multiphoton processes [6]. In the present work, the MPI method is used to investigate electronic excited states, as well as providing information about ionic states. Some other types of MPI investigate vibrational excitations – molecules are pumped into a vibrational state, and then ionised by another photon.

At a given photon fluence it is clear that the longer the lifetime of the neutral excited state, the higher the probability for the molecule to absorb another photon (or photons) that would ionise it. If the process is resonant, i.e. the wavelength of the n photon matches the energy gap between the ground and the excited states, the technique is often called Resonance Enhanced Multiphoton Ionisation (*REMPI*). However, this term is not prefered in this thesis as the electronic excitations occurring in the present experiments are energetically broad. Non-resonant processes via virtual excited states induced by the laser are more experimentally challenging as the virtual excited states are very short lived. Schechter et al. [122] reported seeing weak non-resonant MPI signals from xenon at 266 nm with a fluence of 7.49×10^9 W/cm^2. This is at least one order of magnitude higher fluence than achievable with the nanosecond system used for most of the experiments in this thesis (see Chapter 3 for experimental description and Chapters 4, 5 and 6 for results), but still well below the level where field ionisation becomes noticeable ($\sim 10^{13}$ W/cm^2 [123]).

The evolution of neutral electronic excites states is an extensive research topic with numerous applications. This is often studied with time-resolved multi-photon ionisation, where n photons are supplied by a Pump laser and m photons are provided by a Probe laser. The time delay between pump and probe pulses gives the molecule time to evolve before the probe pulse arrives. Typical timeframes for electronic, vibrational and rotational excitations are $< 10^{-15}$, 10^{-14} to 10^{-12}, and 10^{-13} to 10^{-11} s, respectively. For the technique to be most effective and instructive, laser pulses are to be kept as short as possible, typically on femtosecond timescale[1], while achieving high fluence.

In the non-resonant case [124], the order of non-linearity, K_0, provides an estimation of the number of photons absorbed (the "photon order") and follows relation shown in equation 2.7:

$$K_0 = \frac{\partial \log N_i}{\partial \log I} \tag{2.7}$$

[1]For the OU experiments (Chapters 4, 5 and 7) one-colour nanosecond timescale laser was used. Ultrafast experiments described in Chapter 6 were performed with a two-colour femtosecond timescale laser.

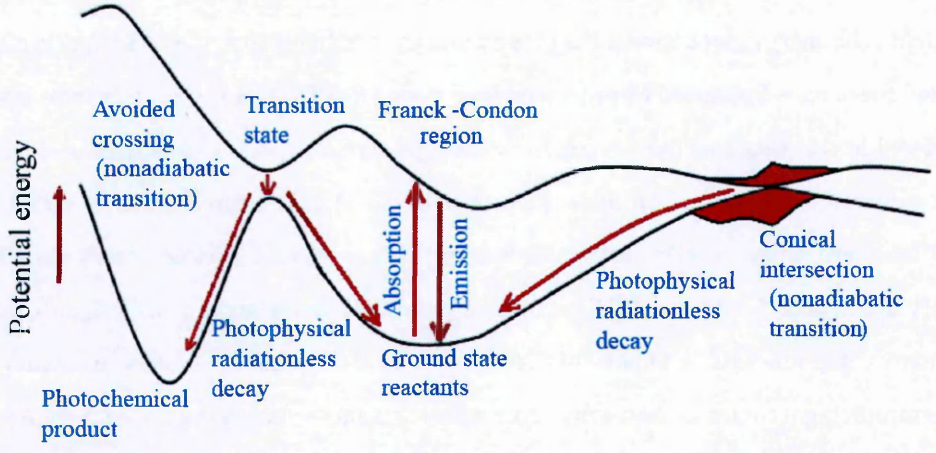

Figure 2.5: Illustration showing potential energy curves for two states. Such curves could be interpreted as fragment of full potential energy hypersurface, plotted in one dimension. Common features found on hypersurfaces are marked. Reproduced from [2].

Where N_i is the number of ions produced (ion yield), and I is the laser pulse intensity. This simple relation is however not true near sharp resonances [125], where a dramatic increase in ion yield is observed[2]. Near resonance, K_0 no longer represents the number of photons absorbed due to the shift of molecular energy levels in the laser-induced electric field (the Stark shift, see Section 2.4.2). The laser intensities used to derive photon orders in the present work (up to 5×10^7 W/cm^2) are below the level where Stark shifts have been reported to be noticeable: $5 \times 10^7 - 10^9$ W/cm^2 [124]. However, this shift is state-dependent. In the context of the OU MPI experiments, where the ionisation relies on an absorption into a broad neutral excited state, it is important to note that broad states are not affected significantly by Stark shifts [126], and therefore relation 2.7 provides valid method to derive photon orders [127, 128].

Non-radiative evolution of the molecule is determined by the shape and features of its potential energy hypersurface, which is a result of plotting the molecule's potential energy as a function of its internuclear distances for all degrees of freedom. The main features commonly found on such hypersurfaces include (see Figure 2.5 for reference) the Franck-Condon region, local minima, avoided crossings and Conical intersections.

[2] e.g. in Section 5.5 of this work.

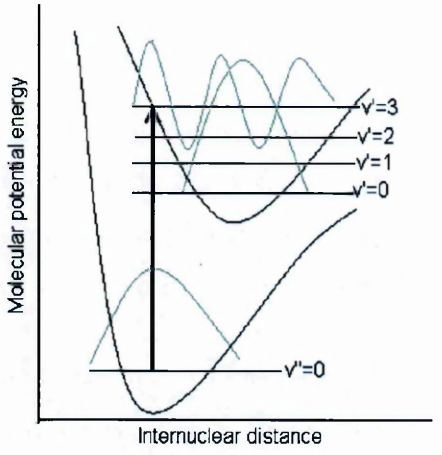

Figure 2.6: Franck-Condon principle illustrated. The most probable electronic transition will induce a change in the vibrational state from V"=0 to V'=3. Reproduced form [2].

2.1.4.1 Franck-Condon principle

Following photon absorption, electronic transitions in molecules occur on a very fast timescale. Indeed, the Franck-Condon principle states that the transition is so fast that the nuclei have no time to change their positions. As a result, the molecule finds itself in a vibrational state with the same internuclear distance as the original state. The most probable transition occurs from a point where vibrational motion is about to reverse, i.e. the kinetic energy associated with the vibration is at its minimum. This can be schematically represented by the vertical line in Figure 2.6. Hence, the associated excitation energy is called *Vertical*. In contrast, in a transition directly into the lowest vibrational level of an electronic excited state, the associated energy is named *Adiabatic*.

2.1.4.2 Radiative decay

After excitation into a neutral excited state, a molecule can de-excite radiatively via one of the following processes:

- Fluorescence – for deactivation involving states of the same multiplicity. Transitions typically occur between 0.01 and 10 μs.

- Phosphorescence – for transitions involving a change in the multiplicity, e.g. triplet-singlet. Phosphorescence generally occurs between ground vibrational states of the excited triplet and the vibrationally-hot electronic ground state. These are slow processes with lifetimes up to several minutes.

The two decay mechanisms described above are too slow to have a significant effect in MPI experiments described in Chapters 4, 5 and 7, as the molecules investigated in this thesis relax in a radiationless way on much shorter timescales.

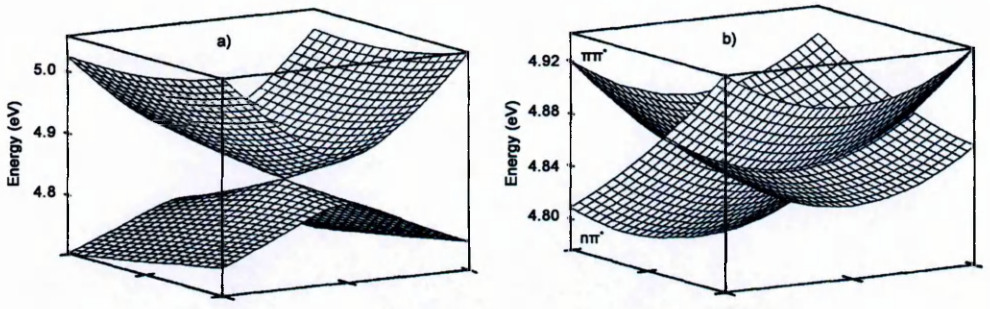

Figure 2.7: Diagrams showing a close-up of the $S_2 - S_1$ conical intersection in pyrazine. Adiabatic surfaces are shown in (a), diabatic in (b) Reproduced from [7]

2.1.4.3 Non-radiative decay

Non-radiative decay mechanisms of polyatomic molecules are discussed in detail in [8]. Potential energy hypersurfaces derived under the Born-Oppenheimer approximation (nuclear motion is slow enough for the electrons to adjust immediately) are referred to as adiabatic potential energy surfaces. When the Born-Oppenheimer approximation breaks down [129, 130, 131] (which is typical in the region where the energy gap between two states is low), a representation using diabatic surfaces is more convenient. Figure 2.7 shows the two approaches for describing the $S_2 - S_1$ conical intersection in pyrazine, studied theoretically by Woywod et al. [7] using *CASSCF* (complete-active-space self-consistent-field) and *MRCI* (multireference configuration interaction) techniques.

To discuss non-radiative evolution in more detail, let us consider Figure 2.8. Two adiabatic surfaces represent excited (upper, E_-) and ground (lower, E_+) electronic states. Each of these surfaces comprises two diabatic lobes–representing products (white) and substrates (grey). The crossing region is called a conical intersection (*CI*). Following electronic excitation in the Franck-Condon region (labelled FC in Figure 2.8), the system finds itself on a slope of the potential energy hypersurface. In the vicinity of the FC region, the E_- potential energy hypersurface has the shape of a well. A side of this valley might have a shape of a local maximum along a particular internuclear coordinate. Then, the top of this local maximum is denoted as the saddle point (TS – transition point in Figure 2.8). Depending on the amount of kinetic (i.e. vibrational) energy, the system might go through the Franck-Condon minimum (M^*) and reach the top of the

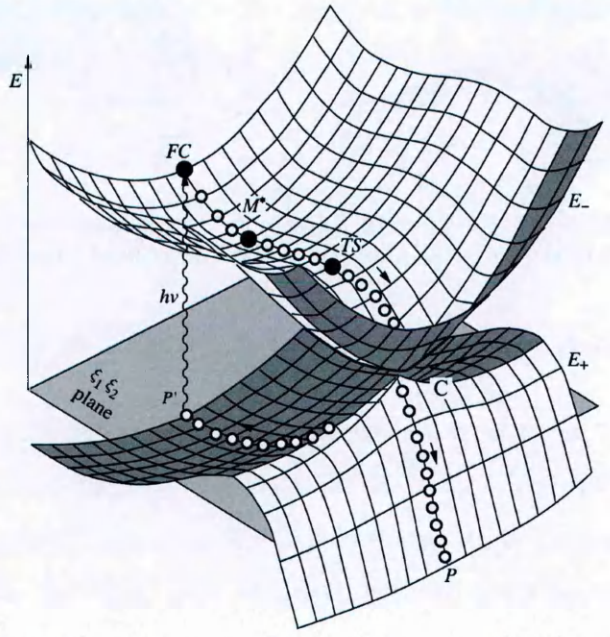

Figure 2.8: Illustration of non-radiative decay via a conical intersection. Reproduced from [8]

saddle point. This local energy barrier might also be overcome by tunnelling. If the system goes over the saddle, it will with near unity probability go through the conical intersection (C) and find itself back on the surface representing the electronic ground state. After going through the conical intersection, the system can either evolve back to the ground state minimum (point P'), or continue the other way, towards point P, which could lead either to dissociation or more complicated dynamics. The total energy of the system must be conserved, so the transition only occurs if there is a way to dissipate the excess energy to either vibrational, rotational or translational degrees of freedom. Furthermore, energy can be transferred to a neighbouring molecule.

The multiplicity of a state of a molecule is equal to $2S + 1$ where S is the sum of the spin quantum numbers of the electrons in the molecule. If all electrons' spins are paired ($S = 0$), this leads to a singlet state. Alternatively, antiparallel orientation of spins leads to $S = 1$ and multiplicity of three. Such states, being triply degenerate (i.e. there are 3 possible orientations of spin vectors and their projections) are called triplet states. Depending on the multiplicity of the states involved, the transition is termed:

- Internal conversion, IC – if there is no change in the multiplicity (i.e. singlet-singlet or triplet-triplet)
- Inter-system crossing, ISC – when the multiplicity changed during transition, i.e. singlet-triplet

Transitions that involve a change of multiplicity are normally strongly forbidden, since the spin-overlap integral is zero (spins are orthonormal). The spin overlap integral, M_s, is shown in equation 2.8.

$$M_s = \int S_i S_j \, \mathrm{d}r_s \tag{2.8}$$

Where S_i and S_j represent spin functions of the respective states involved in the transition. Transitions of this kind can, however, occur due to spin-orbit or vibronic coupling. The Spin-Orbit interaction can be modelled using perturbation theory by introducing for every electron a perturbing Hamiltonian, $\hat{H}_{\mathrm{S-O}}$, that can be written in form of equation 2.9.

$$\hat{H}_{\mathrm{S-O}} = \zeta \cdot \left(\hat{L} \cdot \hat{S}\right) \tag{2.9}$$

Where ζ is the Spin-Orbit coupling constant, L - orbital angular momentum operator, and S - the spin angular momentum operator. It can be shown that the perturbed triplet state can be expressed by equation 2.10:

$$\Psi_{\mathrm{T}} = \Psi^0_{\mathrm{T}} + \sum_i \frac{\langle \Psi^0_{\mathrm{T}\,i} | H_{\mathrm{S-O}} | \Psi^0_{\mathrm{T}} \rangle}{(E_{\mathrm{T}} - E_{\mathrm{S}\,i})} \cdot \Psi^0_{\mathrm{S}\,i} \tag{2.10}$$

Where S_i is the i-th singlet state. Hence the probability of the inter-system crossing is a function of the coupling matrix element. For atoms, the strength of spin-orbit coupling depends on atomic number as z^4 [132]. In molecules, the transition is enhanced in the presence of a heavier atom, but the z^4 dependence needs to be scaled to represent the probability that an electron is near the atom. Indeed, substitution of an oxygen atom by sulphur in nucleobases has been reported to disable IC and make ISC the most

efficient radiationless deactivation pathway (see Richter et al.'s work [37] and references therein).

Transitions forbidden on the ground of mismatched molecular symmetry also can be weakly allowed if the molecular geometry is briefly distorted due to vibrational motion. This mixing of vibrational and electronic motions [133] is called vibronic coupling. The fact that transitions involving a change of multiplicity are only very weakly allowed leads to triplet states having long lifetimes.

2.1.4.4 Dynamics in molecular complexes

In addition to transitions observed in isolated molecules, molecular complexes allow for extra channels of dynamics, mainly:

• Charge-transfer transition – Occurs in complexes containing both electron donors and acceptors [59].

• Formation of Excimers - An excimer is a complex that is weakly bound if one member is electronically excited but dissociates when it returns to ground state [134]. Clusters formed on the same principle as excimers but with more than two species are called exciplexes.

• Proton Transfer – Transfer of a proton from an excited or ionised molecule in a cluster into a neutral partner ([135, 136]). Proton transfers are routinely observed in the hydrogen-bonded clusters studied in this work (see Chapter 7). Indeed, the presence of protonated species is an indicator of good clustering conditions.

• Intra-Penning Ionisation – If molecule A in a complex is excited above the ionisation potential of another member of the cluster (B), the system can [137] lower its total energy by autoionizing B at the expense of A's excitation ($A^*B \rightarrow AB^+ + e^-$).

2.2 Ionisation and appearance energies

The ionisation energy is the energy required to remove an electron from an isolated molecule. The molecule is assumed to be in its ground vibrational state. There are

two ionisation energies: vertical and adiabatic – the naming convention follows that of vertical and adiabatic excitation energies described in Section 2.1.4.1. As the energy required to remove an electron depends on the orbital that the electron is removed from, a term first, second, etc. is often added. Hence, the first ionization energy is the energy required to remove an electron from the HOMO.

By analogy, the appearance energy of a given fragment ion is the minimum energy required to produce the ion by excitation of the ground-state molecule to a dissociative ionic state. The analysis of fragment ion production from molecules and clusters is a major part of this thesis.

2.3 Electron induced processes

Electron induced processes is a general term encompassing all phenomena initiated by an incident electron. In the context of this thesis, the most important ones are Electron Impact Ionisation (*EII*) and Electron attachment (*EA*). The former is routinely used to draw comparisons with MPI in Chapters 4, 5, and 7. EII is also the main probe for optimising the Stark/EA experiment (Section 3.4). If an incident electron has $\geq$ the relevant threshold energy, it can excite a molecule to any neutral or ionic state accessible from the molecule's initial state (i.e. electronic and vibrational ground state in most of the experiments described in this thesis). Electron attachment, however, follows a different mechanism – trapping the electron depends on discrete states, and hence is a resonant process. The study of electron attachment in controlled molecular beams is the main objective of the Stark / EA experiment.

Another electron induced phenomenon, not probed in this work, is electron-induced neutral electronic excitation. Electron collisions can initiate "optically forbidden" transitions with far greater efficiency that photons, as they are not subject to optical selection rules. A detailed description of electron-induced neutral electronic excitations can be found in reference [138].

2.3.1 Electron Impact Ionisation

The theory for electron impact ionisation, despite it being one of the first electron-molecule interactions to be investigated [139], is still not fully resolved [138]. The principal difficulty is the treatment of both continuum electrons (the projectile and the ejected electron), as well as the ion, until they are well apart. This requires a full solution to a three body problem. Additional complexity arises since ionisation is rarely a single channel process. Ions can be produced directly or via autoionisation following impact-induced excitation, including Auger processes (these involve relaxation following the promotion of an electron from an inner shell orbital to an unoccupied orbital). The ionisation of molecules can be non-dissociative or dissociative, often with multiple channels resulting in the production of the same fragment ion.

Electron impact ionisation can be characterised by various cross sections, such as total cross section, partial cross sections and differential cross section. These can be measured experimentally (with varying levels of difficulty; the necessary characterisation of beams seeded with low vapour pressure species such as nucleobases is particularly challenging) or calculated at various levels of theory (such as Binary Encounter Theory, Plane-Wave Born Approximation, or First Born Approximation). Total EII cross sections for DNA bases and uracil, calculated using the binary-encounter-Bethe model, are shown in Figure 2.9. The typical energy (200 eV) used in electron impact experiments described in this thesis has been marked. For these molecules, the cross section increases in an intuitive manner with the molecule's size.

2.3.2 Attachment

Electron attachment (*EA*) will be probed in the future using the Stark/EA experiment (the development of which is described in section Section 3.4. However, this thesis does not present EA results so it is only described very briefly here. References [140, 141] are recommended for the full review of EA processes.

Electron attachment occurs when a free electron attaches to an atom or a molecule to form a transient negative ion (*TNI*). The process reveals information about the

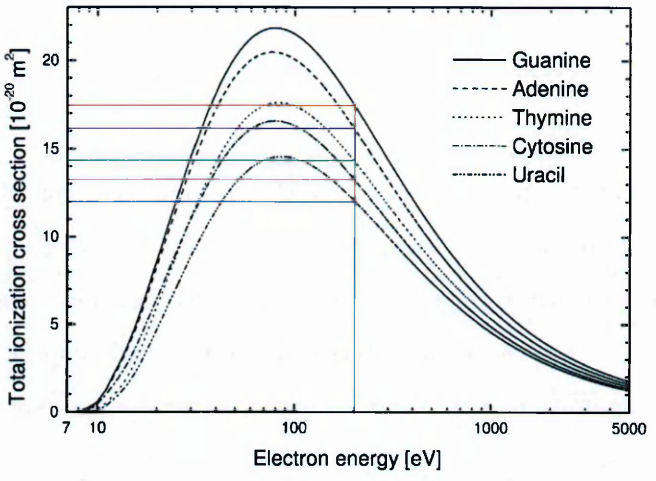

Figure 2.9: Total ionisation cross sections of all DNA bases and uracil, calculated using an Independent Atom Model. Reproduced from [9].

symmetry, binding energies, and spatial charge distributions of molecular orbitals that are not occupied in the neutral molecules. The formation of a TNI is in a resonant process, with resonant energies generally below 20 eV. TNIs are thermodynamically unstable species (with typical lifetimes in the range of $10^{-15} - 10^{-14}$ s) and can decay via two mechanisms: an *autodetachment* or a *dissociation.* In the latter case, the TNI can dissociate into a stable negative ion and a neutral fragment in a process referred to as Dissociative Electron Attachment (*DEA*). DEA processes are of particular importance in biomolecules due to their link with single and double strand breaks of the DNA [88]. TNI resonances can be divided into four categories: *shape resonances*, *core excited shape resonances*, *Feshbach resonances* and *vibrational Feshbach resonances.*

In a shape resonance, the incident electron is trapped in a potential well with the molecule in its ground electronic state. The potential well arises from the interaction of an attractive polarisation potential with a repulsive centrifugal potential, due to the relative motion of the two bodies. The trapping occurs due to the shape of this potential, giving the resonance its name. Most of the shape resonances occur at low energies ($0 - 4$ eV), and have lifetimes in the range of $10^{-15} - 10^{-10}$ s or longer.

Core excited shape resonances (or valence excited resonances) as well as Feshbach resonances form when the target molecule is in an excited electronic state, rather than the

ground state. Similarly to the shape resonances, in the core excited shape resonances the trapping occurs due to the shape of the effective potential well. Feshbach resonances describe the formation of anion with an electron trapped in a virtual state of lower energy that the neutral excited state of the target molecule. Core excited shape resonances have two electrons in orbitals that are normally unoccupied, and a hole in a lower, normally occupied orbital. Typical energies of core excited resonances lie within the $8 - 12$ eV range.

Vibrational Feshbach resonances involve vibronic coupling in the target molecule. The energy of the incident electron is distributed across the vibrational modes of the molecule. The anionic state has energy lower than the ground state of the parent molecule. Hence, this type of a resonance often leads to a production of stable anions. For many polyatomic molecules TNIs exhibit very long lifetimes against autodetachment ($> 10^{-6}$ s) [141].

The long range attraction of electrons to neutral molecules depends on the molecule's dipole moment, while vibrational excitation (vibrational Feshbach resonances), and electronic excitation (core-excited shape resonances) also play key roles. Clustering modifies dipole moments, molecular geometries (and hence vibrational excitation), and electronic states so it has major effects on EA. Accordingly, several papers have demonstrated shifts in DEA resonances [142, 90], as well as in EA cross sections [87] due to clustering. To clarify these effects, we aim to perform the first EA experiments on selected clusters.

2.4 Stark Deflection

In any crossed beam experiment on molecules or clusters, it is clearly advantageous to have the tightest possible control over the target. Ideally, the target should be in a single, and pre-defined state (e.g. the electronic, vibrational and rotational ground state of a specific isomer). Charged particles can be manipulated relatively easily using electric fields, according to their mass-to-charge ratio, or with devices such as ion-mobility spectrometers. The manipulation of neutral beams poses a much greater experimental challenge [143]. The MPI / EII experiments presented in Chapters 4, 5 and 7 only enable

the target to be modified by changing the expansion conditions of the supersonic jet. This offers only limited control. The new Stark / EA experiment (development described in Chapter 3) applies the Stark-deflection technique to manipulate neutral species in our molecular beams. This method uses an inhomogeneous electric field and was first used to deflect small molecules [144], and hence determine their permanent dipole moments. More recently, Filsinger et al. [83] extended it for the separation, alignment and orientation of large polar molecules (3-Aminophenol, Benzonitrile, Iodobenzene). Trippel et al. [85] have recently used this technique for the separation of Indole – H_2O clusters [85] from indole molecules, water molecules, and larger indole–water clusters in a mixed beam.

Stark deflection uses strong inhomogeneous electric fields to interact with a beam of polar molecules or clusters. The method can be rationalised in classical terms as follows. The polar molecules orient themselves in the field direction. Then, due to the inhomogeneity of the electric field, one side of the dipole finds itself in a stronger field than the other. Hence there is a net force applied to the molecule. The resultant acceleration is proportional to its dipole moment over mass ratio. The following sections introduce the key quantum concepts of the technique.

2.4.1 Stark effect on molecules in strong electric field.

Let us consider a molecule in an electric field of intensity defined as $\varepsilon = |\vec{\varepsilon}|$. The symbol ε has been chosen here to avoid confusion with energy E. The Stark shift, i.e. the change of energy of a quantum state due to the presence of an external electric field, can be calculated using second-order perturbation theory, with the states labelled with quantum numbers J, and M, for the angular momentum, and its projections onto the axis of the external field, respectively. In the idealised case of a rigid rotor molecule, it is useful to introduce a dimensionless coupling constant, $\omega = \mu\varepsilon/R$ with the permanent dipole moment μ (in Debye, or C · m in S.I. units) and rotational constant R (in units of energy).

The force acting on a dipole in an electric field depends on the orientation of the dipole with respect to the field. The energy of some quantum states will increase with field,

or, in other words, it is more favourable for them to move to a region of space where the field is lower. Hence, they are called *low-field-seekers*, *LFS*. Similarly, states whose energy decreases with the field are known as *High-field-seekers*, *HFS*. In weak fields, molecules rotate like a pin-wheel, and no net deflection of a population of molecules is observed. However, for the low-lying J states, a strong electric field can induce a transition from pin wheeling rotor into a pendular librator confined to oscillate in a small angle around the direction of the field.

In order to derive the Stark-Shift in a strong field, an assumption has to be made that the transition from freewheeling to pendular states is instantaneous. This is true under the assumption that the strong field arises adiabatically, which is justified by the fact that the domain of rotational motions covers 10^{-11} to 10^{-13} s, while the passage through the fringing field of a Stark deflector is typically of the order of 10^{-5} s [145].

For simplicity [10], let us consider a rigid linear molecule in a uniform electric field. In this case, Schrödinger's equation is as equation 2.11:

$$\left(\mathbf{J}^2 - \omega\cos\theta\right)|J, M; \omega\rangle = E\,|J, M; \omega\rangle \tag{2.11}$$

With $\mathbf{J}^2$ being the squared angular momentum operator, θ the angle between the axis of the dipole moment, and the external field, and E the energy. For $\omega \to 0$, both J and M are good quantum numbers. In the presence of the field, i.e. $\omega \neq 0$, only M remains a good quantum number, as states within each J manifold have now different energies with $|M|$.

For the bound pendular states with energies below field-free $J = 0$ level, the dipole oscillates around the positive side, i.e. with $|\theta| \leq 0$. For the states with energy greater than that of field-free $J = 0$, the dipole overshoots the $|\theta| = 0$ mark, and then slows down until stopped, then the motion is reversed. This means that, for the most of the time, the dipole is pointing in the opposite direction to the external ε field.

In a strong field, a new quantum number ν_p can be introduced, in the form of equation (2.12). The level mapping is illustrated in Figure 2.10. The Stark shift W is given by equation 2.13:

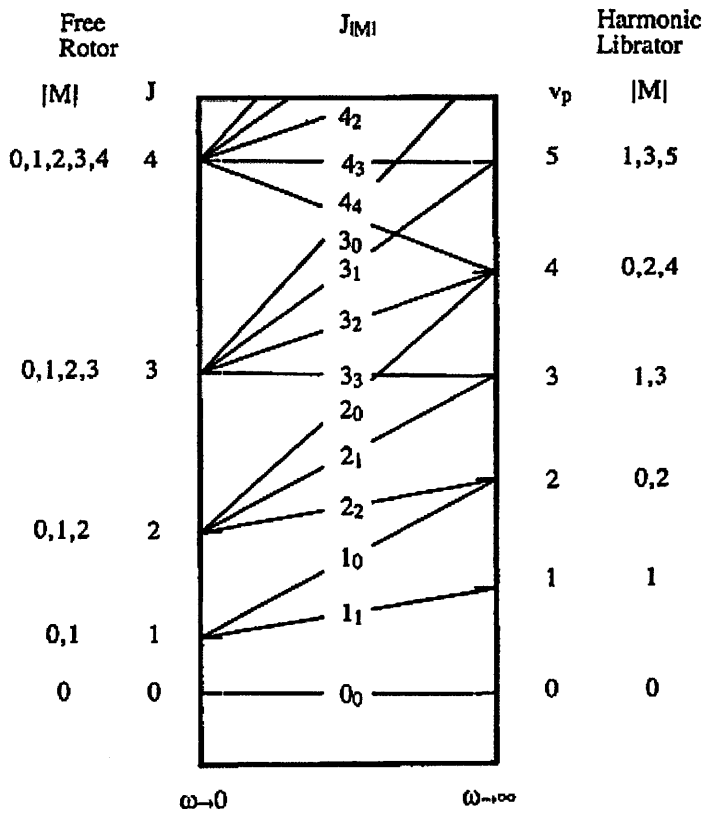

Figure 2.10: Mapping diagram of Field-free ($\omega = 0$) to strong field rotational states. Reproduced from [10].

$$\nu_p = 2J - |M| \tag{2.12}$$

$$W(\nu_{\mathrm{p}}, \omega)/R = -\omega + (\nu_{\mathrm{p}} + 1)(2\omega)^{1/2} \tag{2.13}$$

A detailed description of the calculation method for the asymmetric top molecules, for any orientation of their permanent dipole moment, can be found in [146]. Filsinger et al. [83] calculated Stark energy curves for 3-Aminophenol (Figure 2.11a) and for ytterbium fluoride (Figure 2.11b). Typically, in weak fields small molecules are in low-field-seeking states (*LFS*), that is, their energy decreases with increasing external field strength. For large molecules, however, coupling between closely spaced states of the same symmetry transforms low-field seekers to high-field seekers in the relatively weak

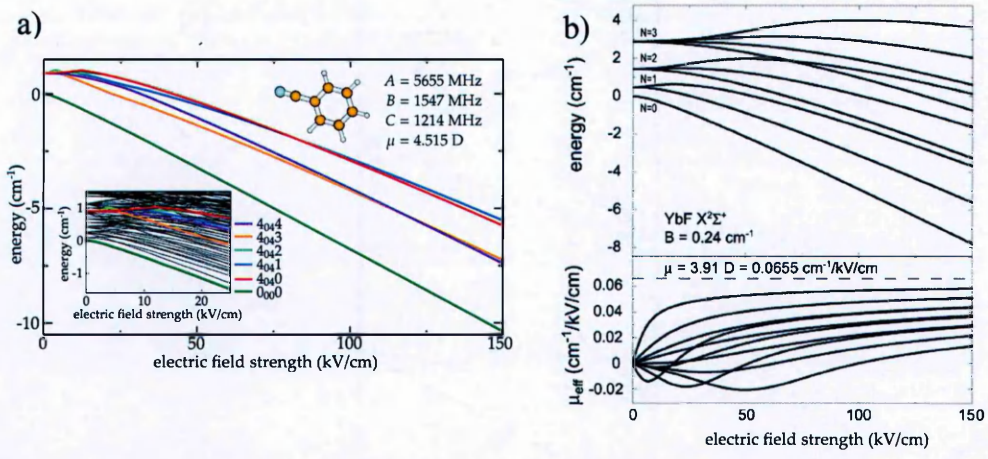

Figure 2.11: Stark energy curves for: a) – selected low rotational states of benzonitrile. The upper inset shows the molecules structure and its relevant parameters [11]. The lower inset shows all states with a field-free energy below $1.2\ \mathrm{cm}^{-1}$ for lower field intensities, and b) - ytterbium fluoride. The transition from low-field-seeking regime to high-field-seeking is visible. The bottom plot shows the effective dipole moment μ_{eff} for the corresponding stark curves. Reproduced from [12]

field regime. Transitions of this kind can be seen in the changes of monotonicity of the curves in Figure 2.11b.

As the energy shift is state-dependent, it is useful to introduce an effective dipole moment, defined in the form of equation 2.14:

$$\mu_{\mathrm{eff}} = -\frac{\partial W}{\partial \varepsilon} \tag{2.14}$$

Hence, the effective dipole moment is the negative slope of the Stark energy curve. This parameter is the most convenient way to describe how a molecule in a given state will respond to the Stark deflection technique, as described in the next section. Combining equations 2.13 and 2.14 in the strong field limit, the effective dipole moment can be given by equation 2.15:

$$\mu_{\mathrm{eff}} = \mu\left(1 - \frac{\nu_p + 1}{\sqrt{2\omega}}\right) \tag{2.15}$$

The state dependency is only lifted when $\sqrt{2\omega} \gg \nu_p + 1$, and the fraction becomes negligible, i.e. the external field is sufficiently strong. Such strong fields are, however,

not within the scope of this work – the maximum achievable field in our Stark-Deflector (see 3.4.1.2) is 120 kV/cm (the main limiting factor is the risk of discharges that could damage the surface). Stronger fields can be achieved by utilizing short intense laser pulses, for example of the order of 10^{15} W/cm^2 [123]. It is therefore clear that the effective dipole moment is largest when the molecule is in a low ν_p state.

Rotational energy levels correspond to the microwave part of the EM spectrum. The spacing between levels is proportional to rotational constants of a molecule, which in turn are inversely proportional to its moments of inertia. Hence, larger and bulkier molecules (higher moments of inertia) have smaller rotational constants and, as a consequence, higher density of rotational states. For example, the CO molecule's $J' \leftarrow J = 1 \leftarrow 0$ transition [147] has an energy of 0.468 meV , whereas an analogous transition in benzene – d_1 has an energy [148] of 0.033 meV, corresponding to temperatures of 5.43 and 0.38 K, respectively. Methods used to achieve such low temperatures are described in 2.4.2.

For a polar molecule in an inhomogeneous electric field, the net force acting on it due to the Stark effect follows the equation 2.16:

$$\vec{F} = \mu_{\text{eff}} \vec{\nabla} \varepsilon \tag{2.16}$$

Above, we have shown that we can manipulate the energy of a polar molecule in a given rotational state by applying a strong external electric field. But how can we use this to move a polar molecule in space? The key is to set up a volume with an electric field gradient, and pass molecules through it. In this case, the net force acts on the passing molecules and gives them a velocity component perpendicular to their propagation axis. For example, benzonitrile (one of molecules used for the optimisation of Stark/EA experiment described in Section 3.4) in a 100 kV/cm field exhibits a Stark shift of -6.71 cm^{-1}, and an effective dipole moment of 0.0711 cm^{-1}/(kV/cm) [12]. Filsinger et al. [84] have observed a $\approx$ 2 mm deflection of benzonitrile at the distance of 0.22 m after their Stark deflector.

2.4.2 Rotationally cold molecular beams.

As shown in equation 2.15, in order to achieve a high effective dipole moment for a Stark-deflection experiment, it is important to produce a target beam which is as rotationally cold as possible. Also, a rotationally cold ensemble has fewer states occupied with significant population. The probability p_i that a system having temperature T will be found in state with energy ϵ_i can be expressed in form of equation 2.17 (Boltzmann rotational distribution [149])

$$p_i = \frac{\exp\left(-\epsilon_i / k_\mathrm{b} T\right)}{Q} \tag{2.17}$$

Where k_b is the Boltzmann constant ($k_\mathrm{b} = 8.617 \cdot 10^{-5}$ eV/K), and Q is the system's partition function, i.e. the sum of Boltzmann factors for all accessible states. Assuming that the population of states is negligible above a certain rotational energy, an ensemble will have "bands" of rotational states for different species in the beam. Narrowing these bands helps to achieve more effective Stark separation, as this reduces the overlap of populations. In the present work, molecular cooling is achieved in a supersonic expansion.

Molecular beams can be produced in two distinctive limiting cases: effusive or supersonic [150]. Effusive beams are formed when the great majority of molecules experience no collisions as they leave the reservoir, i.e. when the mean free (λ_0) path is much larger that the diameter of the orifice (D) ($\lambda_0 \gg D$). As there are no collisions during expansion, effusive beams have similar temperatures (internal temperatures, as well as translational) as the reservoir. Supersonic beams, on the other hand, are perfectly suited for producing beams of internally cold molecules. Due to high number of collisions during expansion, they also allow for nucleation and are widely used as cluster sources - collisions provide the only opportunity to convert one type of thermal energy to another (i.e. internal to translational or vice-versa). Supersonic beams are discussed in more detail in the following section.

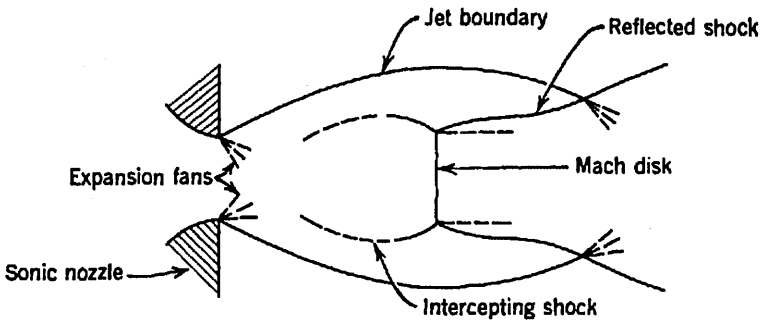

Figure 2.12: Continuous free-jet expansion (Reproduced from [13])

2.4.2.1 Supersonic Expansion of gas

A supersonic jet is formed when a gas is expanded through an orifice that is significantly larger than the mean free path of the gas particles, as summarised in expression 2.18 below.

$$\lambda_0 \ll D \tag{2.18}$$

The expansion can be divided into three regimes [15]:

- Near-nozzle regime the jet density is high enough that collisions are frequent enough to maintain equilibrium conditions. Modelling this expansion stage is relatively easy for monoatomic gases, as it follows ideal-gas models.
- Intermediate stage: the jet density falls to a point where internal degrees of freedom gradually decouple (see Section 2.4.2.6 for detailed description of vibrational and rotational cooling)
- Molecular flow regime: the final stage where jet density has dropped to a point where collisions are so infrequent that no further cooling occurs and the gas flow can be treated as a free molecular flow.

The transition points from one regime to another are not precisely defined, as the process has a continuous nature. However, for the typical conditions of the present experiments

the free molecular flow regime can safely be assumed at a distance of 20 D from the nozzle orifice [151]. This corresponds to 1 mm in most of the experiments in this thesis.

Due to the interaction with the background gases, two distinctive shock zones develop (see diagram in Figure 2.12): barrel shock and Mach disk. The barrel shock forms an envelope around the centreline of the expansion, while the Mach disk is a nearly flat terminal shock wave perpendicular to the propagation axis. The location of the Mach disk can be expressed by a simple formula [151] shown in equation 2.19:

$$x_{\mathrm{M}} = 0.67\, D \sqrt{\frac{p_0}{p_{\mathrm{B}}}} \tag{2.19}$$

Where p_0 is the pressure in the gas reservoir and p_{B} is the residual pressure in the expansion chamber. The "zone of silence" is the area enveloped by the barrel shock and terminated by the Mach disk where the local speed of sound drops to a near-zero value. The flow is nearly undisturbed until the Mach disk, where significant turbulence is to be expected.

In order to perform experiments on the beam in high vacuum conditions, a skimmer is typically place inside the zone of silence. This allows for transmitting the central "core" of the beam into another chamber. By placing the skimmer in the zone of silence, the turbulence from the Mach disk can be avoided. Skimmers are often placed some distance from the chamber wall, to avoid interaction with the gas particles scattered from the back wall, and are of aerodynamic shape with a sharp edge, to minimise the possibility of introducing any turbulence by the skimmer.

2.4.2.2 Translational cooling of expanding gas

Translational cooling is linked to the velocities of the atoms / molecules with respect to each other. Figure 2.13 shows a typical thermal (Maxwell-Boltzmann curve) distribution for a static gas as well as two supersonic jets.

It is often useful to express beam velocity in term of its Mach number, i.e. the ratio of the average flow velocity of the gas to its speed of sound. The flow is then sub-sonic if

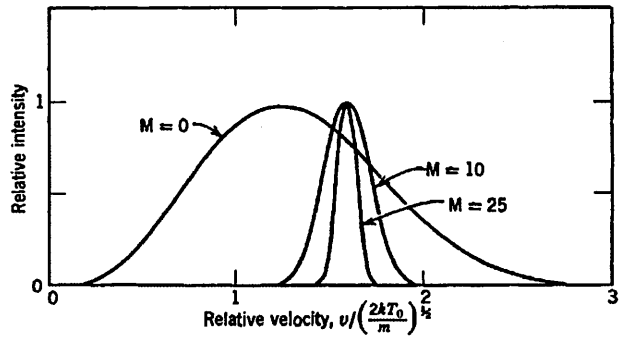

Figure 2.13: Velocity distributions for two Mach numbers in supersonic jets. Maxwell-Boltzmann distribution of the reservoir gas marked as $M = 0$. Reproduced from [13]

the Mach number is lower than unity, and supersonic when higher. Due to substantial cooling of the gas during the supersonic expansion, its local speed of sound is greatly lowered, as it is $\propto \sqrt{T}$ [150]. During the expansion, the enthalpy of the system is conserved (equation 2.20).

$$H(x) + \frac{1}{2}mv(x)^2 = \text{constant} \tag{2.20}$$

Where m is the mass of the atom/molecule, and $H(x)$ and $v(x)$ are the molar enthalpy of the gas and its velocity, respectively, at position x. Since the flow of a supersonic jet is directional, the mean velocity of the gas is no longer equal to 0. This means that the translational temperature of the gas is no longer determined by the root-mean-square of the velocity distribution (proportional to the average kinetic energy of the particles), but by the width of said distribution.

By analysing equation 2.20 one sees that the limit on the maximum velocity, $v_{\max}$, is imposed when all the enthalpy gets transformed into kinetic energy (equation 2.21).

$$v_{\max} = \sqrt{\frac{2H(T_0)}{m}} \tag{2.21}$$

Where $H(T_0)$ is the enthalpy of the gas at the temperature of the source reservoir. Terminal velocities predicted using equation 2.21 for several noble gases, expanded from a reservoir kept at 300 K, are given in Table 2.1.

Table 2.1: Terminal velocities for a selection of noble gases, at room temperature, and at 530 K. This temperature corresponds to a typical temperature of the sample powder in experiments described in Chapters 4, 5 and 7.

Gas	Terminal velocity [m/s]	
	300K	530K
Helium	1770	2300
Neon	786	1032
Argon	559	730
Krypton	386	510
Xenon	308	406

$$\frac{T(x)}{T_0} = B\left(\frac{x - x_0}{D}\right)^{-2(\gamma-1)} \tag{2.22}$$

In this idealised continuous model the cooling happens indefinitely, following the relation in equation 2.22, where B is a parameters specific for the expanding gas, x_0 the position at which the expansion begins, and γ is the ratio of specific heats of the gas. In reality the density of the beam soon drops to a level where collisions are not likely. This prohibits the gas from maintaining thermal equilibrium and the cooling stops. The terminal Mach number, M_T, can be expressed [150] in the form of equation 2.23:

$$M_{\mathrm{T}} = G\left(\frac{D\epsilon}{\lambda_0}\right)^{\frac{(\gamma-1)}{\gamma}} \tag{2.23}$$

Where G is a parameter dependent only on γ. A collisional effectiveness parameter ϵ denotes maximum fractional change in the mean random velocity per collision (dependent on the chosen gas). For argon, equation 2.23 takes the form [151] of equation 2.24, when pressure p_0 is expressed in bars and orifice diameter in centimetres.

$$M_{\mathrm{T}} = 133 \cdot (p_0 D)^{0.4} \tag{2.24}$$

Equation 2.24 in fact approximates any well behaved monoatomic gas, with the notable exception of helium [14]. Classical mechanics calculations for helium, give good approximations at low values of the $p_0 D$ product. For example, $p_0 D$ should be less

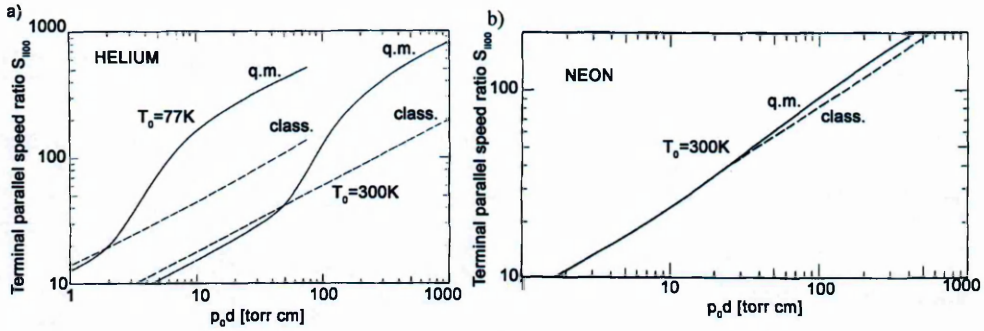

Figure 2.14: Terminal speed ratios ($V_{\max}/V_{\text{Thermal}}$) of a) helium and b) neon, as a function of p_0D product. Solid curves have been produce with quantum-mechanical calculations, whereas the dashed lines are for classical mechanics calculations. Reproduced from [14] .

than 50 mbar · cm to apply classical mechanics calculations to an expansion of helium at room temperature. Above this value quantum mechanical calculations must be used. Figure 2.14 shows the ratios of terminal velocity to mean thermal velocity (directly proportional to terminal temperature) for helium and neon. The quantum-mechanical curve for helium clearly shows improved cooling at high p_0D product values. In neon, this effect is barely observable.

Using the Mach number, equation 2.22 can be rewritten as follows:

$$T(x) = T_0 \cdot \left(1 + \frac{\gamma - 1}{2} \cdot M(x)^2\right) \tag{2.25}$$

The terminal translational velocity of the jet can be obtained by substituting $M(x)$ in equation 2.25 with its terminal value given by 2.23 or, for the case of argon, 2.24. Hence, to obtain a lower final translational temperature, one must

- Use colder gas in the upstream reservoir
- Use gas with fewer degrees of freedom, ideally a monoatomic, or
- Increase p_0D product.

Furthermore, the most effective translational cooling will be achieved in a gas with fewer degrees of freedom (ideally an atomic gas). Internal degrees of freedom are critically

important in Section 3.4 and Chapters 4, 5 and 6. The vibrational and rotation cooling of molecules is described in Section 2.4.2.6.

2.4.2.3 Mass flow

Using the continuity equation and Bernoulli's equation, it is possible to derive the expected flow rate through an orifice [152]:

$$\frac{\mathrm{d}m}{\mathrm{d}t} = \sqrt{\frac{\gamma}{R}\left(\frac{2}{\gamma+1}\right)^{(\gamma+1)/(\gamma-1)}} \cdot \frac{p_0}{\sqrt{T_0}} \cdot A \tag{2.26}$$

Where m is mass and t – time. A is the area of the orifice and R ($R = 8.31$ J/mol/K) is the gas constant. By grouping parameters together, equation 2.26 can be expressed in a simpler form of 2.27.

$$\frac{\mathrm{d}m}{\mathrm{d}t} = \frac{\pi}{4}\frac{C_{\mathrm{gas}}}{\sqrt{T_0}} \cdot p_0 D^2 \tag{2.27}$$

Therefore, for any given gas at a stable temperature, the gas load is proportional only to the reservoir's pressure and nozzle diameter squared.

2.4.2.4 Seeded beams & velocity slip effect

Seeded molecular beams are created by adding a small amount of a second species into the carrier gas. The resulting mixture will behave as a single-species gas with its properties expressed as a weighted average of the constituent gases. Hence, if the amount of the seeded gas is small, the behaviour of the mixture is dominated by the more abundant (and typically lighter) species. During the expansion, if the reservoir pressure is high enough, the lighter buffer gas particles will impact on the slower heavier ones repeatedly, accelerating them nearly to their own velocity. Furthermore, the heavier molecules reach nearly the same terminal temperature as the buffer gas, which is typically much lower than could be achieved by expanding a pure gas of the seeded molecule.

However, if the pressure of the buffer gas is low to moderate, the "velocity slip" effect may be observed. In these conditions, the initial acceleration of the heavier species is incomplete, and the seeded molecules "lag behind" the carrier gas [153], and therefore the two constituents reach different terminal temperatures. The velocity slip effect is more pronounced for the lighter carrier gases. Amirav et al. [153] have investigated this experimentally, and indeed their results suggest the cooling efficiency follows natural order of He < Ne < Ar < Kr < Xe. To achieve the same amount of cooling with He as with Xe, the flow rate of the gas had to be increased by a factor of 400.

2.4.2.5 Clustering

During the initial stage of expansion, multi-body collisions are frequent in supersonic beam, and the temperature of the gas decreases rapidly. These conditions are perfect for cluster formation. This has been noticed very early in the studies of supersonic beams and has led to extensive research [83, 154, 155, 156] on molecular complexes formed this way. Classical nucleation theory cannot be used to describe the clustering process in supersonic expansions [15]. This is believed to be due to the expansion's far-from-equilibrium nature. Furthermore, the specific properties of the small clusters are significantly different from those of the bulk matter and cluster dissociation due to collisions cannot be neglected.

The overall energy of the system decreases during clustering, and therefore a third body is required to remove the excess. The number of three body collisions in the expansion varies as $p_0^2 D$, whereas the number of binary collisions varies as $p_0 D$. At the same time, the mass throughput varies as $p_0 D^2$, as shown in equation 2.27. Therefore, to maximise the production of clusters without increasing gas load, orifice diameter should be decreased while reservoir pressure is increased (maintaining a constant value of $p_0 D^2$).

In addition to the number of collisions, clustering also depends on the temperature of the nozzle. Yang et al.'s [157] studies of methane clusters have shown that the average cluster size was larger for nozzle temperature of $-30°$ C than for $27°$ C. They have also identified the crucial role of the specific buffer gas to promote nucleation.

The effect of nucleation on the translational temperature of the beam is, however, significant [15]. The condensation energy of the clusters is released back into the ensemble, in the form of random motion of all particles in the frame of the propagating beam. This increases the translational temperature of the beam. The detailed energy balance is, however, complicated as the binding energy is highly size-dependent for small clusters.

2.4.2.6 Rotational and vibrational cooling

During the first stage of the expansion, all degrees of freedom are coupled together due to near-equilibrium conditions. In principal, seeded molecules find themselves in a cold bath, and collisions with the carrier gas cool internal degrees of freedom in addition to translational cooling. However, as the expansion progresses, the jet density drops and collisions become less frequent. This lack of collisions causes the degrees of freedom to gradually decouple, and limits the amount of vibrational and rotational cooling. Hence, it is then necessary to introduce the concept of independent translational, vibrational and rotational temperature. The internal degrees of freedom can only be cooled by exchanging quanta of vibrational or rotational energy in a scattering process. The probability of such exchange has to be calculated by solving Schrodinger's equation for the specific molecule, atom and vibrational or rotational state involved. An in-depth analysis of the simplest systems can be found in reference [158], but general conclusions can be applied to most atom-molecule collisions.

Typically, vibrational degrees of freedom decouple first [159], as the translational-vibrational relaxation is a slow process. This is because intra-molecular binding forces are large compared to inter-molecular repulsion forces at scattering distances. Also, the long timescale of vibrational motion means that the collision can be considered instantaneous [158], further reducing the probability of coupling. All these considerations lead to the vibrational temperature being the highest of the three. For example, Amirav et al. [153] reported achieving $T_{\mathrm{V}} = 50\,\mathrm{K}$ for supersonic-expanded tetracene with $p_0 D = 2.3$. By comparison, translational temperature was equal to $T_{\mathrm{T}} = 7\,\mathrm{K}$. It is worth noting, however, that since spacing between vibrational levels is relatively large,

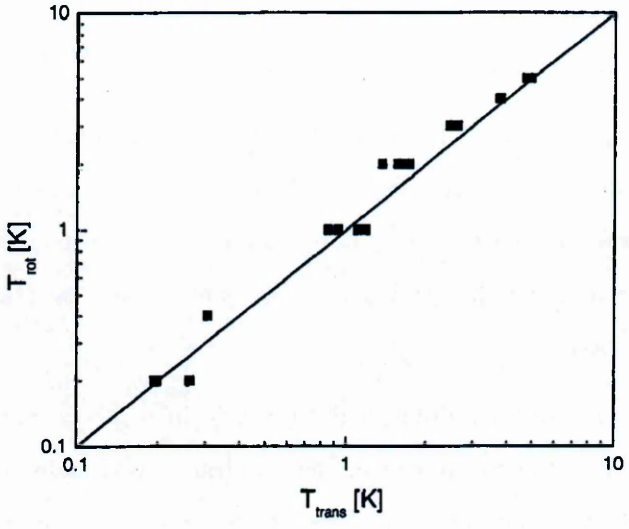

Figure 2.15: Relation between rotational and translational temperatures of aniline in a supersonic expansion. Rotational temperatures have been measured from LIF spectra, while translation temperatures have been calculated based on expansion parameters. Reproduced from [15]

even temperatures as high as 50 K lead to a very limited number of vibrational levels occupied with significant population.

Rotational relaxation is a much faster process, which increases the probability of exchanging a quantum of rotational energy during a scattering event, so rotational degrees of freedom decouple relatively late [15, 153, 158]. This leads to rotational temperature being close to translational temperature [153]. Figure 2.15 shows that the translational and rotational temperatures of aniline indeed closely follow each other. However, a significant number of states can be populated even in a beam with rotational temperature of few K because rotational states in large molecules are separated by very low energies.

2.5 Summary

This chapter gives a brief introduction of the molecular excitation and relaxation processes that are investigated in Chapters 4–7. Conical intersections are of particular importance to understand the electronic excited state dynamics of DNA and RNA bases.

Hydrogen bonding is discussed as it is the strongest bonding mechanism for dry and hydrated clusters discussed in Chapters 4 and 7. The Stark effect in strong electric fields and the production of cold molecular beams are described in some detail. Together, they provide the basis for the manipulation of neutral beams by Stark deflection, as presented in Chapter 3.

It is important to note that although the key principles for excited state dynamics are well established, the complexity of the problem in real molecular systems, and particularly molecular clusters, is too great to be treated by theory alone. Hence, experiments on controlled molecular and cluster targets are of great importance.

Chapter 3

Experimental

3.1 Introduction

This PhD is centred on two parallel research activities in the Molecular Clusters Laboratory at the Open University (UK). The first activity involved applying a multi-photon ionisation (MPI) / electron impact ionisation (EII) mass spectrometry experimental system to study isolated and clustered nucleobases. The second involved designing and building a new experimental system to study MPI, EII, and electron attachment (EA) to molecules and clusters in *Stark deflected* beams. For convenience, the systems are referred to as the MPI / EII experiment and the Stark / EA experiment.

The MPI/EII experiment is presented relatively briefly here, as previous descriptions of the system are available in Barć's thesis [2] and in recent publications [160, 161]. Improvements that have been carried out since the publication of Barć's thesis are highlighted in this chapter. The greatest strength of the experiment is the ability to directly compare MPI and EII mass spectra of supersonic beams. Differences in ion production by MPI (step-wise ionisation via one or more electronic excited states) and EII (direct access to ionic states) can be traced to neutral excited state dynamics and / or to the selective nature of MPI. The compact experimental design (only around 10 cm from the expansion nozzle to the laser or electron beam) enables high signals to be obtained. The MPI / EII experiment was used to acquire the data presented in chapters

4, 5 and 7. The apparatus used for complementary ultrafast pump-probe experiments at Heriot-Watt University is described in Chapter 6.

Most of this chapter is devoted to the Stark / EA experiment. In addition to enabling low-energy electron interactions with molecules and clusters, this new experiment has the great advantage of providing a tool to select specific molecular and cluster targets from mixed neutral beams. To our knowledge, no previous experiment has investigated electron-induced processes in Stark-deflected beams of molecules and clusters. Preliminary results are presented to demonstrate different aspects of the new experiment's performance to date. Low signal levels from the low-energy electron source remain a challenge but a program of measurements exploiting the capabilities of the complete Stark / EA experiment is anticipated in the near future.

3.2 Multi-Photon ionisation / Electron Impact ionisation experiment

This experimental setup, developed mainly by Barć [2], is shown schematically in Figure 3.1. Very briefly, an inert carrier gas seeded with vaporized uracil and / or water flows through a pinhole nozzle into a pumped chamber to form a supersonic jet. The jet passes through a skimmer and crosses a pulsed UV laser beam for MPI measurements or an electron beam from a commercial gun (*Kimball ELG-2*) for EII experiments. The resulting ions are detected using a *reflectron* time-of-flight mass spectrometer (TOF-MS).

Argon or helium carrier gas is introduced via stainless steel tubing (combination of *Swagelok* and *VCR* connections). The pressure is controlled with manual regulators in the typical range $0.5 - 2$ bar and monitored using a transducer (*Swaglok PTU series*). A stainless steel H_2O reservoir is connected to the carrier gas line via a valve. The reservoir and the gas line can be heated using resistive wire and the H_2O temperature is monitored using a thermocouple in contact with the reservoir wall. The resistive wire is wrapped more sparsely around the reservoir than around the gas line in order to prevent condensation. An improvement since Barć's thesis is the replacement of a

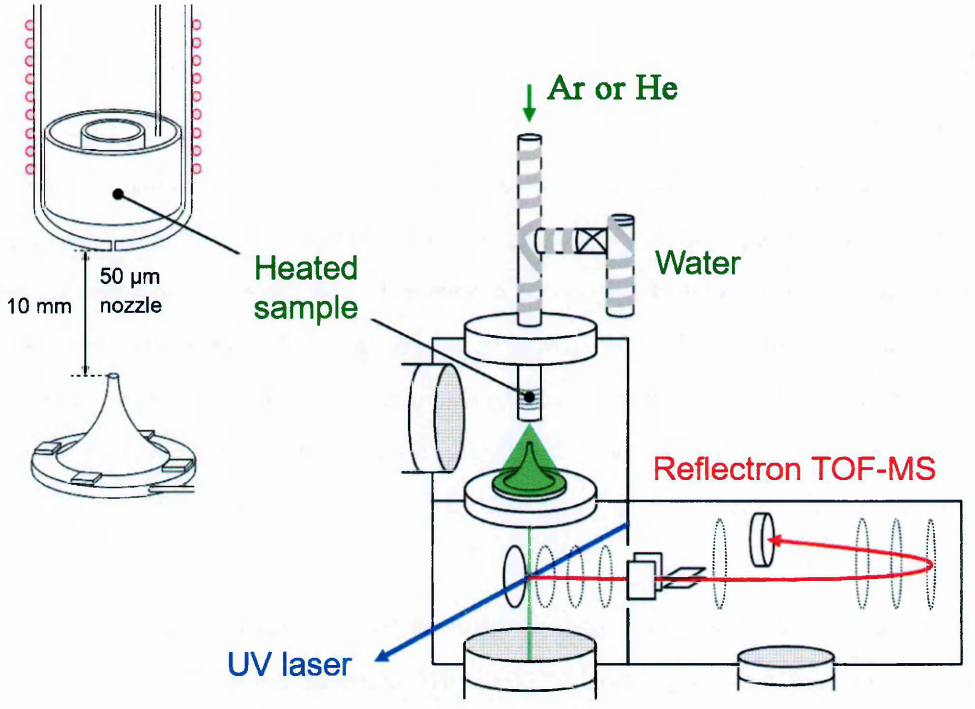

Figure 3.1: Schematic view of the MPI / EII experimental system.

thermally insulated vacuum feed through that provided a weak point for condensation and consequently limited the stability of hydrated beams.

The nozzle is a closed stainless steel tube with a laser-drilled pinhole orifice (*Lennox Laser*). Several interchangeable nozzles are available with different lengths and orifice diameters (50 or 70 μm were used in the present measurements). The investigated molecules are loaded as powders into a cartridge which is then inserted near the nozzle orifice. A design improvement since Barć's thesis [2] is a top-loading system that enables powder to be changed without modifying the beam alignment. The nozzle assembly is heated by a clamp heater and temperature is monitored using a thermocouple inserted directly into the powder cartridge. The clamp heater serves the dual purpose of sublimating the powder and preventing condensation in the nozzle orifice.

The gas mixture flows through the nozzle orifice into a pumped chamber referred to as the *Expansion Chamber*. This is pumped with either one or two turbomolecular pumps (*Pfeiffer Vacuum TMU 521* and *Oerlikon SL 700* with respective argon pumping

speeds of 500 and 690 l/s). Clusters can be formed in the initial stage of the supersonic expansion due to 3-body collisions. The level of clustering in the molecular beam can be varied between measurements by changing the carrier gas, the carrier gas pressure, and the partial pressure(s) of the seeded molecules [150]. The supersonic beam then passes through a conical skimmer (*Beam Dynamics*, model 2) with a 400 μm orifice. The separation between the nozzle and the skimmer can be varied by using different nozzles, as well as by using spacing disks. Typical nozzle–skimmer separation is between 5 and 15 mm. To avoid molecular deposition, the skimmer is heated to 125 °C using a series of resistive heaters.

The skimmed beam enters the Diagnostic chamber which is evacuated by an *Oerlikon MAG W 600* (argon pumping speed 600 l/s) turbomolecular pump. The base pressure in the diagnostic chamber, monitored by an *IONIVAC* gauge with an electronic readout, is in the 10^{-8} mbar range after baking the chamber overnight. Indeed, the background signals at low masses that affected Barć's MPI measurements were removed by extensive baking. The molecular beam is crossed at 90° by a pulsed laser beam. The third harmonic output (355 nm) of an Nd:YAG laser system (*Continuum Powerlight II 8000*) provides the pump source for a dye laser (*Sirah Cobra-Stretch*). Coumarin dyes give access to the wavelength range $220 - 277$ nm and a diffraction grating with groove density $1,800$ lines/mm enables the wavelength to be selected with a resolution better than 10^{-3} nm . The pulse width and frequency are 7 ns and 10 Hz . The average laser pulse energy can be adjusted in the range $100 - 2000$ μJ by changing the delay between the pulses triggering the xenon flash lamps and the Q-switch of the Nd:YAG laser. The energy of each pulse is recorded using a Pyroelectric joulemeter (*Spectrum Detector Inc. SPJ-D-8*). A convex lens on a slider is used to control the laser spot diameter (3 mm without the lens) at the interaction with the molecular beam. We do not have a measure of the temporal fluence structure during pulses (discussed further in Section 5.3).

The physical parts of the reflectron mass spectrometer (schematically shown in Figure 3.2) were designed and constructed by *KORE Technologies*. Its voltage control system

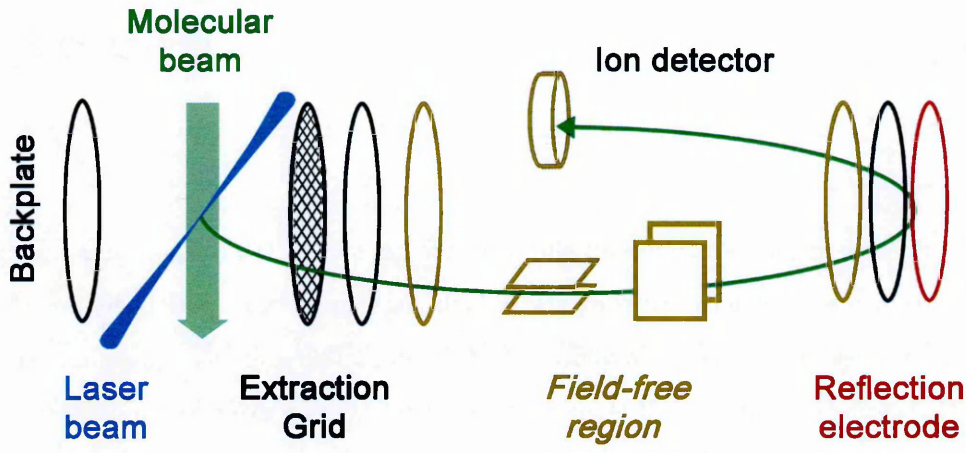

Figure 3.2: Diagram of the mass spectrometer's electrodes.

was home-built with the exception of the ion extraction pulse (-380 V, 2 μs, approximate rise time 1 ns) from a triggered system produced by *KORE Technologies*. Following extraction, acceleration to -2 kV, and deflection to compensate for the molecular beam velocity, the cations pass through the field-free region (FFR) of the flight tube (additionally evacuated using a 145 l/s *Oerlikon TURBOVAC 151* turbomolecular pump) and the reflectron optics. The voltage on the final reflection electrode (V_G) can be adjusted to determine the kinetic energy of an ion in the FFR (discussed further in Chapter 5). The reflectron is a set of ion optics used to decelerate and then reverse the direction of travelling ions. The reversed ions are guided back into the field-free region (FFR), for a second pass. This greatly enhances the mass resolution of the instrument by essentially doubling the length of the drift tube. Moreover, the interaction of ions with the retarding field reduces the effect of different KE on the arrival time of a specific ion mass, because ions with higher KE penetrate deeper into the reflectron and hence spend more time there. The reflectron part of the spectrometer consists physically of three electrodes with external voltage connections: the FFR grid (typically -2,027 V), the retardation grid (typically -1,370 V), and the reflection electrode (typically between 0 and -350 V). To achieve the best possible field uniformity, a series of ring electrodes are mounted along a resistor chain between the externally supplied electrodes (5 rings

between the FFR and retardation grids; 11 between the retardation grid and the reflection electrode).

The discrete dynode electron multiplier detector includes a -10 kV post-acceleration grid to increase the detection efficiency of high-mass ions. The pre-amplified ion signals are timed using a 250 ps resolution *Fast Comtec P7887* time-to-digital conversion (TDC) card. The timing of all components is controlled by an external clock (*Quantum Composer 9520 Series* Pulse Generator). Mass resolutions of $m/\Delta m = 1,000$ are obtained routinely using a focused laser beam. A new data acquisition system was developed using LabVIEW (see Appendix B for more details).

In addition to the MPI experiments, the design of the Diagnostic chamber allows for performing EII measurements. The commercial electron gun, *Kimball ELG-2*, gives an output of $10 - 30$ μA (monitored via the bias current across the electron gun) and the electron energy can be varied from 5 to 2,000 eV. The electron beam is continuous and ions are typically extracted at a frequency of 20 kHz. The output beam is not tightly focused and therefore ions are extracted from a much bigger volume compared to MPI. Furthermore, unlike in the MPI experiments, fragment ions can travel a significant distance away from their ionisation origin due to the potential time lapse between ionisation and extraction. The resultant large extraction volume degrades mass resolution.

3.3 Beam position characterisation using TOF reflectron

As noted in Section 3.3, a convex lens on a slider was used to modify the laser spot diameter at the interaction with the molecular beam and hence gain further control over the UV fluence. This was previously estimated using simple ray diagrams for partially defocused measurements [160], but we did not have a reliable method to determine the spot diameter close to the focal point. This problem was solved by recording MPI signals as a function of the voltage on the reflection electrode - the final electrode in the reflectron part of the mass spectrometer (see Figure 3.2). The reflectron is a set of ion optics used to decelerate and then reverse the direction of travelling ions. The

reversed ions are guided back into the field-free region (*FFR*), for a second pass. This greatly enhances the resolution of the instrument by essentially doubling the length of the drift tube. Moreover, the interaction of ions with the retarding field reduces the effect of different KE on the arrival time of a specific ion mass, because ions with higher KE penetrate deeper into the reflectron and hence spend more time there. The reflectron part of the spectrometer consists physically of three electrodes with external voltage connections: the FFR grid (typically $-2,027$ V), the retardation grid (typically $-1,370$ V), and the reflection electrode (typically between 0 and -350 V). To achieve the best possible field uniformity, a series of ring electrodes are mounted along a resistor chain between the externally supplied electrodes (5 rings between FFR and retardation grids; 11 between retardation grid and reflection electrode).

For the MPI and EII experiments, ions are produced directly at beginning of the mass spectrometer, in the region further referred to as the "*extraction volume*". This volume is spatially limited by the "*backplate*" and "*extraction grid*" electrodes (Figure 3.2). For one example of backplate and "extraction grid" voltages, Figure 3.3 shows the calculated equipotentials (*CPO-3D* version 8) in the extraction volume of the mass spectrometer. Along the central axis of the mass spectrometer, Figure 3.4 shows that the voltage against distance relationship is very close to a straight line. Therefore, knowing the electrode voltages and separations, we can reasonably apply linear interpolation to calculate the voltage at a given position. The laser / molecular beam crossing point is assumed to be on the TOF axis following careful alignment of the experiment.

Mass spectra can then be measured as a function of the *Reflection* voltage (V_G), in order to derive the maximum distance from the extraction grid at which an ion can be produced and then be directed onto the detector. For non-dissociative ionisation (zero kinetic energy release), the key condition for detection is that the voltage at the point in space where the ion is produced must be closer to ground than the reflection voltage. This is because the ion, in order to reach the detector, must be stopped and its trajectory reversed in the TOF's reflectron. The ion will have zero kinetic energy when it reaches a point in space where the voltage is the same as in the place it was created (see Figure 3.5). Therefore the ion signal will not be affected significantly by

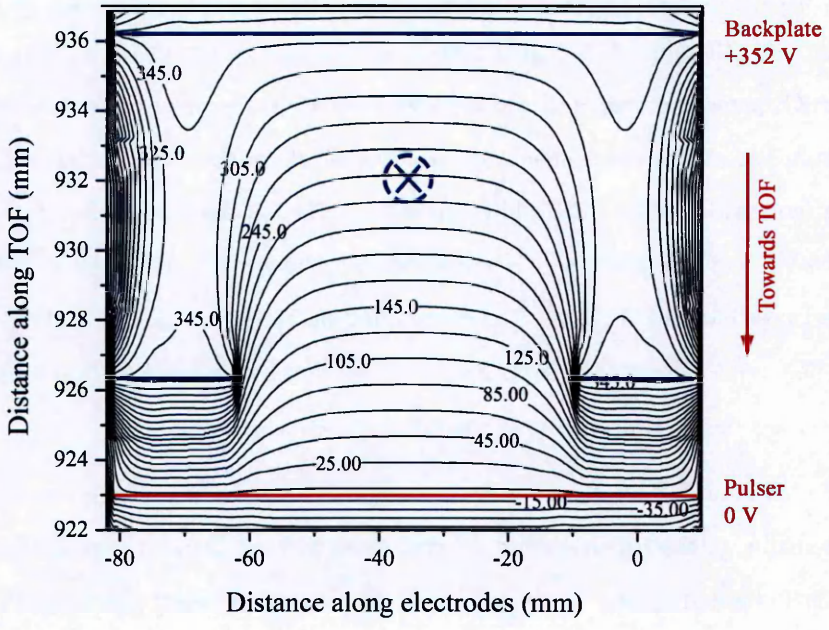

Figure 3.3: Calculated equipotentials in the TOF ion extraction region. A typical crossing point of the laser and molecular beams has been marked with a dashed circle. Note that this calculation was carried out for an experiment with the backplate pulsed at +352 V and the "extraction grid" grid held at ground. However, most experiments were performed with the backplate grounded and the extraction grid pulsed at −380 V.

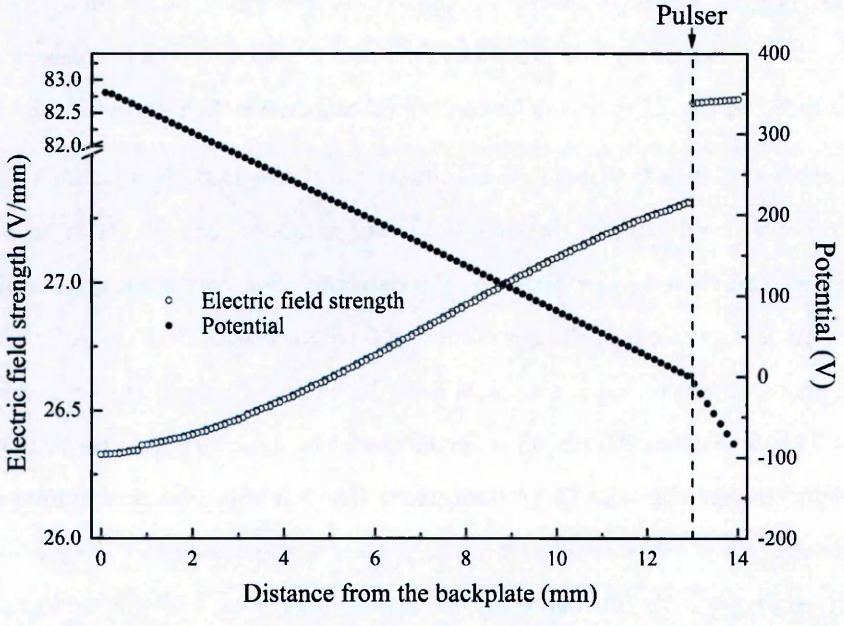

Figure 3.4: Calculated electric field strength (V/mm), and potential (V) along the distance from the backplate (mm). Note that *Distance along the backplate* = 0 mm corresponds to *Distance along TOF* = 936.1 mm in Figure 3.3

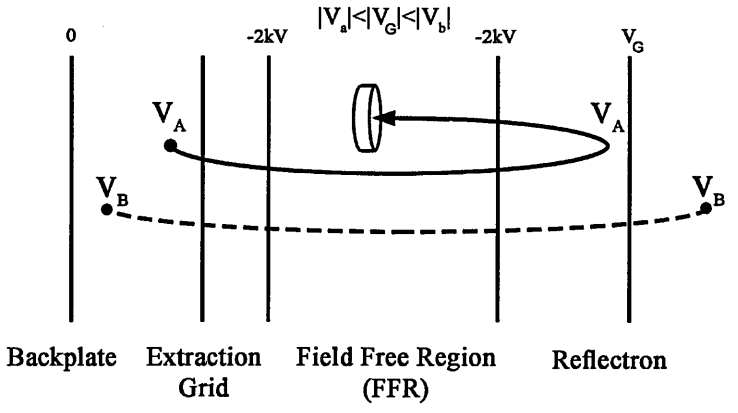

Figure 3.5: Diagram showing the principle of using the reflectron to measure an ion's initial position. Ion A (blue solid line) will be reflected into the detector because the V_A lies within the reflectron. By contrast, ion B (green dashed line) will not be stopped because V_B lies outside the reflectron.

the *reflection* voltage until it corresponds to the crossing position of the focused laser spot and the molecular beam. However, beyond that point the ions will have too high kinetic energy to be stopped by the *reflection* voltage, and will hit the electrode. Such ions are not reflected and never reach the detector. Hence, the ion signal drops. When working with a focused laser beam, the laser spot diameter will be small compared with the molecular beam diameter at the crossing point (typically several mm depending on the nozzle-skimmer separation). Therefore, as shown in Figure 3.6, the reflection voltage range across which the ion signal falls from its maximum to zero provides a measure of the laser spot diameter.

This method can adapted for measurements of the width of the molecular beam. In this case, the *Kimball ELG-2* electron gun is used. Although the Kimball gun has a focusing function, the electron beam is wider than the extraction volume of the mass spectrometer in all the experiments in this thesis (confirmed by measuring the current on the backplate and the extraction grid). Hence, for non-dissociative ionisation, a measurement of the kind shown in Figure 3.6 determines the width of the molecular beam instead of the width of the (much wider) electron beam. Figure 3.7 shows such a measurement carried out to determine the argon beam position and diameter in the

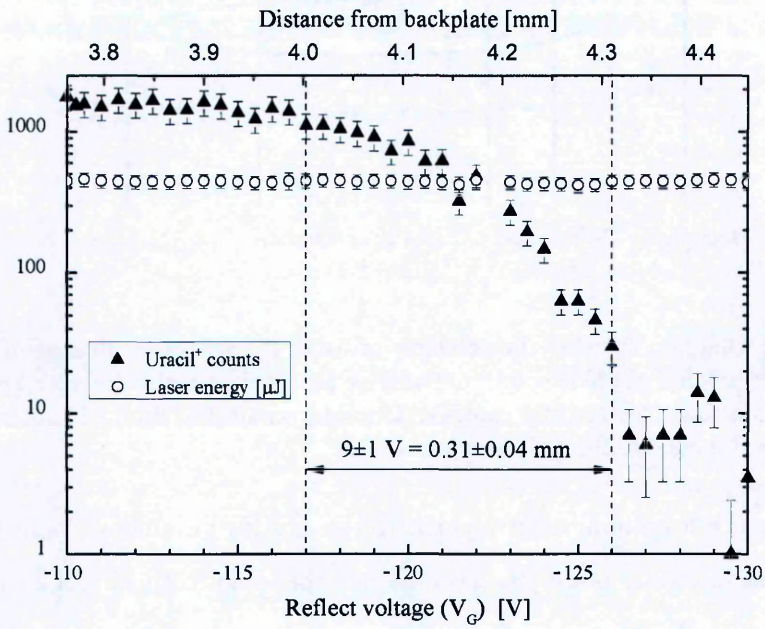

Figure 3.6: MPI measurements (220 nm, He 0.8 bar, powder 264 °C) of uracil$^+$ production as a function of the reflect voltage. The signal cut-off width (9 ± 1 V) can be directly correlated to the diameter (0.31 ± 0.04 mm) of the focused laser spot at the intersection with the molecular beam .

Stark / EA experiment. The two lines correspond to two different positions of the Kimball gun. Evidently, the ions produced outside the mass spectrometer were deflected and this information led to additional shielding being installed in the chamber.

3.4 Stark deflection / EA experiment

3.4.1 Overview

The Stark / EA experiment (shown schematically in Figure 3.8) is designed to study electron and multi-photon driven processes in Stark-selected targets. The Stark deflector applies a strong electric field gradient to deflect molecules and / or clusters in supersonic beams as a function of their effective dipole moment / mass ratio (see Section 2.4 for the key fundamental concepts). Controlled deflection depends strongly on achieving a rotationally cold molecular beam. This requires extensive pumping for the supersonic expansion with a differential pumping stage (the *Intermediate Chamber* in

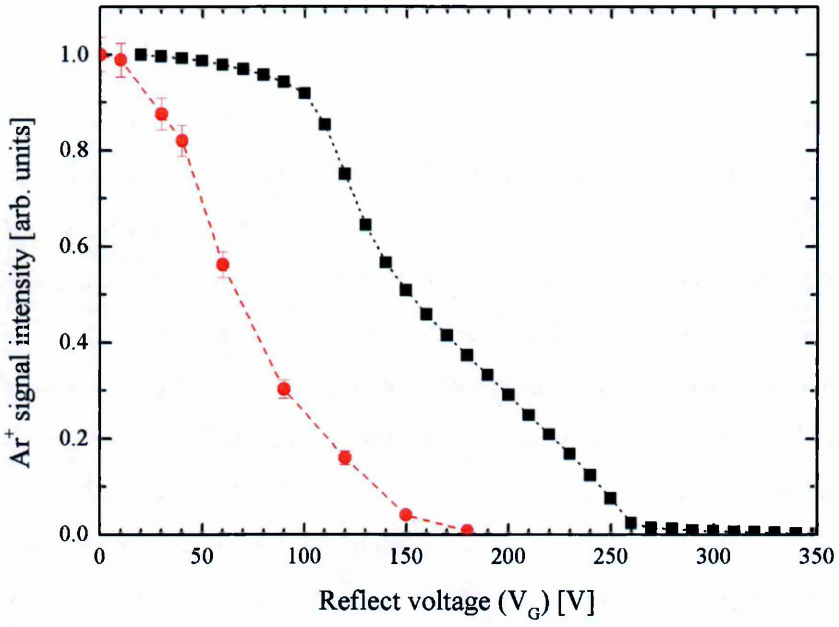

Figure 3.7: Ar^+ signal intensity as a function of the voltage on the reflect (G) electrode. The width of the drop of the curve can be correlated to the width of the molecular beam, while its position relates to the position of the beam within the ion extractor. Black squares show a dependence for a 5.5 mm-wide beam passing through the middle of the ion extractor, while red circled show a beam of a similar width (> 4.7 mm), but passing very close to the backplate electrode.

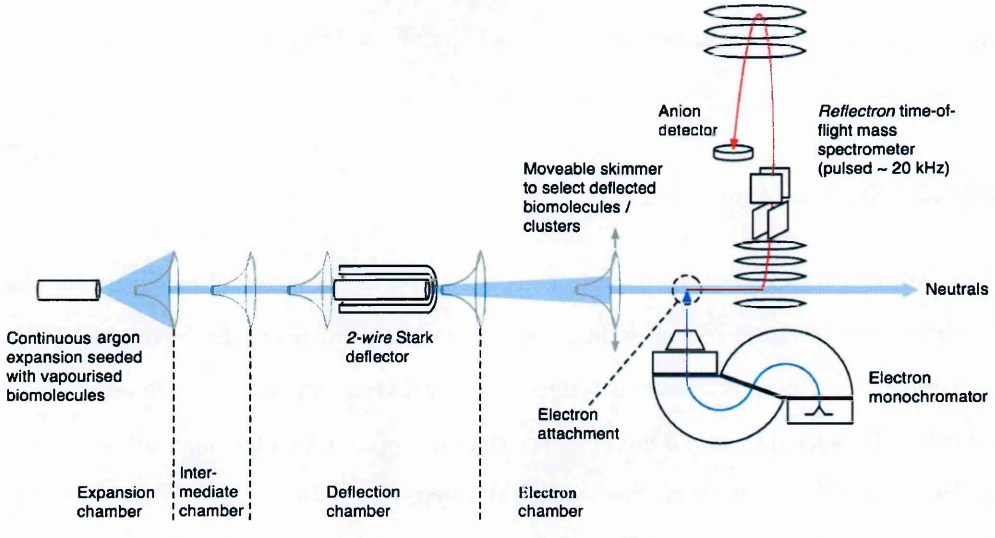

Figure 3.8: Schematic diagram of the Stark/EA experiment. The inset shows a photograph of the Stark-Deflector.

the Figure 3.8). After passing through the deflector, molecules / clusters in the beam are sampled using a moveable skimmer. The selected part of the beam then crosses a beam of electrons. The resultant anions or cations then enter the extraction volume of a time of flight mass spectrometer (several cm downstream from the shielded electron beam). Electron energy resolution is greatest at low electron beam currents and electron attachment cross sections are typically low compared with the MPI cross sections, so the experiment is designed with low signal levels in mind. To counter the low signal levels, the experiment uses a continuous-expansion molecular beam and a continuous electron beam, while the TOF mass spectrometer can be operated with a high duty cycle. It is also possible to probe the selected molecules / clusters using MPI-TOF (ns-timescale UV pulses, described in section Section 3.2) as well as EII-TOF using a broad high-energy electron beam (Kimball electron gun, described in Section 3.2). In these cases, the ions are produced inside the extraction volume of the mass spectrometer. The laser beam and Kimball electron gun beam are not shown in Figure 3.8. The vacuum arrangement of the Stark / EA experiment is shown schematically in Figure 3.9 and controlled using a home-built *Vacuum Security System* (described in Appendix A). The vacuum security system interfaces with a LabVIEW platform for experimental control and data acquisition (described in Appendix B).

3.4.1.1 The molecular beam

This section describes the key parts of the gas supply, the sample molecule introduction systems, the expansion chamber, and the intermediate chamber. As in the MPI / EII experiment, the molecular beam is formed by a continuous expansion of helium or argon seeded with molecules from a liquid reservoir or a powder cartridge mounted very close to the nozzle orifice. However, the horizontal orientation of the nozzle in the Stark / EA experiment reduces the probability of the nozzle becoming blocked with impurities or condensed sample molecules. The Stark / EA design also has the advantage of enabling the powder cartridge to be refilled while maintaining an overpressure of argon in the gas line. Hence it is not necessary to break the vacuum to refill or change the powder. The entire gas line, including the nozzle, is mounted on a 3D movement. The planar

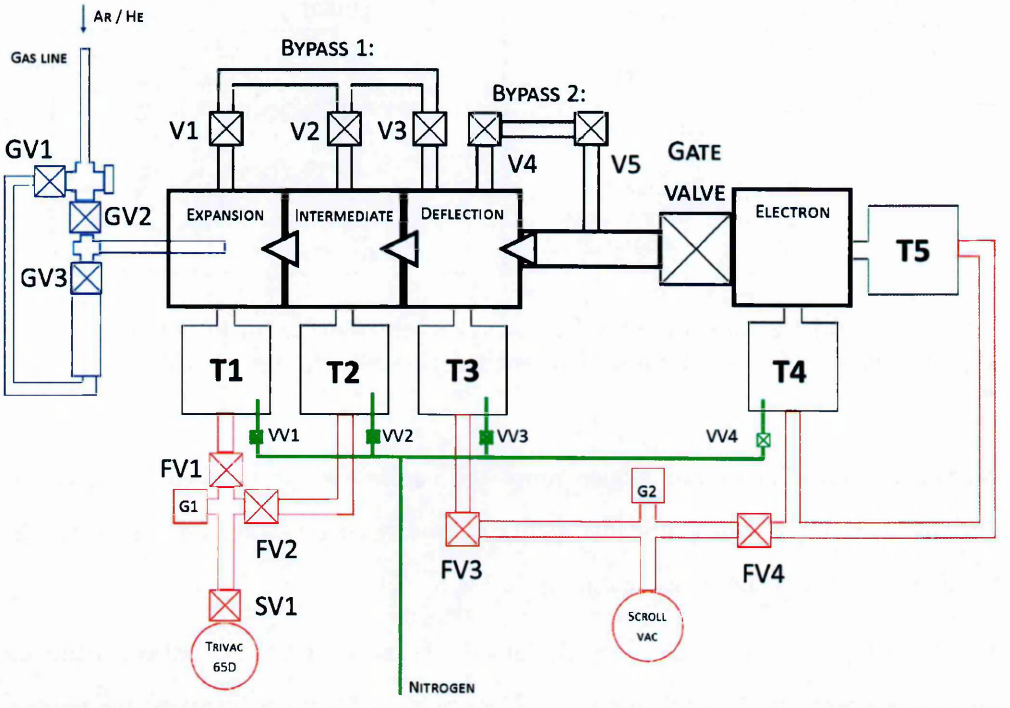

Figure 3.9: Diagram of the vacuum arrangement of the Stark/EA experiment. The colour-coding corresponds as follows: Blue – gas line, Green – Dry nitrogen venting line, Red – Roughing vacuum line.

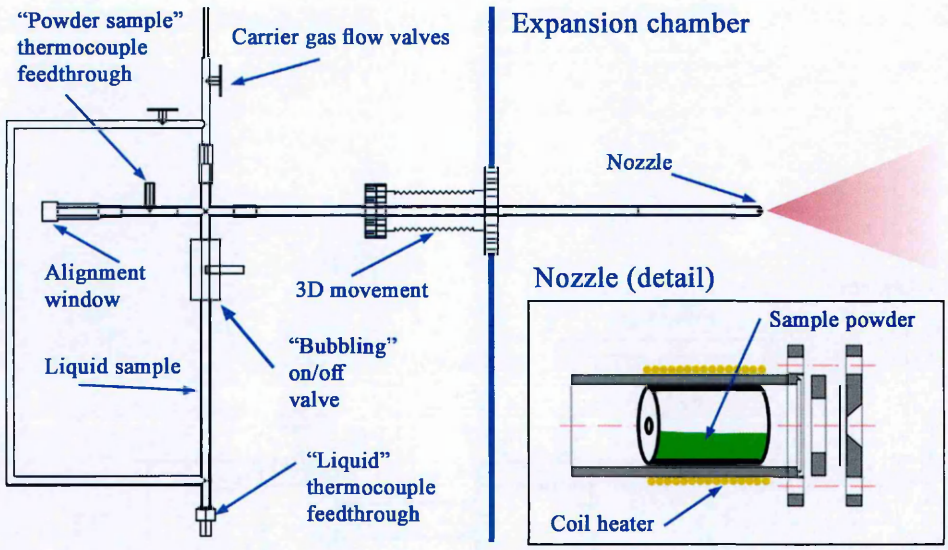

Figure 3.10: (a) Gas line assembly for Stark/EA experiment; (b) Detail of the nozzle assembly diagram for use with interchangeable Agar Scientific fine orifice discs (diameter $30 - 70\ \mu$m).

movement allows for precise alignment of the nozzle with relation to the skimmer. Movement in the third axis provides ability to modify nozzle – skimmer distance. The gas line assembly is shown schematically in Figure 3.10.

The carrier gas can either flow directly into the nozzle or it can be redirected to pass through stainless steel liquid reservoir. This "bubbling" system increases the pick-up rate of molecules from the liquid sample. The reservoir and the gas line can be heated using resistive wire and the temperature is monitored using thermocouples at several control points (inside liquid, inside the powder cartridge, on the outside of tubing on either side of the vacuum feedthrough, and on the outside of the nozzle close to the orifice). The resistive wire is wrapped more sparsely around the reservoir than around the gas line in order to prevent condensation.

In order to optimize rotational cooling, a more refined nozzle is required than the laser-drilled nozzles (*Lennox Laser*) used in the MPI / EII experiment. Therefore a new nozzle assembly was designed to house a platinum / iridium alloy (95 : 5 %) disc with a fine orifice (*Agar Scientific*) as shown schematically in Figure 3.10b. A resistive heater is coiled around the assembly. A selection of discs allows for changing the orifice diameter

between 20 and 70 μm. The orifice shape is nearly ideally circular, helping to minimise turbulence in the expansion. General principles of supersonic expansion are described in details in Section 2.4.2.

The gas mixture ($500 - 2,000$ mbar) is expanded into a chamber (referred to as *Expansion chamber*) evacuated by an *Oerlikon TURBOVAC MAG W 2200 iP* turbomolecular pump (2,100 l/s , backed by *Oerlikon TRIVAC D65 B*, pumping speed 65 m^3/h, typical vacuum pressure during experiments in the $10^{-5} - 10^{-4}$ mbar range). The beam then passes through a conical skimmer (*Beam Dynamics model 2* skimmer, diameter 2 mm) into a second stage of differential pumping. The separation of the nozzle and skimmer orifices is typically in the range $1 - 5$ cm. The *Intermediate chamber* is evacuated by an *Oerlikon TURBOVAC SL 700* turbomolecular pump, with a pumping speed of 690 l/s ($\sim 10^{-6}$ mbar during experiments). The beam passes through a second conical skimmer (orifice diameter 1 mm) into the *Deflection chamber.* The skimmers can be heated using resistive heaters and thermocouples mounted on their assembly systems.

3.4.1.2 The Stark deflector

The Deflection chamber (typical pressure in the 10^{-8} mbar range) houses the Stark deflector and is evacuated by an *Oerlikon SL 700* turbo pump with an oil-free (Scroll) backing pump. The Stark deflector is of the same 2-wire design as used in Filsinger et al.'s [16, 83, 84] and Trippel et al.'s [85] experiments (also discussed in Section 2.4) and has been built by Küpper and co-workers at the Deutsches Elektronen-Synchrotron (DESY), Hamburg. Briefly, the design comprises two electrodes of 200 mm length: a rod that is typically held at 10 kV during experiments and a grounded trough (see Figure 3.11a). The rod and the trough are separated by 1.5 mm and their specific shapes establish the field gradient (Figure 3.11b) that is necessary to deflect a beam of polar molecules that passes between them (see Section 2.4). A skimmer is mounted at the entrance of the deflector in order to prevent the molecular beam from hitting the electrodes and to control the width of the deflected beam (see Section 3.5.1.1). Another skimmer after the deflector can be installed to aid alignment.

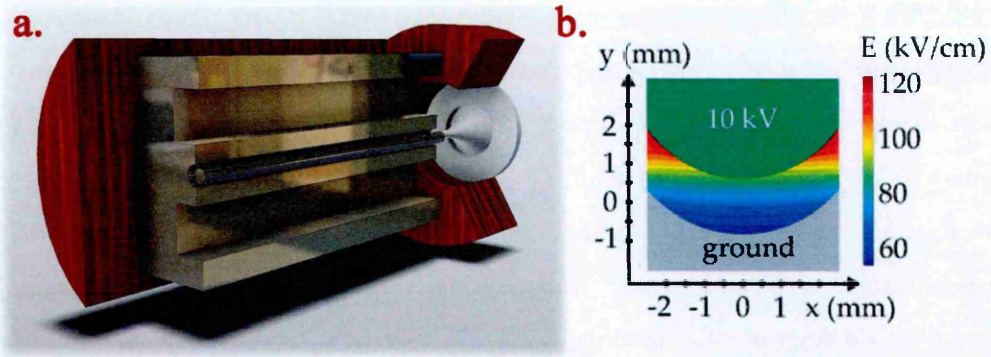

Figure 3.11: (a) 3-D drawing of the Stark deflector (b) Cross-section of the Stark deflector, showing calculated electric field intensity. Reproduced from [16].

Due to the high field strength in the device, the pressure in the chamber must be $< 10^{-6}$ mbar to prevent an arc discharge. Furthermore, a High-Voltage conditioning procedure has to be performed to prepare the electrode surfaces for strong fields following exposure to air (i.e. every time the deflection chamber is vented). The conditioning procedure requires gradual increasing of the voltage on the rod electrode of the deflector while monitoring current flow with a nano-ammeter for any sign of a discharge. More detail on the conditioning procedure is provided in Appendix A.

3.4.1.3 The cross beam apparatus and detection system

After the deflection stage, the beam enters a drift tube. The purpose of this tube is to give extra length to exaggerate any deflection effects. In previous experiments using the same deflector design [85], deflections of 3-aminophenol of up to 5 mm at a distance of 0.5 m after the deflector were achieved. Therefore the same distance between the deflector and the moveable skimmer is used in the present experiment. The extension tube is be connected via a gate valve to the Interaction chamber (see Figure 3.9, evacuated to ultra-high vacuum by an *Oerlikon TURBOVAC SL 700* turbomolecular pump, backed by an *Oerlikon SCROLLVAC SC 30D* Dry pump.

Stark deflected species can be selected using a movable skimmer. The skimmer is mounted on a 3-way movement, so the Stark Deflector can be mounted in either horizontal or vertical position. The molecular beam (selected or not) can then cross a low-energy

electron beam for the purpose of creation of anions. Electrons are emitted from a filament and then energy-selected using a double-pass cylindrical monochromator with controlled angular aberrations [162] (*LK Technologies Inc., model 5000*). The monochromator is mounted on a backplate built in the OU Science Faculty workshop. Low energy electrons are highly sensitive to magnetic fields so the Interaction chamber is made of non-magnetic stainless-steel alloy (316L). Moreover, it houses a 1.5 mm thick MuMetal shield. The electron monochromator is mounted inside an additional MuMetal shielded box, and all components inside the chamber are built from non-magnetic materials (mostly aluminium, copper and titanium). MuMetal is a nickel-iron alloy that has extremely high magnetic permeability after heat treatment ($> 400,000$ relative to free space). The shielding effect arises not from blocking magnetic fields, but from providing the magnetic flux with a low-resistance path. Therefore, the shield should be as close to a closed volume as possible, and thick enough to avoid saturation.

The voltages of the monochromator are controlled by a unit designed and built at the OU by F. Robertson. The monochromator requires 22 separate voltages and one current input. All voltages are referenced to the beam (cathode) voltage, which in turn is referenced to ground. Only 3 of the voltages need to be varied independently (cathode's midpoint potential, "beam", and 2 electrodes in the focusing optics, B_1 and B_2) in order to control the energy and focusing of the beam. Hence the divider was designed for manual control of all the voltages, with additional remote control of beam, B_1, and B_2 via a four channel, 16 bit USB DAC, *Measurement Computing type USB-3101* interfaced with the control software (Appendix B).

The intensity of the electron beam is monitored using a Faraday cup. Typical resolutions in recent DEA experiments in the recent literature range from 14 meV [154] to 120 meV [163]. The monochromator is capable of energy resolution in the sub-meV range, but this is only achievable at very low beam currents. The manufacturers stated that a resolution of 2.5 meV (FWHM) could be achieved with a beam current of 250 pA, while 20 meV is achievable at 10 nA. However the maximum current that we have been able to attain so far was only 1 nA, and this is too low for effective optimisation of the experiment. Therefore the results presented in sections 3.5.1 and 3.5.2.2 were

performed using the Kimball electron gun (described below) or a modified version of the low-energy electron system without the dual-pass energy selector.

Ions produced at the molecular beam / low energy electron beam crossing point drift freely into the extraction volume, where a pulsed voltage extracts them into a reflectron time-of-flight mass spectrometer (*KORE Technology*), similar design to the MPI / EII mass spectrometer. The ion extractor has been built in the Science Faculty Workshop following a series of simulations performed using *CPO-3D* software. For parent anions and for large fragments ions (e.g. parent anions minus one hydrogen atom), the incident velocity of the molecular beam enables efficient ion transport into the TOF extraction region. Fragment ions produced with large kinetic energy release (and hence approximately isotropic velocities) will enter the extraction region with much lower efficiency (< 10 %). The mass spectrometer electrodes are shielded electrically by a copper shield.

The design of the Interaction chamber also enables EII and MPI experiments to be carried out on the selected species with ionisation taking place in TOF extraction volume. In this case, the electron beam is produced by a commercial electron gun (*Kimball ELG-2*). EII typically gives much more intense signals and therefore enables optimisation of the system prior to gaining good control of the low energy electron source. The laser beam, produced with the same setup as described in Section 3.2, also crosses the molecular beam in the extraction region. This can give an independent confirmation of selectivity, as different isomers can show different REMPI features (e.g. associated with vibronic structure). For example, Nir et al. [164] attributed several distinct features in the rich REMPI spectrum of gas phase cytosine exclusively to the -keto or -enol tautomeric forms of the molecule. The width of the beam at the point of the movable skimmer can be estimated using simple geometric considerations. By moving the movable skimmer in one of the axis, and recording mass spectra for each of its positions, it is possible to produce spatial profiles of the beam. Figure 3.12 shows profiles, and lists the expected widths, for several skimmer diameters (1 mm, 0.5 mm, 0.2 mm) in front of the Stark-Deflector. The estimated width is in very good agreement with the measured width. The absolute signal intensity for the three measurements showed 1:0.25:0.04

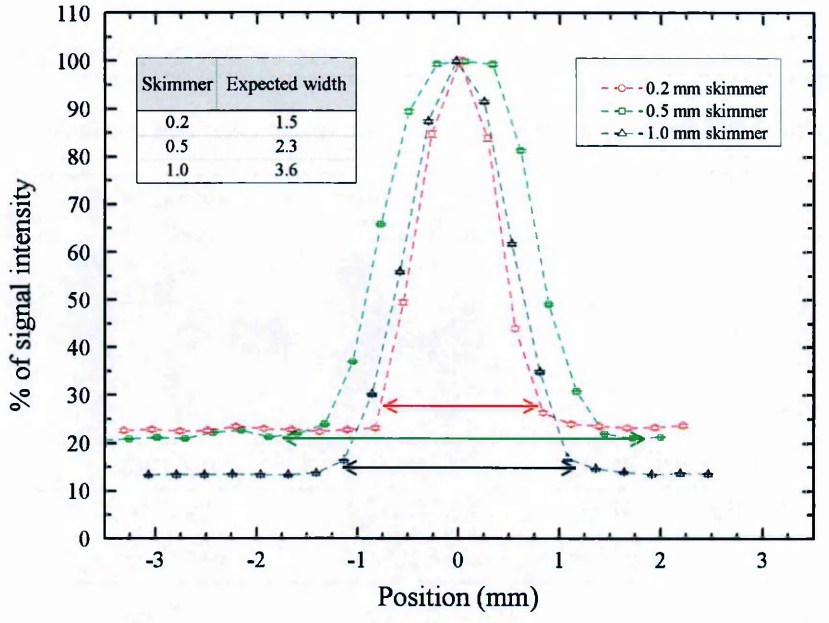

Figure 3.12: 200 eV EII spatial profiles of the argon beam for three skimmer in Front of the Stark-Deflector. The inset table gives expected beam width calculated from simple geometric considerations. The length of the coloured arrows corresponds to these expected widths. .

ratio, i.e. proportional to the area of the skimmers' orifices. This indicates negligible scattering of the molecules out of the beam..

3.5 Performance of Stark / EA experiment

3.5.1 Stark selection characterisation using nitromethane

The first experimental tests were performed using nitromethane. The molecule is a good choice for initial tests for the reasons listed below. Table 3.1 compares a few important properties of nitromethane with a benzonitrile, a molecule studied in previous Stark deflection experiments by Küpper and co-workers [16, 83, 84, 85].

Table 3.1: Selected physical properties of nitromethane and benzonitrile

	Nitromethane (CH_3NO_2)	Benzonitrile (C_7H_5N)
	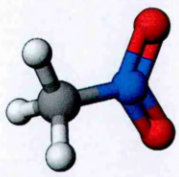	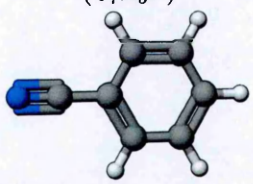
Molecular weight	61.0400	103.1213
Dipole moment	3.46 D [165]	4.52 D [11]
Dipole moment / mass	0.057 D/amu	0.044 D/amu

- Quite high vapour pressures of nitromethane are achievable without significant heating required of the liquid sample (e.g. 28 Torr at 20 °C [45]).
- The molecule has a large dipole moment / mass ratio (see Table 3.1) and hence should be deflected quite readily. Accordingly, Schwettmann et al.'s [166] calculations predicted effective Stark slowing of nitromethane.
- Electrons can attach to nitromethane with high cross sections (e.g. 7×10^{-22} m^2 for NO_2^- production by electron capture at 0.5 eV [167])
- The molecule can be detected with a single-colour ns-timescale pulsed laser in the wavelength range accessible with our system via single photon dissociation producing NO and subsequent 2-photon resonant ionisation of NO [168].

3.5.1.1 Removal of nitromethane molecules from beams by Stark deflection

The simplest Stark deflection experiments with the current system involve measuring the electron impact ionisation signal of a given ion by as a function of the voltage across the deflector electrodes. The results shown in Figures 3.13, 3.14 and A.2 were recorded with 1 mm skimmers positioned directly before and after the Stark-Deflector. The moveable skimmer was positioned far enough above the beam to have no influence. The

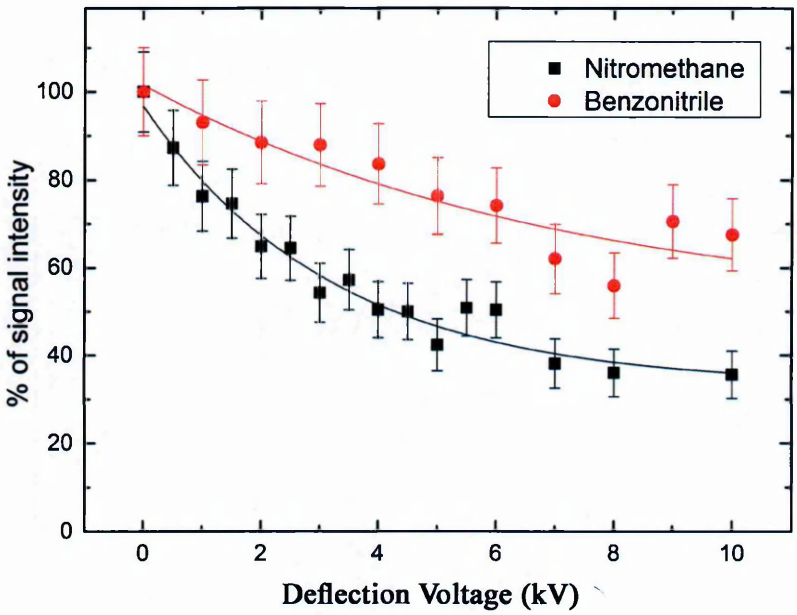

Figure 3.13: Comparison of nitromethane$^+$ and benzonitrile$^+$ signal intensities, as a function of deflection voltage. Nitromethane temperature 25 °C, Benzonitrile temperature 130 °C. Other argon expansion parameters (driving pressure, nozzle diameter, etc.) were kept identical for both sets of measurements.

Table 3.2: Measure of deflection for two driving pressures of helium.

He pressure [mbar]	D(2 kV)	D(6 kV)	D(10 kV)
380	32.22 %	58.69 %	66.37 %
950	6.45 %	15.75 %	21.71 %

200 eV electron beam from the Kimball gun fills the TOF extraction volume essentially isotropically. Therefore, the removal of molecules from the beam is dominated by deflected species hitting the deflector electrodes or the skimmer after the deflector.

Figure 3.13 compares the deflector voltage dependence of nitromethane$^+$ and benzonitrile$^+$ signals. The argon carrier gas pressure (500 mbar) and nozzle diameter (50 μm) were the same in both measurements but to achieve efficient seeding benzonitrile was heated to 130 °C. The figure clearly shows that nitromethane molecules were deflected out of the beam more efficiently than benzonitrile. This is likely to be partially due to the higher dipole moment / mass ratio of nitromethane and partially due to reduced occupation of high rotational states in the beam due lower temperature in the nozzle.

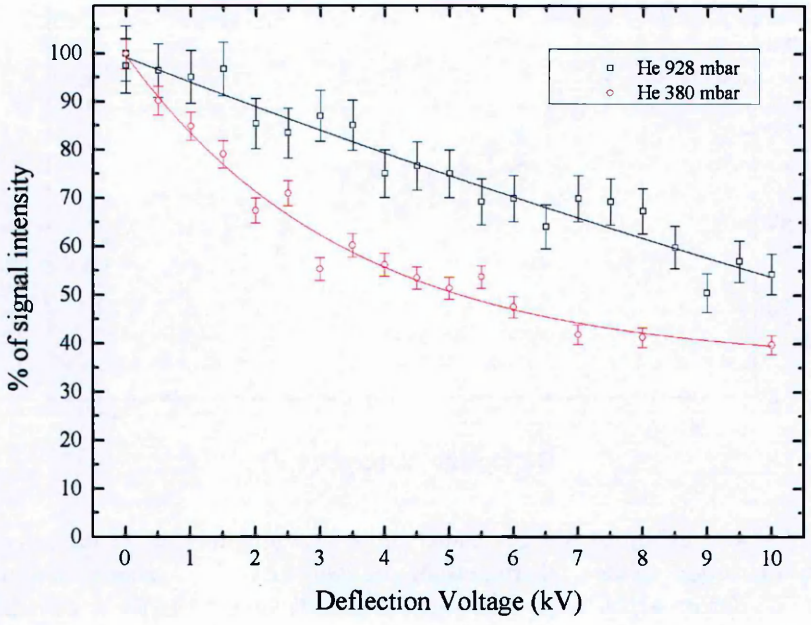

Figure 3.14: Nitromethane$^+$ detection as a function of deflecting voltage for two driving pressures of helium.

The choice of the carrier gas pressure is often a compromise between seeding efficiency (observed to be better in helium than argon in our system) and cooling efficiency (expected to be better in argon than helium due to the velocity slip effect described in Section 2.4.2.4). Figure 3.14 and Table 3.2 show the signal suppression of nitromethane$^+$ as a function of deflection voltage, for room-temperature nitromethane seeded in two different driving pressures of helium. The results clearly demonstrate more efficient deflection of nitromethane in the 380 mbar expansion than in the 950 mbar expansion. As an aside, lower helium pressure also resulted in a higher absolute nitromethane signal due to more efficient seeding (Figure A.2).

Greater nitromethane deflection at lower helium pressure can be attributed to lower rotational temperature. According to equation 2.24, for a given nozzle diameter, higher driving pressure results in better cooling. However, this situation is expected to be complicated in the present continuous expansion. Because the pressure in the expansion chamber is quite high, it is necessary to place the nozzle relatively close to the skimmer and hence the chamber wall. Reflected carrier gas atoms from the chamber wall and the skimmer housing can produce additional shocks that degrade cooling efficiency

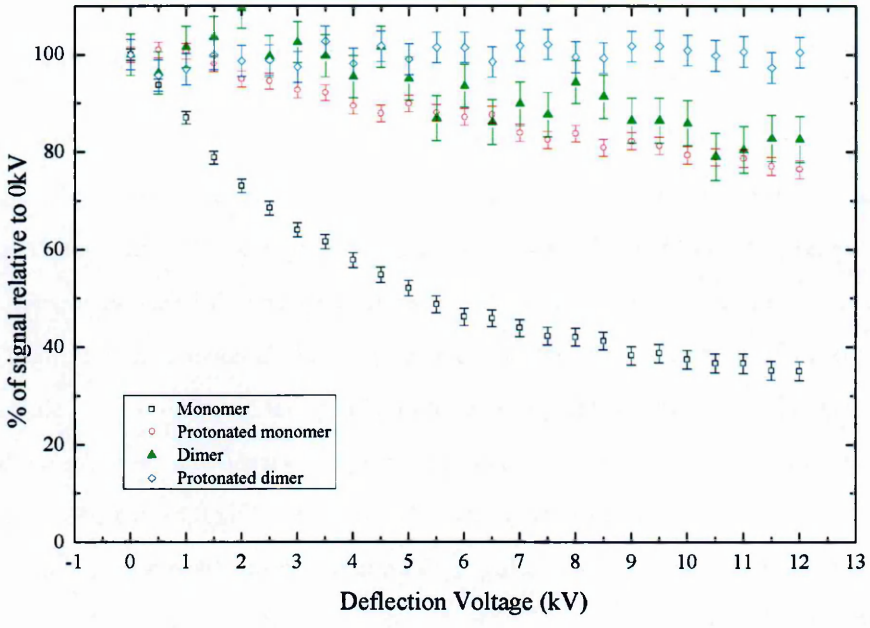

Figure 3.15: 200 eV EII ion yields of different species from a nitromethane–argon beam, as a function of Stark-deflector's voltage. Argon carrier gas pressure 500 mbar, nozzle diameter 20 μm

Therefore, there is an optimum driving pressure that corresponds to the lowest achievable rotational temperature of the beam for a given pumping speed in the expansion chamber.

Figure 3.15 shows how the 200 eV EII signals for several different ions varied with deflection voltage in an argon beam seeded with nitromethane. The neutral beam contained a range of clusters, as demonstrated by peaks up to $(\text{Nitromethane})_5$. The deflection voltage dependence in Figure 3.15 was recorded with a restricted mass/charge range to increase the ions' extraction frequency. Clearly, the strongest signal suppression in Figure 3.15 is observed for the monomer ion (0.057 D/amu , see Table 3.1). No value for nitromethane dimer's dipole moment is available in the literature. However, in Li et al.'s [169] theoretical study on the intermolecular interaction of the nitromethane dimer, the optimised geometry suggests that its dipole moment / mass is very low (the dipole moments of the two molecules are arranged in approximately opposite directions). This explains why the signal suppression for the dimer in Figure 3.15 is much weaker than for the monomer. However, the most interesting feature of Figure 3.15 is the

protonated monomer data which closely follows the dimer's curve. Protonated species can only be products from larger clusters (see Section 2.1.4.4) and protonated monomers are generally produced particularly efficiently from dimers. The protonated dimer, which must originate from trimers or even larger clusters (with smaller overall dipole moments and bigger masses, therefore much lower dipole moment / mass ratios), shows a flat dependence to within the present uncertainties. Hence Figure 3.15 shows that plotting an ion's signal intensity versus the deflection voltage is a powerful method to deduce the origins of fragment ions in mixed beams. This technique provides a valuable complement to the approach of moving the skimmer in order to select just one portion of a deflected beam.

3.5.1.2 Beam profile broadening and full deflection of nitromethane

In order to deflect molecules in the most controlled manner possible, further effort has been devoted to reducing the rotational temperature of the beam. As discussed in Section 2.4.2, increased cooling can be achieved in principle by increasing the p_0D. However, this also increases the gas flow (See equation 2.27) through the nozzle, raising the pressure in the expansion volume and hence tending to increase internal beam temperature as indicated in Figure 3.14. The experiments described in this section investigate the effect of the nozzle diameter on the observed deflection of nitromethane. Argon was the carrier gas in all the measurements presented here [1]. The Stark deflector was mounted horizontally in these experiments.

The results presented in Figure 3.16 were recorded with a 50 μm nozzle and with the expansion conditions optimised for maximum cooling (p_0D = 25 bar $\cdot$ μm, expansion chamber pressure 2.5×10^{-4} mbar). The movable skimmer was scanned in the deflecting and non-deflecting planes with 0, 4 and 8 kV applied to the Stark-deflector. For each skimmer position and deflection voltage a mass spectrum was recorded. The most striking feature of these measurements is the broadening of the nitromethane$^+$ profile in the deflecting plane in plots Figure 3.16a, b and c, red curves. The broadening is not observed in the non-deflecting plane (Figure 3.16a, b and c, black curves) or in any

[1] For more details why argon cools molecules more efficiently, refer to Section 2.4.2.4

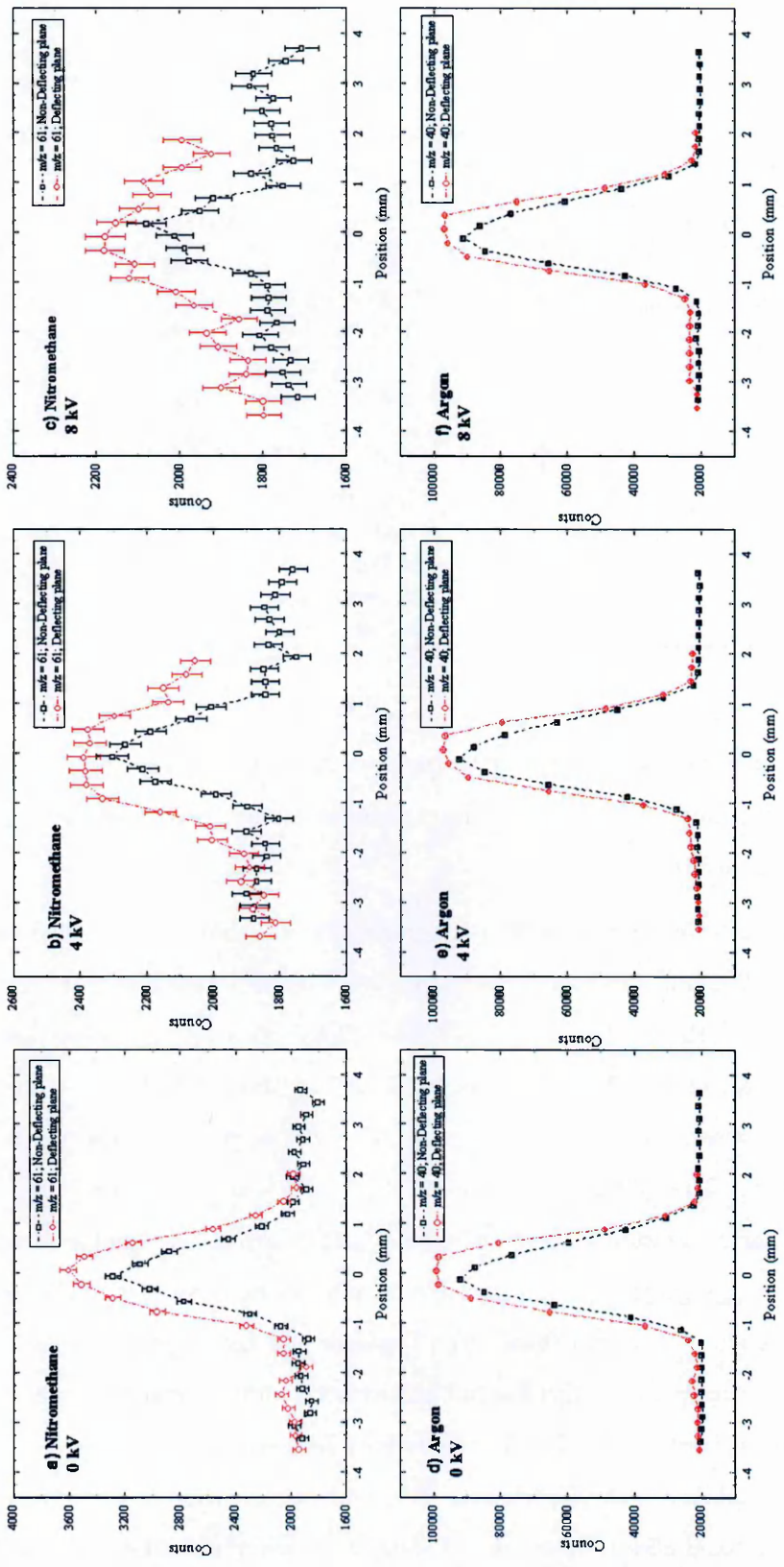

Figure 3.16: Molecular beam profiles for nitromethane$^+$ (a, b and c) and argon$^+$ (d, e and f) for the deflection voltages of 0, 4 and 8 kV obtained with a 50 μm nozzle.

Table 3.3: Profile widths for nitromethane$^+$ and argon$^+$ signals in deflecting and non-deflecting planes for Stark-deflector voltages of 0, 4 and 8 kV.

Target	Voltage [kV]	Plane	FWHM [mm]
Nitromethane	0	Deflecting	1.48
	4	**Deflecting**	**2.62**
	8	**Deflecting**	**2.72**
	0	Non-Deflecting	1.24
	4	Non-Deflecting	1.34
	8	Non-Deflecting	1.2
Argon	0	Deflecting	1.31
	4	Deflecting	1.31
	8	Deflecting	1.31
	0	Non-Deflecting	1.39
	4	Non-Deflecting	1.39
	8	Non-Deflecting	1.39

plane for the argon$^+$ signals (Figure 3.16 d, e and f). To obtain a systematic measure of the broadening, the width of the profiles has been obtained by fitting a Gaussian bell curve the data points. The fits for the argon data are always better than $\bar{R}^2 = 0.98$; Table 3.3 gives the obtained values.

The observed shape broadening, without a significant profile shift, can be explained by assuming that the molecules in the beam are not rotationally cold enough to trigger the transition into the pendular rotational states (See Section 2.4.1). Hence, there is roughly an equal number of molecules deflected "up", as "down". As a consequence, a series of measurements was performed with a 20 μm nozzle in an attempt to achieve increased cooling. The optimized conditions in Figure 3.17 were $p_0 D = 11$ bar $\cdot$ μm and expansion chamber pressure 4×10^{-5} mbar (i.e. greater expansion chamber pressure than Figure 3.16, highlighting the complexity of the cooling conditions). The figure shows 4 kV profiles for nitromethane$^+$ and for argon$^+$ in the deflecting plane. The nitromethane$^+$ maximum position has not shifted but a clear asymmetry is observed in the *Stark-broadened* profile. The four series have been recorded over several hours, indicating the stability of the experiment. The results clearly show that the movable skimmer can be used effectively to select a specific portion of a Stark-Deflection CW beam for collision experiments. In Figure 3.17 conditions, for example, a measurement with the skimmer positioned, at -1.5 mm on the deflection axes would probe the lowest

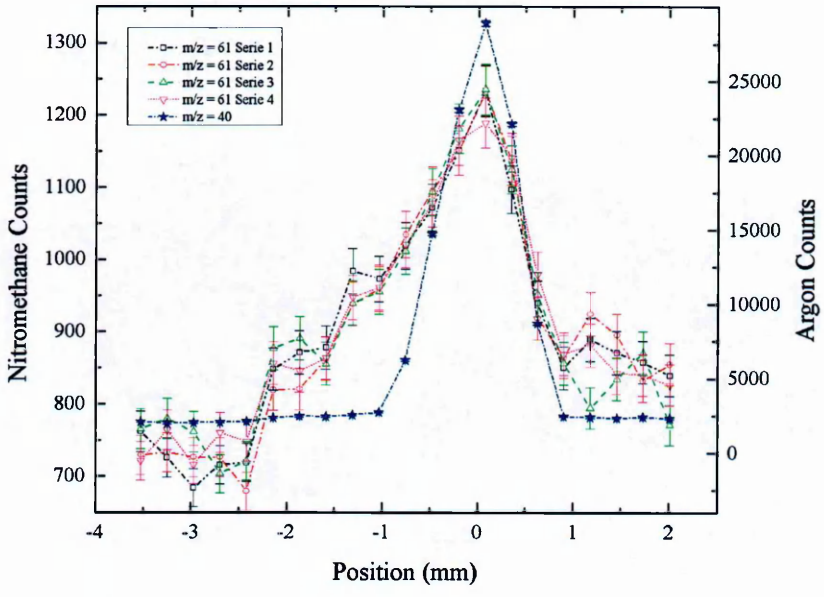

Figure 3.17: Argon and nitromethane profiles in the deflecting plane for 4 kV deflection voltage. High-field seeking molecules are deflected towards negative positions.

J-states of the ensemble in the molecular beam. Further optimisation is required to achieve a *fully deflected* profile ion signal instead of an asymmetric broadening but the present function of the Stark deflection system can already enable a range of interesting experiments on controlled beams.

3.5.2 Low energy electron beams

3.5.2.1 Principles of electron monochromator's optimisation

The device used in the Stark / EA experiment is a double-pass cylindrical monochromator with controlled angular aberrations (Figure 3.18). The principles of cylindrical electron monochromators and aberration control can be found in references [162] and [170]. Briefly, a monochromator works by manipulating the electron beam in electrostatic fields to narrow the energy distribution of the electrons. In most designs, a thermionic emission cathode is used as the source of electrons. The emitted electrons

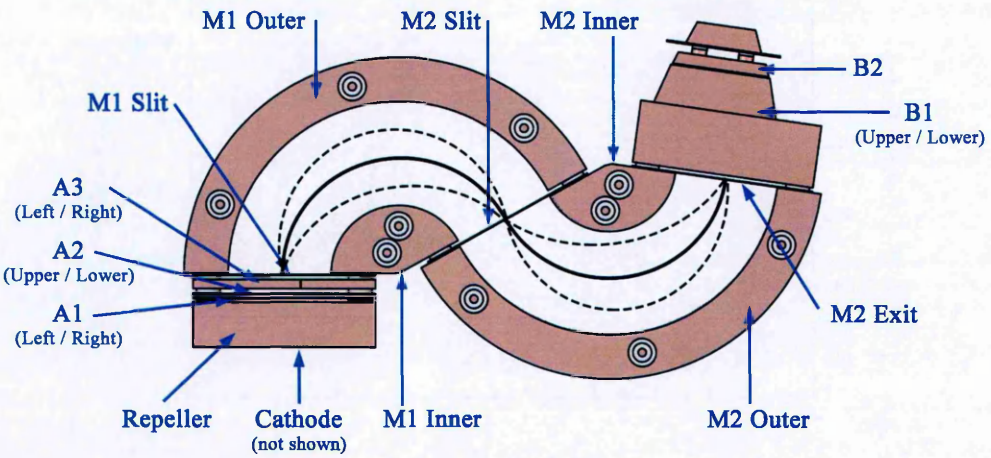

Figure 3.18: Monochromator system with the electrodes labelled. Top and Bottom covers of the two sectors are not shown.

have a Maxwellian distribution of energies, given by equation 3.1.

$$\Delta E_k = 2.54\, k_{\mathrm{B}} \cdot T \tag{3.1}$$

where k_{B} is the Boltzmann constant (11600^{-1} eV/K) and T is the cathode's temperature (in Kelvin). In practice, this means the energy resolution of the emitted electrons is in the range of $0.3 - 0.6$ eV, depending on the exact material of the cathode. The electrons need to be extracted and collimated to form a beam that feeds one (or more) energy dispersive elements, i.e. the sectors. This is commonly done by a triple electrostatic lens and a repeller electrode. The formed beam enters a region enclosed by two cylindrical electrodes, where the electric field curves the path of the beam. The electric field ϵ_r can be written in the form of equation 3.2:

$$\epsilon_r = \frac{\Delta V}{\ln\left(R_1/R2\right)} \cdot \frac{1}{r} \tag{3.2}$$

Where ΔV is the voltage between the two cylinders, R_1 and R_2 their respective radii and r the radial position within the field. Since an electron with a mass m , velocity v , and charge e travels on a circle with a radius r when equation 3.3 is satisfied, the nominal pass energy E_0 , i.e. the energy of the electron that travels on the central path

in the sector, can be then written in the form of equation 3.4.

$$\frac{mV^2}{r} = e\varepsilon_r \tag{3.3}$$

$$E_0 = \frac{e\Delta V}{2\ln(R_1/R_2)} \tag{3.4}$$

For a double-pass monochromator, the pass energies of the two sectors can be different. Note that the resolution of the monochromator, and the monochromatic current, are rather smooth functions of the pass energy in the second sector. To maximise transmission while maintaining good resolution, the second energy dispersive element should be operated at a low pass energy. Therefore, the first sector should be operated in a retarding mode, with a higher pass energy. The precise value of the pass energy is not critical and typically lies between 2 and 10 times the pass energy of the second sector. The retardation factor F_{exit} at the exit of the first sector is given by equation 3.5.

$$F_{\text{exit}} = \frac{E_0}{e\,U_{\text{exit}}} \tag{3.5}$$

Where eU_{exit} is the potential energy at the exit slit. Typical retardation factors range between 1.5 and 5. This can be achieved either by increasing the potential at the entrance slit or by decreasing potential on the exit slit. The latter approach is used more often as the electrons are decelerated over a longer distance, reducing the effect of space-charge impact on performance. The choice of the pass energy in the first sector depends on the properties of its feed beam. In order to maximise transmission, the pass energy should match the maximum in the feed beam's energy distribution. The optimum pass energy for the first sector can be chosen by analysing the output current of the sector (measured as the current on the exit electrode of the second sector) as a function of its pass energy and depends on the *working point* of the first sector (a function of the sector's midpoint potential, the entrance slit potential, and the retardation factor). Physical properties of the sector also play a role in the selection of the optimal pass energy, such as the offsets of positions of the entrance and exit slits from the central

Table 3.4: Raw voltages applied to the electrodes of the electron monochromator. All voltages are referenced to the V_{Beam} voltage, which in turn is referenced to the ground. This set of voltages produced 0.7 nA current measured at the Faraday cup.

Electrode	Voltage [V]	Electrode	Voltage [V]
A1 Left	55.7	A1 Right	58.8
A2 Lower	31.3	A2 Upper	29.9
A3 Left	-0.21	A3 Right	-1.02
M1 Slit	5.82	Repeller	-5.11
M1 Top Cover	7.32	M1 Bottom Cover	1.75
M1 Inner	1.80	M1 Outer	1.77
M1 Exit / M2 Slit	3.47	M2 Exit	3.28
M2 Top Cover	5.12	M2 Bottom Cover	0.60
M2 Inner	0.59	M2 Outer	0.77
B1 Upper	0.79	B1 Lower	0.59
VBeam	-10	B2	21.6

patch. Typically, the potential of the entrance slit is a good starting point for the optimisation.

Space charge plays a major role in the performance of cylindrical monochromators. Most of the effect can be compensated for by modifying the deflection angle of the sector. However, this can only compensate for the electron's beam divergence in the focusing plane, and effects of the space charge are still noticeable in the non-focusing plane, θ_z. Applying a negative bias to the top and bottom covers (with respect to the midpoint of the sector, i.e. the potential corresponding to the central path) helps to minimise the beam's divergence in this plane. The value of the bias depends mainly on the retardation mode of the sector. Bigger compensation is required in the entrance slit retardation mode, than in the exit slit retardation mode. Typical values of the bias are in the range -1 to -3 V.

3.5.2.2 Election beam optimisation for the Stark/EA experiment

By applying the principles described above to the device installed on the electron chamber, it was possible to produce monochromatic beams of up to 1.2 nA. Table 3.4 gives the raw voltages that resulted in a good measurable current and Table 3.5 gives calculated parameters of the monochromator.

Table 3.5: Working point of the electron monochromator. All voltages are referenced to the V_{Beam} voltage, which in turn is referenced to the ground. This set of voltages corresponds to the raw values from Table 3.4.

Property	Value
M1 Delta	5.57
M1 Midpoint	4.54
M1 Covers	-2.75
M1 Nominal pass	3.01
M2 Delta	4.35
M2 Midpoint	2.95
M2 Covers	-2.35
M2 Nominal pass	2.35

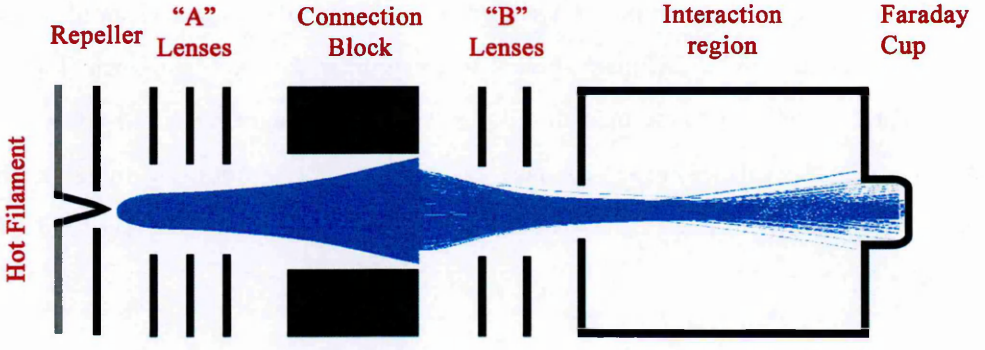

Figure 3.19: Mounting arrangement for the electron source with the two sector removed. The electron trajectory simulation (blue trace) has been calculated using SIMION 8 software.

Table 3.6: List of voltages for the electron beam source resulting in 8 μA recorded on the Faraday cup.

Electrode	Voltage
A1	+9.8 / +10.8
A2	+10.2 / +9.1
A3	+15.8 / +12.6
Block	+80
B1	
B2	+71.9

However, no ions were observed when irradiating the molecular beam with the monochromatic electron beam. This was attributed to stray electric fields between the electron beam and the TOF extraction volume and / or poor focusing conditions for ions entering the TOF extraction from outside. A more intense electron beam was required to identify the specific issues. Therefore the sectors of the monochromator were (temporally) replaced with a single connection block. This new assembly (Figure 3.19) provides much more intense beams (up to 20 μA) at the expense of energy resolution. The list of voltages resulting in 8 μA recorded on the Faraday cup is given in Table 3.6. This system enabled EII mass spectra to be recorded for an argon beam (Figure 3.20). The threshold value for ionisation (16 ± 0.5 eV) is in agreement with literature value (15.76 eV [45]), However, comparisons with measurements using the Kimball gun revealed an approximate signal loss of three orders of magnitude. Further tests are currently in progress.

3.6 Summary

This chapter provides a description of the crossed-beam apparatus at the OU for studying multi-photon ionisation (MPI) and electron impact ionisation (EII) of isolated and clustered molecules. Improvements to the system during this PhD have effectively eliminated background signals in MPI mass spectra and enabled EII measurements to be performed with tuneable mass resolution. Results obtained using the MPI / EII experiment are presented in Chapters 4, 5 and 7. The facility for the ultrafast time-resolved

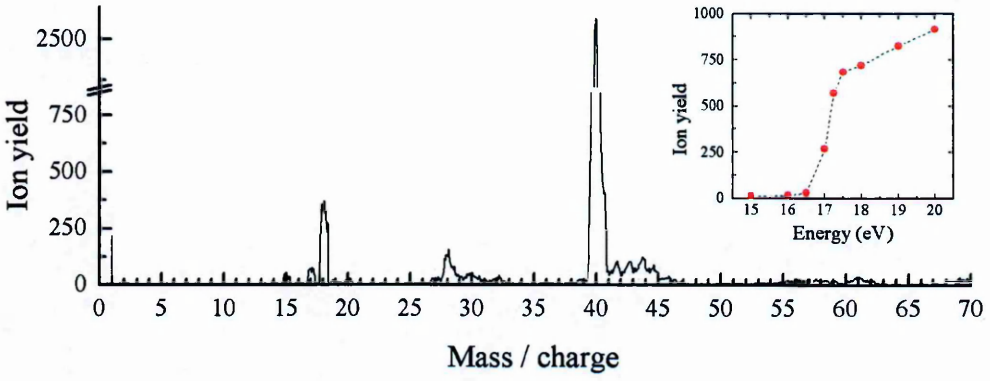

Figure 3.20: Mass spectrum recorded for 70 eV (8 μA) electron interactions with an argon beam. The insert shows the argon ion yield as a function of incident electron energy.

MPI measurements carried out with David Townsend and co-workers at Heriot-Watt University is described in Chapter 6.

A new experiment has been designed and built to study electron attachment (EA), EII, and MPI of molecules and clusters in Stark-deflected beams (Stark / EA). The system is described in detail here and a number of early results are presented to demonstrate its performance to date. EII measurements show that we have been able to manipulate the shape of a nitromethane beam, with the most rotationally cold molecules deflected most. Furthermore, we have successfully modified the composition of a collimated beam of nitromethane molecules and clusters by progressive removal of the species with the largest efective dipole moment / mass. Studying the dependence of a given product ion signal on the deflection voltage can reveal the origin of the ion (e.g. whether it comes from ionised monomers, dimers, and / or larger clusters). This provides a powerful tool for research into radiation-induced processes in clusters.

Chapter 4

Reactivity in adenine–water clusters

This chapter probes unimolecular and intermolecular reactivity in hydrated adenine clusters using multi-photon ionisation (MPI) and electron impact ionisation (EII) mass spectrometry. The effects of clustering with water on fragment ion production from adenine are studied for the first time. Complementary measurements are reported on the closely related molecule hypoxanthine to attain evidence for its formation via theoretically predicted deamination reactions in adenine–water clusters.

4.1 Introduction

The relaxation pathways of both isolated and hydrated adenine ($C_5H_5N_5$) following excitation to the lowest lying bright $\pi\pi^*$ state have been mapped out in considerable detail using ultrafast pump-probe experiments [171, 172, 173] and quantum chemical calculations [174, 175, 176]. Sub-ps-timescale internal conversion to the vibrationally hot electronic ground state via intermediary $n\pi^*$ and $\sigma\pi^*$ states is found to dominate, although evidence for much weaker intersystem crossing pathways to long-lived triplet states have also been reported [177]. Previous studies of reactivity in hydrated adenine have focused on tautomeric transitions [178, 179] and proton transfer in adenine dimer ions [180]. Since the present data was published [161], Alauddin et al. [181] reported infrared photodissociation spectroscopy measurements on $A_2 \cdot (H_2O)_n^+$ $(n = 1 - 4)$

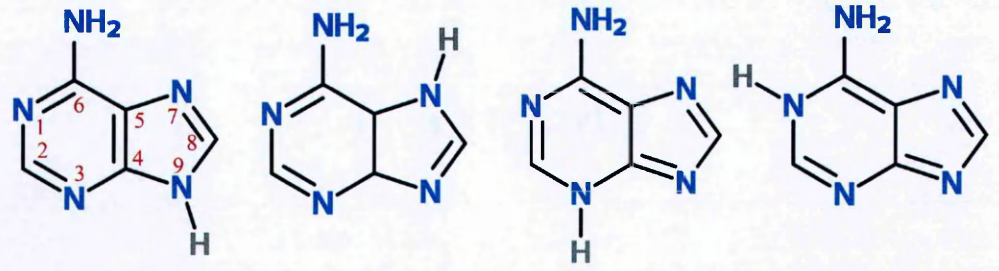

Figure 4.1: Selected tautomers of adenine [17, 2]. From left to right: amine-N9H (the most abundant in the gas-phase), amine-N7H, amine-N3H and amine-N1H.

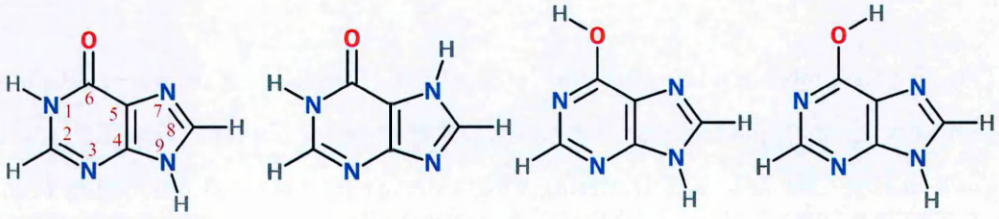

Figure 4.2: Selected tautomers of hypoxanthine [18, 19]. From left to right: keto-N1H/N9H (the most abundant in the gas-phase), keto-N1H/N7H, enol-cis-N1 and enol-trans-N1

clusters in order to probe the local solvation structures. However, no experiments have directly explored the effects of hydration on the dissociative ionisation pathways of adenine. The optimised geometries of adenine–water clusters are shown in Figure 4.3. The present measurements apply UV multi-photon ionisation (MPI) mass spectrometry to analyse fragment ion production from adenine–water clusters. Furthermore, this chapter provides the most detailed analysis to date of MPI and electron impact ionisation (EII) production of hydrated adenine monomer ions and hydrated reaction products (notably hydrated protonated adenine) from larger dissociated clusters. The key interest in directly comparing MPI and EII of mixed clusters stems from the selective nature of MPI, notably with water molecule photoexcitation being inaccessible in the present laser conditions.

The most abundant gas-phase tautomers of adenine are shown schematically in Figure 4.1, while Figure 4.4 shows the optimised geometries of π-stacked and H-bonded adenine dimers. Systematic theoretical works recently showed that the most stable tautomer of neutral adenine is N9H-adenine followed by two other tautomers (N3H-adenine and

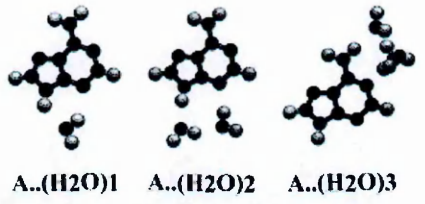

Figure 4.3: Optimized geometries of adenine–$(H_2O)_n$ (n=1, 2, 3) neutral clusters calculated usin a semi-empirical model. Reproduced from [20].

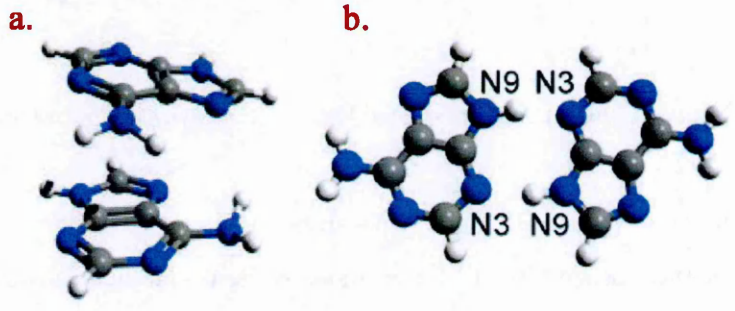

Figure 4.4: Optimised structures (B3LYP-D/6-31+G(d,p)) of the most energetically stable configuration of (a) π-stacked, and (b) H-bonded adenine dimer. Reproduced from [21].

N7H-adenine) at energies of 29 and 31 kJ/mol with respect to N9H-adenine [17, 182, 183]. IR-UV and R2PI double resonance spectroscopy performed by Plützer et al. [184] on oven-vaporised adenine before expansion through a nozzle showed that only the N9H-adenine was present in their experiments. These findings are further supported by MP2 and DFT calculations. In contrast, Nir et al. [185] demonstrated that gas-phase adenine produced by heating and then followed by jet-cooling may lead to the presence of two distinct isomers – N9H and N7H. However, most recently Bravaya et al. [182] proved that jet-cooling of adenine leads only to the most stable tautomer, i.e. N9H. Hence, it is also assumed that N9H-adenine is by far the most abundant gas-phase tautomer in the beams probed in the present work.

One possible reaction product of adenine and water that would not be readily identifiable in the mass spectra of hydrated adenine is hypoxanthine ($C_5H_4N_4O$) with mass 136 a.u., equal to protonated adenine or an adenine isotopomer containing one ^{13}C. Similarly to adenine, the most abundant gas-phase tautomers of hypoxanthine have been reported [186, 187, 188] to be two -keto forms (Figure 4.2), with the more dominant of the

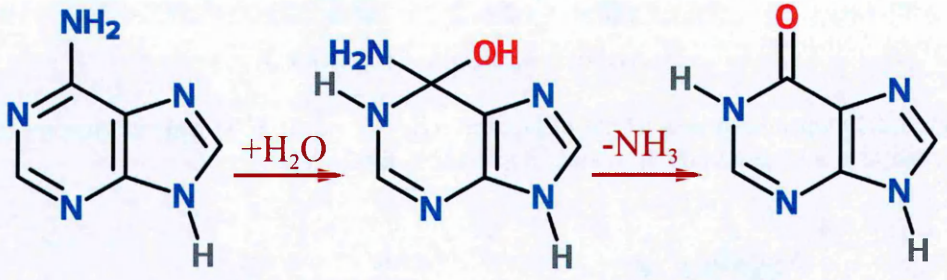

Figure 4.5: Diagram illustrating a predicted [22, 23] hydrolytic deamination reaction of adenine

two being the keto-N1H/N9H [189]. A negative activation barrier for hypoxanthine production in the closing system of four water molecules around adenine has been predicted theoretically (-2.4 kcal/mol), with one water molecule as catalyst and the others as medium [22, 23]. Figure 4.5 shows the predicted reaction schematically.

The reaction starts with four water molecules being hydrogen bonded to adenine. A 6-membered ring transition state is formed, involving the adenine molecule and two water molecules (I and II). The other two water molecules (medium) do not participate actively in the reaction – their sole role in the reaction is lowering the overall barrier. An intermediate state is then reached with one water molecule hydrogen-bonded to the C6 and N1 positions in a tetrahedral configuration. In the next step, the intermediate state decomposes via transferring a H-atom from water I to water II. Simultaneously, another H atom from water II transfers to the NH_2 group bonded to the C6 atom of adenine. Water II does not participate any further in the reaction. As the two H transfers occur at the same time, water II plays the role of a catalyst (the reaction is an associative H shuttling reaction). Finally, the C6—NH_3 bond breaks releasing an ammonia molecule. The OH complex left over from water I breaks – the oxygen creates a double bond with the C6, while hydrogen with the N5. Hence the reaction finishes with the formation of hypoxanthine molecule.

While the main aim of the present MPI and EII experiments on hypoxanthine is to elucidate adenine–water reactivity, the molecule is also interesting as a universal nucleobase that binds without discrimination to natural bases. Its potential applications in polymerase chain reaction (PCR) hybridisation probes and gene therapies have been

discussed by Rutledge et al. [190]. In contrast with adenine, very few experimental studies of the photophysical properties of hypoxanthine have been reported in the literature. Electronic spectra and excited state geometries have been investigated theoretically [191], both in isolated and hydrated conditions. As with DNA bases, $\pi\pi^*$ transitions dominate hypoxanthine absorption in the wavelength range (220–225 nm, 5.64–5.51 eV) of the present MPI experiments. Further studies have been focused on hydrogen bonding and stacking interactions with DNA bases [190], and on gas phase acidity and proton affinity [192].

4.2 Experimental conditions

The experiments discussed in this section have been performed with the MPI/EII experimental setup. A full description of the experiment is given in Section 3.2. Argon seeded with sublimated adenine or hypoxanthine (Sigma-Aldrich, minimum purity 99 %) with or without water vapour flowed continuously through a pinhole (70 μm diameter in the Figure 4.7 measurements, 50 μm in Figure 4.8 and 4.10) into the expansion chamber that was pumped at $1,210$ l/s.

The adenine temperatures ($237 - 276$ °C) were comparable with or lower than those applied in previous supersonic beam experiments that reported no evidence for thermally driven decomposition, isomerisation, or reactivity of adenine [26]. Hypoxanthine was heated to 295 °C in order to obtain clear signals above background. To our knowledge, no previous experiments have been carried out on hypoxanthine seeded in a supersonic beam. Tembreull and Lubman [193] brought the molecule into the gas phase by laser desorption. Dawley et al. [194, 195] produced an effusive beam for electron attachment experiments by heating hypoxanthine to 180 °C under vacuum and observed no evidence of thermal decomposition. However, it should be noted that much lower temperatures are systematically applied in experiments of this kind compared with experiments using seeded carrier gas. For example, Schlathölter et al. [82] carried out ion impact ionisation experiments on adenine vaporized under vacuum at 140 °C, whereas Kim et al.

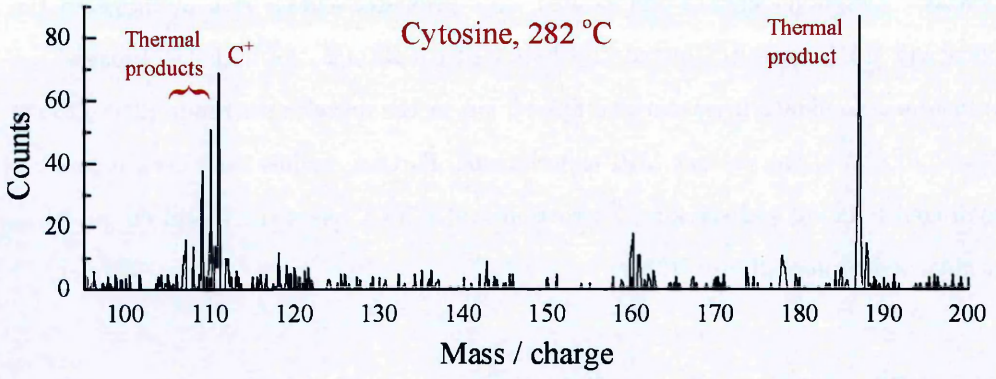

Figure 4.6: MPI (220 nm) mass spectrum of cytosine (282 °C, 0.6 bar Ar) revealing a number of new product ions that indicate thermal damage of the powder sample in the nozzle.

[61, 196] produced a molecular beam for MPI and EII studies (with no evidence for thermal damage) by sublimating adenine at 240 – 250 °C in a helium flow.

The present experimental procedures can reveal evidence for thermal decomposition and / or reactivity via unexplained peaks in the mass spectra, particularly at m/z values that are greater than the parent ion but do not match a plausible cluster ion. Naturally, the relative yields of ions linked to thermal decomposition tend to increase with time as well as at higher temperatures. For example, previous electron impact ionisation mass spectra [45, 197] and our MPI experiments on cytosine at 250 °C showed no evidence for the peaks labelled as thermal products in Figure 4.6. The remaining powder after the measurement at 282 °C was significantly discoloured, providing further evidence for thermal damage. No peaks suggesting thermal damage were observed in the present measurements on adenine and hypoxanthine and no powder discolouration occurred.

4.3 Results and discussion

4.3.1 MPI and EII of gas phase adenine and hypoxanthine

Figure 4.7 shows MPI and EII production of adenine and hypoxanthine radical cations. The same laser and electron beam conditions were applied for both molecules and the same argon pressure (0.5 bar) was used in all four measurements. It was necessary to use

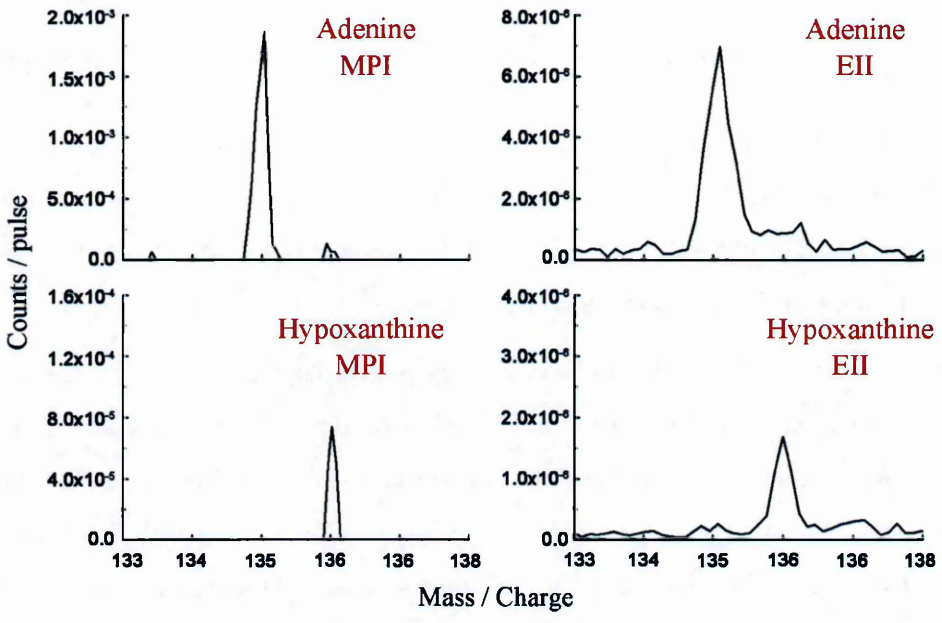

Figure 4.7: Comparison of MPI (220 nm, average fluence 4×10^7 W/cm^2) and EII (200 eV) of adenine and hypoxanthine (Ar 0.5 bar).

a higher powder temperature for hypoxanthine (295 °C) than for adenine (240 °C) in order to achieve a reasonably strong EII signal. Previously, Barć [2] unsuccessfully tried to multi-photon ionise hypoxanthine at 240 °C. This indicates that hypoxanthine has a markedly lower vapour pressure than adenine at any temperature in the present range (to our knowledge, no vapour pressures of hypoxanthine are available in the literature).

The mass spectra do not contain peaks for adenine or hypoxanthine clusters ions. While this does not discount the possible presence of clusters in the neutral beams [198], comparisons with previous experiments on adenine suggest that the supersonic expansion conditions were not suitable for significant cluster formation. For example Kim et al. [196] expanded 2.0 bar of helium seeded with adenine and water vapours through 500 μm diameter pulsed nozzle. As a first approximation, clustering in supersonic beams increases with the pressure above the nozzle and the nozzle diameter squared ($p_0 D^2$; see Section 2.4.2.5 for details). The product of $p_0 D^2$ was 400 times greater in Kim et al.'s experiments than in the measurements shown in Figure 4.7.

The ratio of 4 ± 3 % for m/z = 136/135 counts in the adenine MPI data is broadly consistent with the ratio of 7.4 % expected due to isotopomers [71]. By contrast, Kim

et al.'s [61] MPI experiments (ns-timescale pulses at 266 nm) showed a major increase in the m/z = 136/135 ratio due to intermolecular proton transfer in adenine clusters (discussed further in Section 4.3.2). The MPI signal intensity from hypoxanthine was too low to see any clear signal due to isotopomers.

Whereas adenine MPI has been observed in the present laser fluence regime in a number of previous studies (222–266 nm) [2, 127, 193, 198, 199], the present measurements demonstrate hypoxanthine MPI using ns-timescale laser pulses for the first time. De Vries [200] stated that hypoxanthine can be ionised effectively with 100 fs pulses (wavelength not given) but not with 10 ns pulses. Tembreull and Lubman [193] were unable to ionise hypoxanthine at 222 nm, $\sim 10^6$ W/cm^2. Therefore, it is not surprising that the present hypoxanthine MPI signal (220 nm, average fluence 4×10^7 W/cm^2) is relatively weak. Assuming similar EII cross-sections for the two molecules at 200 eV (a reasonable expectation according to the binary-encounter-Bethe model [9]), Figure 4.7 indicates that adenine MPI is more than six times stronger than hypoxanthine MPI in the present laser conditions. This effect is most likely due to particularly short lifetimes of the electronic excited states of hypoxanthine accessed in the present MPI experiments. Time-resolved experiments are necessary to verify this interpretation and elucidate the relevant excited state dynamics.

4.3.2 Hydration effects on fragment ion production from adenine

Figure 4.8 compares MPI mass spectra of adenine (A) seeded in argon beams with and without water vapour. The measurements were carried out at relatively low laser fluence (average 4×10^5 W/cm^2, 225 nm) in an effort to reduce cluster dissociation via higher order (≥ 3) photon absorption. The measurement in dry conditions showed a very weak peak for A_2^+ (0.2 % of the A^+ signal) and the ratio of m/z = 136 counts over m/z = 135 counts was 8.0 ± 0.4 %, close to the expected isotopomer ratio of 7.4 % [71]. This indicates that the adenine molecules were predominantly isolated. The mass spectrum of adenine with water vapour demonstrates $A^+ \cdot (H_2O)_n$ production up to n = 3. It is interesting to note that the intensity of the A_2^+ signal is approximately doubled in the hydrated measurement ($(9 \pm 2) \cdot 10^{-3}$ counts/pulse compared with $(4 \pm 1) \cdot 10^{-3}$

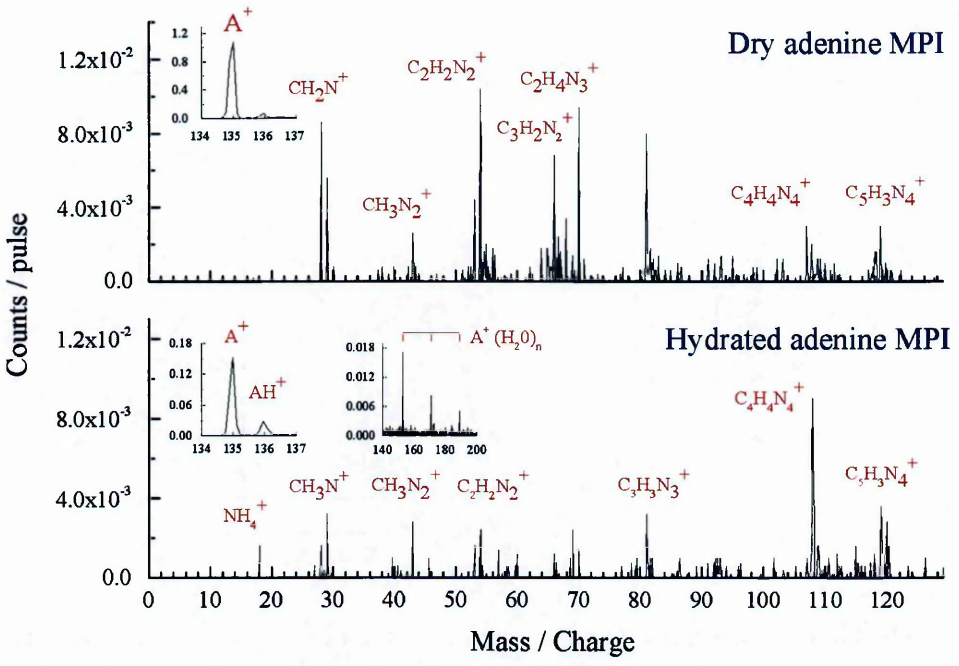

Figure 4.8: MPI mass spectra (225 nm, average fluence 4×10^5 W/cm^2, powder 237 °C, Ar 0.8 bar) of dry adenine and hydrated adenine (water 100 °C).

counts/pulse in dry conditions), suggesting that either the presence of water in the expansion aids the formation of complexes with two or more adenine molecules, or that the presence of water makes it more likely that an adenine cluster survives ionisation intact.

The ratio of m/z = 136 counts over m/z = 135 counts in the hydrated measurement (Figure 4.8) was 23 ± 2 %, clearly larger than the adenine isotopomer ratio. The extra m/z = 136 ions can be assigned to AH^+ formation via intermolecular proton transfer and subsequent cluster dissociation. Hünig et al.'s [180] time-dependent pump-probe experiments on pure adenine complexes demonstrated that AH^+ fragment ions were produced by proton transfer in adenine dimer ions. Indeed, proton transfer from A^+ to A in a dimer cation is exothermic: the proton affinity of neutral adenine is 225.5 kcal/mol (9.78 eV) [45] while the acidity of the adenine radical cation is 220.9 kcal/mol (9.58 eV) [201]. Park et al.'s [136] DFT studies showed that proton transfer in hydrated adenine dimer ions can occur with a barrier lower than 0.5 kcal/mol. Kim et al. [196] discussed the possibility that proton transfer from water to adenine in the $n\pi^*$ excited state

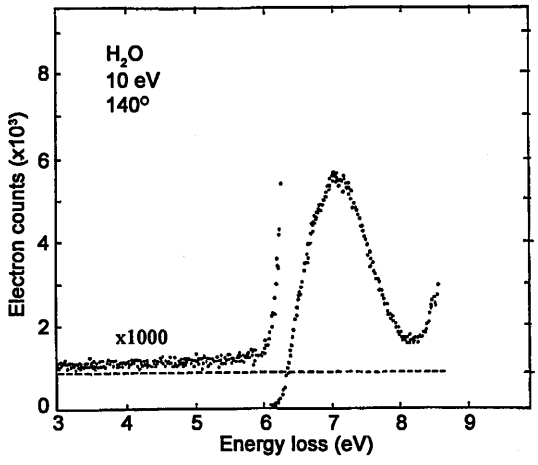

Figure 4.9: Electron energy loss (EEL) spectrum of water for 10 eV impact energy and 140° scattering angle, showing no structures in the energy loss range coinciding with the photon energies used in the present MPI experiments (4.59 – 5.64 eV). [24]

could explain the strong AH^+ production (as well as weak $A^+ \cdot (H_2O)_n$) production) in their 266 nm MPI experiments. They concluded that this reaction was highly unlikely due to its large endothermicity in hydrated adenine. Hydrogen transfer from H_2O (homolytic bond cleavage energy 123 kcal/mol) to the adenine radical cation (H affinity 109 kcal/mol) can also be ruled out [201]. Moreover, no electronic excited states of water are accessible in the wavelength range (220 – 225 nm, 5.64 – 5.51 eV) probed in the present MPI measurements [24, 202, 203, 204]. Figure 4.9 shows Cvejanovic et al.'s [24] electron energy loss (EELS) spectrum of water in the energy region partially covered in this work. Excitations to optically dark states are much more likely in the EELS spectra, compared with UV absorption spectra, and hence the absence of any features in Cvejanovic et al.'s measurements with low incident electron collision energy (< 10 eV) strongly indicate there are no states available in the 5.64 – 5.51 eV range. Therefore, AH^+ production in the present MPI experiments must begin with adenine excitation. The m/z = 136 peak may also contain a contribution of hypoxanthine$^+$ due to deamination reactions in closed-shell adenine–water complexes and subsequent cluster dissociation.

Notwithstanding the low laser fluence, Figure 4.8 demonstrates significant fragment ion production in both dry and hydrated conditions. Table 4.1 lists the fragment ions that

were clearly observed above the background level. Previous MPI-TOF measurements at 222 nm [193] have shown m/z = 28 products from laser-desorbed adenine in a supersonic jet. The only other MPI fragment ion of adenine MPI mentioned in a journal article is H^+ (recorded at 266 nm with a much higher fluence than the present measurements [127]). Barć [2] reported evidence for MPI (226 nm, 4.6×10^6 W/cm^2) fragments at m/z = 28, 54, 66, 70 and 81, but high background levels prevented a detailed analysis. Lin et al. [205] reported significant photo-dissociation of adenine in their 248 nm MPI experiments using ns-timescale laser pulses but did not specify the fragment ions. However, dissociative ionisation of adenine has been studied extensively in ion impact [206, and references therein], electron impact [47], and single photon absorption [43] experiments. Taking into account differences in energy deposition and signal / noise ratios, the previous measurements were broadly consistent in terms of the fragment ions produced. Accordingly, Table 4.1 shows that the present dry adenine MPI mass spectrum includes all the strong fragment ions (> 20 % of the A^+ signal) observed in Jochims et al.'s [43] 20 eV photoionisation measurement. Only one weak peak is observed in the present dry adenine MPI result that had not been reported previously: m/z = 68 ($C_2H_2N_3^+$ or $C_3H_4N_2^+$). However, since the present data were published, a new article has reported that Gaussian fitting of a large data set of electron impact ionisation mass spectra (0 – 200 eV with relatively low mass resolution) revealed evidence for weak fragment ion production at this mass over charge ratio [207]. On the basis of appearance energies and thermochemical data, Jochims et al. [43] proposed that the dominant fragmentation pathways of the excited adenine radical cation involve HCN loss followed by $C_4H_4N_4^+$ (m/z = 108 with the lowest appearance energy) dissociation (notably via further HCN loss), CH_3N_2 loss followed by $C_2H_4N_3^+$ (m/z = 70) dissociation, and direct $C_4H_3N_4$ loss producing H_2CN^+ (m/z = 28).

The only previous studies of adenine dissociative ionisation in clusters were carried out on pure adenine complexes using MPI (266 nm ns-timescale laser pulses) [44] and 50 keV O_5^+ impact [82]. Schlathölter et al. [82]'s ion impact experiments demonstrated strong production of m/z = 118 ions (indicating NH_3 loss, not observed in adenine monomers) as well as enhanced m/z = 119 (NH_2 loss) and m/z = 92 ($C_4H_2N_3^+$) signals due to

Table 4.1: Ions observed following MPI of adenine in dry and hydrated conditions (Figure 4.8 data, not including cluster ions), photoionisation (20 eV) of adenine [43], photo-dissociation of protonated adenine (266 nm, average fluence $\sim 10^7$ W/cm^2) [44], and EII (electron energy not available) of hypoxanthine [45].

	% of the parent ion peak (except in the case of AH^+) with the previously proposed assignments, where available.				
m/z	**Adenine MPI [A]**	**Hydrated adenine MPI [A]**	**Adenine photo-ionisation [43]**	**AH^+ photo-dissociation [44] [B]**	**Hypoxanthine EII[45] [B]**
136	8.0 ± 0.4	23 ± 2	Not shown	Not shown	100
135	100	100	100 ($C_5H_5N_5^+$)	Not shown	10
134	0.3 ± 0.1	0.8 ± 0.3	10 ($C_5H_4N_5^+$)	Not shown	
120	0.08 ± 0.04	1.2 ± 0.4	1 ($C_5H_4N_4^+$)		
119	0.3 ± 0.1	3.3 ± 0.6	3 ($C_5H_3N_4^+$)	100 ($C_5H_3N_4^+$)	
109				31 ($C_4H_5N_4^+$)	10
108	0.2 ± 0.1	10 ± 1	57 ($C_4H_4N_4^+$)		10
107	0.3 ± 0.1	0.7 ± 0.3	10 ($C4H3N4^+$)		
94				13 ($C_4H_4N_3^+$)	
92			9 ($C_4H_2N_3^+$)		
82				5 ($C_3H_4N_3^+$)	
81	1.2 ± 0.2	2.3 ± 0.5	50 ($C_3H_3N_3^+$)		10
80			10 ($C_3H_2N_3^+$)		3
70	0.7 ± 0.1	1.0 ± 0.3	17 ($C_2H_4N_3^+$)		1
68	0.2 ± 0.1				1
67			10 ($C_3H_3N_2^+$)	5 ($C_3H_3N_2^+$)	1
66	0.8 ± 0.1	0.6 ± 0.3	41 ($C_3H_2N_2^+$)		3
65					1
55				5 ($C_2H_3N_2^+$)	
54	0.9 ± 0.1	1.6 ± 0.4	55 ($C_2H_2N_2^+$)		30
53	0.4 ± 0.1	1.1 ± 0.4	28 ($C_2HN_2^+$)		8
43	0.3 ± 0.1	2.0 ± 0.5	34 ($CH_3N_2^+$)		2
42			16 ($CH_3N_2^+$)		
41			7 (CHN_2^+)		
40			1 (CN_2^+)		
39			1 (C_2HN^+)		3
38					3
29	0.6 ± 0.1	1.4 ± 0.4	60 (CH_3N^+)		7
28	0.7 ± 0.1	1.3 ± 0.4	110 (CH_2N^+)	5 (CH_2N^+)	32
27			10 (CHN^+)		4
18		0.6 ± 0.3	Not shown	25 (NH_4^+)	

Fragment ion peaks that have higher MPI count rates in the hydrated measurement than in the dry measurement are highlighted in bold.

[A] The MPI columns only include peaks with count rates that are clearly greater than background measurements. The error boundaries are based on assumed Poisson statistics.

[B] The approximate percentages in the AH^+ photo-dissociation and hypoxanthine EII columns were read from figures. Trace features in the mass spectra are not included.

clustering. The present MPI measurements did not reveal ion production at m/z = 118, although it should be noted that the signal / noise ratios were quite low in this m/z range. It also worth noting that Schlathölter et al. [82] used an aggregation source that produced clusters containing considerably more adenine molecules than the present apparatus. The m/z = 119 and m/z = 109 fragment ions were most intense in Cheong et al.'s [44] MPI experiments on adenine clusters (minor peaks were mentioned but not listed); both strong photodissociation products of protonated adenine. The present work provides the first data on how clustering with water affects fragment ion production from adenine. Figure 4.8 and Table 4.1 show that hydration significantly increased the count rate of m/z = 108 ($C_4H_4N_4^+$) ions as well as slightly enhancing m/z = 120 ($C_5H_4N_4^+$) and m/z = 119 ($C_5H_3N_4^+$) ion production. Conversely, it reduced the count rates of all the other fragment ions in the dry adenine MPI mass spectrum. These observations can be rationalised in terms of energy removal from the excited adenine cation via cluster dissociation tending to enhance the production of large fragment ions with low appearance energies at the expense of smaller ions with relatively high appearance energies, predominantly associated with sequential fragmentation pathways. Hydration also opened a fragment ion channel at m/z = 18 (NH_4^+, discussed below). Cheong et al. [44] analysed AH^+ fragmentation following photoexcitation at 266 and 263 nm (4.66 and 4.71 eV). In agreement with earlier collision induced dissociation (CID) experiments [208], the dominant fragment ions occurred at m/z = 119, m/z = 109 and m/z = 18 (see Table 4.1 for more detail). The hydrated adenine measurement in Figure 4.8 (with enhanced m/z = 136 production), showed a clear increase in the m/z = 119 and m/z = 18 signals. The m/z = 119 fragment was also produced from dry adenine so its enhancement may be (wholly or partially) due to energy removal from the excited radical cation via water molecule loss limiting sequential fragmentation processes. Indeed, the absence of a clear peak at m/z = 109 in the hydrated adenine measurement suggests that AH^+ fragmentation did not contribute very strongly to the present data. However the m/z = 18 signal in the hydrated adenine measurement provides compelling evidence for fragment ion production from AH^+.

MPI experiments on argon–water beams did not produce any m/z = 18 ions, as expected considering water's transparency in the present wavelength range (220–225 nm) [24, 202, 203, 204]. MPI (225 nm, average fluence 7×10^5 W/cm^2) measurements on adenine (248 °C) in an expansion with argon (0.9 bar) and D_2O (100 °C) provided further evidence supporting the assignment of the present m/z = 18 peak to NH_4^+ production following AH^+ dissociation. Extensive hydrogen–deuterium exchange was evidenced by a series of peaks at m/z = 135–141 (maximum at m/z = 138) replacing the m/z = 135 and m/z = 136 peaks observed in adenine–H_2O experiments. The mass spectrum also included a series of weak peaks between m/z = 18 and m/z = 22, with a maximum at m/z = 21 indicating NHD_3^+ production. Detailed figures are given in Appendix A (Figure A.1).

Previous electron impact measurements [45] showed the strongest fragment ions derived from hypoxanthine to be at m/z = 54 and m/z = 28 (both also fragment ions from adenine, as shown in Table 4.1). Ion production at these m/z values was suppressed by hydration in the present data. Therefore, the present data does not provide clear evidence for fragment ions traced to hypoxanthine formation in hydrated adenine complexes. This may be attributed to the fact that hypoxanthine is multi-photon ionised with much lower efficiency than adenine in the present laser fluence regime (Figure 4.7), hence any fragment ion production will also be relatively weak. Similarly, the fact that the total ion count rate in the hydrated measurement is only 21 % of that in the dry measurement can be partially attributed to hypoxanthine production and its low MPI efficiency in the present laser conditions. However, there are several possible concurrent mechanisms that can reduce the total MPI signal. In MPI experiments using ns-timescale laser pulses at 266 nm, Nam et al. [198] observed that hydration increased the number of photons required for A^+ MPI production by one (hence reducing MPI efficiency at a given fluence) and attributed this to energy loss via cluster dissociation in the neutral electronic excited state. Hydration can also cause shifts in the excited states of nucleobases (notably stabilisation of $n\pi^*$ states [106, 209]) and hence modify their relaxation dynamics with resultant changes in MPI efficiency.

4.3.3 Comparing MPI and EII of hydrated adenine complexes

Figure 4.10 compares MPI and EII mass spectra of adenine–water clusters. As $A_2H^+ \cdot (H_2O)_n$ peaks in the EII mass spectrum could not be separated from $(H_2O)_nH^+$ ($n \geq 15$), the present discussion focuses on the production of $A^+ \cdot (H_2O)_n$ and $136^+ \cdot (H_2O)_n$ ($AH^+ \cdot (H_2O)_n$ or hydrated hypoxanthine complexes). EII experiments on adenine–water clusters have been carried out by Kim et al. [65, 196]. However, whereas hydrated protonated thymine and uracil clusters were demonstrated, the presented mass spectra did not distinguish between $A^+ \cdot (H_2O)_n$ and $136^+ \cdot (H_2O)_n$. The EII plot in Figure 4.10 shows a series of $136^+ \cdot (H_2O)_n$ peaks preceded by weaker features attributed to $A^+ \cdot (H_2O)_n$. As discussed above, AH^+ production from pure adenine clusters is attributed to the proton transfer in adenine dimer ions followed by dissociation [180]. However, this mechanism is very unlikely to produce $AH^+ \cdot (H_2O)_n$ because complete loss of water molecules is expected to precede the cleavage of A_2^+ due to its high binding energy (e.g. 1.34 eV in $A_2^+ \cdot (H_2O)$) compared with adenine–water (e.g. 0.49 eV in $A_2^+ \cdot (H_2O)$) [210]. Alternatively, the removal of an electron from water in a hydrated cluster can lead to partial dissociation with a remaining excess proton (as observed for the pure protonated water clusters) that can migrate to adenine due to its markedly higher proton affinity [135]. While hypoxanthine formation may also contribute to the $136^+ \cdot (H_2O)_n$ peaks (the calculated closed-shell deamination reaction barrier is only -0.104 eV [22], so little water molecule loss is expected), the fact that hydrated protonated thymine and adenine have been observed in Kim et al.'s [65] EII measurements indicates that water ionisation followed by dissociation and proton migration to adenine is highly likely to take place in the present EII experiments.

Previous mass spectra of adenine–water clusters have been measured using diverse MPI schemes with both ns-timescale and fs-timescale laser pulses [2, 18, 198]. The novelty of the MPI mass spectrum in Figure 4.10 is that it is presented in sufficient detail (with adequate resolution and signal / noise ration) to reveal $136^+ \cdot (H_2O)_n$ peaks. The production of these ions cannot be initiated by water ionisation at this wavelength [202] and $AH^+ \cdot (H_2O)_n$ formation via proton transfer in hydrated adenine dimer ions

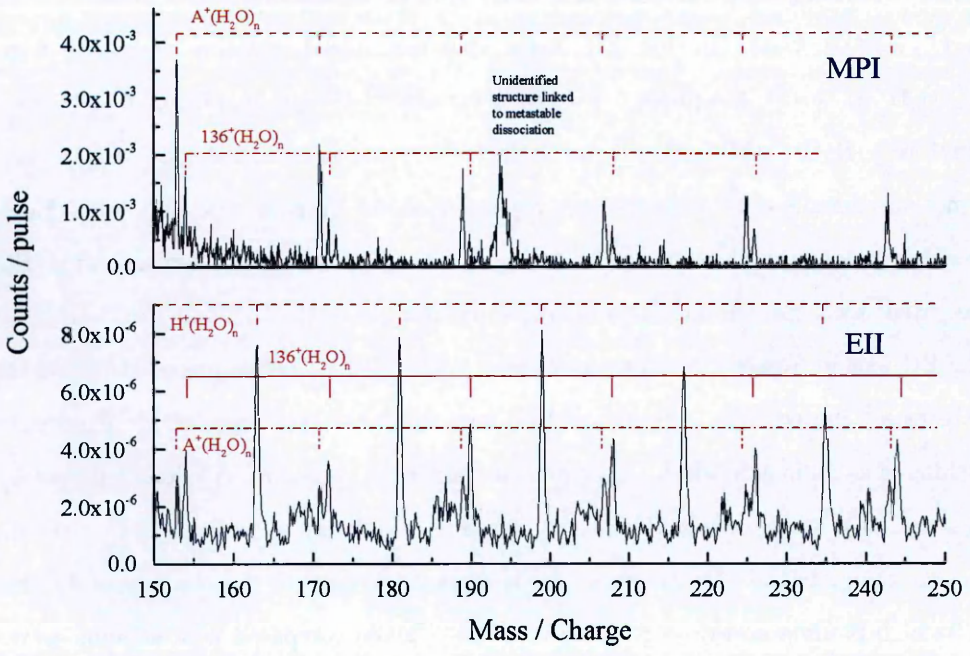

Figure 4.10: Comparison of MPI (upper plot, 220 nm, average fluence 3×10^6 W/cm^2) and EII (lower plot, 200 eV) mass spectra of hydrated adenine (powder 276 °C, water 70 °C, Ar 1.8 bar).

is very unlikely (see argument above). This leaves hypoxanthine$^+ \cdot (H_2O)_n$ as the most probable assignment for the present $136^+ \cdot (H_2O)_n$ MPI signals. Hence the high ratio of $136^+ \cdot (H_2O)_n$ / $A^+ \cdot (H_2O)_n$ counts in the EII measurement compared with the MPI data is consistent with the low MPI efficiency of hypoxanthine (Figure 4.7) as well as the opening of the water ionisation induced proton transfer pathway in EII. Kim et al. [65] reported evidence for analogous hydrolytic deamination reactions in cytosine–water clusters.

The assignment of hypoxanthine$^+ \cdot (H_2O)_n$ peaks in the present MPI mass spectrum has possible implications relevant to the structure of the adenine–water complexes in the neutral beam. The present data and previous mass spectra of adenine–water complexes [196] show evidence for $A^+ \cdot (H_2O)_n$ production extending to at least $n = 7$ and Kim et al.'s [61] calculations support a closed shell structure at $n = 4$. Therefore, deamination reactions in closed shell adenine–water complexes could reasonably be expected lead to negligible production of large $A^+ \cdot (H_2O)_n$ complexes. A possible explanation for $A^+ \cdot (H_2O)_n$ production with $n > 4$ is that a significant proportion of

the $A \cdot (H_2O)_n$ complexes in the neutral beam do not have closed-shell configurations; water–water bonds have formed while at least one hydrogen-bonding site of adenine remains vacant. This interpretation appears to be broadly consistent with semi-empirical optimised structure calculations [20, 211] showing that water molecules preferentially group around a single bonding site in $A \cdot (H_2O)_n$ ($n \leq 3$). It is interesting to note that Liu et al. [89] reported significant hydration effects on the collision induced dissociation of adenosine monophosphate anions (AMP^-) with up to 13 water molecules preferentially clustered on one side of the anion.

The MPI measurements revealed a broad peak centred at $m/z = 193.7$. This feature is most likely due to the dissociation of excited cluster ions in the TOF drift tube. This mechanism is similar to a metastable channel revealed in uracil. A complete discussion on the analysis method is given in Section 5.4.3. Briefly, time-of-arrival of the investigated ion is compared with a known reference peak. The measured time difference is compared with an analogous calculated value. This analysis showed, that either A^+ or AH^+ formation by $A_2{}^+$ dissociation in the drift tube could produce the observed feature. However, the combined experimental uncertainties were too great to distinguish which one is more likely to dominate. None of the alternative metastable dissociations considered, notably from precursor cluster ions containing water molecules, could produce flight times consistent with the observed feature. Further experiments using the reflection voltage to determine the ion's kinetic energy are necessary to identify the fragmentation process unambiguously. Kim et al. [61] also observed evidence for metastable dissociation of pure and hydrated adenine cluster ions, while Alvarado et al. [212] have shown that adenine cation fragmentation can proceed via CN loss followed by neutral H loss after a microsecond-order delay.

4.4 Conclusions

The present MPI and EII data enhance our understanding of the unimolecular and intermolecular reactive processes in adenine–water clusters. With the exception of the $C_5H_4N_4{}^+$, $C_5H_3N_4{}^+$, and $C_4H_4N_4{}^+$ fragment ion channels, clustering with water

stabilised adenine with respect to dissociative multi-photon ionisation. All sequential fragment ion pathways were suppressed. These hydration effects can be attributed to energy dissipation from the excited radical cation via cluster dissociation. Water ionisation followed by partial cluster dissociation and proton migration to adenine is expected to dominate $136^+ \cdot (H_2O)_n$ production in the present EII experiments. Weak $136^+ \cdot (H_2O)_n$ MPI peaks have been observed for the first time. MPI experiments on isolated hypoxanthine were carried out to verify whether the $136^+ \cdot (H_2O)_n$ peaks could be assigned to hydrated hypoxanthine ions following deamination reactions in closed-shell adenine–water clusters. Accordingly, hypoxanthine was successfully ionised using ns-timescale laser pulses for the first time. The low MPI efficiency compared with adenine suggests particularly fast internal conversion to the electronic ground state following $\pi\pi^*$ excitation.

Chapter 5

Multi-photon and electron impact ionisation of jet-cooled uracil, deuterated uracil and thymine

The chapter focuses on structural changes in uracil due to electronic excitation. It is argued here that differences multi-photon ionisation (MPI) and electron impact ionisation (EII) mass spectra can be traced to neutral electronic excited state dynamics. MPI wavelength thresholds for the production of specific fragment ions and comparisons with deuterated uracil and thymine provide further insights into excited state transitions and dissociative ionisation pathways.

5.1 Introduction

The experiments described in this chapter probe the pyrimidine derivative base uracil ($C_4H_4N_2O_2$), which forms two hydrogen bonds with adenine in RNA, using a MPI / EII experiment described in detail in Chapter 3. Uracil's close structural similarity with the DNA base thymine adds to the interest in this molecule, particularly with respect to differences in the photophysical properties of the two bases and their possible radiobiological consequences [213]. Figures 5.1 and 5.2 show the lowest energy conformers

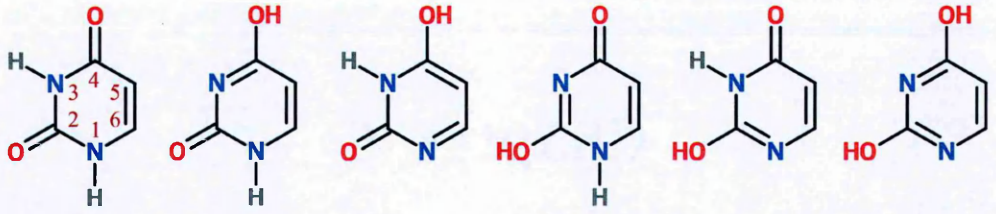

Figure 5.1: Uracil tautomers, from left to right: diketo, O4 / H3, O4 / H1, O2 / H3, O2 / H1 and dienol.

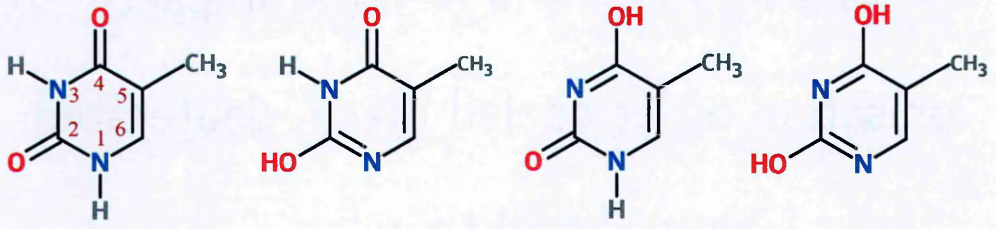

Figure 5.2: Thymine tautomers, from left to right: diketo, O2 / H1, O4 / H3, dienol.

of uracil and thymine, respectively. In the present experiments only the diketo form is expected to be present – infrared spectra of uracil vapour from powder heated at $200 - 325$ °C into $10 - 15$ Torr of argon indicated that only the diketo form was present [26]. Moreover, infrared cavity ringdown spectroscopy experiments of jet-cooled uracil following heating at $210 - 220$ °C also showed that the only gas-phase tautomeric structure was the diketo form [214]. These two experiments were performed in conditions similar to the ones in the present work.

The present MPI wavelength (220–270 nm) range coincides with excitation to the $S_2(\pi\pi^*)$ state that dominates the low-energy part of uracil's UV absorption spectrum [29]. A series of ultrafast spectroscopy and computational chemistry studies (e.g. references [31, 33, 35],) have explored the radiationless decay pathways of $S_2(\pi\pi^*)$-excited uracil in isolation as well as within certain hydrated complexes and base-pairs (see Chapters 6 and 7 for a summaries of the ultrafast and cluster literature). Recently, Carbonniere et al. [215] studied *ab initio* intramolecular vibrational redistribution in the non-radiative excited state decay of uracil. Theoretical calculations have identified ring opening [3] and tautomeric transitions [213] in electronic excited states. Nachtigallová et al. [3] identified a radiationless relaxation pathway from $S_2(\pi\pi^*)$ to the lowest-energy singlet state of uracil, $S_1(\pi\pi^*)$, via a ring-opening conical intersection. More recently

(published at the same time as the present experimental results), Richter et al. [37] carried out dynamics calculations with non-adiabatic and spin–orbit couplings that supported this pathway. However, no previous experiments have been carried out to look for evidence of excited state ring opening. Hence, the non-adiabatic dynamics calculations provided the impetus for the experiments as well as the essential context for the proposed interpretations. Due to the possibility of neutral excited state transitions in the stepwise excitation process, MPI can activate channels that are closed in single photon ionisation or collision induced ionisation experiments where ionic states are directly accessed from the electronic ground state [216]. This chapter also presents equivalent MPI measurements on thymine, for which no analogous ring-opening process has been predicted [3]. A distinctly higher pump energy (5.64 eV, 220 nm) was applied than in the previous MPI studies of thymine ($4.34 - 4.77$ eV, $285.7 - 260$ nm) [31, 32, 33, 217, 218, 219, 220] increasing the likelihood of isomeric transitions during S_2 ($\pi\pi^*$) deactivation.

The main aim of the present experiments was to study fragment ion production by MPI as a tool to observe evidence for excited state transitions. The present MPI scheme using single-colour nanosecond-timescale laser pulses enabled the initial excitation to be carried out in a much wider wavelength range than any previous study. Time resolved pump-probe measurements and experiments on clusters containing uracil are presented in Chapters 6 and 7.

5.2 Experimental

The experiments presented in this chapter have been performed with the MPI / EII setup described in Section 3.2. Argon or helium buffer gas ($0.5 - 1.2$ bar) seeded with sublimated uracil, thymine (both Sigma-Aldrich, minimum purity 99 %), and / or fully deuterated uracil (CDN isotopes, 98.4 %) flowed continuously through a 50 μm diameter pinhole into the pumped expansion chamber (500 l/s in the Figure 5.3, 5.5, 5.6 and 5.8 measurements; 1,000 l/s in Figure 5.12) to form a supersonic jet. The powder temperatures ($250 - 270$ °C) were comparable with or lower than those applied

in previous supersonic beam experiments that reported no evidence for thermally driven decomposition, isomerisation, or reactivity of uracil or thymine [26]. Accordingly the present mass spectra revealed no evidence for thermal reactivity spectra (discussed further in Section 5.4.2) and there was no powder discolouration.

5.3 Non-dissociative MPI of isolated uracil

The experiments in this section were carried out by heating uracil to 250 °C in 0.6 bar of argon. This pressure is lower than the driving pressures applied in previous supersonic expansion experiments probing isolated uracil, and accordingly no evidence was observed for uracil cluster ions or their derivative UH^+ (see Section 7.3 in the chapter on uracil clusters) in the measurements presented in Figures 5.3, 5.5, 5.6, 5.9 and 5.8. Uracil molecules were multi-photon ionised in the wavelength range 220–270 nm with average fluence 10^5–10^8 W/cm^2. Previous single-colour MPI experiments using ns laser pulses at 222 nm, [193] 248 nm [205] and 235–268 nm [221] did not produce any discernible uracil cation signals, whereas Brady et al. [217] were able to record a REMPI spectrum with a 270–285 nm pump and a 193 nm probe (both ns-timescale pulses). Barć [2] used the present MPI system to demonstrate MPI of uracil seeded in argon at 223.8 nm with some presence of clusters ($UH^+/U = 33 \pm 6$ %) and with high background signals severely limiting any analysis of fragment ion production. Figure 5.3 shows weak U^+ production ($\sim 10^{-2}$ counts/pulse) at 220 nm as a function of laser pulse energy. To reduce possibility of saturation effects in the photon order[1] measurements, the data in 5.3 were measured at average fluence (3–7) $\times$ 10^5 W/cm^2, close to the minimum required to accumulate adequate statistics. The observed photon order of 2.3 ± 0.4 indicates 2-photon ionisation.

Chapter 6 presents ultrafast time-resolved experiments on gas-phase uracil using 200 nm pump pulses and provides a short review of the earlier measurements and calculations exploring the excited state dynamics [3, 31, 32, 33, 34, 35, 37, 222]. A weak long-lived decay component is observed and attributed to triplet states accessible via $S_1(n\pi^*)$, following

[1] See Section 2.1.4

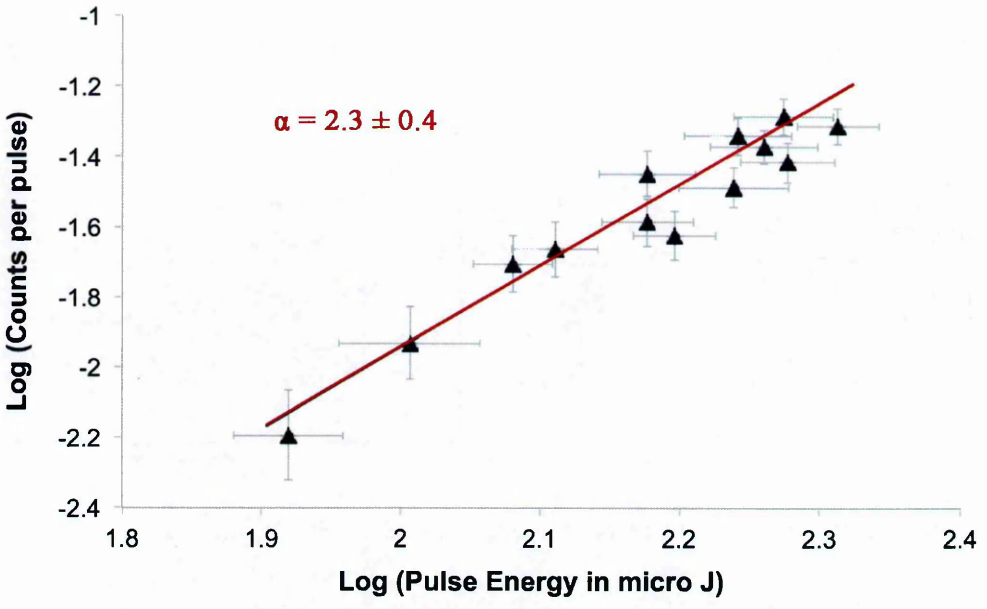

Figure 5.3: Power dependence (α = photon order) of uracil$^+$ production on laser pulse energy. The measurement was carried out at 220 nm with average fluence (3–7) $\times$ 10^5 W/cm^2, powder temperature 250 °C, and argon pressure 0.6 bar. .

Ligare et al.'s [36] recent calculations. Etinski et al. [223] theoretically characterised the lowest lying electronic states of uracil and performed calculations indicating that $T_1(\pi\pi^*)$ can be populated from the S_1 state on a sub-nanosecond time scale. However, single photon ionisation from T_1 is unlikely in the present energy range ($5.64 - 4.60$ eV) in view of its low calculated vertical excitation energy of 3.78 eV (see Table 6.1; Abouaf et al.'s EELS measurements gave a vertical energy of 3.65 eV , cited as a private communication by Nguyen et al. [224]) compared with 5.56 eV for $S_2(\pi\pi^*)$ and 4.67 eV for S_1 [223], while the ionisation energy of uracil is 9.15 ± 0.03 eV [43]. Therefore, the most plausible 2-photon pathway in the present experiments involves ionisation from S_2 or S_1 (both of which can be trapped on ps-timescales, as discussed in Chapter 6). The average fluence values in the Figure 5.3 measurement suggest that successive photon absorption on a ps-timescale would be rare. However, higher longitudinal modes can lead to fluence peaks during ns-timescale laser pulses [225]. Indeed, the fact that processes known to occur via virtual excited states were observed with MPI ($2 + 1$ ionisation of H and CO discussed in Section 5.5) at an average fluence of 2×10^8 W/cm^2 provides

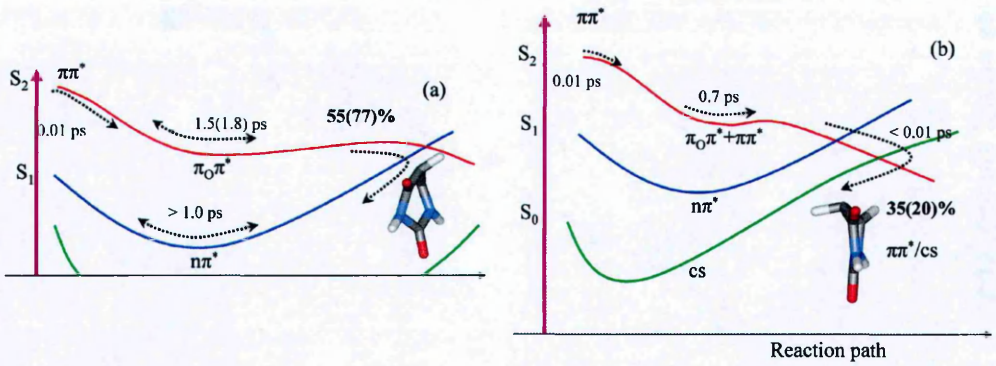

Figure 5.4: Scheme of the reaction mechanisms of uracil. Reproduced from [3]

a strong indication that the laser pulses contained fluence peak structure that can also account for photo-ionisation from the lowest-lying states. The MPI measurements on uracil–water clusters in Chapter 7 provide further evidence suggesting that ionisation from triplet states in unlikely to contribute significantly to the present single-colour MPI signals.

Table 5.1: Photon orders for the production of selected fragment ions from gas-phase uracil irradiated at 220 nm (5.64 eV). Where available, previous photo-ionisation appearance energies (AE) are given [43]

	Photon order (α) for different product ions								
Average fluence	**112** (AE 9.15 eV)	**84**	**69** *meta*[B]	**69** (AE 10.95 eV)	**42** (AE 13.25 eV)	**40** (AE 14.06 eV)	**28** (AE 13.75 eV)	**14**	**12**
3×10^5 -7×10^5	2.3 ± 0.4[A]	2.0 ± 0.3	2.1 ± 0.8	[C]	3.0 ± 0.9	[C]	3.5 ± 0.9	[C]	[C]
1×10^6 -5×10^6	1.5 ± 0.2	1.1 ± 0.2	1.1 ± 0.2	1.5 ± 0.4	2.1 ± 0.3	1.7 ± 0.2	2.6 ± 0.3	2.9 ± 0.6	[C]
9×10^6 -6×10^7	0.2 ± 0.1	0.3 ± 0.2	0.1 ± 0.2	0.1 ± 0.2	0.7 ± 0.1	0.6 ± 0.1	1.2 ± 0.1	1.4 ± 0.1	2.4 ± 0.2

[A] Shown in 5.3
[B] Uracil^{+*} dissociation after $1.3 - 14.6$ μs producing $C_3H_3NO^+$
[C] Insufficient counts to derive a photon order.

5.4 Fragment ion production in MPI and EII of isolated uracil

5.4.1 Dominant fragmentation pathways

Figure 5.5 shows uracil MPI mass spectra as a function of wavelength in the range 220–277 nm. The average fluence in these measurements was 7×10^7 W/cm^2, leading to significant production of fragment ions. Table 5.2 lists the peaks observed at 220 nm. Dissociative ionisation of uracil has been studied extensively by electron impact [45, 46, 81, 226, 227, 228], ion impact [82, 206, 228, 229, 230, 231, 232, 233] and single photon absorption [43]. The peak assignments are discussed further in Section 5.6 and Section 5.7. Taking into account differences in energy deposition and signal / noise ratios, the previous experiments were broadly consistent in terms of the fragment ions produced and three high-resolution examples are summarised in Table 5.2. The only previous measurements probing fragment ion production in uracil MPI were carried out using a 260 nm pump ($\sim$ 50 fs) and a 780 nm probe (40 fs) with a variable delay of up to 10 ps [35, 234]. These previous MPI mass spectra showed no clear evidence for fragment ions that were not observed in the earlier collision and photoabsorption experiments.

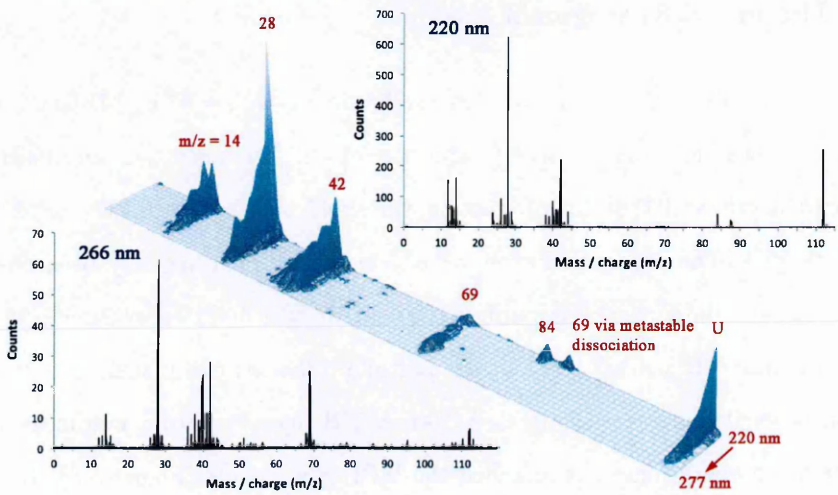

Figure 5.5: Wavelength dependence of uracil MPI (250 °C, Ar 0.6 bar). Mass spectra with 10^4 laser pulses were recorded at 2–7 nm intervals in the range 220–277 nm with average fluence 7×10^7 W/cm^2.

On the basis of appearance energies and thermochemical data, Jochims et al. [43] proposed that the dominant fragmentation pathways of the excited uracil radical cation involve HNCO loss followed by $C_3H_3NO^+$ (m/z = 69) dissociation (particularly H, CO, HCN, and HCNH loss). Matsika et al.'s [35, 234] *ab initio* calculations also supported sequential fragmentation via $C_3H_3NO^+$ as the mechanism to produce the strong fragment ions at m/z = 42, 41, and 28. Only in the case of ion production at m/z = 28 was direct dissociation of the radical cation energetically competitive with the minimum sequential fragmentation pathway. DFT calculations by Sadr-Arani et al. [235] identified plausible sequential fragmentation routes via $C_3H_3NO_2^{\bullet+}$ (m/z = 85) or $C_3H_4NO^+$ (m/z = 70), as well as pathways via $C_3H_3NO^{\bullet+}$ (m/z = 69). Table 5.1 shows photon orders for the strongest product ions recorded at 220 nm, in three fluence ranges, corresponding to different degrees of saturation, as well as previously measured single photon ionisation appearance energies [43]. As would generally be expected, the fragment ions with appearance energies > 11.28 eV (twice the energy of the 220 nm photons) have photon orders that are greater than uracil$^+$.

5.4.2 The m/z = 84 fragment ion

Figure 5.5 and Table 5.2 demonstrate ion production at m/z = 84 by MPI at 220 nm. Figure 5.6 shows that the relative production of this fragment ion increased with falling wavelength and that its production threshold was between 237 and 232 nm (5.29 ± 0.06 eV). The production of m/z = 84 ions from uracil has only been observed after the current data has been published [160], in laser-induced plasmas (266 and 1064 nm ns-timescale pulses) [236] where multiple collisions can plausibly lead to the ionisation of excited neutral isomers. A 200 eV EII mass spectrum was measured in molecular beam conditions that matched the MPI experiments (Figure 5.8). In agreement with the previous work, strong EII signals were obtained at m/z = 112 and 69 but no peak was observed at m/z = 84. The first interpretation considered was that the new fragment ion may be traced to the ionisation of a neutral fragment, following dissociative ionisation of uracil. A process of this kind would have relatively high photon order. For example, consider Matsika et al.'s [35, 234] proposed pathway for CH_2N^+

Table 5.2: Product ions observed following the ionisation of gas-phase uracil by 20 eV photons [43], by fast electrons [46, 47] and by MPI at 220 nm (Figure 5.5 inset).

m/z (where available, intensity is give nas a percentage of the strongest peak)				Proposed ion formula	Notes
220 nm MPI (present work)	70 eV e- impact: Imhoff et al. [46]	70 eV e- impact: Rice and Dudek[47]	70 eV photo ionisation [43]		
113 (2%)	113	-	-	$C_4H_4N_2O_2^+$ with one ^{13}C	
112 (39%)	112	112 (78%)	112 (63%)	$C_4H_4N_2O_2^+$	
-	-	96 - weak	96 - weak	-	
84 (8%)	-	-	-	$C_3H_4N_2O^+$	Deuterated comparison supports $C_3H_4N_2O^+$
-	-	77 - weak	-	-	
-	70[B]	70 (7%)	70 - weak	$C_3H_4NO^+$ [43, 235]	
69 meta (6%) A	-	-	-	Uracil^{+*} dissociation after 1.3 – 14.6 μsproducing $C_3H_3NO^+$	
69 (4%)	69	69 (63%)	69 (52%)	$C_3H_3NO^+$ [43, 235, 35]	
68 (2%)	68	68 (33%)	68 (33%)	$C_3H_2NO^+$ [43]	
-	67	67 - weak	-	-	
-	56	56 - weak	56 - weak	-	
-	53	53 - weak	53 - weak	-	
-	52	52 - weak	52 - weak	-	
-	51	51 - weak	-	-	
44 (5%)	44	44 (8%)	44 -weak	CH_2NO^+ [46]	
43 (4%)	43	43 (15%)	43 (10%)	$CHNO^+$ [43]	
42 (34%)	42	42 (100%)	42 (100%)	$C_2H_2O^+$ [43, 235, 35] / $C_2H_4N^+$ [235, 46]	Deuterated comparison supports $C_2H_2O^+$
41 (10%)	41	41 (48%)	41 (50%)	$C_2H_3N^+$ [43, 35] / C2HO+ [43]	Possible combination
40 (17%)	44	40 (57%)	40 (25%)	C2H2N+ [43]	Deuterated comparison supports $C_2H_2N^+$
39 (7%)	39	39 (15%)	39 - weak	C2HN+	
38 (6%)	38	38 (7%)	-	C2N+	
-	30	-	-	-	
29 (9%)	29	29 - weak	29 - weak	CH3N+ [43, 235]/ HCO+ [43]	Deuterated comparison supports CH_3N^+
28 (100%)	28	28 (78%)	28 (86%)	CH2N+ [43, 235, 35]/ CO^+ [46]	Deuterated comparison supports CH_2N^+
27 (7%)	27	27 - weak	27 - weak	CHN^+ [43]	
26 (18%)	26	26 - weak	26 (5%)	$C_2H_2^+$ [43]	Deuterated comparison supports a CN^+ contribution
25 (3%)	25	-	-	C_2H^+	
24 (9%)	24	-	-	C_2^+	
-	18	Not measured	18 - weak	H_2O^+ impurity[43]	
-	17		17 - weak	NH_3^+ [43]	
-	16		-	-	
15 (2%)	15		-	CH_3^+ [46]	
14 (24%)	14		14 - weak	N^+ [43]/ CH_2^+ [46]	Deuterated comparison supports CH_2^+
13 (4%)	13		Not available	CH^+	
12 (22%)	12			C^+	
-	2			-	
1 (1%)	1			H+ [46]	

The present data columns only include peaks with count rates that are clearly greater than background measurements. In the columns summarizing the data of Jochims et al. [43] and Rice and Dudek [47], channels with intensities < 5 % of the maximum peak are labelled weak. Sadr-Arani et al. [235] reported other possible assignments but proposed those cited above as the most probable.

[A] This metastable channel appears at m/z = 87.6 in the calibrated mass spectra shown in Figure 5.5.

[B] Imhoff et al. [46] suggested that $C_3H_3NO^+$ including a ^{13}C isotope might contribute to this peak.

(m/z = 28) and $C_3H_2NO_2^+$ (84 atomic mass units) production via direct dissociation of the uracil radical cation. To produce $C_3H_2NO_2^+$ via this process would require at least one more photon than CH_2N^+ production. Table 5.1 shows that the error boundaries of $\alpha(84)$ and $\alpha(112)$ overlap in all three fluence conditions probed, while $\alpha(28)$ is approximately one photon greater. Hence the m/z = 84 ions were produced by 2-photon absorption and any hypothetical dissociative ionisation followed by neutral fragment ionisation pathway can be discounted. The production of the new fragment ion must therefore depend on a process that occurs in a neutral excited state. This process is bypassed when uracil is excited directly to an ionic state, as in the present and previous EII measurements. The possible candidates for this neutral excited state process are dissociation (an excited radical fragment can plausibly be ionised by subsequent single photon absorption) or a transition into an isomeric state with its own distinct dissociative ionisation pathways. The absence of the m/z = 84 peak in the previous MPI experiments [35] can be attributed to the 260 nm pump photons having insufficient energy to overcome the dissociation or isomeric transition barrier.

Nachtigallová et al. [3] carried out non-adiabatic dynamics simulations of the decay mechanisms of uracil following excitation to the bright S_2 state. In particular, they calculated the stationary points and minima on the crossing seams of the S_2 and S_1 excited states and the electronic ground state (S_0) at the CASSCF, MR-CISD, and MS-CASPT2 levels. From the perspective of this work, the most interesting relaxation pathway is $S_2(\pi\pi^*)$–$S_1(\sigma(n-\pi)\pi^*)$–S_0 with ring opening at the S_2/S_1 crossing seam. Indeed, Nachtigallová et al. [3] predicted that this ring opening deactivation pathway leads almost certainly to new photochemical products. Two aspects of this pathway specifically link it to the ion at m/z = 84. First, the CASSCF minimum energy of 5.25 eV for the S_2/S_1 crossing seam matches the 5.29 ± 0.06 eV threshold for the present m/z = 84 signal. The equivalent MR-CISD, MR-CISD with Pople corrections, and MS-CASPT2 minimum energies (5.97, 5.57, and 5.84 eV, respectively) agree less closely with the present threshold but are nonetheless consistent with an effect that is only observed significantly above the S_2 band origin (Etinski et al.'s [223] calculations using four methods placed the adiabatic energy between 3.74 and 4.03 eV). Second,

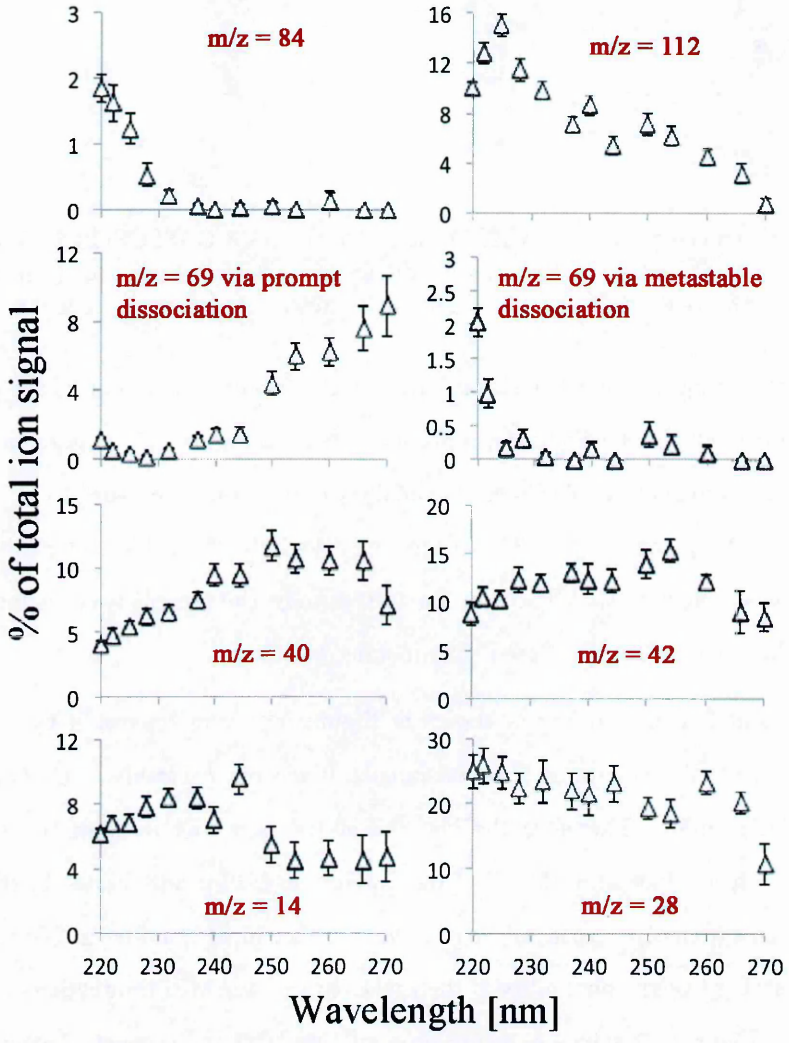

Figure 5.6: MPI wavelength (220–270 nm) dependence of selected ion counts/total counts. Fluence and molecular beam conditions match 5.5

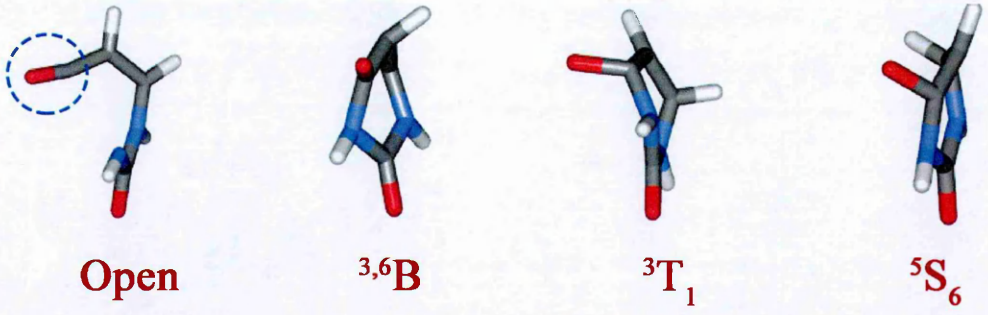

Figure 5.7: Structures of S_2/S_1 MXS optimised at the SA-3-CASSCF(10,8)/6-31G* level of theory. The CO group in the open configuration, which subtraction is the proposed mechanism for creation of the $m/z = 84$ ion, is circled. Reproduced from [3].

the predicted ring opening transition leaves a CO group at one end of the structure (Nachtigallová et al.'s [3] Figure 2, reproduced here in Figure 5.7). Therefore CO loss following photoionisation of this electronically excited isomer appears to be probable, leaving $C_3H_4N_2O^+$ with $m/z = 84$. Hence, the calculations provide a compelling argument to assign the new MPI fragment ion and, equally, the present experimental results support the theoretically predicted ring-opening pathway.

The MPI and EII measurements shown in Figure 5.8, were separated by only a few minutes. The beam conditions were unchanged; it was not necessary to cool and reheat the powder sample. Therefore the absence of the $m/z = 84$ peak in the EII result provides a strong indicator that its presence in the MPI result is not linked to any thermal damage in the nozzle, adding to the evidence already noted in Section 5.2. In order to further test the possibility of thermal effects on the MPI production of $m/z = 84$ fragments, Figure 5.9 shows a comparison of two MPI mass spectra recorded with different powder temperatures (all other experimental conditions were unchanged). The relative signals at $m/z = 84$ and $m/z = 112$ (uracil$^+$) are the same in both measurements to within the statistical uncertainties. This is consistent with the assumption that the jet cooling produces vibrationally cold molecules in both experiments and hence the sublimation temperature has no effect on the MPI pathways.

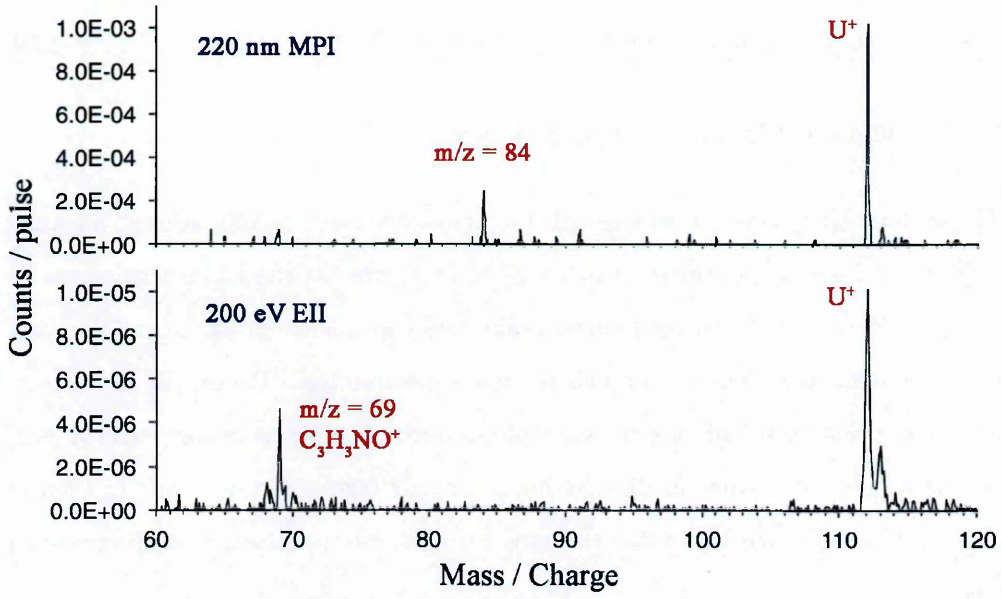

Figure 5.8: Comparison of MPI (220 nm, average fluence 6×10^7 W/cm^2) and electron impact ionisation (200 eV) mass spectra recorded with matching molecular beam conditions.

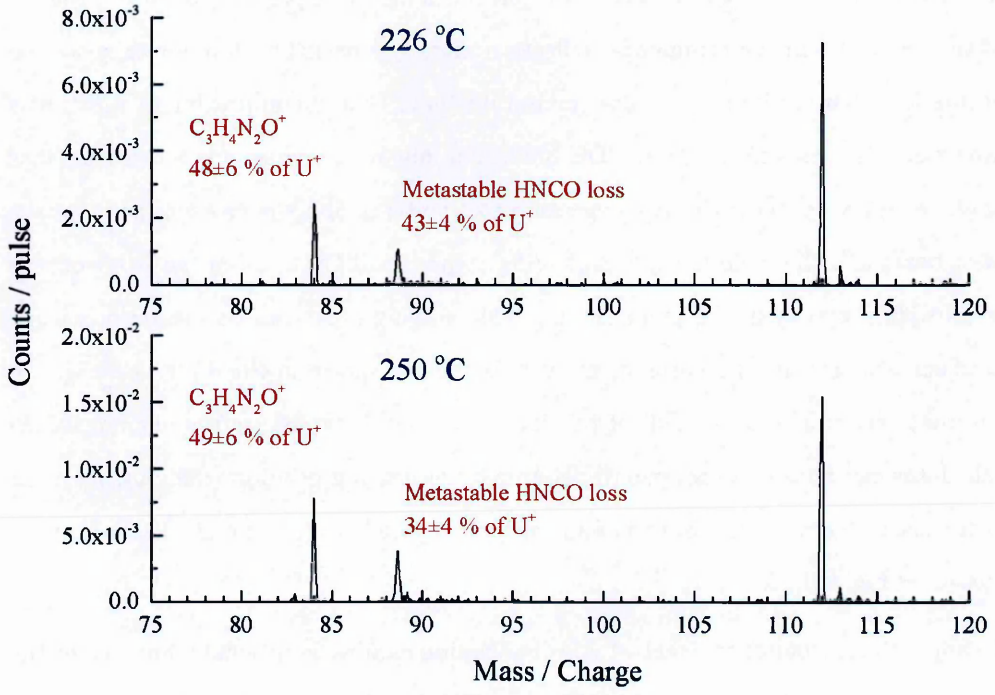

Figure 5.9: Comparison of successive MPI mass spectra (220 nm, average fluence 9×10^7 W/cm^2, helium 0.6 bar) recorded using different uracil powder temperatures: 226 and 250 °C.

5.4.3 Metastable dissociation pathway

The present MPI measurements revealed a metastable dissociation pathway, apparent in Figure 5.5 as a peak centred at m/z = 87.6. In Figure 5.9, the same feature appears at m/z = 88.7. The flight-time-to-mass calibration depends on an ion having the same mass throughout its journey through the mass spectrometer. Hence, the non-integer m/z values (not even half-integer that could in principle indicate doubly charged ions) can be attributed to the ion dissociating during its flight time, with the (no longer meaningful) calibrated m/z value changing for different optimised mass spectrometer voltages.

In order to assign features produced by delayed (or *metastable*) dissociation, a calculator has been produced in MS Excel for ion flight times. Previous fight time calculations by the Molecular Clusters Group were only guidelines due to imprecisely defined positions of the ion optics in the commercial reflectron mass spectrometer. If any fragmentation occurs less than around 10 ns after ionisation (note that the approximate width of a laser pulse is 7 ns and a typical TDC bin size in our measurements is 8 ns), then it is only necessary to know the mass spectrometer voltages and the crossing point of the laser beam and the molecular beam in order to predict flight time (in the range of tens of μs with a precision of around 10 ns). The crossing point can be determined using a reflect voltage cut-off measurement such as the one shown in Figure 3.6 on page 58. Alternatively, if a measurement of this kind is not available for a given alignment, the calculator can be used in reverse to determine the starting position (the crossing point of the laser and molecular beam) of an easily recognised ion (e.g. uracil$^+$) based on the measured flight time.

To apply the calculator to a metastable dissociation requires additional information: the masses of the ions before and after the dissociation and the time of the fragmentation. Therefore the flight time alone is not enough to determine a metastable dissociation unambiguously. In the case of metastable dissociation observed in the present MPI mass spectra of uracil, this additional information is the kinetic energy (KE) of the fragment ion. Dissociation events that take place before the ion has reached the field-free-region of

the mass spectrometer will lead to a broad distribution of modified flight times. Hence, these distributions do not manifest themselves as a distinct peak in a mass spectrum. By contrast, all distributions of a given type (i.e. from one parent ion to one fragment ion) that take place during the first journey through the field-free-region of the reflectron mass spectrometer will result in one flight time and hence a peak in the mass spectrum that can be KE-analysed.

The calculator divides the journey from ion production to detection into two parts: before and after a conceivable metastable dissociation. First, an ion is produced during the laser pulse (7 ns) and travels for a certain time through the mass spectrometer. It then undergoes dissociation into a lower-mass ion and one or more neutrals. The remainder of the time-of-flight is calculated for this new ion. The masses of the ions, as well as the exact location of the dissociation can be varied to accommodate different scenarios. At the same time, the penetration depth into the reflectron part of the mass spectrometer (described in detail in Section 3.2) can be determined. Should this depth be greater than the physical length of the reflectron, the ion hits the last electrode, and is lost. This allows for calculating the cut-off reflection voltages associated with specific metastable dissociation channels, i.e. the voltages corresponding to the ions penetrating the full depth of the reflectron and reaching the last electrode.

The TOF spectrometer's reflection electrode voltage (a diagram showing ion optics of the mass spectrometer in shown in Figure 3.6), enables a cut-off voltage to be determined for any peak in a mass spectrum. For ions produced promptly by the laser pulse, this cut-off voltage is linked to the position at which they were produced, as described in Section 3.4.1.1.

The situation changes if a fragment ion is produced some time after the laser pulse. In this case, the kinetic energy of the fragment ion will be lower and hence it can be reflected in a weaker field. Therefore the cut off voltage for these metastable fragment ions will be more negative than the extraction grid's voltage (-380 V)

The TOF-Calculator can be used in three modes:

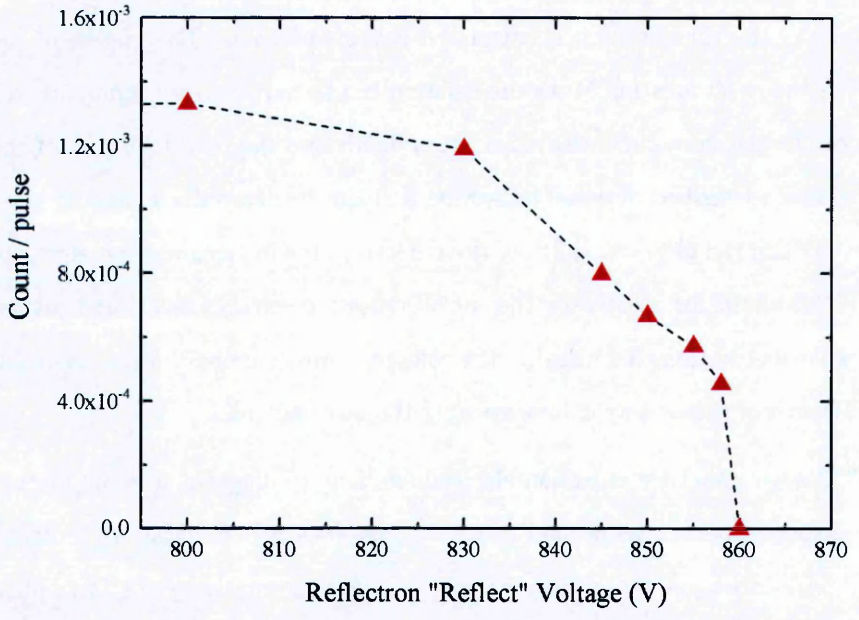

Figure 5.10: The cut-off reflect voltage of the metastable HNCO loss signal from uracil (220 nm, average fluence 7.43×10^7 W/cm^2, argon 0.7 bar uracil temperature 252 °C). The equivalent cut-off voltage for all ions produced by prompt dissociation of the excited uracil radical cation is between 100 and 200 V, depending on the precise alignment of the laser and the molecular beam (see Figure 3.6)

1. Cut-off voltage determination. Masses of the parent ion and the candidate fragment ion are specified. Then dissociation times are tested iteratively to see if the observed cut-off voltage can be reproduced. The calculations can also be carried out for sequential fragmentations; however this naturally becomes more complicated. Therefore the method is best suited to identify metastable decay pathways producing relatively large fragment ions.

2. Calculated difference between time-of-arrival of the investigated ion and a reference peak is compared with the equivalent value obtained experimentally. Typically, the parent ion peak is used as a reference.

3. Calculation of absolute values of time-of-flights. This method predicts the time of flight for the investigated ion in a specific dissociation scenario. Several values corresponding to dissociation taking place in different parts of the mass spectrometer are calculated. Experimentally obtained value is compared. For a well-defined peak, such as a parent ion or the most abundant fragment, this agrees within less than 8 ns, which is the precision of experimental values.

As shown in Figure 5.10, the cut off voltage of the 87-88 peak was found to be between 858 and 860 V. Having determined the position of the ion production, time-of-flight calculations were performed. Direct dissociation ($uracil^+$ fragments after a given amount of time to produce the ion that hits the detector) and intermediate dissociation ($uracil^+$ dissociates promptly followed by a later second fragmentation to produce the ion that hits the detector) were both considered. Cut-off voltages corresponding to dissociation in early stages of the mass spectrometer (i.e. before field-free-region) are never higher than 680 V; therefore they never fit and are not considered. Easily distinguishable is a tendency for the calculations to favour lighter product ions with decreasing intermediate ion mass.

Further calculations were performed in order to narrow down the list of possible ions. The expected difference of time of arrival between the metastable peak and uracil parent ion was calculated and compared with the measured data. Details of the calculations for several considered channels can be seen in the Appendix A.

The only agreement of the calculations with the measurements was obtained for a dissociation of uracil$^+$ (m/z = 112) into m/z = 69 ions in the Field Free Region (*FFR*) of the TOF Spectrometer. The time window for the dissociation in the FFR of the mass spectrometer is 1.31 μs (uracil$^+$ ions reach the entrance to the FFR) to 13.3 μs (product ions reach the first electrode in the reflectron). Recent data from Delaunay et al. [237] also showed evidence for metastable HNCO (m/z = 43) loss on a microsecond timescale from a closely related molecule: bromouracil. Rice et al. [81] also mentioned that they saw evidence for delayed HNCO loss from electron-induced ionised uracil but did not present the data. Interestingly, Figure 5.6 shows that this metastable dissociation signal was above the background level at $\leq$ 222 nm but not at 224 nm (threshold 5.61 $\pm$ 0.03 eV), whereas prompt (< 10 ns after ionisation) ion production at m/z = 69 increased steadily with wavelength as a percentage of total ionisation. Table 5.1 indicates that both peaks were produced by 2-photon ionisation at 220 nm (5.64 eV), consistent with the 10.95 eV appearance energy for the m/z = 69 fragment in previous photoionisation experiments [43]. Note that metastable dissociation channels could not be distinguished in the EII data (Figure 5.8) because the ions were not produced at precisely defined times; the electron beam was continuous and the TOF start coincided with the pulsed extraction voltage.

5.5 Neutral fragment production

Neutral fragments of uracil following dissociation in neutral or ionic states have not been observed directly in any previous experiments. The high laser fluence (average 10^8–10^9 W/cm^2) measurements in Figure 5.11 show an enhancement of the H^+ signal from uracil at the 243.1 nm (2 + 1) resonant wavelength for hydrogen MPI [180]. Jochims et al. [43] assigned the m/z = 68 fragment ion to H loss from $C_3H_3NO^+$ on the basis of appearance energies and thermochemical calculations, although this is clearly not the only plausible pathway for neutral H production. The particular interest in CO is due to it being the neutral by-product of the mechanism that can be associate with ion production at m/z = 84 (see Section 5.4). Figure 5.11 demonstrates strong enhancement of the m/z = 28 signal at the 230.05 nm resonance for CO MPI [238, 239]. While this is broadly consistent with the proposed m/z = 84 pathway, Jochims et al. [43] proposed competitive neutral CO loss mechanisms within the sequential fragmentation processes producing the prominent ions at m/z = 41 ($H_3C_2N^+$) and 40 ($C_2H_2N^+$) (see Table 5.2).

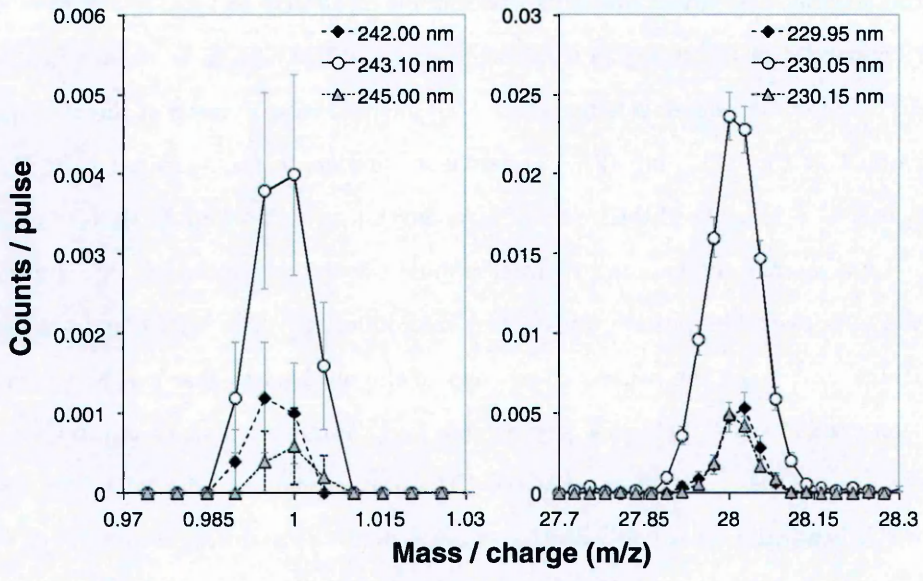

Figure 5.11: Uracil mass spectra showing enhanced MPI at 2 + 1 resonant wavelengths for hydrogen (243.10 nm, left) and CO (230.05 nm, right). The measurements were carried out with powder temperature 250 °C, Argon pressure 0.6 bar, at the maximum laser fluence (average 2×10^8 W/cm^2) for the present system.

5.6 MPI comparisons of gas-phase uracil, deuterated uracil and thymine

Figure 5.12 compares high-mass ion production from gas-phase uracil (U), deuterated uracil and thymine (T). The conditions of the target beam (helium seeded with molecules sublimated at 250 °C) and the focused laser beam were the same in all four measurements. No peaks were observed for cluster ions. Further evidence supporting negligible clustering in the neutral beams was provided by the absence of signals attributable to protonated nucleobases. These are recognised as major dissociation products of nucleobase cluster ions (as discussed in Chapter 4). Zadorozhnaya and Krylov [240]'s calculations showed that the hydrogen-bonded uracil dimer cation relaxes to a proton-transferred form. Similarly, thermochemical calculations have shown that proton transfer from T^+ to T in a dimer cation is exothermic [241, 242]. The (nucleobase ion +1 mass unit) / (nucleobase ion) signal ratios in 5.12 are 6 ± 1 % for

U, and 5 ± 1 % for T. These are in good agreement with the respective natural isotope ratios of 5.2 %, 6.3 %, and 5.1 % [243]. By contrast, the high intensity of the MPI signal from thymine compared with uracil can be partially attributed to its relatively long time constant for relaxation from S_1 (6.4 against 2.4 ps in Ullrich et al.'s [31] 250 nm pump - 200 nm probe experiments). Barć [2] carried out MPI experiments on uracil and thymine in argon beams but did not attempt to draw direct comparisons. Indeed, the measurements were not carried out using matching laser conditions (223.8 – 229 nm), expansion conditions, clustering, and alignments. High background levels presented an additional challenge for analysis.

The ratio of the peaks at $m/z = 115$ and 116 in Figure 5.12b indicates that our molecular beam comprised 20 % $C_4D_3HN_2O_2^+$ and 80 % $C_4D_4N_2O_2^+$. Rice et al. [81] studied electron impact ionisation of various pyrimidine derivatives, including partially deuterated uracil produced by dissolution in D_2O. They assumed that replacement of hydrogen by deuterium occurred exclusively at nitrogen atoms. Accordingly, we assume that our brief exposure of fully deuterated uracil to air (to load the sample in the experiment) led to some hydrogenation at nitrogen sites. The $m/z = 88$ and 87 peaks in Figure 5.12b clearly indicate the loss of 28 mass units from $C_4D_4N_2O_2^+$ and $C_4D_3HN_2O_2^+$. This rules out the possibility of the $m/z = 84$ peak in Figure 5.12 a being due to CNH_2 loss from uracil$^+$. As the loss of two nitrogen atoms (or an N_2 molecule) without further fragmentation would require a very unlikely rearrangement, we assign the peak to CO loss. This is in line with the interpretation of the results from Section 5.4.2.

As noted above, the particular interest in the MPI production of $m/z = 84$ ions from uracil stems from their proposed association with ring opening at the crossing seam of the neutral molecule's two lowest-lying electronic excited states. This fragment ion is not formed by direct excitation of U to ionic states, for example in collisions [81, 160]. Similarly, the electron impact ionisation mass spectrum of T shows no fragment ion peaks that could be traced to CO loss [2]. Therefore any MPI peaks corresponding to

[2]Figure 5.12 does not include an MPI mass spectrum of cytosine because a fragment ion at $m/z = 83$ (the radical cation m/z value minus 28 mass units) has been reported in previous electron impact ionisation experiments [81]

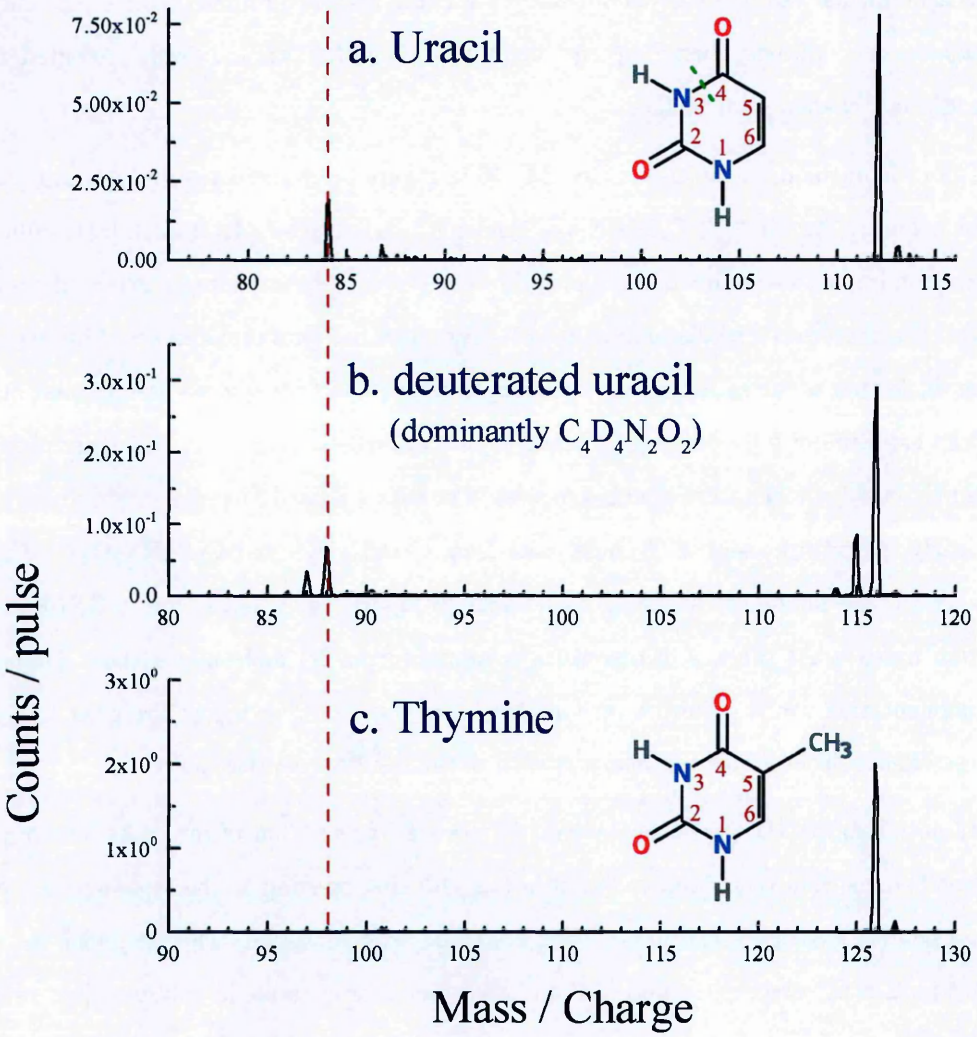

Figure 5.12: MPI mass spectra (220 nm, average fluence 9×10^7 W/cm^2, He 0.8 bar) of uracil, deuterated uracil and thymine: details of the m/z ranges close to the parent ion masses. The red dashed line corresponds to the parent ion minus 28 mass units. The neutral ground state geometries of the dominant gas-phase tautomers [25, 26, 27, 28] are shown as inserts, with a bold dashed line on uracil representing the neutral ring fissure position at the $S_2 - S_1$ crossing seam based on Nachtigallová et al. [3] calculations.

T^+ minus 28 mass units would suggest an analogous ring-opening pathway. Plot c in Figure 5.12 shows no evidence for processes of this kind.

Accordingly, Nachtigallová et al. [3] noted the absence of a ring-opening channel in the calculated relaxation dynamics of thymine following S_2 excitation [244]. The reasons for this specific difference compared with uracil were not discussed, although possible kinematic effects of the CH_3 group of T were mentioned in the context of more general differences in relaxation pathways. S_2/S_1 internal conversion in uracil involves out-of-plane displacement of the C5 hydrogen atom [244], hence it seems plausible that restricted vibrations due to C5 bonding with CH_3 in thymine could disrupt access to a possible ring-opening conical intersection.

5.7 Low-mass fragment ion production from uracil$^+$ and deuterated uracil$^+$

Further to the channels discussed above, Figure 5.6 shows the wavelength dependence of four smaller fragment ions and uracil$^+$ as a percentage of total ionisation. The m/z = 42, 40, 28, and 14 signals (assigned in Table 5.2 and shown to be $\geq$ 3 photon ionisation processes in Table 5.1) did not show threshold behaviour in the 220–270 nm range, while the relative production of uracil$^+$ decreased steadily with increasing wavelength (threshold 4.62 $\pm$ 0.03 eV). The latter effect can be rationalised if one assumes that higher order ($\geq$ 3) photon absorption almost exclusively causes dissociative ionisation. At photon energies only slightly above half the single photon ionisation energy (9.15 $\pm$ 0.03 eV [43]), 2 photon ionisation will be very weak whereas $\geq$ 3 photon ionisation can occur relatively efficiently as long as the $S_2 - S_1$ pathway is accessible. As discussed above, several previous experiments have clearly shown $S_2 - S_1$ deactivation following excitation at 4.64 eV [31, 32, 33].

The deuterated uracil data identifies several other fragment ions that have been debated in the literature (notably CH_2^+, CNH_2^+, and $C_2H_2O^+$). Starting at low masses, the first aspect of Figure 5.13 to note is the absence of any signal at m/z = 13 in the deuterated measurement. CH^+ ions were produced from uracil, both in the present data (albeit weakly) and in previous MPI and EII experiments [46]. The fact that negligible CH^+ ions were produced from the deuterated target (approximately 20 % $C_4D_3HN_2O_2$ and 80 % $C_4D_4N_2O_2$, as noted above) is consistent with our assumption that the carbon sites on the ring have not experienced D / H exchange. Ion production at m/z = 14 has been attributed to CH_2^+ by Imhoff et al. [46] and N^+ by Jochims et al. [43]. Accordingly the strong peaks at m/z = 14 and 16 in Figure 5.13b can be assigned to CD^+ and CD_2^+.

The most striking result in the next ion group (m/z = 24-32) is the shift of the strongest peak from m/z = 28 in Figure 5.13a to m/z = 30 in Figure 5.13b. This clearly indicates that the peaks are respectively dominated by CH_2N^+ and CD_2N^+, whereas Imhoff et al. [46] assigned this feature to CO^+. As weak C_2H^+ production was previously observed from uracil [160, 46] the peak at m/z = 26 in Figure 5.13b is expected to

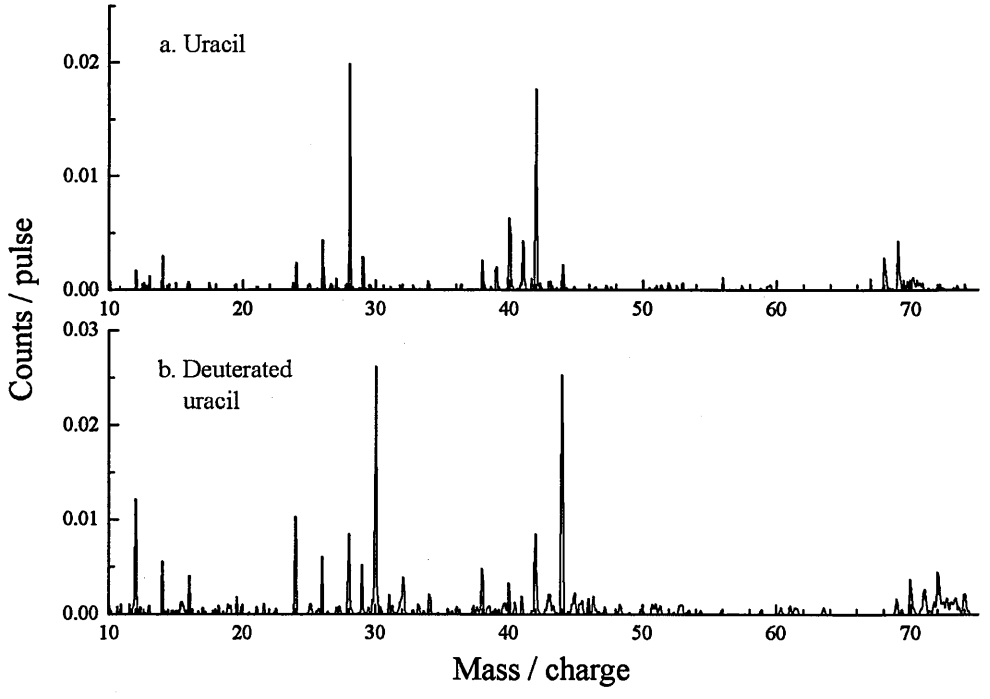

Figure 5.13: MPI mass spectra (220 nm, average fluence 9×10^7 W/cm^2, He 0.8 bar) of uracil and deuterated uracil: detail of the m/z range 10-75.

contain a contribution of C_2D^+. Compared with the m/z = 25 feature in Figure 5.13a, however, the strength of the m/z = 26 peak in both plots suggests a contribution of CN^+ (not proposed in any previous works). The peaks at m/z = 28-30 in Figure 5.13b are expected to contain contributions of $C_2D_2^+$ and CDN^+, as well as possibly $CHDN^+$, CO^+, and CDO^+. The only plausible assignment for the clear feature at m/z = 32 in the deuterated measurement is CD_3N^+, removing previous doubt in the origin of the m/z = 29 peak in the uracil mass spectrometry [43].

The most intense peak in the m/z = 38-45 group is shifted from m/z = 42 in Figure 5.13a to m/z = 44 in Figure 5.13b. This supports assignment to $C_2H_2O^+$ [35, 43, 235], as opposed to $C_2H_4N^+$ [46, 235]. The group's second strongest peak (m/z = 40 from uracil) is also apparently shifted by two mass units in the deuterated measurement, consistent with the accepted assignment to $C_2H_2N^+$. The main peaks in the m/z = 67-74 group are also consistent with the previous assignments to $C_3H_2NO^+$ and $C_3H_3NO^+$ from uracil [35, 43, 235]. It is interesting to note that Figure 5.13a shows a broad tail

structure extending 0.3 μs (approximately 2 m/z units in this part of the calibrated mass spectrum) after the m/z = 69 peak. This tail can be attributed to the same metastable dissociation as discussed in Section 5.4.3, taking place while uracil$^+$ is accelerated from the laser / molecular beam crossing point to the entrance of the TOF drift tube (a journey time of 1.1 μs in the present measurements).

5.8 Conclusions

The work presented in this chapter advances our understanding of UV induced processes in gas-phase uracil. The most striking result is the observation of a new fragment ion at m/z = 84 by 2-photon ionisation. This fragment ion is not formed by direct excitation of gas-phase uracil to ionic states, so its MPI production must depend on neutral excited state dynamics. Measurements on deuterated uracil have identified the m/z = 84 ion from uracil as $C_3H_4N_2O^+$ (uracil$^+$ minus CO). The threshold photon energy (5.29 $\pm$ 0.06 eV) for this product agreed with the calculated energy (5.25 eV at CASSCF level) of the ring-opening crossing seam [3] and the geometry of the predicted isomer indicates likely CO abstraction. Hence there is a compelling case for proposing MPI production of this fragment ion as an experimental marker for ring opening in neutral excited uracil. This suggests possibilities for diverse measurements exploring the process in depth (e.g. using coincidence and / or time-resolved methods). Indeed, the present results provided the motivation for the first study of uracil using ultrafast femtosecond timescale pump-probe experiment using pump photons above the ring-opening threshold energy. The ultrafast measurements are described in Chapter 6. MPI measurements on thymine did not reveal an analogous CO loss process that could suggest an analogous excited state ring-opening pathway. This suggests that substitution of a heavy group at the C5 position of the pyrimidine ring can stabilise excited nucleobases with respect to isomeric transitions.

Aside from the m/z = 84 fragment ion, the present measurements on deuterated uracil have provided unambiguous assignments for a number of fragment ions from uracil that have been debated in the literature. Furthermore, neutral CO has been experimentally

demonstrated as a product from uracil dissociative ionisation for the first time. The chapter also demonstrates the MPI experiment's experimental capability to identify delayed fragmentation of excited ions (HNCO loss from uracil^{+*}). Further investigation is required to interpret the observed MPI wavelength threshold for this process.

The results in this chapter form the basis of one publication in Journal of Chemical Physics [160] and one further publication that is currently *in press* in International Journal of Mass Spectrometry [245].

Chapter 6

Ultrafast studies of uracil

Chapter 5 revealed a new fragment ion ($C_3H_4N_2O^+$) from uracil that depends on a critical process in a neutral excited state. Although this process has not yet been identified definitively, the result appears to be consistent with Nachtigallová et al.'s [3] prediction of new photochemical products due to excited-state ring opening. This chapter presents the first ultrafast experiments with a sufficient pump energy (6.20 eV, 200 nm) to investigate deactivation pathways from the vibrationally hot singlet states accessed in the previous chapter. The main aim was to better understand isomeric transitions and / or dissociation processes in neutral excited states. The measurements were carried out at a newly developed laser desorption spectrometer at Heriot-Watt University.

6.1 Introduction

The electronic excited states of nucleobases and their deactivation pathways have long attracted considerable interest. The greatest number of works have focused on the broad S_2 state that dominates the low-energy part of the UV spectra of DNA and RNA bases. Figure 6.1 shows the experimental and calculated photoabsorption spectrum of gas-phase uracil, while Table 6.1 lists the available vertical and adiabatic energies of the lowest lying singlet and triplet excited states. It worth noting that the adiabatic

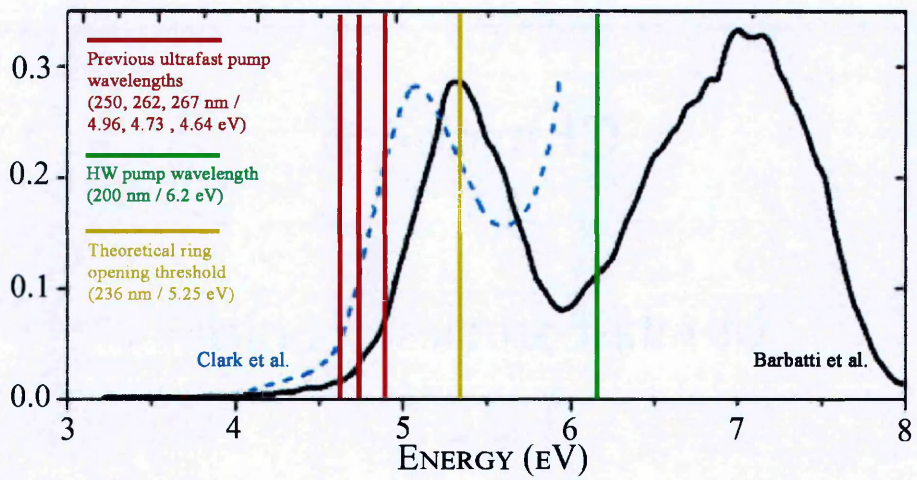

Figure 6.1: Barbatti et al.'s [29] calculated (*ab initio*), and Clark et al.'s [30] experimental UV absorption spectrum. Key photon energies are labelled [3, 31, 32, 33, 34, 35].

Table 6.1: S_3, S_2, S_1, and T_1 energies and oscillator strengths.

State	Excitation energy (eV) Etinski et al. [223] (DFT/MRCI/TZVP//B3-LYP/TZVP)		Oscillator strength Ten and Baranov [246] (CNDO/S)
	vertical	adiabatic	
$S_3(\pi \rightarrow \pi^*)$	6.7 [246]	-	0.18
$S_2(\pi \rightarrow \pi^*)$	5.56	-	0.44
$S_1(n \rightarrow \pi^*)$	4.67	3.96	0.005
$T_1(\pi \rightarrow \pi^*)$	3.78	3.13	-

energies of the S_2 and S_3 states have not been reported explicitly. The UV spectrum of uracil is characterised by two broad bands separated by a low intensity region. Whereas the lower energy band is dominated by absorption into one state of $\pi\pi^*$ character (S_2), the higher energy band is composed of several states (three of $\pi\pi^*$-character and one $^1nR_{3s}$ state). The experimental spectrum [30] in Figure 6.1 shows similar features to the calculations, but shifted towards lower energies. Richter et al.'s [37] CASSCF-simulated absorption plots suggest surprisingly high onsets (around 5.0 eV for S_2 and around $5.7-6.0$ eV for S_3) and much stronger S_2/S_3 overlap than shown in Clark et al.'s experiments so Barbatti et al.'s [29] calculated spectrum is preferred here.

In the last 10-15 years, a series of ultrafast time-resolved pump-probe experiments have provided extensive insights into the relaxation pathways from the optically bright S_2 state. The results are summarised in Table 6.2 (adapted from Richter et al. [37]). Kang

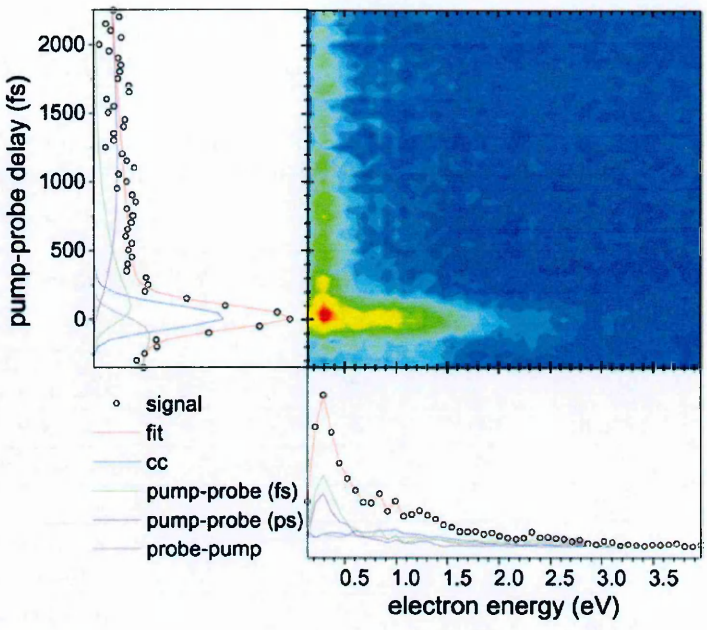

Figure 6.2: Ullrich et al.'s [31] TRPES (250 nm pump, 200 nm probe) of uracil. See text for discussion.

et al. [32] studied intrinsic lifetimes of DNA and RNA bases using time-resolved MPI (267 nm pump, 800 nm probe), albeit with a relatively low temporal resolution (400 fs). All pyrimidines exhibited an ultrafast Gaussian component followed by a longer-lived exponential decay. The authors reported a single exponential decay component for uracil with a time constant of 2.4 ps. An additional ns-timescale decay component in thymine has been attributed to triplet states, but no evidence was observed for an analogous channel in uracil. Ullrich et al.'s [31] Time-Resolved Photoelectron Spectroscopy (*TRPES*) (250 nm pump, 200 nm probe, temporal resolution of 140 fs, reproduced here in Figure 6.2) of uracil showed evidence of three components: an ultrafast Gaussian (< 50 fs), followed by two exponential decay components with time constants of 530 fs and 2.4 ps. However, Canuel et al. [33] suggested that Ullrich et al.'s biexponential decay may be due to the limitations of their experimental setup and fitting procedures, and instead proposed an ultrafast component with a time constant of 130 fs followed by a single exponential decay channel (1.05 ps).

Table 6.2: Summary of decay times of uracil measured by pump–probe experiments. No direct experimental evidence has been reported for longer time constants associated with triplet states. Based on [37].

Setup		τ_1 (fs)	τ_2 (fs)	τ_2 (ps)	Reference
λ_{pump} (nm)	λ_{probe} (nm)				
267	$n\times$800	-	-	2.4	Kang et al. [32]
250	200	< 50	530	2.4	Ullrich et al. [31]
267	2×400	130	-	1.1	Canuel et al. [33]
267	330[a]	96	-	-	Gustavsson et al. [247]
267	330[a]	< 100	-	-	Gustavsson et al. [247]
262	$n\times$780	70	-	2.2	Kotur et al. [34] (parent ion)
262	$n\times$780	90	-	3.2	Kotur et al. [34] (69^+ fragment)
262	$n\times$780	70	-	2.4	Matsika et al. [35] (parent ion)
262	$n\times$780	90	-	2.6	Matsika et al. [35] (69^+ fragment)

[a] Fluorescence upconversion in aqueous solution.

Further insights have emerged from adiabatic and diabatic dynamics calculations. Hudock et al. [244] studied dynamics of electronically excited uracil at the FMS:CASSCF(8,6) level, but did not report decay time constants. Single time constants were suggested by Nieber and Doltsinis [248] ($551 - 608$ fs at the SH:CPMD/BLYP level) and Fingerhut et al. [249] (516 fs, SH:CAS(14,10)). However, Lan et al.'s [250] calculations at the SH:OM2/MRCI level support an ultrafast (21 fs) channel followed by a 570 fs channel. Barbatti et al. 's [251] SH:CAS(10,8) calculations also suggest duel decay, but with much longer time constants: $650 - 740$ fs followed by a long-lived $1.5 - 1.8$ ps channel. Etinski et al.'s calculations showed S_1 is unlikely to correspond to the dark state in uracil, and suggested an ISC from S_1 to a triplet state. The most recent combined experimental and *ab initio* study by Ligare et al. [36] is the only one to probe the dark state directly, assigning it to a $^3\pi\pi^*$ state with time constants in the range of $49 - 64$ ns.

Overall, the current consensus on the main decay routes from S_2-excited uracil can be summarised in Figure 6.3. The S_2 state can decay directly into the electronic ground state (S_0) via a barrierless path involving two CI's: $S_2 - S_1$ ($n\pi^*$) followed by $S_1 - S_0$. This pathway is responsible for the ultrafast decay component. An alternative decay

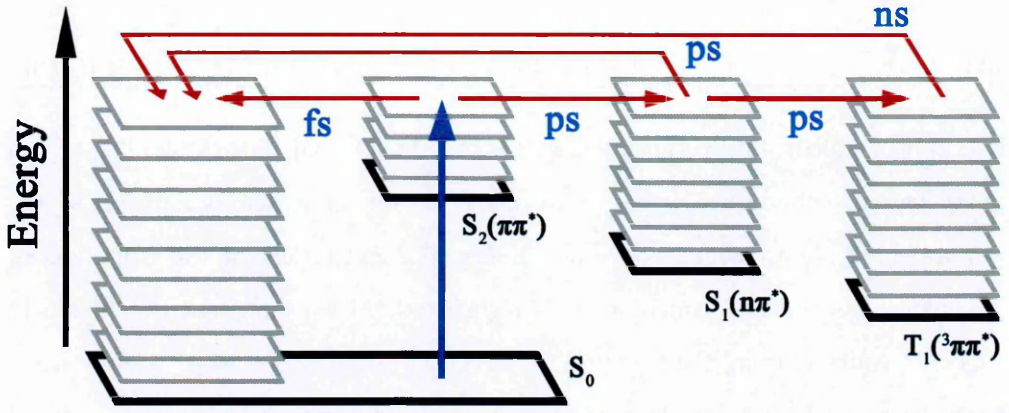

Figure 6.3: Jabłoński-type diagram summarizing the main deactivation pathways following the excitation to S_2. The diagram combines aspects of Fig. 6 in Ligare et al. [36] and Fig. 7 in Richter et al. [37].

path giving rise to the ps-timescale component involves trapping in S_2 for a few picoseconds, followed by decay into either S_1 or S_0. Ps-timescale trapping can also take place on the S_1 state prior to internal conversion to S_0 or intersystem crossing to a triplet state. Indeed, Ligare et al. [36] used double resonant (UV+IR) spectroscopy to observe a triplet state with a time constant in the range of $49 - 64$ ns, with a $^3\pi\pi^*$ character. Richter et al. [37] reported that the S_1 state can decay directly into the T_2 triplet state, which can subsequently decay to T_1. The same authors' calculations also indicated that S_3-excited uracil decays to S_2 in < 100 fs. As an aside it is worth recalling that the photon fluence that can be produced using OU focused laser is not sufficient for non-negligible successive photon absorption on fs-timescales.

The only available ultrafast time-resolved studies of uracil fragment ion production are those of Matsika and co-workers [34, 35, 222] (262 nm pump, 780 nm probe). Decay curves were reported for fragments with $m/z = 28$, 41, 42 and 69, but full analysis was limited to the parent ion and the $m/z = 69$ fragment ion. Decay components of 70 fs and 2.6 ps have been identified, and attributed to ionisation from S_2. However, the authors also reported a longer (> 10 ps) component, and tentatively assigned it to ionisation ($260 + 780$ nm MPI) from S_1 minimum. The production of lower mass fragment ions has been attributed to sequential fragmentation of the $m/z = 69$ ion, and the decays were qualitatively similar to the $m/z = 69$ result.

The previous ultrafast experiments used 250 [31], 262 [34, 35], and 267 nm [31, 32, 33] pump beams; nobody has carried out experiments on the dynamics initiated by the absorption of more energetic photons. Hence, the motivation for this work was to study gas-phase uracil's dynamics with a significantly higher pump energies (6.20 and 5.64 eV) available using the Heriot-Watt (HW) setup described below. Indeed, short pump wavelengths can lead to new photochemical products. Nachtigallová et al. [3] and Richter et al. [37] predicted a ring opening transition at the $S_2(\pi\pi^*) - S_1(\sigma(n - \pi)\pi^*)$ crossing seam with a threshold photon energy of 5.25 eV and a time delay of about 500 fs. Similarly, our MPI experiments have demonstrated a new fragment ion from uracil excited with $\leq 5.29 \pm 0.06$ eV (Chapter 5). Townsend and co-workers' experiment enables ultrafast ($\sim$ 50 fs) pump pulses to be generated with energies above this threshold.

6.2 Experimental

6.2.1 The ultrafast pump-probe experiment at Heriot Watt University

Townsend and co-workers at Heriot Watt University have recently built a new laser desorption spectrometer that offers exceptional versatility for 2-dimensional ultrafast pump-probe experiments. Although the present data is restricted to a single pump wavelength (200 nm), further measurements on uracil have been planned that will exploit the broad range of near-UV wavelengths accessible using the Heriot-Watt system. The experimental setup consists of an ultrafast laser system, a Laser Induced Acoustic Desorption (*LIAD*) source, and a time-of-flight (TOF) mass spectrometer. The laser system is shown schematically in Figure 6.4 and is described briefly in the paragraph below. The *LIAD* source and the time-of-flight extraction optics are mounted in an ultra-high vacuum chamber, as shown in Figure 6.5. The chamber and the spectrometer were evacuated using separate turbomolecular pumps. The layout of the mass spectrometer is shown in Figure 6.5. A thorough description of the experimental system will be published in the near future.

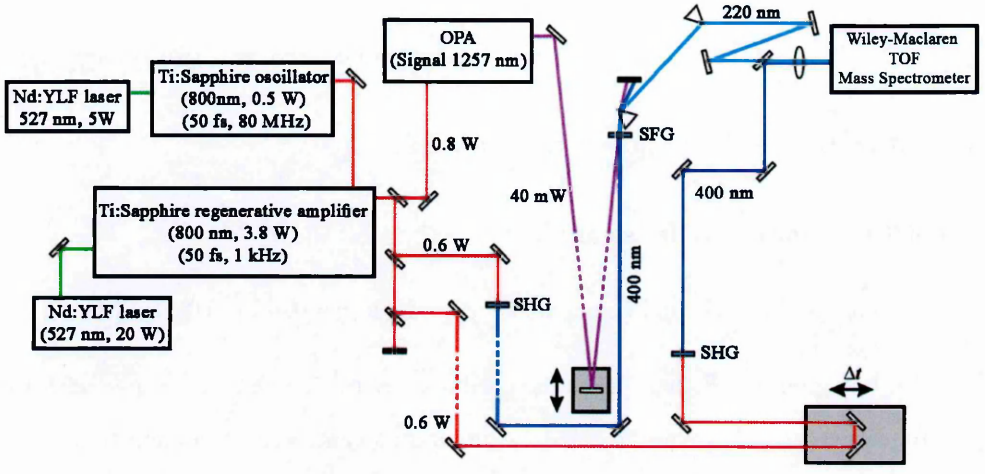

Figure 6.4: Overview of the laser setup (adapted from Figure 3 in reference [38]). The specific configuration corresponds to 220 nm pump, 400 nm probe experiments.

The pump and probe pulses for the time resolved measurements both originated from the fundamental output of a regeneratively amplified Ti:Sapphire laser system, operating with a pulse duration of 60 fs and a central wavelength of 800 nm. The fundamental output was split into several beamlines, to produce the required wavelengths for the experiments by Sum Frequency Generation (SFG, equation 6.1). Although not used in the present measurements, the option of mixing with the output of an optical parametric amplifier (*Spectra Physics, OPA 800C*) provides access to an essentially continuous range of wavelengths for future experiments (for example using a 220 nm pump, as shown in Figure 6.4). The SFG efficiency scales with the square of the power of the incident light and depends on crystal properties such as the effective mode area, the length of the crystal and the effective nonlinearity. Furthermore, phase-matching must be satisfied to achieve non-zero SFG. Effectively, SFG efficiency can vary from few % [252] up to $80-90$ % [253, 254]. A full description of the technique and its physics can be found in reference [252].

$$\frac{1}{\lambda_3} = \frac{1}{\lambda_1} + \frac{1}{\lambda_2} \tag{6.1}$$

The wavelengths used in the present experiments are:

- 800 nm (probe) - fundamental.
- 400 nm (probe) - Second harmonic generated using a 0.1 mm BBO crystal.
- 200 nm (pump) - Fourth harmonic produced by mixing third harmonic with the fundamental. The required third harmonic was generated by mixing the second harmonic with the fundamental.

The time delay between the pump and the probe pulses was varied precisely using a motorised linear translation stage (*Physik Instrumente, M 403.62S* with a *Physik Instrumente, Mercury Step* controller) that interfaced with a data acquisition platform developed in MATLAB. A pump-probe cross correlation of 160 ± 15 fs was obtained, and verified via non-resonant, two-colour (1 + 2' or 1 + 3') multiphoton ionisation measurements of butadiene.

The molecular target was introduced into the vacuum using a Laser Induced Acoustic Desorption (*LIAD*) source. Calvert et al. [255] have described the method in detail. Despite its name, shake-off has been ruled out as a possible mechanism of desorption in *LIAD*, as the system functions most effectively using a CW laser. This relatively new technique has been used successfully to introduce large molecules into vacuum [256, 257]. Poully et al. [256] have used the technique to introduce nucleosides into vacuum, referring to it as the "laser thermal heating source". Zinovev et al. [258] studied properties of *LIAD* systems and proposed a mechanism of liberating molecules form the surface due to a combination of the thermal and acoustic waves. Furthermore they reported that the molecular velocities are consistent with a thermal desorption in the range of $230 - 430$ °C ($\frac{3}{2}k_{\mathrm{B}}T = 0.065 - 0.090$ eV).

The Heriot-Watt LIAD source is shown schematically in Figure 6.5. Powdered sample has been deposited on a 15 mm diameter, 10 μm thick stainless steel foil using methanol to aid adhesion (subsequently removed by pumping). The foil was then clamped into the repeller electrode of the spectrometer, and mounted in the interaction chamber. Following evacuation of the system to its base pressure of 5×10^{-8} mbar, the

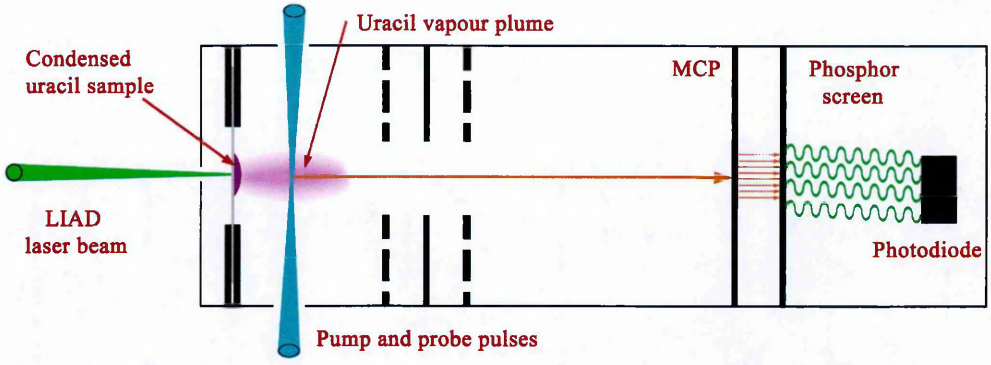

Figure 6.5: The Heriott-Watt LIAD source and mass spectrometer

back of the foil was irradiated by a 445 nm CW desorption laser. The spot area of the laser is estimated to be 0.5 by 3 mm, further focused by a 30 cm lens. The delivered power could be varied between 100 and 600 mW. After desorption from the foil, the plume of the vaporised sample was intersected by the co-propagating pump and probe pulses. The interaction between the light pulses and the desorbed plume of the vaporised molecules took place $2-3$ mm from the surface of the repeller electrode. The resulting ions travelled through a single pass time-of-flight mass spectrometer operated in Wiley-Maclaren mode [259], and were detected using a MCP detector and a phosphor screen. Ions impacting on the MCP / phosphor screen assembly were recorded on an oscilloscope using a photodiode. A PC software interface, developed using MATLAB, was used to both download data and to control the oscilloscope. The mass resolution of the spectrometer was relatively low ($m/\Delta m \approx 28$), due to the short length of the TOF flight tube, as well as the resolution of the oscilloscope. However, this still provided sufficient mass resolution for the experiments

6.2.2 The adapted source to produce vibrationally-excited molecular targets for MPI experiments at the Open University

Modifications for the OU MPI / EII experiment have been commissioned to produce uracil targets with internal temperature close to the Heriot-Watt experiment. The design exploits a new aluminium (chosen for its high thermal conductivity and ease of machining) modified backplate of the TOF mass ion extractor as shown in Figure

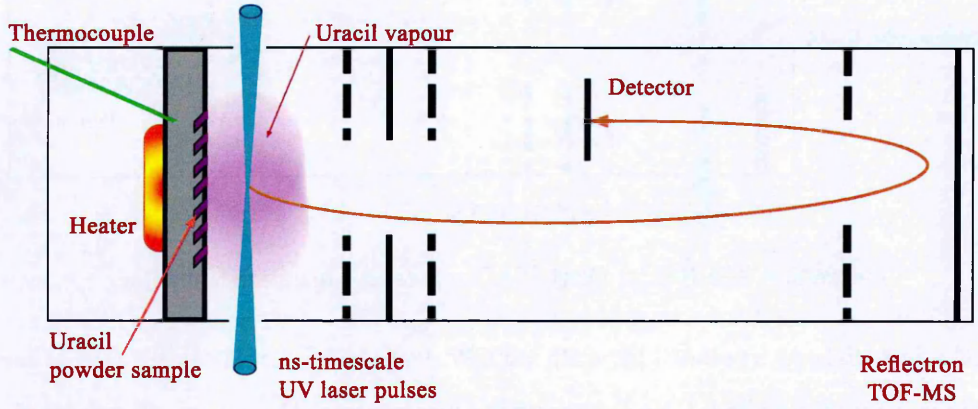

Figure 6.6: The OU MPI experiment featuring the new heated backplate source.

6.6. The plate houses an array of closely spaced 1 mm diameter holes, drilled at a 45^o angle to the surface, spread across a 2 cm diameter area. The holes face the interaction region, and can be filled with powdered sample to produce vapour very close to the laser beam. To enhance sublimation, a resistive heater is attached to the other side of the backplate and a thermocouple has been used to monitor the temperature of the surface. The maximum temperature of the plate attained in the present configuration was 83 °C ($\frac{3}{2}k_{\mathrm{B}}T = 0.041$ eV). The uracil signal intensity increases steeply when moving the laser beam closer to the backplate. Considerable care has been taken to avoid scattered laser light hitting the surface (verified by looking at the beam shape and measuring the pulse intensity after the exit window). Moreover, the measurements were carried out with -20 V on the reflect electrode of the mass spectrometer. This means that any ions produced at the surface of the grounded backplate will attain too much KE during their acceleration into the mass spectrometer's field free region to be reflected onto the detector (see Section 3.3)

6.3 Results and discussion

6.3.1 Time-resolved (0-10 ps) uracil$^+$ and fragment ion production following excitation at 200 nm (6.20 eV)

Figure 6.7 shows time-resolved pump-probe mass spectra of uracil. The 200 + 800 nm (Figure 6.7a) data was recorded with 29 linear steps of 25 fs each, followed by another 109 exponential steps ranging from 19 to 5056 fs. For the 200 + 400 nm (Figure 6.7b) data, 79 linear steps were recorded (25 fs each) with 59 additional exponential steps (111 – 6871 fs). Stronger signals and a significant increase in the relative production of fragment ions with high appearance energies are observed in the 200 + 800 nm measurement compared with the 200+400 nm. Both of these effects can be attributed to the 800 nm (fundamental) probe pulse being 100 times more powerful than the 400 nm probe pulse.

Figure 6.8 shows decay curves from the 200 + 800 nm measurement for the ion groups at m/z = 112, 69, 42 and 28. Canuel et al. [33] noted that the time constants derived from decay curves can be highly dependent on the specific fitting procedure adopted. Hence, Townsend and co-workers' expertise in fitting procedures will be applied in the near future. Notwithstanding the preliminary nature of the present analysis, it is clear that the fragment ion curves in Figure 6.8 show qualitative agreement with Matsika et al.'s [35] decays recorded with a pump wavelength of 262 nm (reproduced here in Figure 6.9). A Gaussian feature with fs-timescale width is followed by a ps-timescale exponential decay curve that is superimposed on a long-lived component (extending beyond the 10 ps limit of both Figure 6.8 and Figure 6.10). The general similarity of the decay curves for the three fragment ion groups suggests that similar excited state dynamics dominate. This can be viewed as being broadly consistent with the sequential fragmentation pathways of the excited radical cation reported in previous works [35, 43, 47].

Matsika et al. [35] tentatively assigned the long-lived component to ionisation from the S_1 minimum. However this suggestion was made before Ligare et al.'s [36] calculations

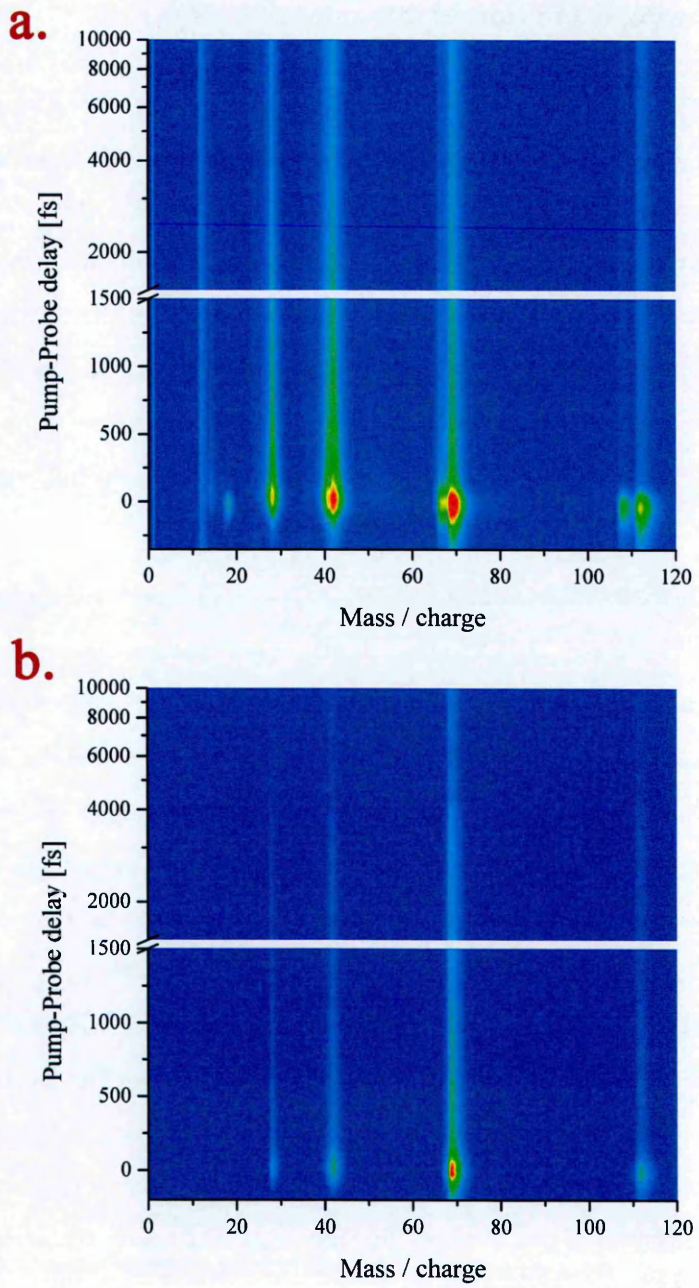

Figure 6.7: False-colour map showing a. 200 nm (0.4 mW, 1.13×10^8 W/cm^2) + 800 nm (250 mW, 2.55×10^{10} W/cm^2) and b. 200 nm (0.4 mW, 1.13×10^8 W/cm^2) + 400 nm (2.5 mW, 2.55×10^8 W/cm^2) (B) MPI pump-probe experiment. Note the dual linear+log Y scale. The raw data are presented. The double peak structure $\sim$m/z = 112 in plot a is a TOF artefact.

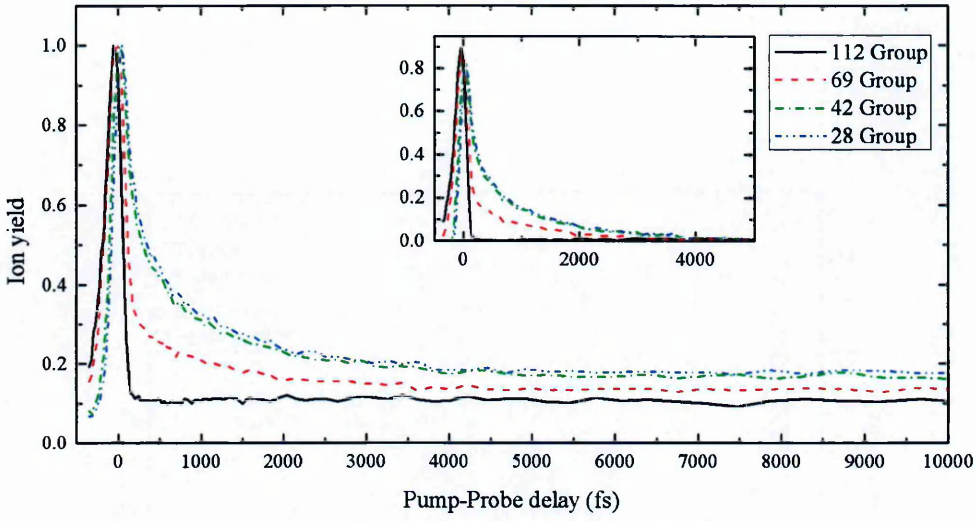

Figure 6.8: Decay plots for the production of uracil+ and fragment ions in the m/z groups $\sim$ 69, $\sim$ 42 and $\sim$ 28. The curves have been normalised to the peak maxima. The inset graph presents the curves normalised to the peak maximum (= 1) and also to the long-lived component (= 0).

revealed intersystem crossing from S_1 to triplet states with lifetimes of tens of ns. The insert in Figure 6.8 suggests that the ps-timescale component of the fragment ion production is essentially complete within 5 ps and no calculations have reported trapping on S_1 at longer times than this. Therefore we propose that the long-lived component in the present data is most likely due to ionisation from triplet states.

Matsika et al. [35] observed uracil$^+$ production with a ps-timescale decay (time constant 2.4 ps) but this component was much weaker than the corresponding feature in the fragment ion curves (2.6 ps for m/z = 69). This difference is exaggerated in the present 200 + 800 nm result: the only features visible in the uracil$^+$ curve are the fs-timescale Gaussian and the long-lived component. Figure 6.10 shows the decay curves recorded with relatively weak pulses of 400 nm photons. Despite relatively poor signal / noise ratio, the 200 + 400 nm curve for uracil$^+$ production provides evidence for a weak ps-timescale decay component. This difference compared with the 200 + 800 nm result highlights the fact that the probe wavelength and / or intensity can have significant effects on the observed dynamics.

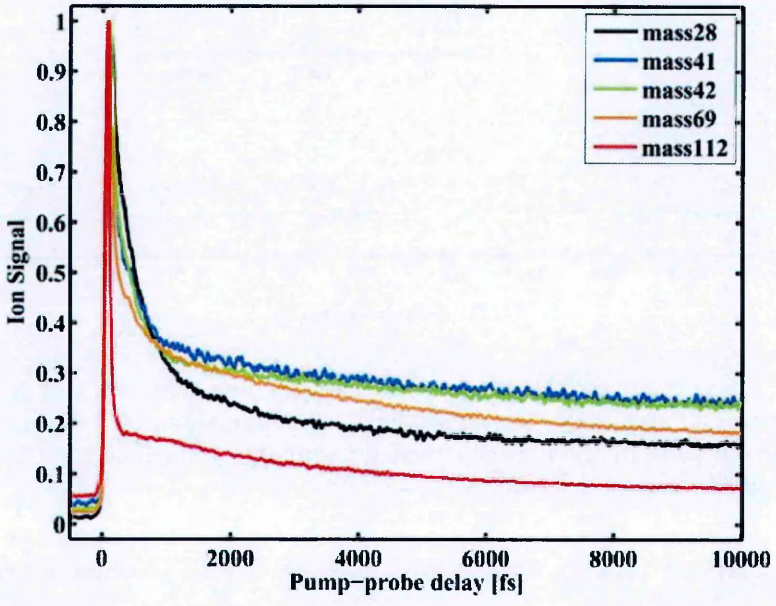

Figure 6.9: Ion yields of the parent and selected fragment ions of uracil versus pump (262 nm) – probe (720 nm) delay for uracil. Reproduced from Matsika et al. [35].

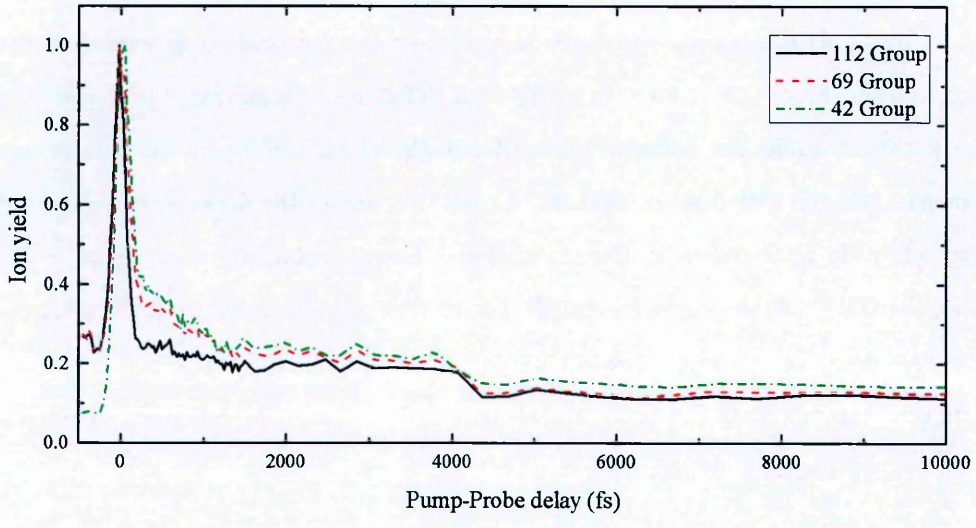

Figure 6.10: Decay plots for the production of uracil$^+$ and fragment ions in the m/z groups ~ 69 and ~ 42. The curves have been normalised to the peak maxima.

Consideration of earlier time-resolved photoelectron spectroscopy can provide an interpretation for the results in Figures 6.8 and 6.10. Figure 6.2 (measured with 250 nm pump and 200 nm probe pulses) shows that the production of high-energy photoelectrons (i.e. more than 0.5 eV) is essentially restricted to the ultrafast Gaussian component of the decay curve [31]. The geometries of uracil in its neutral electronic ground state (S_0) and in its ionic ground state (D_0) are very similar [3], whereas major differences in the electronic excited state geometries have been reported [3]. Therefore, when ionisation takes place on a faster timescale than nuclear rearrangement following excitation to S_2, low vibrational levels of the ionic ground state can be accessed with strong Franck-Condon factors. Hence, most of the excess energy will be carried away by the photoelectrons and ionic fragmentation will be rare. Conversely, once sufficient time has elapsed for vibration to take place around the average positions of the nuclei in uracil's S_2 or S_1 states, only high vibrational levels of D_0 (or higher ionic states D_1, D_2 etc.) will be accessible with strong Franck-Condon factors. In this case, most photoelectrons will have low energies and most ions will fragment.

The pump photon energy (6.20 eV) in the present ultrafast experiments is markedly higher than the energy of the ring-opening $S_2 - S_1$ CI (5.25 eV) predicted by Nachtigallová et al. [3] at a time delay of $\sim$ 500 fs. Similarly, it is greater than the 5.29 ± 0.06 eV threshold for $m/z = 84$ production in the OU MPI experiments using single colour ns-timescale laser pulses (Chapter 5). However, Figure 6.7 shows no evidence for ion production at $m/z = 84$. Figure 6.1 and Table 6.2 indicate that absorption into the S_3 band will dominate at 6.20 eV (200 nm). Therefore the absence of the $m/z = 84$ peak at delays up to 10 ps could conceivably be linked to the specific relaxation dynamics of S_3-excited uracil. However Richter et al.'s [37] calculations showed that S_3 relaxes to S_2 in < 100 fs (distinctly earlier than the predicted ring-opening CI). Therefore, the S_2 relaxation dynamics are still expected to play a critical role the present ultrafast experiments.

6.3.2 Discussion of absence of m/z = 84 ions in the ultrafast measurements.

A selection of possible reasons why m/z = 84 ions ($C_3H_4N_2O^+$) were observed in Chapter 5's single colour 2-photon ionisation experiments but not in the present ultrafast pump-probe results are listed below.

1) Delay time ($\leq$ 10 ps at HW; $\leq$ 7 ns at the OU)

We could hypothesise that a critical step of the excited state dynamics responsible for the m/z = 84 peak takes place on a slower timescale than 10 ps (the time delay window probed in the ultrafast measurements). In particular, a late ring-opening conical intersection between two triplet states could be envisaged.

It is possible that delayed CO loss could take place from an excited neutral. Indeed, Chapter 5 gives an example of fragmentation on a slow timescale (HNCO loss from excited uracil$^+$ up to several micro-seconds after ionisation). In this case, 2-photon production of $C_3H_4N_2O^+$ in the Chapter 5 experiments would involve single-photon access to a long-lived state (a vibrationally-hot triplet state or the even-hotter electronic ground state), followed by CO-loss and single-photon ionisation of $C_3H_4N_2O$. Such single-photon ionisation is unlikely but not inconceivable as unstable neutrals can have very low ionisation energies. For example, the calculated vertical ionisation energy adenine with an additional hydrogen ($AH^\bullet$) is 5.32 eV [260].

2) Pump photon energy (6.20 eV at HW; 5.64 – 5.29 eV at the OU)

We could speculate that the increased level of vibrational excitation in S_2 (predominantly accessed via S_3 as described above) in the HW measurements could lead to a critical ring-opening CI being avoided. To explore this possibility, further experiments are required with pump photon energies that directly overlap with the OU experiments that produced the m/z = 84 ion.

3) Probe photon energy (1.55 or 3.10 eV at HW; 5.64 – 5.29 eV at the OU)

It is conceivable that excessive energy absorption at the ionisation stage could destabilise the $C_3H_4N_2O^+$ ion and hence lead to very weak signals. The probe energy steps in the HW measurements (notably 3×800 nm = 4.65 eV and 4×800 nm = 6.20 eV) do not overlap with the OU photon energy range that produced m/z = 84 ions (5.29 – 5.64 eV). However, total energy deposition in the two experiments does overlap (10.58 – 11.27 eV at the OU, compared with $200 + 3 \times 800$ nm = 10.85 eV at HW) so this seems to be an unlikely cause of the observed difference.

4) Vibrational excitation of the target molecules

It can reasonably be assumed that the supersonic target jets in the OU measurements only contained vibrationally cold molecules, whereas the HW *LIAD* system is expected to produce vibrationally excited molecules. Vibrational excitation clearly plays an important role in multi-photon ionisation dynamics. However, both experiments access high vibrational levels of uracil's singlet states. For example, the 220 nm photons used in the OU experiments are 1.68 eV above the calculated adiabatic energy of S_1. Compared with this, the levels of vibrational excitation in the HW neutral target (average internal energy expected to be in the range 0.065 – 0.090 eV [48]) were very minor. Nonetheless, Section 6.3.3 describes an attempt to repeat the OU measurements on target molecules with internal energies close to the HW experiments.

5) Tautomeric forms of the target molecules

Any differences in the tautomeric structure of the target molecules of the two experiments could plausibly lead to different dynamics and fragmentation patterns. However, infrared spectra of uracil vapour from powder heated at 200 – 325 °C into 13 – 20 mbar of static argon [26] only showed evidence for the diketo form. Infrared cavity ringdown spectroscopy experiments of jet-cooled uracil following heating at 210 – 220 °C also showed that only diketo tautomers were present [214]. To our knowledge there are no studies of uracil tautomeric populations from laser desorption sources or *LIAD*. There

are precedents for different tautomeric populations between simple heating and laser desorption (for example in Guanine [261]) but it would be extremely surprising if the HW *LIAD* source did not produce (at least) a significant proportion of the diketo tautomer.

6.3.3 MPI mass spectra of vibrationally-excited molecular targets

Figure 6.11 compares three MPI mass spectra recorded using the OU modified backplate source. The background measurement with no uracil powder shows no peaks at m/z = 84 or 112. Figure 6.11b demontsrates that MPI signals of uracil$^+$ and the m/z = 84 fragment can be attained from uracil vapour at room temperature. Although further optimisation is required to eliminate nearby background features in the mass spectrum, this result indicates that the method has potential for interesting experiments. To our knowledge, all the measurements in the literature on gas-phase nucleobases have been carried out at temperatures > 100 °C (heated effusive beams, heated static gas cells, laser desorption or *LIAD* sources) or at low temperatures (supersonic jets). MPI studies of biomolecules at room temperature can strengthen analogies with biological environments.

Figure 6.11c and d show that m/z = 84 fragments can be produced with hight efficiency by multi-photon ionisation of uracil molecules at 83 °C ($\frac{3}{2}k_T = 0.041$ eV). This average internal energy is distinctly greater than the activation energies of the ν_{30} and ν_{29} modes of uracil (see Table 6.3 [48]). The HW *LIAD* system is expected to produce targets with average internal energies in the range $0.065 - 0.090$ eV [258] but a significant overlap of the vibrationally excited populations is expected in the two experiments according to the Boltzmann energy distribution. Therefore it is very unlikely that the absence of m/z = 84 peak in the HW experiments can be explained by a mismatch of the target's internal energy compared with the OU measurements.

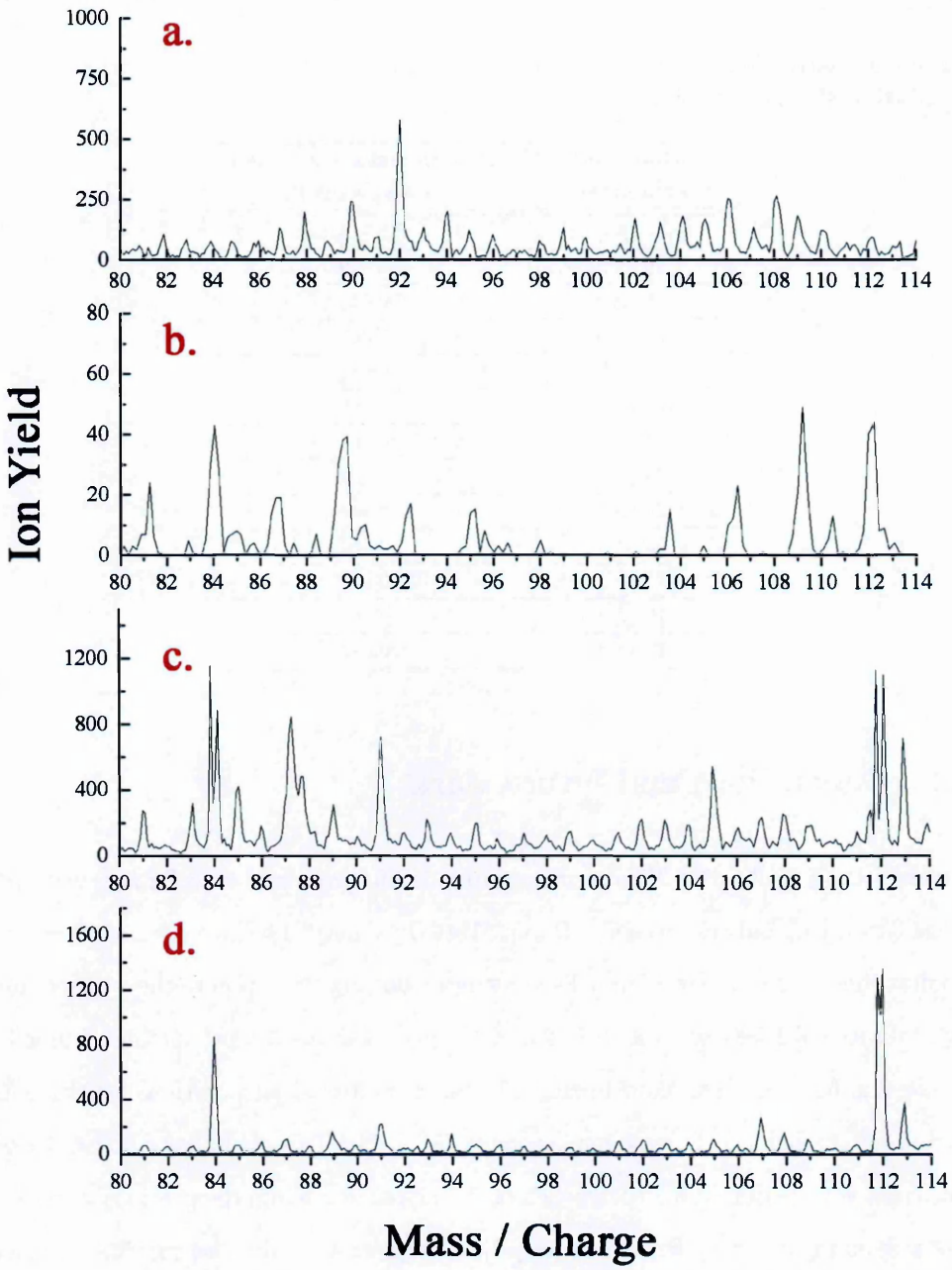

Figure 6.11: Multi-photon ionisation (7 ns pulses, average laser fluence 9×10^7 W/cm^2) measurements carried out at the OU using the modified backplate system: a) 220 nm, background measurement, no powder , b) 220 nm, uracil powder at 25 °C, c) 220 nm, uracil powder at 83 °C, uracil and m/z = 84 signal highly saturated, d) 232 nm uracil powder at 83 °C, minor signal saturation.

Table 6.3: Activation energies of the lowest-lying (up to 0.1 eV) vibrational modes of uracil (reproduced from [48]).

Mode and symmetry	Experimental activation energy (eV)
30 (A")	0.018
29 (A")	0.020
28 (A")	0.046
27 (A")	0.067
26 (A")	0.082
25 (A")	0.088
24 (A")	0.094
23 (A")	0.099
21 (A')	0.049
20 (A')	0.063
19 (A')	0.065
18 (A')	0.067
17 (A')	0.094

6.4 Conclusions and future work

Ultrafast time-resolved MPI experiments have been performed in collaboration with David Townsend and co-workers at Heriot Watt University. The measurements provide the first time-resolved view of uracil's dynamics following excitation to the S_3 band and high vibrational levels of S_2 and S_1 states. Decay plots for the production of uracil$^+$ and several fragment ions show broadly similar characteristics to previous experiments carried out with much lower pump energies [35, 222]. This similarity appears to be consistent with fs-timescale deactivation of S_3-excited uracil into the previously studied S_2 state, as predicted by Richter et al. [37]. The present results also provide evidence supporting access to long-lived triplet states identified theoretically by Ligare et al. [36].

The MPI experiments in Chapter 5 using ns-timescale laser pulses at the OU revealed a fragment ion at $m/z = 84$. This was proposed as a potential marker for ring opening at the $S_2(\pi\pi^*) - S_1(\sigma(n-\pi)\pi^*)$ crossing seam [3]. However, the present ultrafast experiments did not produce this fragment ion over time delays up to 10 ps. Repeating the OU experiments on a vibrationally-excited molecular target showed that this different result is very unlikely to be linked to the internal energies of the target molecules. We

consider that the absence of the m/z = 84 ion in the HW measurements is most likely to be due to the channel's dependence on a so-far unidentified process on a timescale > 10 ps. Hence it seems that the specific ring-opening CI identified theoretically by Nachtigallová et al. ~ 500 fs after S_2 excitation is unlikely be involved. Further ultrafast pump-probe experiments with longer time delays are planned, as well as measurements with pump energies that directly overlap with the OU experiments.

Chapter 7

Hydrated uracil and uracil-adenine clusters

This chapter investigates clustering effects on the dissociative ionisation pathways of uracil. Particular attention is focused on MPI production of $C_3H_4N_2O^+$, in view of its proposed link to excited-state ring opening of gas phase uracil (Chapter 5). Hydrated uracil clusters are analysed as simple models for the hydrogen-bonded cellular environments. As a further step towards understanding the radiation response of uracil within RNA, crossed beam experiments have been carried out on uracil–adenine clusters.

7.1 Introduction

The experiments described in this chapter probe the pyrimidine derivative base uracil ($C_4H_4N_2O_2$) in clustering conditions. The first experimental comparison of uracil MPI in dry and hydrated clustering conditions has been obtained in order to advance understanding of how the local water environment can modify the molecule's response to UV excitation and ionisation. This question has attracted considerable interest with respect to the specific excitation and relaxation dynamics [247, 262, 263] but no previous experimental or theoretical research has directly addressed hydration effects on the fragmentation pathways of the excited molecule or ion. Furthermore, MPI and EII experiments on uracil-adenine clusters are presented and compared with equivalent measurements on pure uracil clusters. Figure 7.1 shows the most stable configurations

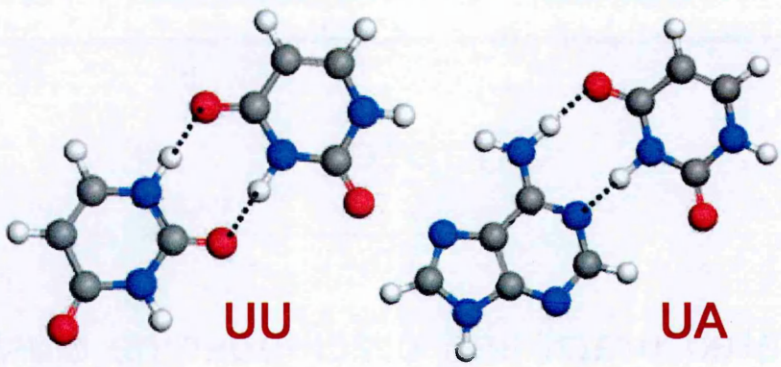

Figure 7.1: The most stable configurations of the H-bonded uracil dimer and uracil--adenine base pair. Adapted from [39].

of H-bonded uracil dimer and uracil-adenine base pair. Figure 7.2 shows π-stacked configuration of these clusters.

The effect of H-bonding and π – stacking has been extensively studied recently [240, 264]. Calculations performed by Golubeva and Krylov [264] at the EOM-IP-CCSD / 6-311(+)G(d,p) level of theory showed that π – stacking and hydrogen-bonding interactions lower the ionisation energy of the uracil dimer by 0.34 and 0.13 eV, respectively, relative to uracil. Hence, uracil dimers are ionised more easily than the monomer. The calculations also indicated that the ionisation can change the bonding from non-covalent to covalent, thus inducing significant geometrical rearrangement in the cation. Zadorozhnaya and Krylov [240] showed that ionisation changes relative order of the isomers in energy, from H-bonded $<$ π – stacked $<$ T-Shaped in the neutral into proton-transferred H-bonded $<$ T-shaped $<$ π – stacked in the cation.

Proton Transfer (PT) reactions have been hypothesised to be responsible for spontaneous mutation in the DNA, as they could form rare tautomeric forms of base pairs that disturb the genetic code [265]. Herrera and Toro-Labbé [266] argued that the stepwise Double Proton Transfer (DPT), which is reported to be more favourable than the single proton transfer [267], in uracil–adenine complexes requires significant structural rearrangement of both the donor and the acceptor, and hence has a significant energy barrier (11.20 kcal/mol and 5.71 kcal/mol for the first and second step, respectively). Cerón-Carrasco et al.'s [268] BP86/6-311++G(d,p) calculations confirm that the DPT

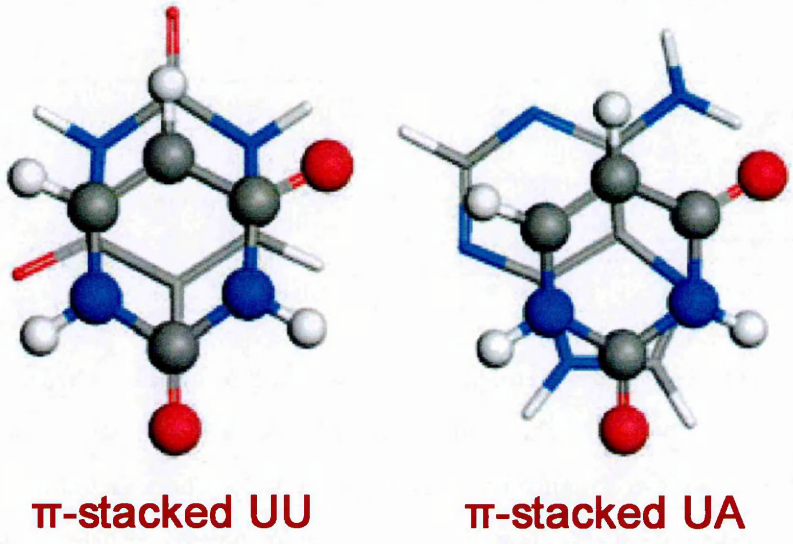

Figure 7.2: The most stable configurations of π-stacked uracil dimer and uracil–adenine base pair. Adapted from [39].

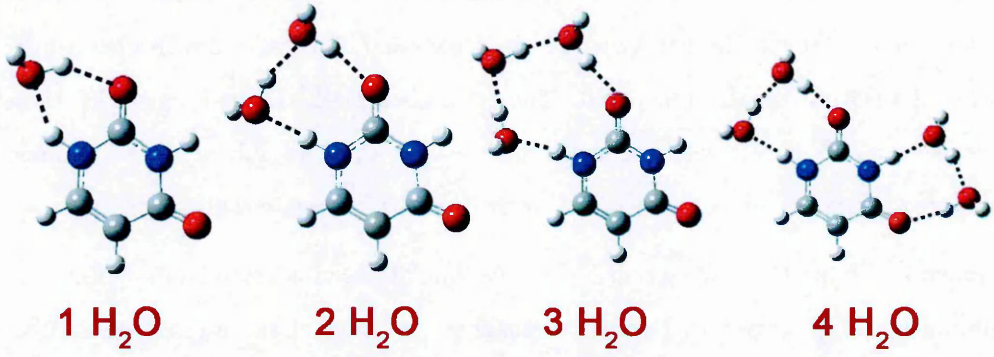

Figure 7.3: The most favourable uracil–water cluster configurations calculated by Bachrach and Dzierlenga [40].

Table 7.1: Calculated interaction energy ΔE for relevant nucleobase pairs. Reproduced for [39].

Systems	Interaction energy $\Delta E_{\text{H-bond}}$ (eV) for H-bonded pair	Interaction energy $\Delta E_{\text{stacked}}$ (eV) for stacked pair	$\Delta E_{\text{H-bond}}$ / $\Delta E_{\text{stacked}}$
AA	-0.76	-0.47	1.62
UU	-0.81	-0.36	2.25
AU	-0.76	-0.44	1.73

in gas-phase clusters may not occur, and also show that it is unlikely in hydration. The role of water environment on the proton transfer has been investigated by Khistyaev et al. [105] in a combined experimental and theoretical study. They concluded that solvation quenched the PT between bases which is efficient in dry uracil clusters. This effect is observed for both H-bonded and π – stacked structures. Bachrach and Dzierlenga [40] optimised uracil–water cluster configurations with up to six water molecules. The energetically most favourable geometries for clusters with up to four water molecules are reproduced here in Figure 7.3. Pedersen et al. [269] argue that attachment of a single water molecule changes the relative abundance of tautomers at room temperature. However, they argue that more than one water molecule is required to obtain solution-phase characteristics, but the exact number remains unknown. Kim and Schaefer [270] calculated most stable molecular structures for mono- and dihydrated uracil–adenine pair using the B3LYP density functional. The calculation predicted structures with three hydrogen bonds, albeit with the third much weaker than the others. The optimised hydrated structures do not vary significantly from the gas phase configuration.

Sequential Monte Carlo Quantum Mechanics simulations of adenine in an aqueous environment [271] suggest that solvation changes the order of the excited states from $^1n\pi^*$, $^1(\pi\pi^*\ \mathrm{L_b})$, $^1(\pi\pi^*\ \mathrm{L_a})$ to $^1(\pi\pi^*\ \mathrm{L_b})$, $^1(\pi\pi^*\ \mathrm{L_a})$, $^1n\pi^*$. Furthermore, Epifanovsky et al.'s [272] calculations showed that solvation in water lowered the vertical excitation energies for uracil's lowest singlet $^1n\pi^*$ and $^1\pi\pi^*$ states by 0.5 eV and 0.1 eV. A similar stabilising effect has been reported for Ionisation Energy Thresholds (*IET*) by Close et al. [67]. Their B3LYP calculations showed a decrease in IET of about 0.15 eV for the

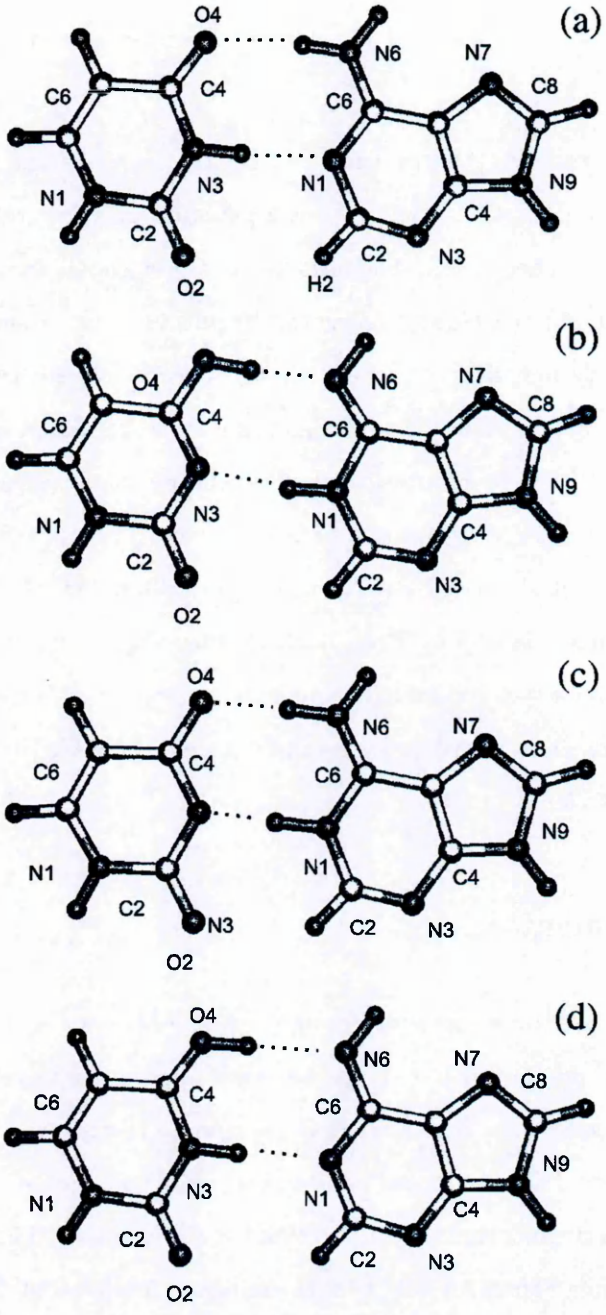

Figure 7.4: A selection of uracil–adenine configurations in the gas phase. Reproduced from [41]. Zhanpeisov and Leszczynski were unable to stabilise configuration d in their calculations.

monohydrate. Attaching the second and third water molecules further lowers the IET by 0.07 eV each.

Section 5.4.2 and reference [160] presents evidence that suggests that MPI production of m/z = 84 ions ($C_3H_4N_2O^+$) from uracil is a potential experimental marker for ring opening in neutral excited uracil. The ultrafast measurements presented in Chapter 6 were not successful in terms of reproducing this fragment ion and potentially confirming its proposed association with the $S_2 - S_1$ crossing seam. Nonetheless, the fact that m/z = 84 ions cannot be detected in experiments involving direct access to uracil's ionic states show that their production must depend on some critical neutral excited state dynamics (an isomeric transition or a dissociation). This raises the question: do these critical neutral excited state dynamics in UV-excited gas-phase uracil also occur within irradiated biological RNA? If so, can they lead to radiation damage in the macromolecule? As a step towards answering these questions, MPI experiments have been carried out on clusters that provide approximations for the chemical environment of uracil within RNA.

7.2 Experimental

The experiments have been performed using the MPI / EII system, described in detail in Section 3.2. To produce hydrated clusters, water vapour was mixed with the argon carrier, by connecting a stainless steel H_2O reservoir to the gas line via a valve. The reservoir and the gas line were heated using resistive wire and the H_2O temperature was monitored using a thermocouple in contact with the reservoir wall. The sample powders were purchased from Sigma-Aldrich, with the minimum purity of 99 %. In the case of adenine-uracil base pair clusters, the cartridge was loaded with an equal mixture (by mass) of the two sample powders. The powders were subsequently manually mixed by vigorous shaking. Variations of this simple mixed powder technique have been shown to be effective in the past, notably for the production of adenine–thymine clusters [21, 71, 273]. The method was also applied for preliminary MPI experiments on uracil-adenine clusters by Molecular Physics Group in 2011 [2]. However, the clustering was

very weak in these results (500 l/s was used to pump the expansion chamber compared with 1,000 l/s in the present adenine–uracil measurements) and the signal/background ratio was too low for the analysis of fragment ion production. Aside from Barc's thesis, no previous crossed beam experiments on uracil-adenine clusters have been reported in the literature.

The chosen nozzle orifice size in the present experiments was 50 μm (Lennox-Laser drilled). The temperatures (250 – 270 °C) of powders were comparable with or lower than those applied in previous supersonic beam experiments that reported no evidence for thermally driven decomposition, isomerisation, or reactivity of uracil or adenine [26]. Examination of the remaining powder after the experiment and the absence of any unexplained peaks in the mass spectra supported the absence of thermally driven reactivity. The carrier gas pressure, the powder temperature, and the pumping speed on the expansion chamber were modified in order to achieve significant clustering in the jet.

7.3 Uracil Hydrated clusters

The first step was to look at uracil-water clusters to approximate the hydrated cellular environment. Whereas various theoretical studies have been carried out on uracil–water clusters [274, 275, 276, 277, 278, 279], experimental studies are scarce. The only previous MPI measurements on uracil–water clusters were reported in Barć's PhD thesis [2]. Working at 224 nm ($1 \times 10^6 - 4 \times 10^6$ W/cm^2), Barc observed hydrated uracil ions up to $U^+ \cdot (H_2O)_7$ and hydrated uracil dimer ions up to $U_2^+ \cdot (H_2O)_3$. Barc also showed that at least three photons were required to produce protonated uracil in hydrated clustering conditions. However, high background signals at low m/z values prevented Barć from being able to carry out a comparison of fragment ion production in dry and hydrated conditions.

The only MPI measurement of dry uracil clusters found in the literature was recorded in dry conditions by Kim et al. [280] using 274 nm ns-timescale laser pulses. The same group reported EII mass spectra of hydrated uracil clusters showing evidence

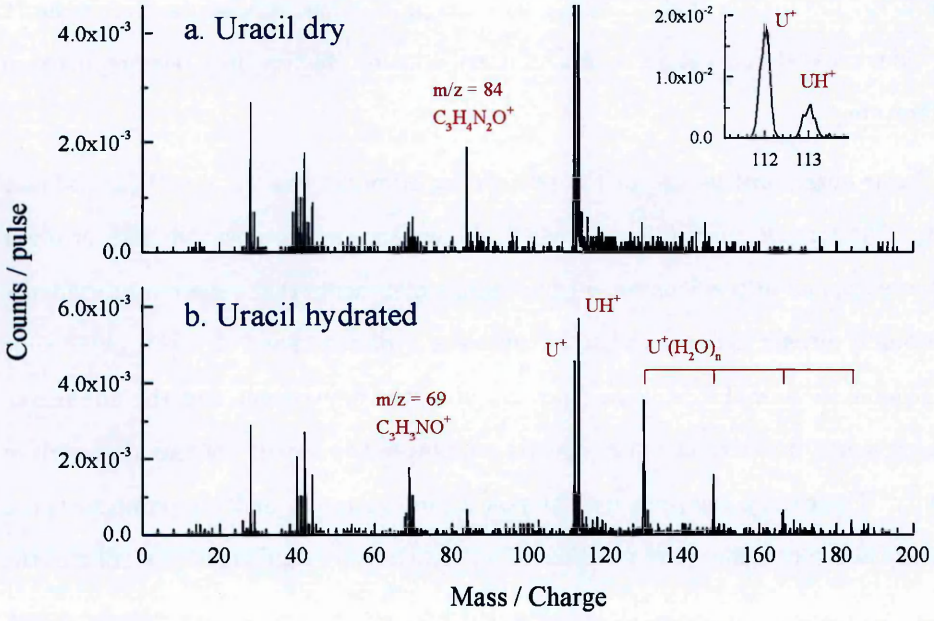

Figure 7.5: Single-colour MPI (220 nm, average fluence 4×10^6 W/cm^2, powder 250 °C, Ar 0.8 bar) of uracil in (a) - dry and (b) - hydrated conditions (water temperature 60 °C).

for $U_mH \cdot (H_2O)_n$ series as well as $U_m \cdot (H_2O)_n$. [65] The only previous experiment in the literature that explored clustering effects on fragment ion production from uracil (dry clusters only) was carried out for 100 keV O^{5+} impact ionisation [82]. Signals at m/z = 83 (U^+ minus HCO) and 95 (U^+ minus OH) were only observed in clustering conditions and were linked to hydrogen bonding effects, as opposed to stacking. Mass spectra showing the differences between dry and hydrated MPI are presented in Figure 7.5. A summary of the observed ion intensities is presented in Table 7.2. No evidence for new fragment ion channels from uracil due to clustering was observed in the present data.

He et al. [262] reported that hydration significantly represses access to the long-lived triplet states of methyl-substituted uracil and thymine. In this context, the fact that the total MPI count rate is only reduced by 22 % ± 3 % due to clustering with water (Figure 7.5 and Table 7.2) provides an indicator that the dominant MPI pathways in the present experiments do not involve these triplet states. Further discussion of the singlet excited states of gas phase uracil is provided in Chapters 5 and 6.

Table 7.2 and Figure 7.5 show that the signal at m/z = 69 ($C_3H_3NO^+$, recognised as the precursor to further strong dissociation channels) was markedly stronger in the hydrated measurement. This result may be attributed to energy removal from the excited uracil cation via cluster dissociation tending to stop certain sequential fragmentation processes at an early stage. The reduction in the signal at m/z = 40 (assigned to H loss from $C_3H_3NO^+$, followed by CO loss) due to hydration is consistent with this interpretation. By contrast, other ion signals linked to $C_3H_3NO^+$ fragmentation (for example m/z = 28) did not change significantly. Therefore the presently observed hydration effects on the dissociative MPI pathways of uracil cannot be understood purely on the basis of generalised energetic arguments. This is unsurprising as theoretical studies have demonstrated shifts (generally stabilisation) of the $^1\pi\pi^*$ and $^1n\pi^*$ states of uracil and their relaxation dynamics [247, 263] due to hydrogen bonding with water, as well increased excited state tautomerisation [213]. In this context, it is interesting that the production of the m/z = 84 fragment ion ($C_3H_4N_2O^+$) was repressed by hydration in the present data. This may indicate that the presence of hydrogen-bonded water moieties disrupts access to the neutral excited state dynamics required for this dissociative MPI channel (e.g. the proposed S_1/S_2 ring-opening conical intersection discussed in Section 5.4). The result bears resemblance to absence of an equivalent CO loss channel in thymine, as compared with pure or deuterated uracil. Full discussion is given in Section 5.6.

Significant production of ions with m/z = 113 was observed both in the dry and hydrated measurements: $\sim$ 34 % and $\sim$ 140 % of the respective signals at m/z = 112. These peaks are assigned to protonated uracil (UH^+) and a small contribution due to carbon isotopes in uracil (5.2 % [281]). UH^+ has been detected following electron collisions with $U_m \cdot (H_2O)_n$ [65] but the previous papers on the ionisation of dry uracil clusters [82, 280] did not mention this product. Its production evidently involves intermolecular hydrogen or proton transfer and its presence in the dry mass spectrum shows that the process does not require the presence of water. Indeed, water is transparent at 220 nm [202, 24, 204, 203] so UH^+ production in the present experiments must begin with uracil

Table 7.2: Hydration effects on the production of ions, cluster ions, and selected fragment ions following uracil MPI at 220 nm. The corresponding mass spectra are shown in 7.5 The total ion counts in 10^4 laser pulses were 1960 (including 640 fragment ions) and 1520 (including 670 fragment ions) in dry and hydrated conditions, respectively.

Selected ion		% of total ion counts	
Mass / charge	**Assignment**	**Dry**	**Hydrated**
225	U_2H^+ and U_2^+ isotopes	0.3 ± 0.2	-
224	U_2^+	0.2 ± 0.1	0.6 ± 0.3
184	$U^+(H_2O)_4$	-	0.7 ± 0.3
166	$U^+(H_2O)_3$	-	1.6 ± 0.5
148	$U^+(H_2O)_2$	-	5 ± 1
130	$U^+(H_2O)$	-	13 ± 2
113	UH^+ and U^+ isotopes	17 ± 2	21 ± 2
112	U^+	50 ± 3	15 ± 2
<112	All fragment ions[a]	33 ± 2	44 ± 3
84	$C_3H_4N_2O^+$	4 ± 1	1.8 ± 0.5
69 meta[b]	U^{+*} dissociation after 1.3 – 14.6 μs producing $C_3H_3NO^+$	1.8 ± 0.5	0.7 ± 0.3
69	$C_3H_3NO^+$	1.1 ± 0.3	7 ± 1
42	$C_2H_2O^+$ / $C_2H_4N^+$	4 ± 1	3 ± 1
40	$C_2H_2N^+$	4 ± 1	1.2 ± 0.4
28	CH_2N^+ / CO^+	6 ± 1	7 ± 1

[a] Includes counts for fragment ions that have not been included in the table.
[b] This metastable channel appears at m/z = 87.6 in the calibrated mass spectra shown in Figure 5.5 and 7.5

excitation. Zadorozhnaya and Krylov's [240] calculations showed that the hydrogen-bonded uracil dimer cation relaxes to a proton-transferred form that is much more strongly bound than the most stable stacked or T-shaped dimer cation configurations. Therefore, the present UH^+ MPI signals are attributed to a negative barrier reaction from U^+U to UH^+(U–H) followed by cluster ion dissociation. This interpretation is broadly consistent with the absence of $UH^+ \cdot (H_2O)_n$ peaks in the MPI mass spectrum (conversely, these species were observed by electron impact ionisation [65] and attributed to water ionisation followed by proton transfer to uracil). Due to the weaker binding energies of uracil and water molecules (depending on bonding configuration between 1.42 and 2.49 kcal/mol for the monohydrate and 2.03 – 6.11 kcal/mol for doubly hydrated uracil [282]) UH^+(U–H) fissure can be expected to involve extensive water loss.

While clustering with water is evidently not essential in the presently observed MPI-induced proton transfer processes, it is interesting to note that the hydrated measurement in Figure 7.5 shows a strong increase in the UH^+ signal. This may indicate that the presence of water in the expansion aids the formation of complexes with two or more uracil molecules. It should also be noted that MPI-induced proton transfer might play a role in determining the observed clustering effects on fragment ion production discussed above.

7.4 Pure uracil clusters

Figure 7.6's plots a) and b) compare MPI and electron impact ionisation (EII) measurements carried out on uracil in an argon expansion. High pumping speed pumping speed (1,000 l/s) and high powder temperature was applied in order to achieve good clustering conditions.. The uracil dimer ion and the protonated uracil dimer ion are clearly visible in both the MPI and EII measurements. The MPI signal intensities for cluster ions and fragment ions are given in Table 7.3, while the complete analysis of this dataset is presented in the Appendix A. Strong production of UH^+ relative to U^+ (125 %) in Figure 7.6a-d demonstrates significant presence of clusters containing uracil in the target beams. The relative production of protonated uracil (UH^+) in the EII measurement is even higher, perhaps due to neutral dissociation of excited $U_2{}^+$ in the high-energy collisions. MPI mass spectra of pure uracil clusters have previously been carried out using 274 nm ns-timescale laser pulses but no information on fragment ions was reported [280]. The only experiment in the literature that probed fragment ion production from pure uracil clusters was Schlathölter et al.'s [82] 100 keV O^{5+} impact ionisation with an aggregation source that produced considerably larger clusters whereas the present apparatus produced mainly dimers and trimers (evidenced by the U_2H^+ signal). Signals at m/z = 83 (U^+ minus HCO) and 95 (U^+ minus OH) were interpreted as providing evidence for hydrogen bonding instead of stacking. The present MPI and EII measurements did not reveal ion production at these m/z values, suggesting that the m/z = 83 and 95 ions are produced from large clusters.

Considering our particular interest in the MPI production of m/z = 84 ions, it is worth highlighting that this peak is clearly present in the mass spectrum for uracil in clustering conditions (Figure 7.6a). However, as we do not have an independent verification of the presence of isolated uracil molecules in the neutral beam, this result does not necessarily demonstrate that this dissociative MPI channel is available for uracil clusters.

7.5 Uracil-adenine base pair clusters

As discussed in Section 7.3 clustering with water suppressed $C_3H_4N_2O^+$ production while most other fragment ion channels were not significantly affected. This is in agreement with the proposed mechanism for the production of the ion - hydrogen bonding with water stabilises (or "protects") uracil with respect to the proposed ring opening [3]. However, experiments discussed in Section 7.4 on dry uracil clusters did not reveal clear evidence for a similar stabilisation due to uracil–uracil clustering. As uracil pairs with adenine in RNA, experiments to test whether or not hydrogen bonding with adenine has a significant effect on UV-induced dynamics have been performed.

The hydrogen bonding configuration of adenine–uracil base pair depends on the tautomeric forms of the two molecules. Discussion about the most likely tautomeric form of adenine (amine-N9H, refer to Figure 4.1) is already given in Chapter 4. The most abundant gas phase tautomers of uracil are discussed in Section 5.1, and shown in Figure 5.1. Predicted cluster geometries [41] are shown in Figure 7.4 with the most likely hydrogen bonded complex being the adenine amine-N9H bonded with uracil diketo (Figure 7.4a).

To our knowledge, no previous experiments have probed fragment ion production from uracil–adenine clusters. For both hydrogen-bonded and $\pi-$stacked optimised configurations, the calculated stabilities of AU pairs are greater than AA or UU [283], so mixed clusters are expected to form a significant part of the target beam. No new species were observed; the fragment ions in the Figure 7.6c and Figure 7.6d have previously been observed from dissociated uracil$^+$ (e.g. $C_3H_3NO^+$ at m/z = 69 [160]), adenine$^+$ (e.g. $C_4H_4N_4^+$ at m/z = 108 [283]), and / or protonated adenine (e.g. $C_4H_5N_4^+$ at m/z = 109 [44]).

In view of our particular interest in $C_3H_4N_2O^+$ with its proposed link to excited-state ring opening, it is noteworthy that the production of this ion approximately doubled in the uracil–adenine measurement compared with the pure uracil result (0.021 ± 0.003 counts per pulse in Figure 7.6c compared with 0.011 ± 0.002 in Figure 7.6a). No peak at this m/z value has been observed from isolated, clustered, or protonated adenine

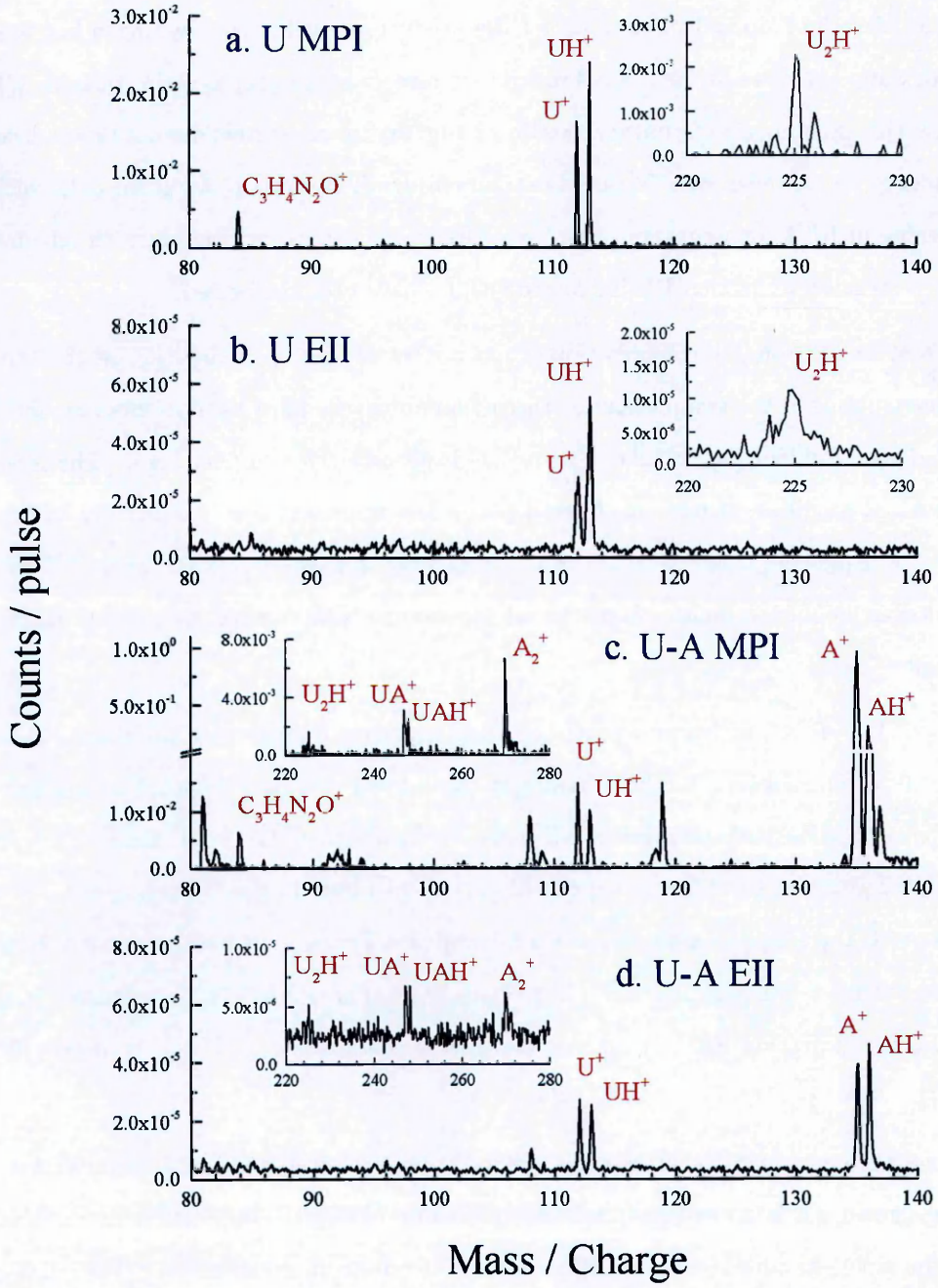

Figure 7.6: MPI mass spectra (220 nm, average fluence 9×10^7 W/cm) and EII (200 eV) of uracil (plots a) and b)) and a mixture of uracil and adenine (plots c) and d)) vaporised at 270 °C in 1.0 bar of argon.

[44, 161, 207], or from protonated uracil [284]. The fact that the U^+ signals were the same (to within the uncertainty limits) in plots a and c as well as in plots b and d suggests that this result was not simply due to different populations of isolated uracil molecules in the neutral beams. Therefore the result supports $C_3H_4N_2O^+$ production from multiphoton ionised uracil–adenine complexes. Zhanpeisov and Leszczynski [41] and [285] calculated that the most stable adenine-uracil configuration involves one (U) N3H $\cdots$ N1 (A) bond and one (U) C4O $\cdots$ HC6 (A) bond. Considering the proximity of these bonds to the proposed N3-C4 rupture site, the formation of hydrogen-bonded AU pairs is expected to have a suppressive effect on the uracil ring opening process identified by Nachtigallová et al. [3]. Hence the present result may be rationalised by supposing that the target beam contained a range of adenine-uracil configurations, including stacked complexes in which excited state ring opening is more plausible. It is interesting to note that the calculated interaction energy (MP2 level) of the optimised AU stacked pair is -9.08 kcal/mol, compared with -6.52 kcal/mol for its pure uracil counterpart [283]. Therefore, we suggest that the enhanced MPI production of $C_3H_4N_2O^+$ in the adenine-uracil measurement compared with the pure uracil result may be traced to the relative populations of π – stacked clusters in the neutral beams.

The U^+ / A^+ signal ratio was 71 % in Figure 7.6d, very close to the 75 % ratio between the calculated EII cross sections [285]. This indicates similar target densities of the two molecules in the expansion, as expected from the reported vapor pressures [206]. However the MPI signal of A^+ was around 80 times stronger than U^+ (Figure 7.6c). Ullrich et al. [31] 267 nm pump - 200 nm probe measurements on adenine indicated access to states with ns-timescale lifetimes (assigned to triplets) whereas their equivalent experiments on uracil revealed no evidence for states with longer lifetimes than S_1 (2.4 ps). Therefore, although a deactivation pathway from $S_1(n\pi^*)$ excited uracil to $T_1(\pi\pi^*)$ has been predicted theoretically [37], the relatively strong A^+ signal in the present laser conditions may be partially due to more efficient access to triplet states. Alternatively (or concurrently), it may be traced to MPI via long-lived exciplex states in π – stacked nucleobases [286], [287]. Takaya et al. [287] reported A^+U^- and A^+A^-

Table 7.3: Signal intensities for of ions, cluster ions, and selected fragment ion following uracil or uracil-adenine mixture MPI at 220 nm. The corresponding mass spectra are shown in 7.6. The total number of pulses were 16647 and 18000 for pure uracil and uracil-adenine mixture, respectively.

m/z	Assignment	Signal intensity (counts / pulse) in strong clustering conditions	
		Uracil 220 nm MPI	Uracil-adenine 220 nm MPI
270	A_2^+	-	0.020 ± 0.001
248	UAH^+	-	0.007 ± 0.001
247	UA^+	-	0.012 ± 0.001
225	U_2H^+	0.0059 ± 0.0012	0.0043 ± 0.0009
224	U_2^+	0.0010 ± 0.0006	0.0015 ± 0.0007
136	AH^+	-	0.80 ± 0.02
135	A^+	-	2.72 ± 0.03
119	$C_5H_3N_4^+$	-	0.044 ± 0.002
113	UH^+	0.040 ± 0.003	0.030 ± 0.003
112	U^+	0.032 ± 0.003	0.034 ± 0.003

states in ApU and ApA dinucleosides with respective decay constants of 240 ± 70 and 105 ± 30 ps.

Li et al. [288] stated that proton transfer from N3 on adenine to N1 on uracil is expected in AU^+. This expectation appears to be based on analogies with other purine-pyrimidine radical cations, notably the Watson-Crick pairs [267]. The stabilities of UA^+ with and without proton transfer are not available in the literature, nor are any associated reaction barriers. If Li et al.'s [288] expectation is correct and there is no barrier to prevent fast proton transfer then UH^+ would be a major dissociative ionisation product of UA. However, Figure 7.6 shows that the UH^+ signals were reduced significantly in the present measurements on adenine-uracil compared with pure uracil. Once again, this result is consistent with the neutral beam containing a range of mixed cluster configurations including π – stacked complexes as well as hydrogen-bonded base pairs. Specific calculations on UA cluster ions and experiments with greater control of target cluster configurations (for example, exploiting Stark selection methods, as discussed in Section 3.4) are required to clarify the proton transfer processes.

7.6 Conclusions

Previous studies have identified mechanisms by which hydration tends to increase the photo-stability of uracil, notably shifting key singlet states to higher energies [247, 263], and restricting intersystem crossing into long-lived triplet states [262]. The present work shows that the new MPI fragment ion at m/z = 84 ($C_3H_4N_2O^+$), proposed in Section 5.4.2 as a potential marker for theoretically predicted [3] ring opening in electronically-excited uracil, is also stabilised by clustering with water. Further research is necessary to understand the specific mechanism responsible for this hydration effect.

Fragment ion production from uracil-adenine clusters has been probed for the first time. MPI measurements revealed evidence for enhanced $C_3H_4N_2O^+$ production from uracil–adenine clusters compared with pure uracil clusters. As the formation of hydrogen-bonded AU pairs is expected to suppress the proposed uracil ring opening process, this may indicate a significant presence of π – stacked complexes in the neutral beam. In contrast with the deamination reactions in adenine–water clusters investigated in Chapter 4, no evidence for intermolecular reactivity aside from proton transfer was observed in uracil–water and uracil–adenine clusters.

Chapter 8

Conclusions and outlook

This thesis investigates radiation effects on DNA and RNA bases in the gas phase as well as in clusters that represent simple model systems for biological environments. The three most important contributions are listed below.

(i) Comparing multi-photon ionization (MPI) of uracil with electron impact ionization (EII) provides the first experimental demonstration that neutral electronic excited states dynamics in a nucleobase (uracil) can lead to bond breaking in the aromatic ring and the production of new photochemical products.

(ii) The effects of hydration on the dissociative ionization of nucleobases (adenine and uracil) have been studied for the first time. Significant suppression and enhancements of specific channels have been observed but the range of different species (monomers and various clusters) in the target beams limits the interpretations.

(iii) The contribution above highlights the importance of experiments with greater control over the neutral targets. In response to this challenge, a new experiment has been built that enables radiation effects to be studied on molecules in Stark-deflected beams. Early results include a demonstration that studying EII as a function of the *Stark deflector* voltage can be used to deduce

whether certain product ions came from monomers or from clusters in a beam (nitromethane in an argon expansion).

The first contribution highlights the importance of including the (unimolecular and intermolecular) reactivity of excited nucleobases in nanoscale simulations of radiation damage in biological material. The assumption that ultrafast relaxation back to the vibrationally hot electronic ground state prevents damage in neutral excited nucleobases may be an over-simplification. Moreover, our ultrafast pump-probe experiments provided evidence supporting theoretically predicted access to long-lived ($>$ 10 ps) triplet states of uracil. The second contribution demonstrates that clustering has major effects on the fragmentation pathways of nucleobases, many of which cannot be explained purely on the basis of efficient energy removal from intra-molecular vibrational modes to inter-molecular modes. The third contribution opens a new route to understanding these specific effects, as required for integration into radiation damage models and for rigorous comparisons with theory.

The main specific conclusions from each chapter of the thesis are summarised below:

Summary of conclusions from Chapters 4 – 7

Chapter 3: Experimental

- Improvements to the system during this PhD have effectively eliminated background signals in MPI mass spectra and enabled EII measurements to be performed with tuneable mass resolution.
- A new experimental system to study MPI, EII and EA processes in Stark-selected biomolecules has been designed and built.
- The data acquisition system based on LabVIEW software interface has been integrated with the experiment to allow semi-automatic acquisition of data. The system controls both the MPI / EII and the Stark / EA experiments, allowing for recording ion flight times together with corresponding parameters such as laser

pulse energy, spectrometer voltages, deflector voltage, gas pressure or temperatures measured in several places in the experiments. A vacuum security system has been implemented.

- The ability to control the neutral molecular beam has been presented. Experiments showed deflection of nitromethane out of the axis of the beam.
- An alternative method to remove the species with the highest effective dipole moment / mass ratios out the neutral beam has been shown.

Chapter 4: Reactivity in adenine–water clusters

This chapter discussed MPI of adenine in isolation and clustered with water. The key result obtained is the evidence for production of hypoxanthine via a barrierless deamination reaction in a closed hydration shell of adenine.

- With the exception of the three fragment ions ($C_5H_4N_4^+$, $C_5H_3N_4^+$, and $C_4H_4N_4^+$ fragments ions) channels, clustering with water stabilises adenine with respect to dissociative MPI ionisation.
- All sequential fragment ion pathways are suppressed. These hydration effects have been attributed to energy dissipation from the excited radical cation via cluster dissociation.
- Hypoxanthine was successfully ionised using ns-timescale laser pulses for the first time. The low MPI efficiency compared with adenine suggests particularly fast internal conversion to the electronic ground state following $\pi\pi^*$ excitation.
- Strong EII production of $136^+ \cdot (H_2O)_n$ ions has been observed and attributed to water ionisation followed by proton migration to adenine and partial cluster dissociation.
- $136^+ \cdot (H_2O)_n$ MPI peaks have been observed for the first time. This provides the first experimental evidence supporting the deamination reactions in closed-shell adenine–water clusters leading to the production of hydrated hypoxanthine ions.

Chapter 5: MPI and EII of uracil, d-uracil and thymine

Uracil has been studied by ns timescale MPI and 200 eV EII, and compared with several of its derivatives in the gas phase. The main result indicated a ring opening leading to the production of an m/z = 84 ion:

- The first experimental evidence for a new UV damage process in uracil – production of $C_3H_4N_2O^+$ ion (uracil$^+$ minus CO). The appearance energy of the ion matches calculated threshold for accessing the $S_2(\pi\pi^*) - S_1(\sigma(n-\pi)\pi^*)$ crossing seam [3]. EII experiment have shown this channel is not produced by direct ionisation by 200 eV electrons.

- Power dependence for the production of several fragment ions is measured, 2-photon processes lead to production of both U^+ and m/z = 84 ion. This rules out dissociative ionisation followed by ionisation of a neutral product as a possible source of this ion.

- Further research on deuterated uracil supported the interpretation that the ring-opening followed by a CO group subtraction is the most plausible pathway leading to the production of the m/z = 84 fragment.

- Studies of thymine have shown not shown an analogous process. This suggests that substitution of a heavy group at the C5 position of the pyrimidine ring can stabilize excited nucleobases with respect to isomeric transitions.

- A metastable dissociation channel of the uracil radical cation producing $C_3H_3NO^+$ and neutral CO fragments has been identified. The identification method cross-checks measured and calculated times-of-flight with a reflectron cut-off voltage to identify the metastable ion,

- Studies of 4-deuterated uracil lift several ambiguities previously reported in literature in assignment of m/z = 42, 40, 29, 28, 26 and 14 fragment ions.

Chapter 6: Ultrafast studies of uracil

Ultrafast fs-timescale time resolved pump-and-probe MPI has been performed on uracil as a continuation of research described in Chapter 5. The measurements were carried out at Heriot-Watt University (HW) and provide the first time-resolved view of uracil's dynamics following excitation to the S_3 band and high vibrational levels of S_2 and S_1 states.

- Pump-probe measurements on uracil have been carried out at a much lower pump wavelength (200 nm) than any previous ultrafast experiments (250 – 267 nm).
- Decay plots for the production of uracil$^+$ and several fragment ions show broadly similar characteristics to previous experiments carried out with much lower pump energies. This similarity appears to be consistent with fs-timescale deactivation of S_3-excited uracil into the previously studied S_2 state.
- A long-lived component of the decay curves is clearly visible and provides evidence supporting access to long-lived triplet states.
- No evidence for the production of the $m/z = 84$ ion (observed in the single-colour MPI experiments at the OU using ns-timescale laser pulses) was observed with pump–probe delays up to 10 ps.
- Experiments on a vibrationally-excited molecular target with the modified OU setup showed that this different result is very unlikely to be linked to the internal energies of the target molecules. Therefore we consider that the absence of the $m/z = 84$ ion in the HW measurements is most likely to be due to the channel's dependence on a so-far unidentified process on a timescale > 10 ps.

Chapter 7: Hydrated uracil and uracil-adenine clusters

The final results chapter presents MPI and EII studies of uracil in clusters. For the first time, the experiments explore how bonding with water and with adenine modifies fragment ion production.

• No evidence for intermolecular reactivity aside from proton transfer was observed in uracil–water and uracil–adenine clusters.

• The m/z = 84 fragment ion ($C_3H_4N_2O^+$) was repressed by hydration. This may indicate that the presence of hydrogen-bonded water moieties disrupts access to the neutral excited state dynamics required for this dissociative MPI channel.

• Enhanced $C_3H_4N_2O^+$ production from uracil–adenine clusters compared with pure uracil clusters was observed. As the formation of hydrogen-bonded AU pairs is expected to suppress ring opening, this may indicate a significant presence of π-stacked complexes in the neutral beam.

Outlook

The current work brings new insights into radiation-induced unimolecular and intermolecular processes in DNA / RNA bases and their clusters. The main steps to continue this research in the near future are given below.

- The production of a new fragment ion at m/z = 84 has been identified and traced to so-far unidentified dynamics in neutral excited uracil. This process is mediated by clustering. However, further research is necessary to understand the specific dynamics.
  - Ultrafast experiments will be carried out at Heriot Watt University on uracil with a 220 nm pump beam. This will allow the time-resolved dynamics of uracil to be investigated following absorption into exactly the same part of S_2 manifold as the single-colour MPI experiments at the OU.
  - Ultrafast measurement will be carried out with pump-probe delays up to 100 ps to look for the m/z = 84 production from a long-timescale process (notably triplet dynamics).
- Complete the development of the new experimental setup (Stark / EA experiment)

- Use the Stark / EA system to perform MPI experiments on Stark-selected clusters. In particular, this can enable the production of $m/z = 84$ ions from uracil–adenine clusters to be studied as a function of specific cluster configuration. This has potential to test our hypothesis that the production of these ions in the present mixed beams can be traced to pi-stacked complexes. Similarly, experiments of this kind can elucidate the mechanism by which hydration suppresses this fragment ion channel.
- Optimise the electron attachment probe for the Stark / EA experiment. Perform EA experiments on biologically significant molecules and their cluster utilising the target selection technique.

As discussed in Chapter 1, structural modifications and dissociations of nucleobases in neutral or ionic excited states are important radiation damage processes in DNA and RNA. Moreover, the products (particularly radical fragments) can induce further damage by reacting with the nearby subunits of the macromolecule. This thesis reveals new detail on the response of isolated nucleobases to UV and electron irradiation, notably providing insights into the electronic excited state dynamics of uracil and identifying dissociative ionization products that have been debated in the literature. This information can be incorporated into models of radiation-induced damage in biological material. Indeed, the key input data for the most precise (nanoscale) Monte Carlo simulations of radiation tracks in condensed material [91] is currently provided by experiments and calculations of radiation interactions with isolated molecules.

Accounting for phase and intermolecular bonding in nanoscale radiation damage simulations represents a major challenge. The study of molecular clusters presented in this thesis extends our understanding of how specific processes observed in irradiated isolated molecules evolve in a multi-molecular environment as a step closer to biological material. This provides valuable data and understanding for the development of multi-dimensional simulations of radiation effects that can overcome the limitations of models based purely on gas-phase data or macroscopic data. As those radiation damage models are the basis for cancer treatment planning, their completeness is crucial for accurate dosing. The significant changes in fragment ion channels due to clustering observed

in this thesis highlight the importance of integrating nanoscale intermolecular bonding effects into radiation damage models.

The understanding of hydrated biomolecular clusters is still far from complete. For example, it is challenging to derive detailed interpretations for presently observed clustering effects on fragment ion production from multi-photon ionized nucleobases. A significant barrier for interpretations is the difficulty in acquiring good control over the neutral targets. The present development of the Stark / EA experiment is a significant step towards overcoming this difficulty. The inclusion of a low-energy electron system, as well as options to perform MPI and EII experiments can offer exceptional breadth in the analysis of radiation effects in selected biomolecular clusters. The preliminary data obtained using the Stark / EA experiment shows that this system will indeed be an invaluable contribution to the existing advanced methods to probe radiation-induced processes in controlled neutral targets. The system is one of new generation of experiments that will enable unprecedented levels of control on neutral molecular / cluster targets.

Appendix A

Supporting information

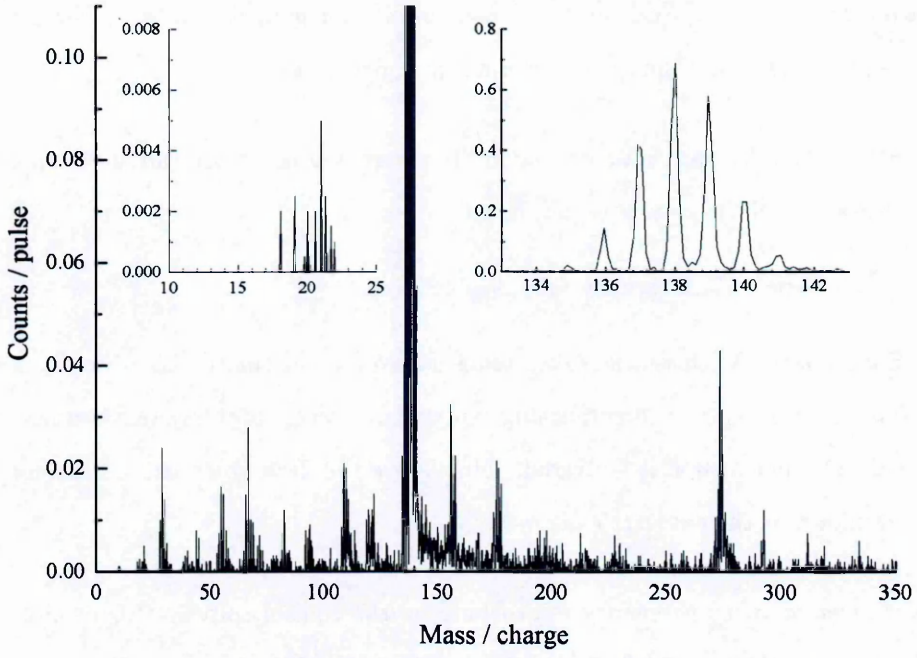

Figure A.1: MPI spectrum (225 nm, average fluence 7×10^5 W/cm^2) of adenine (248 °C) in an expansion with argon (0.9 bar) and D_2O (100 °C), showing a sequence of peaks between m/z = 18 and m/z = 22, supporting the assignment of the m/z = 18 peak to NH_4^+ production following AH^+ dissociation.

Vacuum Security System

The Vacuum Security System overlooks the state of the vacuum and, if necessary, is able to securely shut it down. The system allows for turning on and off 2 roughing pump, 5 turbomolecular pumps and a pneumatic security valve, that prevents oil backstreaming into the chambers, in case of turbopump malfunction. The system is interfaced with vacuum gauges at both roughing lines, and emergency shutdown is initiated if pressure in either of them rises above a specified triggering level (typically 5.0×10^{-1} mbar), or if a turbomolecular pump reports an error (such as gas overload, motor temperature too high etc.). The system provides several relay outputs for controlling devices that need to be disabled in case of a system shutdown, e.g. the electron gun, electron monochromator and the MCP detector. The system operates in three modes:

- Safe – for fully automatic operation. If the system is tripped, an alarm siren is sounded, and the system is shut down.
- Pump/Vent – With security fully disabled and
- Experiment – With sensing subsystem engaged, but automatic shutdown disabled. This mode is used when performing experiment. In case of the system is triggered, only the alarm siren is activated. This leaves the decision to either continue or shutdown at the operator's discretion.

Further layer of vacuum security is provided by the control software (Appendix B), which can lower the Stark-deflector's voltage sufficiently slow.

Stark Deflector conditioning

The Stark deflector's power supply is remotely controlled via the LabVIEW experimental control platform, with security checks monitoring the pressure in the deflection chamber. In case of a sudden increase in of the pressure in the vessel, the deflector's voltage is lowered, at a safe rate, to avoid discharges. This rate is about three times the advised increase rate (1 kV/min), and is a compromise between lowering the voltage fast enough not to risk discharges due to increased pressure, and risking discharges due to draining the charge too fast.

Table A.1: Stark Deflector high voltage conditioning.

Time [min][A]	Voltage [kV]	Max current [10^{-8}A][B]
0	$0 \rightarrow 3$	16.0
15	3	0.2
18	$3 \rightarrow 6$	11.0
33	6	0.7
36	$6 \rightarrow 7$	8.3
51	7	1.4
52	$7 \rightarrow 8$	10.4
67	8	1.5
68	$8 \rightarrow 9$	8.0
83	9	0.5
84	$9 \rightarrow 10$	20.0
99	10	1.6
100	$10 \rightarrow 10.5$	7.3
115	10.5	0.5
116	$10.5 \rightarrow 11$	6.7
131	11	1.2
132	$11 \rightarrow 11.5$	9.2
147	11.5	2.1
148	$11.5 \rightarrow 12$	4.4
173	12	3.2

[A] Maximum voltage increase rate: 1 kV/min

[B] maximum current observed during either increasing or observing the voltage.

Nitromethane seeding

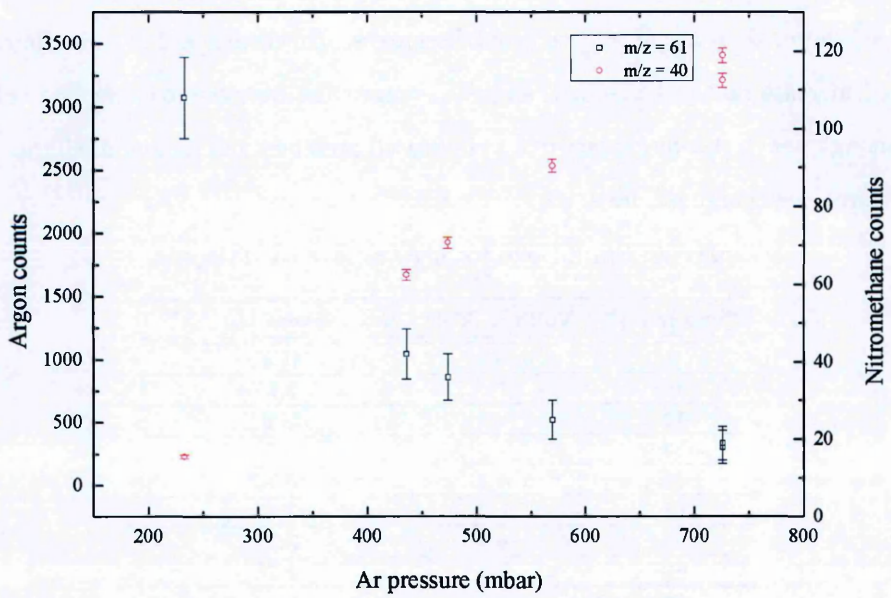

Figure A.2: Nitromethane signal intensity as a function of argon gas pressure.

Uracil metastable fragmentation pathway

This section described the calculation performed to identify the metastable decay of uracil, as discussed in Section 5.4.3. Reflect cut-off voltages were calculated for the most plausible metastable dissociation schemes, and compared with experimental values in tables A.2 (low fluence MPI mass spectrum) and A.3 (high fluence). Direct dissociation (a single dissociation of uracil$^+$ at a given delay time after ionisation) and sequential dissociation (uracil$^+$ dissociates promptly followed by a delayed second fragmentation to produce the ion that hits the detector) were both considered. Colour-coding corresponds to the difference between calculated and measured values. Green cells correspond to < 5 V difference while yellow cells correspond to < 15 V difference.

Further calculations were performed in order to narrow down the list of possible ions. The expected difference of time of arrival between the metastable peak and uracil parent ion was calculated and compared with the measured data. The difference, between these

Table A.2: Calculated Cut-Off Voltages (Low fluence) for metastable dissociation in the FFR. Cut-off 898 ± 1 V. (220 nm, average fluence 4×10^6 W/cm^2, argon 0.7 bar uracil temperature 250 °C)

Unfocused	Intermediate Ion						
Product Ion	Direct dissociation	*111* (H loss)	*110* (2H loss)	*109* (3H loss)	*108* (4h loss)	*99* (CH loss)	*97* (NH loss)
85	643	631	618	605	592	462	430
84	659	647	634	622	609	480	449
72	854	843	832	822	810	700	673
71	870	860	849	838	827	719	692
70	886	876	865	855	844	737	711
69	902	892	882	872	861	755	729
68	919	909	898	888	878	774	748
67	935	925	915	905	895	792	767
66	951	941	931	922	911	810	786
56	1113	1105	1096	1088	1079	994	973

Table A.3: Calculated Cut-Off Voltages (High fluence) for metastable dissociation in the FFR. Cut-off 860 ± 1 V, conditions as Figure 5.10.

Focused	Intermediate Ion						
Product Ion	Direct dissociation	*111* (H loss)	*110* (2H loss)	*109* (3H loss)	*108* (4h loss)	*99* (CH loss)	*97* (NH loss)
85	588	575	561	548	534	399	366
84	604	592	579	565	552	418	385
72	807	796	785	773	762	647	619
71	824	813	802	791	779	666	638
70	840	830	819	808	797	685	658
69	857	847	836	825	814	705	677
68	874	864	853	843	832	724	697
67	891	881	870	860	849	743	716
66	907	898	888	877	867	762	736
56	1076	1068	1059	1050	1041	952	930

two values for several schemes, is shown in tables A.5 on the following page (high fluence) and A.4 on the next page (low fluence).

Each value in Tables A.5 and A.4 is averaged over 4 measurements with different voltage on the "reflect" electrode. High-fluence measurements were performed with voltages: 86, 95, 127 and 131 Volts, while low-fluence measurements with 86, 190, 195 and 202 Volts.

Table A.4: Average difference between calculated and measured time-of-flight difference between metastable and uracil peak [ns] (Low Fluence). Experimental conditions as Table A.2.

Unfocused	Intermediate Ion						
Product Ion	Direct dissociation	*111* *(H loss)*	*110* *(2H loss)*	*109* *(3H loss)*	*108* *(4h loss)*	*99* *(CH loss)*	*97* *(NH loss)*
85	1518	1453	1388	1322	1257	673	545
84	1423	1357	1291	1226	1160	572	442
72	277	207	136	65	-6	-644	-786
71	182	111	37	-32	-103	-746	-889
70	86	14	-57	-129	-200	-847	-480
69	-10	-82	-154	-226	-298	-949	-1094
68	-94	-178	-250	-323	-395	-1051	-1196
67	-201	-274	-347	-420	-493	-1152	-1299
66	-297	-370	-443	-517	-590	-1253	-1401
56	-621	-1335	-1412	-1489	-1567	-2272	-2429

The tendency from tables A.2 and A.3 two is reversed in tables A.5 and A.4 – with decreasing mass of intermediate ions, heavier product ions are favoured. Cells colour-coded green, in tables A.5 and A.4, correspond to < 24 ns difference, which is a typical width of a well-resolved peak, while yellow code correspond to a < 48 ns difference.

Table A.5: Average difference between calculated and measured time-of-flight difference between metastable and uracil peak [ns] (High Fluence). Experimental conditions as A.3 on the previous page.

Focused	Intermediate Ion						
Product Ion	Direct dissociation	*111* *(H loss)*	*110* *(2H loss)*	*109* *(3H loss)*	*108* *(4h loss)*	*99* *(CH loss)*	*97* *(NH loss)*
85	1498	1432	1367	1302	1236	650	521
84	1405	1339	1274	1208	1142	552	421
72	250	225	154	83	13	-627	-770
71	204	132	61	-10	-82	-726	-869
70	111	39	-33	-104	-176	-824	-969
69	18	-54	-126	-198	-270	-922	-1068
68	-74	-147	-219	-292	-365	-1021	-1167
67	-167	-240	-313	-386	-459	-1119	-1266
66	-260	-333	-406	-480	-553	-1217	-1366
56	-1186	-1263	-963	-1418	-1496	-2202	-2360

Uracil clusters

Tables A.6 and A.7 show the summary of the ions observed in uracil and adenine in current work, and in selected literature. Gaussian fitting of a large data set of electron impact ionization mass spectra of gas-phase adenine (0−200 eV with relatively low mass resolution) revealed evidence for weak fragment ion production at m/z = 65 (labelled with a start in the tables) and assigned it to $C_3HN_2^+$ [207]

Table A.6: Ions observed by MPI of uracil (U) and adenine (A) in clustering conditions, compared with MPI and photo-ionization of gas phase uracil and adenine and photo-dissociation of protonated adenine (266 nm). The assignments expected to dominate are given for each m/z value. For the present data, the counts per pulse of particularly interesting ions are given in brackets.

m/z	Uracil 220 nm MPI (Chapter 5)	Uracil photo-ionization Jochims et al. [43]	Adenine 220 nm MPI (Chapter 4)	Adenine photo-ionization Jochims et al. [43]	AH+ photo-dissociation Cheong et al. [44]	Uracil 220 nm MPI (clustering conditions)	Uracil-adenine 220 nm MPI (clustering conditions)
271	-	-	-	-	-	-	A_2H^+ (0.0046±0.0009)
270	-	-	-	-	-	-	A_2^+ (0.020±0.003)
248	-	-	-	-	-	-	UAH^+ (0.0064±0.002)
247	-	-	-	-	-	-	UA^+ (0.012±0.002)
225	-	-	-	-	-	U_2H^+ (0.0059±0.0012)	U_2H^+ (0.0043±0.0009)
224	-	-	-	-	-	U_2^+ (0.0010±0.0006)	U_2^+ (0.0015±0.0007)
136	-	-	A^+ with ^{13}C	-	-	-	AH^+ (0.80±0.02)
135	-	-	Adenine$^+$	A^+	-	-	A^+ (2.72±0.03)
134	-	-	$C_5H_4N_5^+$	$C_5H_4N_5^+$	-	-	-
120	-	-	$C_5H_4N_4^+$	$C_5H_4N_4^+$	-	-	-
119	-	-	$C_5H_3N_4^+$	$C_5H_3N_4^+$	$C_5H_3N_4^+$	-	$C_5H_3N_4^+$
113	U^+ with ^{13}C	-	-	-	-	UH^+ (0.040±0.003)	UH^+ (0.030±0.003)
112	Uracil$^+$	U^+	-	-	-	U^+ (0.032±0.003)	U^+ (0.034±0.003)
109	-	-	-	-	$C_4H_5N_4^+$	-	$C_4H_5N_4^+$
108	-	-	$C_4H_4N_4^+$	$C_4H_4N_4^+$	-	-	$C_4H_4N_4^+$
107	-	-	$C_4H_3N_4^+$	$C_4H_3N_4^+$	-	-	-
96	-	Unassigned	-	-	-	-	-
94	-	-	-	-	$C_4H_4N_3^+$	-	$C_4H_4N_3^+$
92	-	-	-	$C_4H_2N_3^+$	-	-	$C_4H_2N_3^+$ (broad feature)
84	$C_3H_4N_2O^+$	-	-	-	-	$C_3H_4N_2O^+$ (0.011±0.002)	$C_3H_4N_2O^+$ (0.021±0.003)
82	-	-	-	-	$C_3H_4N_3^+$	-	$C_3H_4N_3^+$
81	-	-	$C_3H_3N_3^+$	$C_3H_3N_3^+$	-	-	$C_3H_3N_3^+$
80	-	-	-	$C_3H_2N_3^+$	-	-	-
70	-	$C_3H_4NO^+$	$C_2H_4N_3^+$	$C_2H_4N_3^+$	-	-	$C_2H_4N_3^+$
69	$C_3H_3NO^+$	$C_3H_3NO^+$	-	-	-	$C_3H_3NO^+$	$C_3H_3NO^+$
68	$C_3H_2NO^+$	$C_3H_2NO^+$	Unassigned	-	-	$C_3H_2NO^+$	$C_3H_2NO^+$
67	-	-	-	$C_3H_3N_2^+$	$C_3H_3N_2^+$	-	$C_3H_3N_2^+$
66	-	-	$C_3H_2N_2^+$	$C_3H_2N_2^+$	-	-	$C_3H_2N_2^+$

Table A.7: Ions observed by MPI of uracil (U) and adenine (A) in clustering conditions, compared with MPI and photo-ionization of gas phase uracil and adenine and photo-dissociation of protonated adenine (266 nm). The assignments expected to dominate are given for each m/z value. For the present data, the counts per pulse of particularly interesting ions are given in brackets (continued).

m/z	Uracil 220 nm MPI (Chapter 5)	Uracil photo-ionization Jochims et al. [43]	Adenine 220 nm MPI (Chapter 4)	Adenine photo-ionization Jochims et al. [43]	AH+ photo-dissociation Cheong et al. [44]	Uracil 220 nm MPI (clustering conditions)	Uracil-adenine 220 nm MPI (clustering conditions)
65*	-	-	-	-	-	-	$C_3HN_2^+$
56	-	Unassigned	-	-	-	-	Unassigned
55	-	-	-	-	$C_2H_3N_2^+$	-	$C_2H_3N_2^+$
54	-	-	$C_2H_2N_2^+$	$C_2H_2N_2^+$	-	-	$C_2H_2N_2^+$
53	-	Unassigned	$C_2HN_2^+$	$C_2HN_2^+$	-	-	$C_2HN_2^+$
52	-	Unassigned	-	-	-	-	Unassigned
44	CH_2NO^+	CH_2NO^+	-	-	-	CH_2NO^+	CH_2NO^+
43	$CHNO^+$	$CHNO^+$	$CH_3N_2^+$	$CH_3N_2^+$	-	-	$CH_3N_2^+$
42	$C_2H_2O^+$	$C_2H_2O^+$	-	$CH_3N_2^+$	-	$C_2H_2O^+$	$C_2H_2O^+$
41	$C_2H_3N^+$	$C_2H_3N^+$	-	CHN_2^+	-	$C_2H_3N^+$	$C_2H_3N^+$
40	$C_2H_2N^+$	C_2H2N^+	-	CN_2^+	-	$C_2H_2N^+$	CN_2^+
39	C_2HN^+	C_2HN^+	-	C_2HN^+	-	C_2HN^+	C_2HN^+
38	C_2N^+	-	-	-	-	C_2N^+	$C2N^+$
36	-	-	-	-	-	Unassigned	Unassigned
29	CH_3N^+	CH_3N^+	CH_3N^+	CH_3N^+	-	CH_3N^+	CH_3N^+
28	CH_2N^+	CH_2N^+	CH_2N^+	CH_2N^+	CH_2N^+	CH_2N^+	CH_2N^+
27	CHN^+	CHN^+	-	CHN^+	-	CHN^+	CHN^+
26	$C_2H_2^+$	$C_2H_2^+$	-	-	-	$C_2H_2^+$	$C_2H_2^+$
25	$C2H^+$	-	-	-	-	C_2H^+	C_2H^+
24	C_2^+	-	-	-	-	C_2^+	C_2^+
18	-	H_2O+	-	-	NH_4^+	-	NH_4^+
17	-	NH_3^+	-	-	-	-	NH_3^+
15	CH_3^+	-	-	-	-	CH_3^+	CH_3^+
14	N^+ / CH_2^+	N^+	-	-	-	N^+ / CH_2^+	N^+ / CH_2^+
13	CH^+	-	-	-	-	-	CH^+
12	C^+	-	-	-	-	C^+	C^+
1	H^+	-	-	-	-	-	-

Appendix B

Control Software

Software for controlling the two OU experiments has been designed and implemented. The front panel is shown in B.1. Written in LabView dataflow visual programming language, the newest version (v.34) of the software allows for controlling the following devices:

- Mass spectrometer Start, stop and pause measurements.
  - Load and save spectra.
  - Perform automatic Gaussian fitting to a peak.
  - Set range, binwidth and sweep preset.
  - Display properties of current spectrum (runtime, no. of sweeps, no. and rate of count in the current view).
  - Automatically consecutively name spectra and save them to disk.
  - Automatically create a single CSV files with all spectra along with their names.
  - Automatically calibrate spectra based on the voltages on the mass spectrometer.

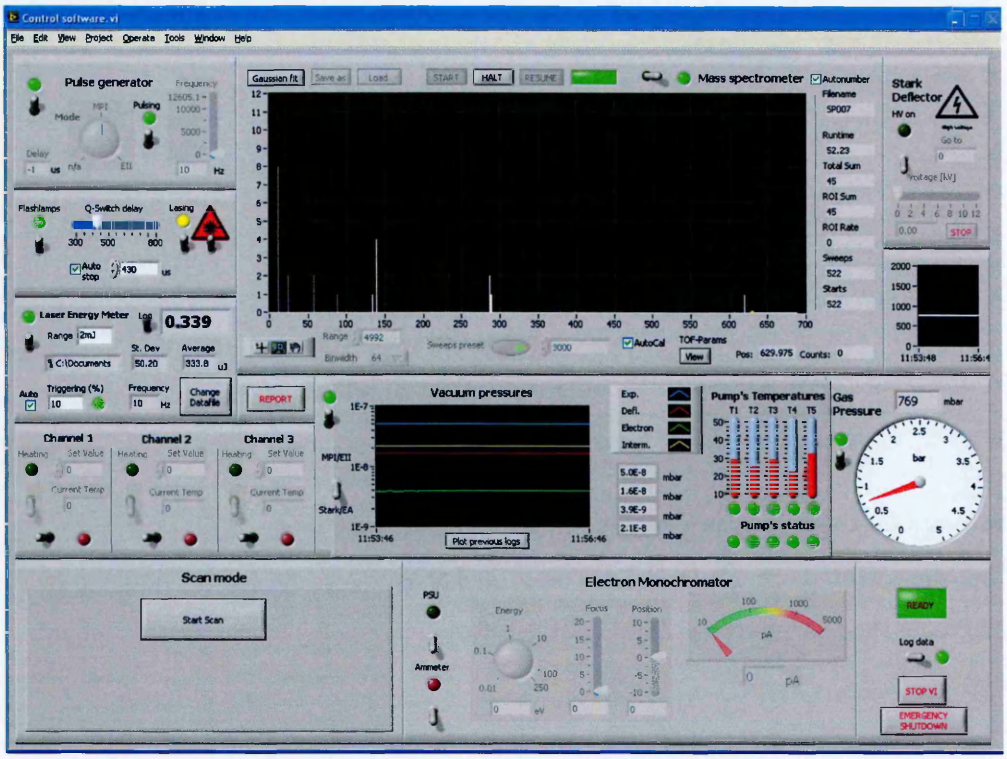

Figure B.1: Front panel of the Control Software (v.34)

- Pulse generator
  - Start and stop pulsing.
  - Automatically set pulse generator's settings for MPI or EII experiments.
  - Set pulsing frequency
  - In MPI mode:
    * Turn flashlamps on/off Turn Laser output on/off. Two switch system implemented as a safety measure against accidentally turning beam output. User has to switch ARM switch, and then LASING switch within 3 seconds.
    * Set Flashlamps - Q-Switch delay, and hence control pulse energy.
    * Set Laser pulse - ion extraction delay

- Stark-Deflector
  - Turn high voltage output of the Glassman High Voltage PSU on/off
  - Slowly raise or lower Stark-deflector's voltage. The change rate is below 1kV/min to avoid discharges.
- Laser energy meter
  - Measure laser pulse energy and pulsing frequency.
  - Save energies to a CSV file.
  - Automatically calculate average pulse energy and standard deviation of the dataset in real time.
- Vacuum gauges
  - Read, save and plot vacuum pressures. Six channels can be processed simultaneously, grouped into two section, for each of the experiments.
  - Plot old pressure log files.
  - Warning message is played if pressures in MPI's diagnostic and Stark/EA's electron chamber rises above safe level.
- Turbomolecular pumps
  - Read, save and show temperature of five turbomolecular pumps.
  - A warning message is played if any of pump's temperature is too low or too high.
  - In case of critical temperature, the experiment can be safely shut down via the Vacuum Security System. Any warning messages reported by the pumps are displayed and logged.
  - Status of each of the pumps (off, no rotation, active, acceleration / deceleration) is displayed

- Gas line
  - Gas line pressure is displayed and logged
- Temperature controllers
  - Three Czaki temperature controllers' values can be read and saved.
  - Option to turn on controller's relay on/off and set desired temperature on the controller.
- Nano-ammeter
  - Read and display current measured by the nano-ammeter.

Further to these features, the control software cross-correlates the devices. The list of features that takes advantage of simultaneous control of two or more devices is given below:

- Option to automatically stop laser output when spectrum acquisition has finished.
- Option to automatically save laser pulse energies to a filename matching current spectrum's filename.
- Control checks on the pressure are performed when used attempt to turn on high voltage on the stark- deflector. In case of a rise of pressure in the Stark chamber, voltage on the Stark deflector is automatically lowered to avoid discharges.
- Automatically limit the pulsing frequency based on the current range and binwidth setting to avoid sweep overlap.

The software allows for running semi-automatic scans. Scan parameters, such as initial and final voltage o the deflector, initial and final position of the movable skimmer, etc. and their respective steps, can be set. The approximate time required to run a scan is determined and displayed. The software records spectra automatically and changes the parameter whenever it is possible. If a parameter cannot be set automatically (e.g.

the movable skimmer's position has to be adjusted manually), an appropriate message is displayed.

The software has an extensive system of log generation. Parameters are automatically saved for each spectrum (such as experiment used, MPI/EII, carried gas, energy/wavelength, target, spectrometers voltages etc.). Also, events such as pump warning, change of Stark-Deflectors voltage etc. are logged. In addition, the user has an option to manually add a message which is saved along the timestamp in the report file. Vacuum and gas line pressures are automatically logged in CSV files with a filename matching the date. Files are automatically changed at midnight UTC time.

Most events have associated voice messages. For example, a message "Acquisition completed" is played when a spectrum acquisition has completed. The voice messages are extremely valuable in situations that otherwise might not be noticed by the user, e.g. when the pressure in electron chamber rises above safe limit for operating the electron gun.

Appendix C

Proof of publication

THE JOURNAL OF CHEMICAL PHYSICS 139, 244311 (2013)

Multi-photon ionization and fragmentation of uracil: Neutral excited-state ring opening and hydration effects

B. Barc, M. Ryszka, J. Spurrell, M. Dampc, P. Limão-Vieira,[a] R. Parajuli,[b] N. J. Mason, and S. Eden[c]
Department of Physical Sciences, The Open University, Walton Hall, Milton Keynes MK7 6AA, United Kingdom

(Received 4 November 2013; accepted 4 December 2013; published online 31 December 2013)

Multi-photon ionization (MPI) of the RNA base uracil has been studied in the wavelength range 220–270 nm, coinciding with excitation to the $S_2(\pi\pi^*)$ state. A fragment ion at m/z = 84 was produced by 2-photon absorption at wavelengths ≤232 nm and assigned to $C_3H_4N_2O^+$ following CO abstraction. This ion has not been observed in alternative dissociative ionization processes (notably electron impact) and its threshold is close to recent calculations of the minimum activation energy for a ring opening conical intersection to a $\sigma(n\text{-}\pi)\pi^*$ closed shell state. Moreover, the predicted ring opening transition leaves a CO group at one end of the isomer, apparently vulnerable to abstraction. An MPI mass spectrum of uracil-water clusters is presented for the first time and compared with an equivalent dry measurement. Hydration enhances certain fragment ion pathways (particularly $C_3H_3NO^+$) but represses $C_3H_4N_2O^+$ production. This indicates that hydrogen bonding to water stabilizes uracil with respect to neutral excited-state ring opening. © *2013 AIP Publishing LLC*. [http://dx.doi.org/10.1063/1.4851476]

I. INTRODUCTION

The electronic excitation and ionization dynamics of nucleobases have attracted interest for many years with the central aim of understanding the pathways that can initiate reactivity and the formation of DNA and RNA lesions.[1] Isolated molecules are the natural starting point to probe the photophysics, while parallel studies on pure and mixed clusters enable closer analogies to be drawn with biological environments where different isomeric forms, intermolecular energy transfer processes and reactivity can be significant.

The present experiments probe the pyrimidine derivative base uracil ($C_4H_4N_2O_2$), which forms two hydrogen bonds with adenine in RNA. Its close structural similarity with the DNA base thymine adds to the interest in this molecule, particularly with respect to differences in the photophysical properties of the two bases and their possible radiobiological consequences.[2] A series of ultrafast spectroscopy and computational chemistry studies (e.g., Refs. 3–5) have significantly advanced our understanding of the radiationless decay pathways from the bright $\pi\pi^*$ state of uracil in isolation as well as within certain hydrated complexes and base-pairs. In particular, theoretical calculations have identified ring opening[6] and tautomeric transitions[2] in electronic excited states. This provides the impetus for our experiments as well as the essential context for the proposed interpretations. Due to the possibility of neutral excited state transitions in the stepwise excitation process, MPI can activate channels that are closed in single-photon absorption or collision induced ionization experiments where ionic states are directly accessed from the electronic ground state.[7] Accordingly, the first aim of the present work was to study fragment ion production by MPI as a tool to observe evidence for excited state transitions. These were recognizable via major differences between MPI and electron impact ionization (EII) mass spectra and distinct wavelength thresholds for the production of specific fragment ions. Although time resolved analysis was not possible, the present MPI scheme using single-color nanosecond-timescale laser pulses enabled the initial excitation to be carried out in a much wider wavelength range (220–270 nm) than any previous study. Furthermore, we performed the first experimental comparison of uracil MPI in dry and hydrated clustering conditions in order to advance our understanding of how the local water environment can modify the molecule's response to UV excitation and ionization. This question has attracted considerable interest with respect to the specific excitation and relaxation dynamics[8–10] but no previous research has directly addressed hydration effects on the fragmentation pathways of the excited molecule or ion.

II. EXPERIMENTAL

The experimental system developed for these studies is described here for the first time. As shown in Fig. 1, argon seeded with vaporized uracil and/or water flowed through a CW nozzle into a pumped chamber to form a supersonic jet. The jet passed through a skimmer and crossed a pulsed UV laser beam for MPI measurements or an electron beam from a commercial gun (*Kimball ELG-2*) for EII experiments. The resulting ions were detected using a *reflectron* time-of-flight (TOF) mass spectrometer.

[a]Permanent address: Laboratório de Colisões Atómicas e Moleculares, CEFITEC, Departamento de Física, Faculdade de Ciências e Tecnologia, Universidade Nova de Lisboa, 2829-516 Caparica, Portugal.
[b]Permanent address: Department of Physics, Amrit Campus, Tribhuvan University, Kathmandu, Nepal.
[c]Author to whom correspondence should be addressed. Electronic mail: s.p.eden@open.ac.uk

International Journal of Mass Spectrometry 365–366 (2014) 194–199

Contents lists available at ScienceDirect

International Journal of Mass Spectrometry

journal homepage: www.elsevier.com/locate/ijms

Multi-photon and electron impact ionisation studies of reactivity in adenine–water clusters

B. Barc[a], M. Ryszka[a], J.-C. Poully[b], E. Jabbour Al Maalouf[a,c], Z. el Otell[a,c], J. Tabet[c], R. Parajuli[d], P.J.M. van der Burgt[e], P. Limão-Vieira[f], P. Cahillane[a], M. Dampc[a], N.J. Mason[a], S. Eden[a,*]

[a] Department of Physical Sciences, The Open University, Walton Hall, Milton Keynes MK7 6AA, United Kingdom
[b] CIMAP/GANIL, Boulevard Henri Becquerel, BP 5133, 14070 Caen Cedex 5, France
[c] Department of Physics, Faculty of Sciences II, Lebanese University, Fanar-Matn, Lebanon
[d] Department of Physics, Amrit Campus, Tribhuvan University, Kathmandu, Nepal
[e] Department of Experimental Physics, National University of Ireland Maynooth, Maynooth, Co. Kildare, Ireland
[f] Laboratório de Colisões Atómicas e Moleculares, CEFITEC, Departamento de Física, Faculdade de Ciências e Tecnologia – Universidade Nova de Lisboa, P-2829-516 Caparica, Portugal

ARTICLE INFO

Article history:
Received 15 November 2013
Received in revised form 14 January 2014
Accepted 15 January 2014
Available online 31 January 2014

Keywords:
Adenine
Cluster
Dissociative ionisation
Hypoxanthine
Multi-photon ionisation
Electron impact ionisation

ABSTRACT

Multi-photon ionisation (MPI) and electron impact ionisation (EII) mass spectrometry experiments have been carried out to probe unimolecular and intermolecular reactivities in hydrated adenine clusters. The effects of clustering with water on fragment ion production from adenine have been studied for the first time. While the observation of NH_4^+ fragments indicated the dissociation of protonated adenine, the dominant hydration effects were enhanced $C_4H_4N_4^+$ production and the suppression of dissociative ionisation pathways with high activation energies. These observations can be attributed to energy removal from the excited adenine radical cation via cluster dissociation. Comparisons of MPI and EII measurements provided the first experimental evidence supporting hypoxanthine formation in adenine–water clusters via theoretically predicted barrierless deamination reactions in closed shell complexes.

1. Introduction

Radiation induced processes in DNA bases have been investigated intensively in recent years in order to better understand the fundamental process that can initiate DNA lesions [1]. Further interest relates to the mechanisms underpinning the remarkable photo-stability of DNA bases and their possible evolutionary implications. While studies of isolated molecules generally provide the clearest data interpretations, equivalent experiments on hydrogen-bonded complexes enable closer analogies to be drawn with biological environments where different isomeric forms, intermolecular energy transfer processes, and reactivity can be significant. The relaxation pathways of both isolated and hydrated adenine ($C_5H_5N_5$) following excitation to the lowest lying bright $\pi\pi^*$ state have been mapped out in considerable detail using ultrafast pump-probe experiments [2–4] and quantum chemical calculations [5–7]. Sub-ps-timescale internal conversion to the vibrationally hot electronic ground state via intermediary $n\pi^*$ and $\sigma\pi^*$ states is found to dominate, although evidence for much weaker intersystem crossing pathways to long-lived triplet states has also been reported [8]. Previous studies of reactivity in hydrated adenine have focused on tautomeric transitions [9,10] and proton transfer in adenine dimer ions [11]. However, no experiments have directly explored the effects of hydration on the dissociative ionisation pathways of adenine. The present work applies UV multi-photon ionisation (MPI) mass spectrometry to analyse fragment ion production from adenine–water clusters. Furthermore, we have carried out the most detailed analysis to date of MPI and electron impact ionisation (EII) production of hydrated adenine monomer ions and hydrated reaction products (notably hydrated protonated adenine) from larger dissociated clusters. The key interest in directly comparing MPI and EII of mixed clusters stems from the selective nature of MPI, notably with water molecule photo-excitation being inaccessible in the present laser conditions.

One possible reaction product of adenine and water that would not be readily identifiable in the mass spectra of hydrated adenine

* Corresponding author. Tel.: +44 (0)1908858255.
E-mail address: s.p.eden@open.ac.uk (S. Eden).

1387-3806/$ – see front matter © 2014 Elsevier B.V. All rights reserved.
http://dx.doi.org/10.1016/j.ijms.2014.01.007

G Model
MASPEC 155461-7

ARTICLE IN PRESS

International Journal of Mass Spectrometry xxx (2015) xxx–xxx

Contents lists available at ScienceDirect

International Journal of Mass Spectrometry

journal homepage: www.elsevier.com/locate/ijms

Dissociative multi-photon ionization of isolated uracil and uracil-adenine complexes

M. Ryszka[a], R. Pandey[a], C. Rizk[a,b], J. Tabet[b], B. Barc[a], M. Dampc[a,c], N.J. Mason[a], S. Eden[a,*]

[a] Dept. of Physical Sciences, The Open University, Walton Hall, Milton Keynes MK7 6AA, United Kingdom
[b] Dept. of Physics, Faculty of Sciences II, Lebanese University, Fanar, Matn, Lebanon
[c] Dept. of Physics of Electronic Phenomena, Gdańsk University of Technology, 80-952 Gdańsk, Poland

ARTICLE INFO

Article history:
Received 20 October 2015
Received in revised form
21 December 2015
Accepted 28 December 2015
Available online xxx

Keywords:
Uracil
Adenine-uracil clusters
Fragmentation
Multi-photon ionization
Electron impact ionization
Mass spectrometry

ABSTRACT

Recent multi-photon ionization (MPI) experiments on uracil revealed a fragment ion at m/z 84 that was proposed as a potential marker for ring opening in the electronically excited neutral molecule. The present MPI measurements on deuterated uracil identify the fragment as $C_3H_4N_2O^+$ (uracil$^+$ less CO), a plausible dissociative ionization product from the theoretically predicted open-ring isomer. Equivalent measurements on thymine do not reveal an analogous CO loss channel, suggesting greater stability of the excited DNA base. MPI and electron impact ionization experiments have been carried out on uracil-adenine clusters in order to better understand the radiation response of uracil within RNA. Evidence for $C_3H_4N_2O^+$ production from multi-photon-ionized uracil-adenine clusters is tentatively attributed to a significant population of π-stacked configurations in the neutral beam.

1. Introduction

The dynamics and stabilities of nucleobases following excitation to their bright $S_2(\pi\pi^*)$ states have been researched intensively in recent years [1]. Time resolved pump-probe experiments [2] and calculations [3] on isolated molecules have yielded rich insights into their excited state dynamics, while studies of base pairs and hydrated clusters have enabled closer analogies to be drawn with cellular environments [4]. Internal conversion to the vibrationally hot electronic ground state (either directly or via S_1 states of mainly $n\pi^*$ and $\sigma\pi^*$ character) dominates $S_2(\pi\pi^*)$ deactivation [5,6], although intersystem crossing to long-lived triplet states has also been identified [7,8]. The present work investigates dissociative multi-photon ionization (MPI) of uracil ($C_4H_4N_2O_2$) as a tool to gain additional understanding of its relaxation pathways from $S_2(\pi\pi^*)$ and from excited ionic states. Uracil forms two hydrogen bonds with adenine in RNA and is geometrically similar to the DNA base thymine ($C_5H_6N_2O_2$; uracil methylated at the C5 site of the pyrimidine ring system).

Structural modifications and bond breaking in electronically excited or ionized DNA and RNA bases are of particular interest as they represent potential radiation damage pathways in the respective macromolecules. Nachtigallová et al. [9] theoretically identified ring-opening at the $S_2(\pi\pi^*)$-$S_1(\sigma(n\text{-}\pi)\pi^*)$ crossing seam. More recently, Richter et al. [10] carried out dynamical calculations with non-adiabatic and spin–orbit couplings that supported this pathway. The ring-opening process was predicted to lead to new photochemical products [9]. Barc et al. [11] observed a new fragment ion at m/z 84 (uracil$^+$ minus CO or CNH_2) by single-color 2-photon ionization of uracil. The threshold photon energy (5.29 ± 0.06 eV) for this product agreed with the calculated energy (5.25 eV at CASSCF level) of the ring-opening crossing seam [9] and the geometry of the predicted isomer indicates likely CO abstraction. Therefore MPI production of this fragment ion was proposed as a potential experimental marker for ring opening in neutral excited uracil, suggesting possibilities for diverse measurements exploring the process in depth (e.g. using coincidence and/or time-resolved methods). The first aim of the present work was to test if the new fragment ion is indeed due to CO loss by studying MPI of deuterated uracil (dominantly $C_4D_4N_2O_2$). These results have the added value of identifying several previously debated fragments from the radical cation, while further evidence to assign specific

* Corresponding author. Tel.: +44 01908858255.
E-mail address: s.p.eden@open.ac.uk (S. Eden).

http://dx.doi.org/10.1016/j.ijms.2015.12.006
1387-3806/

Please cite this article in press as: M. Ryszka, et al., Int. J. Mass Spectrom. (2015), http://dx.doi.org/10.1016/j.ijms.2015.12.006

Bibliography

[1] Vossman. Pre-mrna-1ysv-tubes. ix, 10

[2] B. Barć. *Hydrated clusters of nucleic acid bases in supersonic beams probed by multi-photon ionization (MPI) mass spectrometry.* PhD thesis, The Open University, Department of Physical Sciences, Milton Keynes, United Kingdom, 2012. ix, xii, 4, 10, 22, 23, 49, 50, 51, 52, 84, 89, 90, 93, 97, 104, 121, 156, 157

[3] D. Nachtigallová, A. J. A. Aquino, J. J. Szymczak, et al. Nonadiabatic dynamics of uracil: Population split among different decay mechanisms. *J. Phys. Chem. A*, **115**(21), pp. 5247–5255, 2011. ix, xii, xiii, 3, 14, 102, 103, 104, 106, 110, 112, 122, 123, 126, 129, 130, 134, 143, 148, 149, 163, 165, 167, 172

[4] C. R. Martinez and B. L. Iverson. Rethinking the term "π-stacking". *Chem. Sci.*, **3**, pp. 2191–2201, 2012. ix, 17, 18

[5] K. Modig, B. G. Pfrommer, and B. Halle. Temperature-dependent hydrogen-bond geometry in liquid water. *Phys. Rev. Lett.*, **90**, pp. 075502, 2003. ix, 19

[6] C. Weickhardt, F. Moritz, and J. Grotemeyer. Multiphoton ionization mass spectrometry: principles and fields of application. *Eur. J. Mass Spectrom.*, **2**, pp. 151–160, 1996. ix, 20

[7] C. Woywod, W. Domcke, A. L. Sobolewski, and J. Werner, Hans. Characterization of the $S_1 - -S_2$ conical intersection in pyrazine using *ab initio* multiconfiguration self-consistent-field and multireference configuration-interaction methods. *J. Chem. Phys.*, **100**(2), pp. 1400–1413, 1994. ix, 25

[8] L. Piela. *Ideas of Quantum Chemistry.* Elsevier, Amsterdam, 1st edition, 2007. ix, 14, 15, 25, 26

[9] P. Możejko and L. Sanche. Cross section calculations for electron scattering from DNA and RNA bases. *Radiat. Environ. Biophys.*, **42**(3), pp. 201–211, 2003. ix, 31, 90

[10] J. Rost, J. Griffin, B. Friedrich, and D. Herschbach. Pendular states and spectra of oriented linear molecules. *Phys. Rev. Lett.*, **68**(9), pp. 1299, 1992. x, 34, 35

[11] K. Wohlfart, M. Schnell, J.-U. Grabow, and J. Küpper. Precise dipole moment and quadrupole coupling constants of benzonitrile. *J. Mol. Spectrosc.*, **247**(1), pp. 119–121, 2008. x, 36, 68

[12] J. Küpper. Manipulating the motion of neutral molecules. Habilitationsschrift, Department of Physics at the Free University Berlin, 2009. x, 36, 37

[13] J. B. Anderson, R. P. Andres, and J. B. Fenn. *Molecular Beams*, volume 10 of *Advances in Chemical Physics*, chapter 8: Supersonic Nozzle Beams, pages 275–317. John Wiley & Sons, Inc., 2007. x, 39, 41

[14] J. P. Toennies and K. Winkelmann. Theoretical studies of highly expanded free jets: Influence of quantum effects and a realistic intermolecular potential. *J. Chem. Phys.*, **66**(9), pp. 3965–3979, 1977. x, 42, 43

[15] M. Hillenkamp, S. Keinan, and U. Even. Condensation limited cooling in supersonic expansions. *J. Chem. Phys.*, **118**(19), pp. 8699–8705, 2003. x, 39, 45, 46, 47

[16] F. Filsinger, G. Meijer, H. Stapelfeldt, H. N. Chapman, and J. Küpper. State- and conformer-selected beams of aligned and oriented molecules for ultrafast diffraction studies. *Phys. Chem. Chem. Phys.*, **13**, pp. 2076–2087, 2011. xi, 4, 63, 64, 67

[17] C. Fonseca Guerra, F. M. Bickelhaupt, S. Saha, and F. Wang. Adenine tautomers: Relative stabilities, ionization energies, and mismatch with cytosine. *J. Phys. Chem. A*, **110**(11), pp. 4012–4020, 2006. xii, 84, 85

[18] M. Fernández-Quejo, M. de la Fuente, and R. Navarro. Theoretical calculations and vibrational study of hypoxanthine in aqueous solution. *J. Mol. Struct.*, pages 749–757, 2005. xii, 84, 97

[19] M.-E. Costas and R. Acevedo-Chávez. Density functional theory study of hypoxanthine tautomerism in both the isolated state and a modeled-ideal aqueous solution at several heterocyclic protonation levels. *J. Solution Chem.*, **41**(5), pp. 864–878, 2012. xii, 84

[20] V. Periquet, A. Moreau, S. Carles, J. Schermann, and C. Desfrançois. Cluster size effects upon anion solvation of n-heterocyclic molecules and nucleic acid bases. *J. Electron. Spectrosc. Relat. Phenom.*, **106**(2-3), pp. 141–151, 2000. xii, 85, 99

[21] K. B. Bravaya, O. Kostko, M. Ahmed, and A. I. Krylov. The effect of π-stacking, h-bonding, and electrostatic interactions on the ionization energies of nucleic acid bases: adenine-adenine, thymine-thymine and adenine-thymine dimers. *Phys. Chem. Chem. Phys.*, **12**, pp. 2292–2307, 2010. xii, 85, 156

[22] A. Zhang, B. Yang, and Z. Li. Theoretical study on the hydrolytic deamination reaction mechanism of adenine $(H_2O)_n$ (n = 1–4). *Journal of Molecular Structure: THEOCHEM*, **819**, pp. 95–101, 2007. xii, 86, 97

[23] H. Zheng and F. Meng. Theoretical study of water-assisted hydrolytic deamination mechanism of adenine. *Struct. Chem.*, **20**(5), pp. 943–949, 2009. xii, 86

[24] D. Cvejanovic, L. Andric, and R. I. Hall. Excitation of high vibrational levels of H_2O and D_2O by electron impact. *J. Phys. B: At., Mol. Opt. Phys.*, **26**(17), pp. 2899, 1993. xii, 92, 96, 159

[25] J. Rejnek, M. Hanus, M. Kabeláč, F. Ryjáček, and P. Hobza. Correlated *ab initio* study of nucleic acid bases and their tautomers in the gas phase, in a microhydrated environment and in aqueous solution. Part 4. uracil and thymine. *Phys. Chem. Chem. Phys.*, **7**, pp. 2006–2017, 2005. xiii, 122

[26] P. Colarusso, K. Zhang, B. Guo, and P. F. Bernath. The infrared spectra of uracil, thymine, and adenine in the gas phase. *Chem. Phys. Lett.*, **269**(1-2), pp. 39–48, 1997. xiii, 87, 102, 104, 122, 145, 157

[27] J.-C. Fan, Z.-C. Shang, J. Liang, X.-H. Liu, and H. Jin. Systematic theoretical investigations on the tautomers of thymine in gas phase and solution. *Journal of Molecular Structure: THEOCHEM*, **939**(1-3), pp. 106–111, 2010. xiii, 122

[28] B. Li. Theoretical studies on tautomers of 5-fluorouracil and 5-chlorouracil. *ACTA CHIMICA SINICA*, **63**(16), pp. 1495, 2005. xiii, 122

[29] M. Barbatti, A. J. A. Aquino, and H. Lischka. The UV absorption of nucleobases: semi-classical *ab initio* spectra simulations. *Phys. Chem. Chem. Phys.*, **12**, pp. 4959–4967, 2010. xiii, 102, 130

[30] L. B. Clark, G. G. Peschel, and I. Tinoco. Vapor spectra and heats of vaporization of some purine and pyrimidine bases. *J. Phys. Chem.*, **69**(10), pp. 3615–3618, 1965. xiii, 130

[31] S. Ullrich, T. Schultz, M. Z. Zgierski, and A. Stolow. Electronic relaxation dynamics in DNA and RNA bases studied by time-resolved photoelectron spectroscopy. *Phys. Chem. Chem. Phys.*, **6**, pp. 2796–2801, 2004. xiii, 102, 103, 104, 121, 124, 130, 131, 132, 134, 143, 165

[32] H. Kang, K. T. Lee, B. Jung, Y. J. Ko, and S. K. Kim. Intrinsic lifetimes of the excited state of DNA and RNA bases. *J. Am. Chem. Soc.*, **124**(44), pp. 12958–12959, 2002. xiii, 103, 104, 124, 130, 131, 132, 134

[33] C. Canuel, M. Mons, F. Piuzzi, et al. Excited states dynamics of DNA and RNA bases: Characterization of a stepwise deactivation pathway in the gas phase. *J. Chem. Phys.*, 122(7):074316, 2005. xiii, 102, 103, 104, 124, 130, 131, 132, 134, 139

[34] M. Kotur, T. Weinacht, C. Zhou, and S. Matsika. Following ultrafast radiationless relaxation dynamics with strong field dissociative ionization: A comparison between adenine, uracil, and cytosine. *IEEE Journal of Selected Topics in Quantum Electronics*, **18**(1), pp. 187–194, 2012. xiii, 104, 130, 132, 133, 134

[35] S. Matsika, C. Zhou, M. Kotur, and T. C. Weinacht. Combining dissociative ionization pump-probe spectroscopy and *ab initio* calculations to interpret dynamics and control through conical intersections. *Faraday Discuss.*, **153**, pp. 247–260, 2011. xiii, xiv, 102, 104, 107, 108, 109, 110, 125, 130, 132, 133, 134, 139, 141, 142, 148

[36] M. Ligare, F. Siouri, O. Bludsky, D. Nachtigallova, and M. S. de Vries. Characterizing the dark state in thymine and uracil by double resonant spectroscopy and quantum computation. *Phys. Chem. Chem. Phys.*, **17**, pp. 24336–24341, 2015. xiii, 105, 132, 133, 139, 148

[37] M. Richter, S. Mai, P. Marquetand, and L. González. Ultrafast intersystem crossing dynamics in uracil unravelled by *ab initio* molecular dynamics. *Phys. Chem. Chem. Phys.*, **16**(44), pp. 24423–24436, 2014. xiii, xviii, 28, 103, 104, 130, 132, 133, 134, 143, 148, 165

[38] R. A. Livingstone, J. O. F. Thompson, M. Iljina, et al. Time-resolved photoelectron imaging of excited state relaxation dynamics in phenol, catechol, resorcinol, and hydroquinone. *J. Chem. Phys.*, 137(18):184304, 2012. xiii, 135

[39] N. Ding, X. Chen, C.-M. L. Wu, and H. Li. Adsorption of nucleobase pairs on hexagonal boron nitride sheet: hydrogen bonding versus stacking. *Phys. Chem. Chem. Phys.*, **15**, pp. 10767–10776, 2013. xiv, xviii, 152, 153, 154

[40] S. M. Bachrach and M. W. Dzierlenga. Microsolvation of uracil and its conjugate bases: A DFT study of the role of solvation on acidity. *J. Phys. Chem. A*, **115** (22), pp. 5674–5683, 2011. xiv, 153, 154

[41] N. U. Zhanpeisov and J. Leszczynski. The specific solvation effects on the structures and properties of adenine–uracil complexes: A theoretical *ab Initio* study. *J. Phys. Chem. A*, **102**(30), pp. 6167–6172, 1998. xiv, 155, 163, 165

[42] H. Nikjoo. Radiation track and DNA damage. *Iran J. Radiat. Res.*, **1**(1), pp. 3–16, 2003. xvii, 6

[43] H.-W. Jochims, M. Schwell, H. Baumgärtel, and S. Leach. Photoion mass spectrometry of adenine, thymine and uracil in the 6-22 eV photon energy range. *Chemical Physics*, **314**, pp. 263–282, 2005. xvii, 93, 94, 105, 106, 107, 108, 109, 118, 119, 124, 125, 139, 184, 185

[44] N. R. Cheong, S. H. Nam, H. S. Park, et al. Photofragmentation in selected tautomers of protonated adenine. *Phys. Chem. Chem. Phys.*, **13**, pp. 291–295, 2011. xvii, 93, 94, 95, 163, 165, 184, 185

[45] http://webbook.nist.gov for NIST Chemistry WebBook; accessed 2015. xvii, 68, 80, 88, 91, 94, 96, 107

[46] M. Imhoff, Z. Deng, and M. A. Huels. Ionizing fragmentation of uracil and 5-bromouracil by electron impact in gas phase and hyperthermal Ar+ ion irradiation in condensed phase. *Int. J. of Mass Spectrom.*, **262**, pp. 154–160, 2007. xvii, 107, 109, 124, 125

[47] J. M. Rice and G. O. Dudek. Mass spectra of nucleic acid derivatives. II. guanine, adenine, and related compounds. *J. Am. Chem. Soc.*, **89**(11), pp. 2719–2725, 1967. xvii, 3, 93, 109, 139

[48] S. V. Krasnoshchekov, N. Vogt, and N. F. Stepanov. *Ab Initio* anharmonic analysis of vibrational spectra of uracil using the numerical-analytic implementation of operator van vleck perturbation theory. *J. Phys. Chem. A*, **119**(25), pp. 6723–6737, 2015. xviii, 145, 146, 148

[49] C. T. Middleton, K. de La Harpe, C. Su, et al. DNA excited-state dynamics: From single bases to the double helix. *Annu. Rev. Phys. Chem.*, **60**(1), pp. 217–239, 2009. 1, 3

[50] Nano-scale insights in ion beam cancer therapy (nano-IBCT). COST action. 2010-2014. 1

[51] Advanced radiotherapy, generated by exploiting nanoprocesses and technologies (FP7 ITN ARGENT). COST action. 2014. 1

[52] Origins and evolution of life on earth and in the universe (ORIGINS), *http* : *//www.cost.eu/cost$_a$ctions/tdp/td*1308. 2014. 1

[53] I. Bald, J. Langer, P. Tegeder, and O. Ingólfsson. From isolated molecules through clusters and condensates to the building blocks of life. *Int. J. of Mass Spectrom.*, **277**(1-3), pp. 4–25, 2008. 2

[54] Z. Y. Li, N. P. Young, M. Di Vece, et al. Three-dimensional atomic-scale structure of size-selected gold nanoclusters. *Nature*, **451**(7174), pp. 46–48, 2008. 2

[55] N. Gonzalez Szwacki, A. Sadrzadeh, and B. I. Yakobson. B_{80} fullerene: An *Ab Initio* prediction of geometry, stability, and electronic structure. *Phys. Rev. Lett.*, **98**, pp. 166804, 2007. 2, 16

[56] J. Screen, E. Stanca-Kaposta, D. Gamblin, et al. IR-spectral signatures of aromatic–sugar complexes: Probing carbohydrate–protein interactions. *Angew. Chem. Int. Ed.*, **46**(20), pp. 3644–3648, 2007. 2

[57] M. Kjellberg, O. Johansson, F. Jonsson, et al. Momentum-map-imaging photoelectron spectroscopy of fullerenes with femtosecond laser pulses. *Phys. Rev. A*, **81**, pp. 023202, 2010. 2

[58] I. Martin, J. Langer, M. Stano, and E. Illenberger. Reactions in clusters of acetone and fluorinated acetones triggered by low energy electrons. *Int. J. of Mass Spectrom.*, **280**(1–3), pp. 107–112, 2009. 2

[59] A. Boatwright, J. Jeffs, and A. J. Stace. Ion-molecule reactions and fragmentation patterns in helium nanodroplets. *J. Phys. Chem. A*, **111**(31), pp. 7481–7488, 2007. 2, 28

[60] K. Kreidi, P. V. Demekhin, T. Jahnke, et al. Photo- and auger-electron recoil induced dynamics of interatomic coulombic decay. *Phys. Rev. Lett.*, **103**, pp. 033001, 2009. 2

[61] N. J. Kim, Y. S. Kim, G. Jeong, T. K. Ahn, and S. K. Kim. Hydration of DNA base cations in the gas phase. *Int. J. of Mass Spectrom.*, **219**(1), pp. 11–21, 2002. 2, 88, 89, 90, 98, 99

[62] B. Qiu, J. Liu, Z. Qin, G. Wang, and H. Luo. Quintets of uracil and thymine: a novel structure of nucleobase self-assembly studied by electrospray ionization mass spectrometry. *Chem. Commun.*, pages 2863–2865, 2009. 2

[63] I. K. Yanson, A. B. Teplitsky, and L. F. Sukhodub. Experimental studies of molecular interactions between nitrogen bases of nucleic acids. *Biopolymers*, **18** (5), pp. 1149–1170, 1979. 2

[64] K. Rajabi, K. Theel, E. A. L. Gillis, G. Beran, and T. D. Fridgen. The structure of the protonated adenine dimer by infrared multiple photon dissociation spectroscopy and electronic structure calculations. *J. Phys. Chem. A*, **113**(28), pp. 8099–8107, 2009. 2

[65] S. K. Kim, W. Lee, and D. R. Herschbach. Cluster beam chemistry: Hydration of nucleic acid bases; ionization potentials of hydrated adenine and thymine. *J. Phys. Chem.*, **100**(19), pp. 7933–7937, 1996. 2, 97, 98, 158, 159, 161

[66] L. Belau, K. R. Wilson, S. R. Leone, and M. Ahmed. Vacuum-ultraviolet photoionization studies of the microhydration of DNA bases (guanine, cytosine, adenine, and thymine). *J. Phys. Chem. A*, **111**(31), pp. 7562–7568, 2007. 2

[67] D. M. Close, C. E. Crespo-Hernández, L. Gorb, and J. Leszczynski. The influence of microhydration on the ionization energy thresholds of uracil and thymine. *J. Phys. Chem. A*, **109**(41), pp. 9279–9283, 2005. 2, 9, 154

[68] Z. Lan, L. M. Frutos, A. L. Sobolewski, and W. Domcke. Photochemistry of hydrogen-bonded aromatic pairs: Quantum dynamical calculations for the pyrrole–pyridine complex. *Proceedings of the National Academy of Sciences*, **105** (35), pp. 12707–12712, 2008. 2

[69] G. Grégoire, C. Dedonder-Lardeux, C. Jouvet, S. Martrenchard, and D. Solgadi. Has the excited state proton transfer ever been observed in phenol-$(NH_3)_n$ molecular clusters? *J. Phys. Chem. A*, **105**(25), pp. 5971–5976, 2001. 2

[70] R. I. Cukier. A theory that connects proton-coupled electron-transfer and hydrogen-atom transfer reactions. *J. Phys. Chem. B*, **106**(7), pp. 1746–1757, 2002. 2

[71] N. Gador, E. Samoylova, V. R. Smith, et al. Electronic structure of adenine and thymine base pairs studied by femtosecond electron-ion coincidence spectroscopy. *J. Phys. Chem. A*, **111**(46), pp. 11743–11749, 2007. 2, 89, 90, 156

[72] J. R. Gord, A. W. Garrett, R. E. Bandy, and T. S. Zwier. REMPI fragmentation as a probe of hydrogen bonding in aromatic-x clusters. *Chem. Phys. Lett.*, **171** (5), pp. 443–450, 1990. 2

[73] M. Mons, I. Dimicoli, and F. Piuzzi. Gas phase hydrogen-bonded complexes of aromatic molecules: Photoionization and energetics. *Int. Rev. Phys. Chem.*, **21** (1), pp. 101–135, 2002. 2

[74] P. Jena and A. W. Castleman. Clusters: A bridge across the disciplines of physics and chemistry. *Proceedings of the National Academy of Sciences*, **103**(28), pp. 10560–10569, 2006. 2

[75] S. A. Claridge, J. A. W. Castleman, S. N. Khanna, et al. Cluster-assembled materials. *ACS Nano*, **3**(2), pp. 244–255, 2009. 2

[76] A. P. Alivisatos. Birth of a nanoscience building block. *ACS Nano*, **2**(8), pp. 1514–1516, 2008. 2

[77] A. W. Castleman and S. Wei. Cluster reactions. *Annu. Rev. Phys. Chem.*, **45**(1), pp. 685–719, 1994. 2

[78] M. A. Śmiałek. Early models of DNA damage formation. *Journal of Physics: Conference Series*, **373**(1), pp. 012013, 2012. 3, 6

[79] M. Boniol, P. Autier, P. Boyle, and S. Gandini. Cutaneous melanoma attributable to sunbed use: systematic review and meta-analysis. *BMJ: British Medical Journal*, **345**, 2012. 3

[80] D. Alloni, A. Campa, M. Belli, et al. A Monte Carlo study of the radiation quality dependence of DNA fragmentation spectra. *Radiat. Res.*, **173**(3), pp. 263–271, 2010. 3

[81] J. M. Rice, G. O. Dudek, and M. Barber. Mass spectra of nucleic acid derivatives. pyrimidines. *J. Am. Chem. Soc.*, **87**(20), pp. 4569–4576, 1965. 3, 107, 118, 121

[82] T. Schlathölter, F. Alvarado, S. Bari, et al. Ion-induced biomolecular radiation damage: From isolated nucleobases to nucleobase clusters. *ChemPhysChem*, **7** (11), pp. 2339–2345, 2006. 4, 87, 93, 95, 107, 158, 159, 162

[83] F. Filsinger, J. Küpper, G. Meijer, et al. Pure samples of individual conformers: The separation of stereoisomers of complex molecules using electric fields. *Angew. Chem. Int. Ed.*, **48**(37), pp. 6900–6902, 2009. 4, 33, 35, 45, 63, 67

[84] F. Filsinger, J. Küpper, G. Meijer, et al. Quantum-state selection, alignment, and orientation of large molecules using static electric and laser fields. *J. Chem. Phys.*, 131(6):064309, 2009. 4, 37, 63, 67

[85] S. Trippel, Y.-P. Chang, S. Stern, et al. Spatial separation of state- and size-selected neutral clusters. *Phys. Rev. A*, **86**(3), pp. 033202, 2012. 4, 33, 63, 64, 67

[86] S. Riahi, S. Eynollahi, M. Ganjali, and P. Norouzi. Electronic and geometry studies on swainsonine, DNA base pairs and its complex. *Int. J. Electrochem. Sci*, **5**, pp. 355–366, 2010. 4

[87] I. I. Fabrikant, S. Caprasecca, G. A. Gallup, and J. D. Gorfinkiel. Electron attachment to molecules in a cluster environment. *J. Chem. Phys.*, 136(18):184301, 2012. 5, 32

[88] B. Boudaïffa, P. Cloutier, D. Hunting, M. A. Huels, and L. Sanche. Resonant formation of DNA strand breaks by low-energy (3 to 20 eV) electrons. *Science*, **287**(5458), pp. 1658–1660, 2000. 5, 7, 11, 31

[89] B. Liu, S. B. Nielsen, P. Hvelplund, et al. Collision-induced dissociation of hydrated adenosine monophosphate nucleotide ions: Protection of the ion in water nanoclusters. *Phys. Rev. Lett.*, **97**, pp. 133401, 2006. 5, 99

[90] M. Neustetter, J. Aysina, F. F. da Silva, and S. Denifl. The effect of solvation on electron attachment to pure and hydrated pyrimidine clusters. *Angew. Chem. Int. Ed.*, **54**(31), pp. 9124–9126, 2015. 5, 32

[91] A. G. Sanz, M. C. Fuss, A. Muñoz, et al. Modelling low energy electron and positron tracks for biomedical applications. *Int. J. Radiat. Biol.*, **88**(1-2), pp. 71–76, 2012. 6, 175

[92] M. M. Dawley and S. Ptasińska. Dissociative electron attachment to gas-phase n-methylformamide. *Int. J. of Mass Spectrom.*, **365–366**, pp. 143–151, 2014. 6

[93] A. Kumar and M. D. Sevilla. *Radical And Radical Ion Reactivity In Nucleic Acid Chemistry*, chapter Theoretical Modeling of Radiation-Induced DNA Damage, page 1. John Wiley & Sons, Inc., Hoboken, New Jersey, 2009. 7

[94] T. Douki, J.-L. Ravanat, J.-P. Pouget, I. Testard, and J. Cadet. Minor contribution of direct ionization to DNA base damage inducedby heavy ions. *Int. J. Radiat. Biol.*, **82**(2), pp. 119–127, 2006. 7

[95] J. D. Watson and F. H. C. Crick. Molecular structure of nucleic acids: A structure for deoxyribose nucleic acid. *Nature*, **171**(4356), pp. 737–738, 1953. 7

[96] J.-P. Schermann. *Spectroscopy and modelling of biomolecular building blocks.* Elsevier, Amsterdam ; Boston :, 2008. 7

[97] S. G. Gregory, K. F. Barlow, K. E. McLay, et al. The DNA sequence and biological annotation of human chromosome. *Nature*, **441**(7091), pp. 315–321, 2006. 7

[98] A. Kumar and M. D. Sevilla. Proton-coupled electron transfer in DNA on formation of radiation-produced ion radicals. *Chem. Rev.*, **110**(12), pp. 7002–7023, 2010. 8

[99] M. Dampc. *Zderzenia niskoenergetyczych elektronów z molekułami tetrahydrofuranu.* PhD thesis, Politechnika Gdańska, Wydział Fizyki Technicznej i Matematyki Stosowanej, Katedra Fizyki Zjawisk Elektronowych, 2012. 8

[100] T. M. Pawlik and K. Keyomarsi. Role of cell cycle in mediating sensitivity to radiotherapy. *Int. J. Radiat. Oncol. Biol. Phys.*, **59**(4), pp. 928 – 942, 2004. 8

[101] M. Chaplin. Do we underestimate the importance of water in cell biology? *Nat. Rev. Mol. Cell Biol.*, **7**(11), pp. 861–866, 2006. 8, 9

[102] R. E. Dickerson, H. R. Drew, B. N. Conner, et al. The anatomy of A-, B-, and Z-DNA. *Science*, **216**(4545), pp. pp.475–485, 1982. 8

[103] S. K. Pal, , and A. H. Zewail. Dynamics of water in biological recognition. *Chem. Rev.*, **104**(4), pp. 2099–2124, 2004. 9

[104] H. Khesbak, O. Savchuk, S. Tsushima, and K. Fahmy. The role of water h-bond imbalances in B-DNA substate transitions and peptide recognition revealed by time-resolved FTIR spectroscopy. *J. Am. Chem. Soc.*, **133**(15), pp. 5834–5842, 2011. 9

[105] K. Khistyaev, A. Golan, K. B. Bravaya, et al. Proton transfer in nucleobases is mediated by water. *J. Phys. Chem. A*, **117**(31), pp. 6789–6797, 2013. 9, 154

[106] L. Blancafort and A. Migani. Water effect on the excited-state decay paths of singlet excited cytosine. *J. Photochem. Photobiol., A*, **190**(2-3), pp. 283–289, 2007. 9, 96

[107] B. Alberts, A. Johnson, J. Lewis, et al. *Molecular Biology of the Cell.* Garland Science, Ney York, 4th edition, 2002. 9

[108] P. Byfield, John E.and Calabro-Jones, I. Klisak, and F. Kulhanian. Pharmacologic requirements for obtaining sensitization of human tumor cells in vitro to combined 5-fluorouracil or ftorafur and X-Rays. *Int. J. Radiat. Oncol. Biol. Phys.*, **8**(11), pp. 1923 – 1933, 1982. 9

[109] T. S. Lawrence, M. A. Davis, and J. Maybaum. The eighth international conference on chemical modifiers of cancer treatment part 2 dependence of 5-fluorouracil-mediated radiosensitization on dna-directed effects. *Int. J. Radiat. Oncol. Biol. Phys.*, **29**(3), pp. 519 – 523, 1994. 9

[110] S. E. Whitmore, C. S. Potten, C. A. Chadwick, P. T. Strickland, and W. L. Morison. Effect of photoreactivating light on uv radiation-induced alterations in human skin. *Photodermatology, Photoimmunology & Photomedicine*, **17**(5), pp. 213–217, 2001. 9

[111] P. Sung and H. Klein. Mechanism of homologous recombination: mediators and helicases take on regulatory functions. *Nat. Rev. Mol. Cell Biol.*, **7**(10), pp. 739–750, 2006. 11

[112] M. R. Lieber. The mechanism of human nonhomologous DNA end joining. *J. Biol. Chem.*, **283**(1), pp. 1–5, 2008. 11

[113] A. Yokoya, N. Shikazono, K. Fujii, et al. DNA damage induced by the direct effect of radiation. *Radiat. Phys. Chem.*, **77**(10-12), pp. 1280–1285, 2008. 11

[114] J. M. Hollas. *Modern Spectroscopy.* John Wiley & Sons, 4th edition, 2003. 15

[115] C. Leidlmair, P. Bartl, H. Schöbel, et al. Ionization of methane clusters in helium nanodroplets. *ChemPhysChem*, **13**(2), pp. 469–476, 2012. 16

[116] C. Leidlmair, Y. Wang, P. Bartl, et al. Structures, energetics, and dynamics of helium adsorbed on isolated fullerene ions. *Phys. Rev. Lett.*, **108**, pp. 076101, 2012. 16

[117] P. Bartl, C. Leidlmair, S. Denifl, P. Scheier, and O. Echt. Cationic complexes of hydrogen with helium. *ChemPhysChem*, **14**(1), pp. 227–232, 2013. 16

[118] R. L. Johnston. *Atomic and Molecular Clusters.* Taylor and Francis, 2002. 16, 17, 18

[119] T. R. Dyke, B. J. Howard, and W. Klemperer. Radiofrequency and microwave spectrum of the hydrogen fluoride dimer; a nonrigid molecule. *J. Chem. Phys.*, **56**(5), pp. 2442–2454, 1972. 17

[120] J. Emsley. Very strong hydrogen bonding. *Chem. Soc. Rev.*, **9**, pp. 91–124, 1980. 19

[121] J. W. Larson and T. B. McMahon. Gas-phase bihalide and pseudobihalide ions. an ion cyclotron resonance determination of hydrogen bond energies in XHY- species (X, Y = F, Cl, Br, CN). *Inorg. Chem.*, **23**(14), pp. 2029–2033, 1984. 19

[122] I. Schechter, H. Schröder, and K. L. Kompa. A simplified method for absolute MPI cross-section measurements. application to three-photon non-resonant ionization of Xe at 266 nm. *Chem. Phys. Lett.*, **194**(1), pp. 128–134, 1992. 21

[123] P. B. Corkum. Plasma perspective on strong field multiphoton ionization. *Phys. Rev. Lett.*, **71**, pp. 1994–1997, 1993. 21, 37

[124] J. Morellec, D. Normand, and G. Petite. Resonance shifts in the multiphoton ionization of cesium atoms. *Phys. Rev. A*, **14**, pp. 300–312, 1976. 21, 22

[125] B. Held, G. Mainfray, C. Manus, J. Morellec, and F. Sanchez. Resonant multiphoton ionization of a cesium atomic beam by a tunable-wavelength Q-switched neodymium-glass laser. *Phys. Rev. Lett.*, **30**, pp. 423–426, 1973. 22

[126] P. M. Johnson and C. E. Otis. Molecular multiphoton spectroscopy with ionization detection. *Annu. Rev. Phys. Chem.*, **32**(1), pp. 139–157, 1981. 22

[127] K. Wells, G. Roberts, and V. Stavros. Dynamics of H-loss in adenine via the $^1\pi\sigma^*$ state using a combination of ns and fs laser spectroscopy. *Chem. Phys. Lett.*, **446** (1-3), pp. 20–24, 2007. 22, 90, 93

[128] C. E. Otis and P. M. Johnson. The AC stark effect in molecular multiphoton ionization spectroscopy. *Chem. Phys. Lett.*, **83**(1), pp. 73–77, 1981. 22

[129] J. Makarewicz. Breakdown of the adiabatic approximation for strong coupled oscillators. *J. Phys. A: Math. Gen.*, **18**(4), pp. 557, 1985. 25

[130] B. Johnson and W. Reinhardt. Adiabatic separations of stretching and bending vibrations: Application to H_2O. *J. Chem. Phys.*, **85**, pp. 4538–4556, 1986. 25

[131] S. Pisana, M. Lazzeri, C. Casiraghi, et al. Breakdown of the adiabatic Born-Oppenheimer approximation in graphene. *Nat. Mater.*, **6**(3), pp. 198–201, 2007. 25

[132] N. Turro, V. Ramamurthy, and J. Scaiano. *Principles of Molecular Photochemistry: An Introduction.* University Science Books, 2009. 27

[133] D. R. Yarkony. *Nonadiabatic Derivative Couplings.* John Wiley & Sons, Ltd, 2002. 28

[134] T. Hirata, H. Ikeda, and H. Saigusa. Dynamics of excimer formation and relaxation in the T-Shaped benzene dimer. *J. Phys. Chem. A*, **103**(8), pp. 1014–1024, 1999. 28

[135] M. Meot-Ner. Ion thermochemistry of low-volatility compounds in the gas phase. 2. intrinsic basicities and hydrogen-bonded dimers of nitrogen heterocyclics and nucleic bases. *J. Am. Chem. Soc.*, **101**(9), pp. 2396–2403, 1979. 28, 97

[136] H. S. Park, S. H. Nam, J. K. Song, S. M. Park, and S. Ryu. Density functional study of intradimer proton transfers in hydrated adenine dimer ions, $A_2 + (H_2O)_n$ (n = 0–2). *J. Phys. Chem. A*, **112**(38), pp. 9023–9030, 2008. 28, 91

[137] B. Brutschy. Reactions in molecular clusters following photoionization. *J. Phys. Chem.*, **94**(24), pp. 8637–8647, 1990. 28

[138] A. Chaudhry and H. Kleinpoppen. *Analysis of Excitation and Ionization of Atoms and Molecules by Electron Impact*, volume 60 of *Springer Series on Atomic, Optical, and Plasma Physics.* Springer New York, 2011. 29, 30

[139] T. D. Märk and G. H. Dunn, editors. *Electron Impact Ionization.* Springer Vienna, 1985. 30

[140] S. H. Massey. *Negative Ions.* Cambridge University Press, 1976. 30

[141] L. Christophorou, editor. *Electron-Molecule Interactions and Their Applications*, volume 1. Academic Press INC, 1984. 30, 32

[142] I. I. Fabrikant and H. Hotop. Theory of electron attachment to co_2 clusters. *Phys. Rev. Lett.*, **94**, pp. 063201, 2005. 32

[143] H. Kallmann and F. Reiche. Über den durchgang bewegter moleküle durch inhomogene kraftfelder. *Zeitschrift für Physik*, **6**(1), pp. 352–375, 1921. 32

[144] G. Scoles. *Atomic and Molecular Beam Methods.* Atomic and Molecular Beam Methods. Oxford University Press, 1988. 33

[145] H. Loesch and A. Remscheid. Brute force in molecular reaction dynamics: A novel technique for measuring steric effects. *J. Chem. Phys.*, **93**(7), pp. 4779–4790, 1990. 34

[146] W. Kong and J. Bulthuis. Orientation of asymmetric top molecules in a uniform electric field: Calculations for species without symmetry axes. *J. Phys. Chem. A*, **104**(5), pp. 1055–1063, 2000. 35

[147] H. Mader, A. Guarnieri, J. Doose, et al. Comparative studies of j'-j=1-0 Co line parameters in frequency and time domains. *J. Mol. Spectrosc.*, **180**(1), pp. 183–187, 1996. 37

[148] M. Oldani and A. Bauder. Pure rotational spectrum of benzene-d1. *Chem. Phys. Lett.*, **108**(1), pp. 7–10, 1984. 37

[149] D. P. Pullman, B. Friedrich, and D. R. Herschbach. Facile alignment of molecular rotation in supersonic beams. *J. Chem. Phys.*, **93**(5), pp. 3224–3236, 1990. 38

[150] M. D. Morse. *Methods of Experimental Physics: Atomic, Molecular, and Optical Physics*, volume II. Atoms and Molecules, chapter 2: Supersonic beam sources, pages 21–47. Academic Press, Inc, 1996. 38, 41, 42, 52

[151] D. M. Lubman, C. T. Rettner, and R. N. Zare. How isolated are molecules in a molecular beam? *J. Phys. Chem.*, **86**(7), pp. 1129–1135, 1982. 40, 42

[152] X. Zou, X. Wang, C. Luo, and M. Han. Measuring the gas flow from a supersonic nozzle used in a 1.5-MA gas puff z pinch. *Plasma Science, IEEE Transactions on*, **30**(2), pp. 482–487, 2002. 44

[153] A. Amirav, U. Even, and J. Jortner. Cooling of large and heavy molecules in seeded supersonic beams. *Chemical Physics*, **51**, pp. 31–42, 1980. 45, 46, 47

[154] M. Allan. Electron collisions with formic acid monomer and dimer. *Phys. Rev. Lett.*, **98**, pp. 123201, 2007. 45, 65

[155] G. Berden, W. L. Meerts, M. Schmitt, and K. Kleinermanns. High resolution UV spectroscopy of phenol and the hydrogen bonded phenol-water cluster. *J. Chem. Phys.*, **104**(3), pp. 972–982, 1996. 45

[156] G. Bruny, S. Eden, S. Feil, et al. A new experimental setup designed for the investigation of irradiation of nanosystems in the gas phase: A high intensity mass-and-energy selected cluster beam. *Rev. Sci. Instrum.*, 83(1):013305, 2012. 45

[157] S. Yang, L. Philippe, and M. Châtelet. Formation of $(CH_4)_n$ van der waals clusters by seeded supersonic expansion. *Int. J. of Mass Spectrom.*, **263**(23), pp. 190–194, 2007. 45

[158] C. Zener. Interchange of translational, rotational and vibrational energy in molecular collisions. *Phys. Rev.*, **37**(5), pp. 556, 1931. 46, 47

[159] D. H. Levy. The spectroscopy of very cold gases. *Science*, **214**(4518), pp. 263–269, 1981. 46

[160] B. Barc, M. Ryszka, J. Spurrell, et al. Multi-photon ionization and fragmentation of uracil: Neutral excited-state ring opening and hydration effects. *J. Chem. Phys.*, 139(24):244311, 2013. 49, 54, 108, 121, 124, 127, 156, 163

[161] B. Barc, M. Ryszka, J.-C. Poully, et al. Multi-photon and electron impact ionisation studies of reactivity in adenine-water clusters. *Int. J. of Mass Spectrom.*, **365-366**, pp. 194–199, 2014. 49, 83, 165

[162] H. Ibach. Electron energy loss spectroscopy with resolution below 1 meV. *J. Electron. Spectrosc. Relat. Phenom.*, **64-65**, pp. 819–823, 1993. 65, 75

[163] S. Denifl, S. Ptasińska, M. Probst, et al. Electron attachment to the gas-phase DNA bases cytosine and thymine. *J. Phys. Chem. A*, **108**(31), pp. 6562–6569, 2004. 65

[164] E. Nir, M. Müller, L. Grace, and M. de Vriess. REMPI spectroscopy of cytosine. *Chem. Phys. Lett.*, **355**, pp. 59–64, 2002. 66

[165] R. Antunes, D. Almeida, G. Martins, et al. Negative ion formation in potassium-nitromethane collisions. *Phys. Chem. Chem. Phys.*, **12**, pp. 12513–12519, 2010. 68

[166] A. Schwettmann, J. Franklin, K. R. Overstreet, and J. P. Shaffer. Stark slowing asymmetric rotors: Weak-field-seeking states and nonadiabatic transitions. *J. Chem. Phys.*, **123**, pp. 194305, 2005. 68

[167] E. Alizadeh, F. F. da Silva, F. Zappa, et al. Dissociative electron attachment to nitromethane. *Int. J. of Mass Spectrom.*, **271**, pp. 15–21, 2008. 68

[168] G. W. Lemire, J. B. Simeonsson, and R. C. Sausa. Monitoring of vapor-phase nitro compounds using 226-nm radiation: fragmentation with subsequent no resonance-enhanced multiphoton ionization detection. *Anal. Chem.*, **65**(5), pp. 529–533, 1993. 68

[169] J.-S. Li, H.-M. Xiao, and H.-S. Dong. A theoretical study on the intermolecular interaction of energetic system—nitromethane dimer. *Chin. J. Chem.*, **18**(6), pp. 815–819, 2000. 71

[170] H. Ibach. *Electron energy loss spectrometers: the technology of high performance*, volume 63. Springer, 2013. 75

[171] N. L. Evans and S. Ullrich. Wavelength dependence of electronic relaxation in isolated adenine using UV femtosecond time-resolved photoelectron spectroscopy. *J. Phys. Chem. A*, **114**(42), pp. 11225–11230, 2010. 83

[172] H. Kang, J. Chang, S. H. Lee, et al. Excited-state lifetime of adenine near the first electronic band origin. *J. Chem. Phys.*, 133(15):154311, 2010. 83

[173] V. R. Smith, E. Samoylova, H.-H. Ritze, W. Radloff, and T. Schultz. Excimer states in microhydrated adenine clusters. *Phys. Chem. Chem. Phys.*, **12**, pp. 9632–9636, 2010. 83

[174] H.-H. Ritze, H. Lippert, E. Samoylova, et al. Relevance of $\pi\sigma^*$ states in the photoinduced processes of adenine, adenine dimer, and adenine-water complexes. *J. Chem. Phys.*, 122(22):224320, 2005. 83

[175] R. González-Luque, T. Climent, I. González-Ramírez, M. Merchán, and L. Serrano-Andrés. Singlet-triplet states interaction regions in DNA/RNA nucleobase hypersurfaces. *J. Chem. Theory Comput.*, **6**(7), pp. 2103–2114, 2010. 83

[176] R. Mitrić, U. Werner, M. Wohlgemuth, G. Seifert, and V. Bonačić-Koutecký. Nonadiabatic dynamics within time-dependent density functional tight binding method. *J. Phys. Chem. A*, **113**(45), pp. 12700–12705, 2009. 83

[177] S. Ullrich, T. Schultz, M. Z. Zgierski, and A. Stolow. Direct observation of electronic relaxation dynamics in adenine via time-resolved photoelectron spectroscopy. *J. Am. Chem. Soc.*, **126**(8), pp. 2262–2263, 2004. 83

[178] X. Chen, E. A. Syrstad, M. T. Nguyen, P. Gerbaux, and F. Tureček. Distonic isomers and tautomers of the adenine cation radical in the gas phase and aqueous solution. *J. Phys. Chem. A*, **108**(42), pp. 9283–9293, 2004. 83

[179] Y. Nosenko, M. Kunitski, C. Riehn, et al. The structure of adenine monohydrates studied by femtosecond multiphoton ionization detected IR spectroscopy and quantum chemical calculations. *Phys. Chem. Chem. Phys.*, **12**, pp. 863–870, 2010. 83

[180] I. Hünig, C. Plützer, K. A. Seefeld, et al. Photostability of isolated and paired nucleobases: N-H dissociation of adenine and hydrogen transfer in its base pairs examined by laser spectroscopy. *ChemPhysChem*, **5**(9), pp. 1427–1431, 2004. 83, 91, 97, 119

[181] M. Alauddin, M. Roy, J. K. Song, and S. M. Park. Infrared photodissociation of adenine dimer$(H_2O)_n^+$(n = 1-4) clusters. *Int. J. of Mass Spectrom.*, **381-382**, pp. 41–47, 2015. 83

[182] K. B. Bravaya, O. Kostko, S. Dolgikh, et al. Electronic structure and spectroscopy of nucleic acid bases: Ionization energies, ionization-induced structural changes, and photoelectron spectra. *J. Phys. Chem. A*, **114**(46), pp. 12305–12317, 2010. 85

[183] M. Piacenza and S. Grimme. Systematic quantum chemical study of DNA-base tautomers. *J. Comput. Chem.*, **25**(1), pp. 83–99, 2004. 85

[184] C. Plützer, E. Nir, M. S. de Vries, and K. Kleinermanns. IR-UV double-resonance spectroscopy of the nucleobase adenine. *Phys. Chem. Chem. Phys.*, **3**, pp. 5466–5469, 2001. 85

[185] E. Nir, C. Plützer, K. Kleinermanns, and M. de Vries. Properties of isolated DNA bases, base pairs and nucleosides examined by laser spectroscopy. *Eur. Phys. J. D*, **20**(3), pp. 317–329, 2002. 85

[186] J. Lin, C. Yu, S. Peng, et al. Ultraviolet photoelectron studies of the ground-state electronic structure and gas-phase tautomerism of hypoxanthine and guanine. *J. Phys. Chem.*, **84**(9), pp. 1006–1012, 1980. 85

[187] R. Ramaekers, A. Dkhissi, L. Adamowicz, and G. Maes. Matrix-isolation FT–IR study and theoretical calculations of the hydrogen-bond interaction of hypoxanthine with h_2o. *J. Phys. Chem. A*, **106**(18), pp. 4502–4512, 2002. 85

[188] M. K. Shukla and J. Leszczynski. Theoretical study of proton transfer in hypoxanthine tautomers: Effects of hydration. *J. Phys. Chem. A*, **104**(13), pp. 3021–3027, 2000. 85

[189] G. Sheina, S. Stepanian, E. Radchenko, and Y. Blagoi. IR spectra of guanine and hypoxanthine isolated molecules. *J. Mol. Struct.*, **158**, pp. 275–292, 1987. 86

[190] L. R. Rutledge, C. A. Wheaton, and S. D. Wetmore. A computational characterization of the hydrogen-bonding and stacking interactions of hypoxanthine. *Phys. Chem. Chem. Phys.*, **9**, pp. 497–509, 2007. 87

[191] M. K. Shukla and J. Leszczynski. Electronic spectra, excited-state geometries, and molecular electrostatic potentials of hypoxanthine: A theoretical investigation. *J. Phys. Chem. A*, **107**(29), pp. 5538–5543, 2003. 87

[192] X. Sun and J. K. Lee. Acidity and proton affinity of hypoxanthine in the gas phase versus in solution: Intrinsic reactivity and biological implications. *J. Org. Chem.*, **72**(17), pp. 6548–6555, 2007. 87

[193] R. Tembreull and D. M. Lubman. Pulsed laser desorption of biological molecules in supersonic beam mass spectrometry with resonant two-photon ionization detection. *Anal. Chem.*, **59**(8), pp. 1082–1088, 1987. 87, 90, 93, 104

[194] M. M. Dawley, K. Tanzer, W. A. Cantrell, et al. Electron ionization of the nucleobases adenine and hypoxanthine near the threshold: a combined experimental and theoretical study. *Phys. Chem. Chem. Phys.*, **16**, pp. 25039–25053, 2014. 87

[195] M. M. Dawley, K. Tanzer, I. Carmichael, S. Denifl, and S. Ptasińska. Dissociative electron attachment to the gas-phase nucleobase hypoxanthine. *J. Chem. Phys.*, 142(21):215101, 2015. 87

[196] N. J. Kim, H. Kang, G. Jeong, et al. Anomalous fragmentation of hydrated clusters of DNA base adenine in UV photoionization. *J. Phys. Chem. A*, **104**(28), pp. 6552–6557, 2000. 87, 88, 89, 91, 97, 98

[197] P. J. van der Burgt. Electron impact fragmentation of cytosine: partial ionization cross sections for positive fragments. *Eur. Phys. J. D*, **68**(5), pp. 135, 2014. 88

[198] S. H. Nam, H. S. Park, J. K. Song, and S. M. Park. Photoinduced dynamics of hydrated adenine clusters. *J. Phys. Chem. A*, **111**(18), pp. 3480–3484, 2007. 89, 90, 96, 97

[199] J. H. Hahn, R. Zenobi, and R. N. Zare. Subfemtomole quantitation of molecular adsorbates by two-step laser mass spectrometry. *J. Am. Chem. Soc.*, **109**(9), pp. 2842–2843, 1987. 90

[200] M. de Vries. *Radiation Induced Molecular Phenomena in Nucleic Acids,*, chapter Isolated DNA base pairs, interplay between theory and experiment, page 323. Springer, Netherlands, 2008. 90

[201] C. Hwang, C. L. Stumpf, Y.-Q. Yu, and H. I. Kenttämaa. Intrinsic acidity and redox properties of the adenine radical cation. *Int. J. of Mass Spectrom.*, **182-183** (0), pp. 253–259, 1999. 91, 92

[202] R. Mota, R. Parafita, A. Giuliani, et al. Water VUV electronic state spectroscopy by synchrotron radiation. *Chem. Phys. Lett.*, **416**, pp. 152–159, 2005. 92, 96, 97, 159

[203] M. R. Querry, D. M. Wieliczka, and D. J. Segelstein. *Handbook of Optical Constants of Solids II*, chapter Water (H_2O), page 1059–1077. Academic, San Diego, Calif., 1998. 92, 96, 159

[204] Y. Itikawa and N. Mason. Cross sections for electron collisions with water molecules. *J. Phys. Chem. Ref. Data*, **34**(1), pp. 1–22, 2005. 92, 96, 159

[205] C.-H. Lin, J. Matsumoto, S. Ohtake, and T. Imasaka. Supersonic jet/time-of-flight mass spectrometry of adenine using nanosecond and femtosecond lasers. *Talanta*, **43**(11), pp. 1925–1929, 1996. 93, 104

[206] J. Tabet, S. Eden, S. Feil, et al. Absolute total and partial cross sections for ionization of nucleobases by proton impact in the Bragg peak velocity range. *Phys. Rev. A*, **82**, pp. 022703, 2010. 93, 107, 165

[207] P. J. van der Burgt, S. Finnegan, and S. Eden. Electron impact fragmentation of adenine: partial ionization cross sections for positive fragments. *Eur. Phys. J. D*, 69(7):173, 2015. 93, 165, 183

[208] C. C. Nelson and J. A. McCloskey. Collision-induced dissociation of adenine. *J. Am. Chem. Soc.*, **114**(10), pp. 3661–3668, 1992. 95

[209] J. J. Szymczak, T. Müller, and H. Lischka. The effect of hydration on the photodeactivation pathways of 4-aminopyrimidine. *Chemical Physics*, **375**(1), pp. 110–117, 2010. 96

[210] S. H. Nam, H. S. Park, S. Ryu, J. K. Song, and S. M. Park. Photodissociation dynamics of adenine dimer radical ions and hydrated adenine dimer ions, (n = 0–6). *Chem. Phys. Lett.*, **450**(4-6), pp. 236–242, 2008. 97

[211] S. Carles, F. Lecomte, J. P. Schermann, and C. Desfrançois. Gas-phase experimental and theoretical studies of adenine, imidazole, pyrrole, and water noncovalent complexes. *J. Phys. Chem. A*, **104**(46), pp. 10662–10668, 2000. 99

[212] F. Alvarado, S. Bari, R. Hoekstra, and T. Schlathölter. Interactions of neutral and singly charged keV atomic particles with gas-phase adenine molecules. *J. Chem. Phys.*, 127(3):034301, 2007. 99

[213] M. Shukla and J. Leszczynski. Phototautomerism in uracil: a quantum chemical investigation. *J. Phys. Chem. A*, **106**(37), pp. 8642–8650, 2002. 101, 102, 159

[214] R. N. Casaes, J. B. Paul, R. P. McLaughlin, R. J. Saykally, and T. van Mourik. Infrared cavity ringdown spectroscopy of jet-cooled nucleotide base clusters and water complexes. *J. Phys. Chem. A*, **108**(50), pp. 10989–10996, 2004. 102, 145

[215] P. Carbonniere, C. Pouchan, and R. Improta. Intramolecular vibrational redistribution in the non-radiative excited state decay of uracil in the gas phase: an *ab initio* molecular dynamics study. *Phys. Chem. Chem. Phys.*, **17**, pp. 11615–11626, 2015. 102

[216] A. Gedanken, M. Robin, and N. Kuebler. Nonlinear photochemistry in organic, inorganic, and organometallic systems. *J. Phys. Chem.*, **86**(21), pp. 4096–4107, 1982. 103

[217] B. B. Brady, L. A. Peteanu, and D. H. Levy. The electronic spectra of the pyrimidine bases uracil and thymine in a supersonic molecular beam. *Chem. Phys. Lett.*, **147**(6), pp. 538–543, 1988. 103, 104

[218] M. Schneider, R. Maksimenka, F. J. Buback, et al. Photodissociation of thymine. *Phys. Chem. Chem. Phys.*, **8**, pp. 3017–3021, 2006. 103

[219] E. Samoylova, T. Schultz, I. Hertel, and W. Radloff. Analysis of ultrafast relaxation in photoexcited DNA base pairs of adenine and thymine. *Chemical Physics*, **347**(1-3), pp. 376–382, 2008. 103

[220] J. Gonzalez-Vazquez, L. Gonzalez, E. Samoylova, and T. Schultz. Thymine relaxation after UV irradiation: the role of tautomerization and $\pi\sigma^*$ states. *Phys. Chem. Chem. Phys.*, **11**, pp. 3927–3934, 2009. 103

[221] M. Schneider, C. Schon, I. Fischer, L. Rubio-Lago, and T. Kitsopoulos. Photodissociation of uracil. *Phys. Chem. Chem. Phys.*, **9**, pp. 6021–6026, 2007. 104

[222] S. Matsika, M. Spanner, M. Kotur, and T. C. Weinacht. Ultrafast relaxation dynamics of uracil probed via strong field dissociative ionization. *J. Phys. Chem. A*, **117**(48), pp. 12796–12801, 2013. 104, 133, 148

[223] M. Etinski, T. Fleig, and C. M. Marian. Intersystem crossing and characterization of dark states in the pyrimidine nucleobases uracil, thymine, and 1-methylthymine. *J. Phys. Chem. A*, **113**(43), pp. 11809–11816, 2009. 105, 110, 130, 132

[224] M. T. Nguyen, R. Zhang, P.-C. Nam, , and A. Ceulemans. Singlet–triplet energy gaps of gas-phase RNA and DNA bases. a quantum chemical study. *J. Phys. Chem. A*, **108**(31), pp. 6554–6561, 2004. 105

[225] C. Lecompte, G. Mainfray, C. Manus, and F. Sanchez. Laser temporal-coherence effects on multiphoton ionization processes. *Phys. Rev. A*, **11**, pp. 1009–1015, 1975. 105

[226] S. Denifl, B. Sonnweber, G. Hanel, P. Scheier, and T. Märk. Threshold electron impact ionization studies of uracil. *Int. J. of Mass Spectrom.*, **238**(1), pp. 47–53, 2004. 107

[227] S. Feil, K. Gluch, S. Matt-Leubner, et al. Partial cross sections for positive and negative ion formation following electron impact on uracil. *J. Phys. B: At., Mol. Opt. Phys.*, **37**(15), pp. 3013, 2004. 107

[228] B. Coupier, B. Farizon, M. Farizon, et al. Inelastic interactions of protons and electrons with biologically relevant molecules. *Eur. Phys. J. D*, **20**(3), pp. 459–468, 2002. 107

[229] A. L. Padellec, P. Moretto-Capelle, M. Richard-Viard, J. P. Champeaux, and P. Cafarelli. Ionization and fragmentation of DNA, RNA bases induced by proton impact. *Journal of Physics: Conference Series*, **101**(1), pp. 012007, 2008. 107

[230] T. Schlathölter, F. Alvarado, and R. Hoekstra. Ion-biomolecule interactions and radiation damage. *Nuclear Instruments and Methods in Physics Research Section B: Beam Interactions with Materials and Atoms*, **233**, pp. 62–69, 2005. 107

[231] J. de Vries, R. Hoekstra, R. Morgenstern, and T. Schlathölter. C q+ -induced excitation and fragmentation of uracil: effects of the projectile electronic structure. *J. Phys. B: At., Mol. Opt. Phys.*, **35**(21), pp. 4373, 2002. 107

[232] J. de Vries, R. Hoekstra, R. Morgenstern, and T. Schlathölter. Charge driven fragmentation of nucleobases. *Phys. Rev. Lett.*, **91**, pp. 053401, 2003. 107

[233] J. de Vries, R. Hoekstra, R. Morgenstern, and T. Schlathölter. Ionization and fragmentation modes of nucleobases after collisions with multiply charged ions. *Phys. Scr.*, **2004**(T110), pp. 336, 2004. 107

[234] C. Zhou, S. Matsika, M. Kotur, and T. C. Weinacht. Fragmentation pathways in the uracil radical cation. *J. Phys. Chem. A*, **116**(37), pp. 9217–9227, 2012. 107, 108

[235] L. Sadr-Arani, P. Mignon, H. Abdoul-Carime, et al. DFT study of the fragmentation mechanism of uracil RNA base. *Phys. Chem. Chem. Phys.*, **14**, pp. 9855–9870, 2012. 108, 109, 125

[236] I. Lopez-Quintas, M. Oujja, M. Sanz, et al. Characterization of laser-induced plasmas of nucleobases: Uracil and thymine. *Applied Surface Science*, **302**, pp. 299–302, 2014. 108

[237] R. Delaunay, J.-P. Champeaux, S. Maclot, et al. Prompt and delayed fragmentation of bromouracil cations ionized by multiply charged ions. *Eur. Phys. J. D*, 68 (6):162, 2014. 118

[238] W. Li, S. A. Lahankar, C. Huang, et al. Multiphoton processes of CO at 230 nm. *Phys. Chem. Chem. Phys.*, **8**, pp. 2950–2957, 2006. 119

[239] A. Dogariu and R. B. Miles. Detecting localized trace species in air using radar resonance-enhanced multi-photon ionization. *Appl. Opt.*, **50**(4), pp. A68–A73, 2011. 119

[240] A. A. Zadorozhnaya and A. I. Krylov. Ionization-induced structural changes in uracil dimers and their spectroscopic signatures. *J. Chem. Theory Comput.*, **6**(3), pp. 705–717, 2010. 120, 152, 161

[241] M. Liu, T. Li, F. S. Amegayibor, et al. Gas-phase thermochemical properties of pyrimidine nucleobases. *J. Org. Chem.*, **73**(23), pp. 9283–9291, 2008. 120

[242] C. L. Stumpf. *Application of Fourier transform ion cyclotron resonance mass spectrometry to a mechanistic study, examination of the properties of nucleobase radical cations, and chemical ionization reagent development.* PhD thesis, Purdue University, Indiana,USA, 2000. 120

[243] J. J. Manura and D. J. Manura. Scientific instrument services isotope distribution calculator, accessed 2015. 121

[244] H. R. Hudock, B. G. Levine, A. L. Thompson, et al. *Ab Initio* molecular dynamics and time-resolved photoelectron spectroscopy of electronically excited uracil and thymine. *J. Phys. Chem. A*, **111**(34), pp. 8500–8508, 2007. 123, 132

[245] M. Ryszka, R. Pandey, C. Rizk, et al. Dissociative multi-photon ionization of isolated uracil and uracil–adenine complexes. *Int. J. of Mass Spectrom.*, In Press, 2016. 127

[246] G. N. Ten and V. I. Baranov. Analysis of electronic–vibrational spectra of uracil, thymine, and cytosine. *Opt. Spectrosc.*, **97**(2), pp. 195–203, 2004. 130

[247] T. Gustavsson, Á. Bányász, E. Lazzarotto, et al. Singlet excited-state behavior of uracil and thymine in aqueous solution: A combined experimental and computational study of 11 uracil derivatives. *J. Am. Chem. Soc.*, **128**(2), pp. 607–619, 2006. 132, 151, 159, 167

[248] H. Nieber and N. L. Doltsinis. Elucidating ultrafast nonradiative decay of photoexcited uracil in aqueous solution by *ab initio* molecular dynamics. *Chemical Physics*, **347**(1–3), pp. 405–412, 2008. 132

[249] B. P. Fingerhut, K. E. Dorfman, and S. Mukamel. Monitoring nonadiabatic dynamics of the rna base uracil by UV pump–ir probe spectroscopy. *J. Phys. Chem. Lett.*, **4**(11), pp. 1933–1942, 2013. 132

[250] Z. Lan, E. Fabiano, and W. Thiel. Photoinduced nonadiabatic dynamics of pyrimidine nucleobases: On-the-fly surface-hopping study with semiempirical methods. *J. Phys. Chem. B*, **113**(11), pp. 3548–3555, 2009. 132

[251] M. Barbatti, A. J. A. Aquino, J. J. Szymczak, et al. Relaxation mechanisms of UV-photoexcited DNA and RNA nucleobases. *Proceedings of the National Academy of Sciences*, **107**(50), pp. 21453–21458, 2010. 132

[252] R. W. Boyd. *Nonlinear Optics.* Academic Press, Burlington, third edition edition, 2008. 135

[253] Y. B. Band, D. F. Heller, J. R. Ackerhalt, and J. S. Krasinski. Spectrum of second-harmonic generation for multimode fields. *Phys. Rev. A*, **42**, pp. 1515–1521, 1990. 135

[254] R. Paschotta, P. Kürz, R. Henking, S. Schiller, and J. Mlynek. 82% efficient continuous-wave frequency doubling of 1.06μm with a monolithic mgo:linbo3resonator. *Opt. Lett.*, **19**(17), pp. 1325–1327, 1994. 135

[255] C. R. Calvert, L. Belshaw, M. J. Duffy, et al. LIAD-fs scheme for studies of ultrafast laser interactions with gas phase biomolecules. *Phys. Chem. Chem. Phys.*, **14**, pp. 6289–6297, 2012. 136

[256] J.-C. Poully, J. Miles, S. De Camillis, A. Cassimi, and J. B. Greenwood. Proton irradiation of DNA nucleosides in the gas phase. *Phys. Chem. Chem. Phys.*, **17**, pp. 7172–7180, 2015. 136

[257] F. Calegari, D. Ayuso, A. Trabattoni, et al. Ultrafast electron dynamics in phenylalanine initiated by attosecond pulses. *Science*, **346**(6207), pp. 336–339, 2014. 136

[258] A. V. Zinovev, I. V. Veryovkin, J. F. Moore, and M. J. Pellin. Laser-driven acoustic desorption of organic molecules from back-irradiated solid foils. *Anal. Chem.*, **79**(21), pp. 8232–8241, 2007. 136, 146

[259] W. C. Wiley and I. H. McLaren. Time-of-flight mass spectrometer with improved resolution. *Rev. Sci. Instrum.*, **26**(12), pp. 1150–1157, 1955. 137

[260] X. Chen, E. A. Syrstad, M. T. Nguyen, P. Gerbaux, and F. Tureček. Adenine radicals in the gas phase: an experimental and computational study of hydrogen atom adducts to adenine. *J. Phys. Chem. A*, **109**(36), pp. 8121–8132, 2005. 144

[261] J. Zhou, O. Kostko, C. Nicolas, et al. Experimental observation of guanine tautomers with VUV photoionization. *J. Phys. Chem. A*, **113**(17), pp. 4829–4832, 2009. 146

[262] Y. He, C. Wu, and W. Kong. Photophysics of methyl-substituted uracils and thymines and their water complexes in the gas phase. *J. Phys. Chem. A*, **108**(6), pp. 943–949, 2004. 151, 158, 167

[263] M. Etinski and C. M. Marian. *Ab initio* investigation of the methylation and hydration effects on the electronic spectra of uracil and thymine. *Phys. Chem. Chem. Phys.*, **12**, pp. 4915–4923, 2010. 151, 159, 167

[264] A. A. Golubeva and A. I. Krylov. The effect of π-stacking and h-bonding on ionization energies of a nucleobase: uracil dimer cation. *Phys. Chem. Chem. Phys.*, **11**, pp. 1303–1311, 2009. 152

[265] A. Jefrey and W. Saenger. *Hydrogen Bonding in Biolgical Systems.* Springer-Verlag: Berlin, 1991. 152

[266] B. Herrera and A. Toro-Labbé. The role of reaction force and chemical potential in characterizing the mechanism of double proton transfer in the adenine-uracil complex. *J. Phys. Chem. A*, **111**(26), pp. 5921–5926, 2007. 152

[267] J. Bertran, A. Oliva, L. Rodríguez-Santiago, and M. Sodupe. Single versus double proton-transfer reactions in Watson-Crick base pair radical cations. a theoretical study. *J. Am. Chem. Soc.*, **120**(32), pp. 8159–8167, 1998. 152, 166

[268] J. P. Cerón-Carrasco, A. Requena, E. A. Perpète, C. Michaux, and D. Jacquemin. Double proton transfer mechanism in the adenine–uracil base pair and spontaneous mutation in RNA duplex. *Chem. Phys. Lett.*, **484**(1–3), pp. 64–68, 2009. 152

[269] S. Ø. Pedersen, C. S. Byskov, F. Turecek, and S. B. Nielsen. Structures of protonated thymine and uracil and their monohydrated gas-phase ions from ultraviolet action spectroscopy and theory. *J. Phys. Chem. A*, **118**(24), pp. 4256–4265, 2014. 154

[270] S. Kim and H. F. Schaefer. Effects of microsolvation on the adenine-uracil base pair and its radical anion: adenine-uracil mono- and dihydrates. *J. Phys. Chem. A*, **111**(41), pp. 10381–10389, 2007. 154

[271] V. Ludwig, Z. M. da Costa, M. S. do Amaral, et al. Photophysics and photostability of adenine in aqueous solution: A theoretical study. *Chem Phys Lett*, **492** (1–3), pp. 164–169, 2010. 154

[272] E. Epifanovsky, K. Kowalski, P.-D. Fan, et al. On the electronically excited states of uracil. *J. Phys. Chem. A*, **112**(40), pp. 9983–992, 2008. 154

[273] C. Plützer, I. Hünig, K. Kleinermanns, E. Nir, and M. S. de Vries. Pairing of isolated nucleobases: Double resonance laser spectroscopy of adenine-thymine. *ChemPhysChem*, **4**(8), pp. 838–842, 2003. 156

[274] S. R. Gadre, K. Babu, and A. P. Rendell. Electrostatics for exploring hydration patterns of molecules. 3. uracil. *J. Phys. Chem. A*, **104**(39), pp. 8976–8982, 2000. 157

[275] T. van Mourik, S. L. Price, and D. C. Clary. *Ab Initio* calculations on uracil–water. *J. Phys. Chem. A*, **103**(11), pp. 1611–1618, 1999. 157

[276] T. van Mourik, D. M. Benoit, S. L. Price, and D. C. Clary. *Ab initio* and diffusion Monte Carlo study of uracil-water, thymine-water, cytosine-water, and cytosine-$(water)_2$. *Phys. Chem. Chem. Phys.*, **2**, pp. 1281–1290, 2000. 157

[277] V. B. Delchev, I. G. Shterev, and H. Mikosch. Theoretical investigation (DFT and MP2) of the intermolecular proton transfer in the supersystems uracil-$(H_2O)_n$ and uracil-$(CH_3OH)_n$ (n = 1, 2). *Monatshefte für Chemie - Chemical Monthly*, **139**(4), pp. 349–362, 2008. 157

[278] V. I. Danilov, T. van Mourik, and V. I. Poltev. Modeling of the "hydration shell" of uracil and thymine in small water clusters by DFT and MP2 methods. *Chem. Phys. Lett.*, **429**(1-3), pp. 255–260, 2006. 157

[279] T. van Mourik, V. Danilov, V. Dailidonis, et al. A DFT study of uracil and 5-bromouracil in nanodroplets. *Theor. Chem. Acc.*, **125**(3-6), pp. 233–244, 2010. 157

[280] N. J. Kim, H. Kang, G. Jeong, et al. Even-odd alternation in mass spectrum of thymine and uracil clusters: Evidence of intracluster photodimerization. *Proceedings of the National Academy of Sciences*, **98**(9), pp. 4841–4843, 2001. 157, 159, 162

[281] See http://winter.group.shef.ac.uk/chemputer/ for M. Winter, University of Sheffield;, accessed 2013. 159

[282] A. M. Rasmussen, M. C. Lind, S. Kim, and H. F. Schaefer. Hydration of the lowest triplet states of the DNA/RNA pyrimidines. *J. Chem. Theory Comput.*, **6** (3), pp. 930–939, 2010. 161

[283] J. Šponer, J. Leszczyński, and P. Hobza. Nature of nucleic acid-base stacking: Nonempirical *ab initio* and empirical potential characterization of 10 Stacked base dimers. comparison of stacked and h-bonded base pairs. *J. Phys. Chem.*, **100**(13), pp. 5590–5596, 1996. 163, 165

[284] L. Sadr-Arani, P. Mignon, H. Chermette, and T. Douki. Theoretical and experimental study of the fragmentation of protonated uracil. *Chemical Physics Letters*, **605-606**, pp. 108–114, 2014. 165

[285] A. Martínez. Do anionic gold clusters modify conventional hydrogen bonds? The interaction of anionic Au_n (n = 2-4) with the adenine-uracil base pair. *J. Phys. Chem. A*, **113**(6), pp. 1134–1140, 2009. 165

[286] K. Kleinermanns, D. Nachtigallová, and M. S. de Vries. Excited state dynamics of DNA bases. *Int. Rev. Phys. Chem*, **32**(2), pp. 308–342, 2013. 165

[287] T. Takaya, C. Su, K. de La Harpe, C. E. Crespo-Hernández, and B. Kohler. UV excitation of single DNA and RNA strands produces high yields of exciplex states between two stacked bases. *Proceedings of the National Academy of Sciences*, **105** (30), pp. 10285–10290, 2008. 165

[288] X. Li, Z. Cai, , and M. D. Sevilla. Energetics of the radical ions of the AT and AU base pairs: A density functional theory (DFT) study. *J. Phys. Chem. A*, **106** (40), pp. 9345–9351, 2002. 166